LHCb reoptimized detector design and performance : Technical Design Report

R. Antunes Nobrega, A. Franca Barbosa, I. Bediaga, G. Cernicchiaro, E. Correade Oliveira, J. Magnin, J. Marquesde Miranda, A. Massafferri, E. Polycarpo, A. Reis, et al.

To cite this version:

R. Antunes Nobrega, A. Franca Barbosa, I. Bediaga, G. Cernicchiaro, E. Correade Oliveira, et al.. LHCb reoptimized detector design and performance : Technical Design Report. 2003, pp.x-127. in2p3-00025912

HAL Id: in2p3-00025912
https://in2p3.hal.science/in2p3-00025912v1

Submitted on 7 Apr 2006

CERN/LHCC 2003-030
LHCb TDR 9
9 September 2003

LHCb

Technical Design Report

Reoptimized Detector Design and Performance

Printed at CERN
Geneva, 2003
ISBN 92-9083-209-6

The LHCb Collaboration

Brasilian Center for Research in Physics, CBPF, Rio de Janeiro, Brasil
R. Antunes Nobrega, A. Franca Barbosa[1)], I. Bediaga, G. Cernicchiaro, E. Correa de Oliveira, J. Magnin, J. Marques de Miranda, A. Massafferri, E. Polycarpo, A. Reis

Federal University of Rio de Janeiro, UFRJ, Rio de Janeiro, Brasil
K. Akiba, S. Amato, T. da Silva, J.R.T. de Mello Neto, B. de Paula, L. de Paula, M. Gandelman, J.H. Lopes, B. Marechal, F. Marinho, D. Moraes[2)], N. Pelloux[1)], C. Perreira Nunes

LAPP Annecy, IN2P3-CNRS, Annecy-Le-Vieux, France
J. Ballansat, D. Boget, P. Delebecque, I. De Bonis, D. Decamp, C. Drancourt, N. Dumont Dayot, C. Girard, B. Lieunard, M.-N. Minard, B. Pietrzyk, H. Terrier

LPC Clermont, IN2P3-CNRS and University Blaise Pascal, Clermont-Ferrand, France
Z. Ajaltouni, G. Bohner, C. Carloganu, R. Cornat, O. Deschamps, P. Henrard, J. Lecoq, R. Lefevre, S. Monteil, P. Perret, C. Rimbault, A. Robert

CPPM Marseille, IN2P3-CNRS and University of Aix-Marseille II, Marseille, France
E. Aslanides, J.-P. Cachemiche, B. Dinkespiler, P.-Y. Duval, R. Le Gac, V. Garonne, O. Leroy, P.-L. Liotard, M. Menouni, A. Tsaregorodtsev, B. Viaud

LAL Orsay, IN2P3-CNRS and University of Paris-Sud, Orsay, France
G. Barrand, C. Beigbeder-Beau, R. Beneyton, D. Breton, O. Callot[1)], D. Charlet, B. D'Almagne, B. Delcourt, O. Duarte, F. Fulda Quenzer, B. Jean-Marie, J. Lefrançois, F. Machefert, P. Robbe, M.-H. Schune, V. Tocut, K. Truong

Technical University of Dresden, Dresden, Germany
R. Schwierz, B. Spaan

Max-Planck-Institute for Nuclear Physics, Heidelberg, Germany
M. Agari, C. Bauer, D. Baumeister, J. Blouw, N. Bulian, H.P. Fuchs, W. Hofmann, K.T. Knöpfle, S. Löchner, A. Ludwig, M. Schmelling, B. Schwingenheuer

Physics Institute, University of Heidelberg, Heidelberg, Germany
S. Bachmann, P. Bock, H. Deppe, F. Eisele, S. Henneberger, P. Igo-Kemenes, R. Rusnyak, U. Stange, U. Trunk, M. Walter, D. Wiedner, U. Uwer

Kirchhoff Institute for Physics, University of Heidelberg, Heidelberg, Germany
I. Kisel, V. Lindenstruth, M.W. Schulz[2)]

Laboratori Nazionali dell' INFN, Frascati, Italy
G. Bencivenni, C. Bloise, F. Bossi, P. Campana, G. Capon, P. de Simone, C. Forti, G. Lanfranchi, F. Murtas, L. Passalacqua, V. Patera[3)], M. Poli Lener, A. Sciubba[3)]

University of Bologna and INFN, Bologna, Italy
G. Avoni, G. Balbi, M. Bargiotti, A. Bertin, M. Bruschi, A. Carbone, S. de Castro, P. Faccioli, L. Fabbri, D. Galli, B. Giacobbe, F. Grimaldi, I. Lax, U. Marconi, I. Massa, M. Piccinini, N. Semprini-Cesari, R. Spighi, V. Vagnoni, S. Vecchi, M. Villa, A. Vitale, A. Zoccoli

University of Cagliari and INFN, Cagliari, Italy
W. Bonivento, S. Cadeddu, A. Cardini, V. de Leo, C. Deplano, A. Lai, D. Raspino, B. Saitta

University of Ferrara and INFN, Ferrara, Italy
W. Baldini, V. Carassiti, A. Cotta Ramusino, P. Dalpiaz, S. Germani, A. Gianoli, M. Martini, F. Petrucci, M. Savrié

University of Florence and INFN, Florence, Italy
A. Bizzeti, M. Lenti, M. Lenzi, G. Passaleva, P.G. Pelfer, M. Veltri

University of Genoa and INFN, Genoa, Italy
S. Cuneo, F. Fontanelli, V. Gracco, G. Mini, P. Musico, A. Petrolini, M. Sannino

University of Milano-Bicocca and INFN, Milano, Italy
T. Bellunato, M. Calvi, C. Matteuzzi, M. Musy, P. Negri, D. Perego, L. Trentadue[4]

University of Rome, "La Sapienza" and INFN, Rome, Italy
G. Auriemma[5], V. Bocci, C. Bosio, E. Dane, D. Fidanza[5], A. Frenkel, G. Martellotti, G. Penso, S. Petrarca, D. Pinci, G. Pirozzi, W. Rinaldi, R. Santacesaria, C. Satriano[5], A. Satta

University of Rome, "Tor Vergata" and INFN, Rome, Italy
G. Carboni, S. de Capua, D. Domenici, R. Messi, G. Natali, L. Pacciani, E. Santovetti

NIKHEF, The Netherlands
G. van Apeldoorn(i,iii), N. van Bakel(i,ii), T.S. Bauer(i), M. van Beuzekom(i), J.F.J. van den Brand(i,ii), H.J. Bulten(i,ii), M. Doets(i), R. Hierck(i), L. Hommels(i), J. van Hunen(i), E. Jans(i), T. Ketel(i,ii), S. Klous(i,ii), M.J. Kraan(i), M. Merk(i), F. Mul(ii), J. Nardulli(i), A. Pellegrino(i), G. Raven(i,ii), H. Schuijlenburg(i), T. Sluijk(i), P. Vankov(i), J. van Tilburg(i), H. de Vries(i), L. Wiggers(i), M. Zupan(i)
(i) Foundation of Fundamental Research of Matter in the Netherlands
(ii) Free University Amsterdam
(iii) University of Amsterdam

Research Centre of High Energy Physics, Tsinghua University, Beijing, P.R.C.
M. Bisset, J.P. Cheng, Y.G. Cui, Y. Dai, Y. Gao, H.J. He, C. Huang, C. Jiang, Y.P. Kuang, Q.Li, Y.J. Li, Y. Liao, J.P. Ni, B.B. Shao,J.J. Su, Y.R. Tian, Q. Wang, Q.S. Yan

Institute of Nuclear Physics and University of Mining and Metallurgy, Krakow, Poland
K. Ciba, K. Galuszka, L. Hajduk, P. Kapusta, J. Michalowski, B. Muryn, Z. Natkaniec, A. Oblakowska-Mucha, G. Polok, M. Stodulski, M. Witek[1], P. Zychowski

Soltan Institute for Nuclear Studies, Warsaw, Poland
M. Adamus, A. Chlopik, Z. Guzik, A. Nawrot, K. Syryczynski, M. Szczekowski

National Institute for Physics and Nuclear Engineering, IFIN-HH, Bucharest-Magurele, Romania
C. Coca, O. Dima, G. Giolu, C. Magureanu, M. Orlandea, S. Popescu[1], A.M. Rosca[6], P.D. Tarta

Institute for Nuclear Research (INR), Moscow, Russia
S. Filippov, J. Gavrilov, E. Guschin, V. Kloubov, L. Kravchuk, S. Laptev, V. Laptev, V. Postoev, G. Rybkine, A. Sadovski, I. Semeniouk, V. Strigin

Institute of Theoretical and Experimental Physics (ITEP), Moscow, Russia
S. Barsuk[1], I. Belyaev[1], B. Bobchenko, V. Dolgoshein, A. Golutvin, O. Gouchtchine, V. Kiritchenko, V. Kochetkov, I. Korolko, G. Pakhlova, E. Melnikov[1], A. Morozov, P. Pakhlov, A. Petriaev, D. Roussinov, V. Rusinov, S. Semenov, S. Shuvalov, A. Soldatov, E. Tarkovski

Budker Institute for Nuclear Physics (INP), Novosibirsk, Russia
K. Beloborodov, A. Berdiouguine, A. Bondar, A. Bozhenok, A. Buzulutskov, S. Eidelman, V. Golubev, P. Krokovnyi, S. Oreshkin, A. Poluektov, S. Serednyakov, L. Shekhtman, B. Shwartz, Z. Silagadze, A. Sokolov, A. Vasiljev

Institute for High Energy Physics (IHEP-Serpukhov), Protvino, Russia
K. Beloous, V. Brekhovskikh, R.I. Dzhelyadin, Yu.P. Gouz, I. Katchaev, V. Khmelnikov, V. Kisselev, A. Kobelev, A.K. Konoplyannikov, A.K. Likhoded, V.D. Matveev, V. Novikov, V.F. Obraztsov, A.P. Ostankov, V.Romanovski, V.I. Rykalin, M.M. Shapkin, A. Sokolov, M.M. Soldatov, V.V. Talanov, O.P. Yushchenko

Petersburg Nuclear Physics Institute, Gatchina, St. Petersburg, Russia
G. Alkhazov, V. Andreev, B. Botchine, V. Ganja, V. Goloubev, S. Guetz, A. Kashchuk, V. Lazarev, E. Maev, O. Maev, G. Petrov, N. Saguidova, G. Sementchouk, V. Souvorov1), E. Spiridenkov, A. Vorobyov, An. Vorobyov, N. Voropaev

University of Barcelona, Barcelona, Spain
E. Aguilo, R. Ballabriga7), M. Calvo, S. Ferragut, Ll. Garrido, D. Gascon, R. Graciani Diaz, E. Grauges Pous, S. Luengo7), D. Peralta, M. Rosello7), X. Vilasis7)

University of Santiago de Compostela, Santiago de Compostela, Spain
B. Adeva, P. Conde8), C. Lois Gomez9), A. Pazos, M. Plo, J.J. Saborido, M. Sanchez Garcia, P. Vazquez Regueiro

University of Lausanne, Lausanne, Switzerland
A. Bay, B. Carron, O. Dormond, L. Fernandez, R. Frei, G. Haefeli, J.-P. Hertig, C. Jacoby, P. Jalocha, S. Jimenez-Otero, F. Legger, L. Locatelli, N. Neufeld1), J.-P. Perroud, F. Ronga, T. Schietinger, O. Schneider, L. Studer, M.T. Tran, S. Villa, H. Voss

University of Zürich, Zürich, Switzerland
R. Bernet, R.P. Bernhard, Y. Ermoline, J. Gassner, St. Heule, F. Lehner, M. Needham, P. Sievers, St. Steiner, O. Steinkamp, U. Straumann, A. Vollhardt, D. Volyanskyy, M. Ziegler10)

Institute of Physics and Technologies, Kharkiv, Ukraine
A. Dovbnya, Yu. Ranyuk, I. Shapoval

Institute for Nuclear Research, National Academy of Sciences, Kiev, Ukraine
V. Aushev, V. Kiva, I. Kolomiets, Yu. Pavlenko, V. Pugatch, Yu. Vasiliev

University of Bristol, Bristol, UK
N.H. Brook, R.D. Head, A. Muir, A. Phillips, A. Presland, F.F. Wilson

University of Cambridge, Cambridge, UK
A. Buckley, K. George, V. Gibson, K. Harrison, C.R. Jones, S.G. Katvars, J. Storey, C.P. Ward, S.A. Wotton

Rutherford Appleton Laboratory, Chilton, UK
C.J. Densham, S. Easo, B. Franek, J.G.V. Guy, R.N.J. Halsall, G. Kuznetsov, P. Loveridge, D. Morrow, J.V. Morris, A. Papanestis, G.N. Patrick, M.L. Woodward

University of Edinburgh, Edinburgh, UK
R. Chamonal, S. Eisenhardt, A. Khan, J. Lawrence, F. Muheim, S. Playfer, A. Walker

University of Glasgow, Glasgow, UK
A.G. Bates, A. MacGregor, V. O'Shea, C. Parkes, A. Pickford, M. Rahman, F.J.P. Soler[11)]

University of Liverpool, Liverpool, UK
S. Biagi, T. Bowcock, G. Casse, R. Gamet, M. George, D. Hutchcroft, J. Palacios, G. Patel, I. Stavitskiy, M. Tobin, A. Washbrook

Imperial College, London, UK
L. Allebone, G.J. Barber, W. Cameron, D. Clark, P. Dornan, A. Duane, U. Egede, A. Howard, S. Jolly, R. Plackett, D.R. Price, T. Savidge, D. Websdale, R. White

University of Oxford, Oxford, UK
M. Adinolfi, J.H. Bibby, M.J. Charles[12)], C. Cioffi, G. Damerell, N. Harnew, F. Harris, I.A. McArthur, C. Newby, J. Rademacker, L. Somerville, A. Soroko, N.J. Smale, S. Topp-Jorgensen, G. Wilkinson

CERN, Geneva, Switzerland
G. Anelli, F. Anghinolfi, N. Arnaud, F. Bal, A. Barczyk, J.C. Batista Lopes, M. Benayoun[13)], V. Bobillier, A. Braem, J. Buytaert, M. Campbell, M. Cattaneo, Ph. Charpentier, J. Christiansen, J. Closier, P. Collins, G. Corti, C. D'Ambrosio, H. Dijkstra, J.-P. Dufey, D. Eckstein, M. Ferro-Luzzi, W. Flegel, F. Formenti, R. Forty, M. Frank, C. Frei, C. Gaspar, P. Gavillet, A. Guirao Elias, T. Gys, F. Hahn, S. Haider, J. Harvey, J.A. Hernando Morata, E. van Herwijnen, H.J. Hilke, R. Jacobsson, P. Jarron, C. Joram, B. Jost, J. Knaster Refolio, S. Koestner, D. Lacarrère, M. Letheren, C. Lippmann[14)], R. Lindner, M. Losasso, P. Mato Vila, M. Moritz, H. Müller, T. Nakada[15)], C. Padilla, U. Parzefall, W. Pokorski, S. Ponce, F. Ranjard, W. Riegler, G. Aglieri Rinella, E.M. Rodrigues[16)], D. Rodriguez de Llera Gonzalez, S. Roiser, T. Ruf, H. Ruiz Perez, B. Schmidt, T. Schneider, A. Schopper, A. Smith, F. Teubert, N. Tuning, O. Ullaland, P. Vannerem, W. Witzeling, K. Wyllie, Y. Xie

[1)] also at CERN, Geneva
[2)] now at CERN, Geneva
[3)] also at Dipartimento di Energetica, University of Rome, "La Sapienza"
[4)] also at Universita degli Studi di Parma
[5)] also at University of Basilicata, Potenza
[6)] also at Humbolt University, Berlin
[7)] also at departament d'Engineria Electronica La Salle, Universitat Ramon Llull, Barcelona
[8)] now at DESY, Hamburg
[9)] now at University of Zürich
[10)] now at University of California, Santa Cruz
[11)] also at Rutherford Appleton Laboratory, Chilton
[12)] now at University of Iowa, Iowa City
[13)] now at Universités de Paris VI et VII (LPNHE), Paris
[14)] now at GSI, Darmstadt
[15)] also at Lausanne, on leave from PSI, Villigen
[16)] supported by a Marie Curie Fellowship under contract number HPMF-CT-2002-01708

Technical Associates Institutes
Espoo-Vantaa Institute of Technology, Espoo, Finland
Ecole d'ingénieurs, Geneva, Switzerland

Acknowledgements

The LHCb Collaboration is greatly indebted to all the technical and administrative staff of the participating institutes for their important contributions. We acknowledge the particular contribution from G. Foffano, A. Rossi and R. Veness for the beam pipe study.

Contents

Chapter 1 Overview

1.1 Introduction

The LHCb experiment has been conceived to study CP violation and other rare phenomena in B meson decays with very high precision. This should provide a profound understanding of quark flavour physics in the framework of the Standard Model, and may reveal a sign of the physics beyond. In order to achieve these goals, the LHCb detector must have a high track reconstruction efficiency, π–K separation capability from a few to $\sim$100 GeV/c, very good proper-time resolution of ~ 40 fs and high trigger efficiencies, not only for final states including leptons but also for those with hadrons alone. The detector described in the Technical Proposal (TP) [1], approved in September 1998, was designed to fulfil those requirements. This document describes a reoptimization of the detector, that has been made to reduce the material budget and to improve the trigger performance.

At the time of the TP the material budget up to the second Ring Imaging Cherenkov detector (RICH 2) was 40% of X_0 (10% of λ_I), where X_0 (λ_I) is the radiation (nuclear interaction) length. This increased to 60% (20%) by the time the Outer Tracker Technical Design Report (TDR) [2] was submitted in September 2001, due to various technological constraints. Additional material deteriorates the detection capability of electrons and photons, increases the multiple scattering of charged particles, and increases occupancies of the tracking stations. With a larger fraction of nuclear interaction length, more kaons and pions interact before traversing the complete tracking system. The number of reconstructed B mesons therefore decreases, even if the efficiency of the tracking algorithm is maintained high for those tracks that do traverse the full spectrometer. This leads to a noticeable loss in the number of reconstructed B mesons from many-body final states. For example, one of the most promising CP violation measurements, from $\mathrm{B_s} \to \mathrm{D_s K}$ decays, requires five charged tracks (including one for tagging) to be reconstructed. For these reasons, an effort has been made to reduce the material budget back to the level at the time of the TP.

The trigger is one of the biggest challenges of the LHCb experiment[1]. It is designed to distinguish minimum-bias events from events containing B mesons through the presence of particles with a large transverse momentum (p_T) and the existence of secondary vertices. Events are first triggered by requiring at least one lepton or hadron with a p_T exceeding 1 to 3 GeV/c (Level-0) reducing the event rate to 1 MHz. It was realised that the robustness and efficiency of the second trigger level (Level-1) could be significantly improved by not only using information from the Vertex Locator (VELO), as done in the TP, but also adding p_T information to tracks with a large impact parameter. This can be achieved by associating the high-p_T calorimeter clusters and muons obtained at Level-0 to the tracks found in the VELO [3]. A complementary approach that is more efficient for hadrons is to get a rough p_T estimate from the tracking. This requires the introduction of a small amount of magnetic field in the region of RICH 1. The design of RICH 1 then has to be modified in order to protect its photon detectors from the field.

1.2 Reoptimized detector

Figure 1.1 shows the layout of the reoptimized LHCb detector. The basic layout of the spectrometer remains unchanged from that of the TP. It consists of the beam pipe, VELO, dipole magnet, tracking system, two Ring Imaging Cherenkov detectors with three radiators (RICH 1 and RICH 2), calorimeter system and muon system.

The first (25 mrad cone) section of the beam pipe will be made from pure beryllium. The middle section (10 mrad cone) is foreseen to be made from beryllium-aluminium alloy, however it may also be changed to beryllium, depending on the price. The last section, passing through the calorimeter and muon systems, remains unchanged, made of stainless steel.

No major change in the VELO design has been

---

[1] Details of the trigger implementation and performance are discussed in the trigger TDR [3] submitted at the same time as this document.

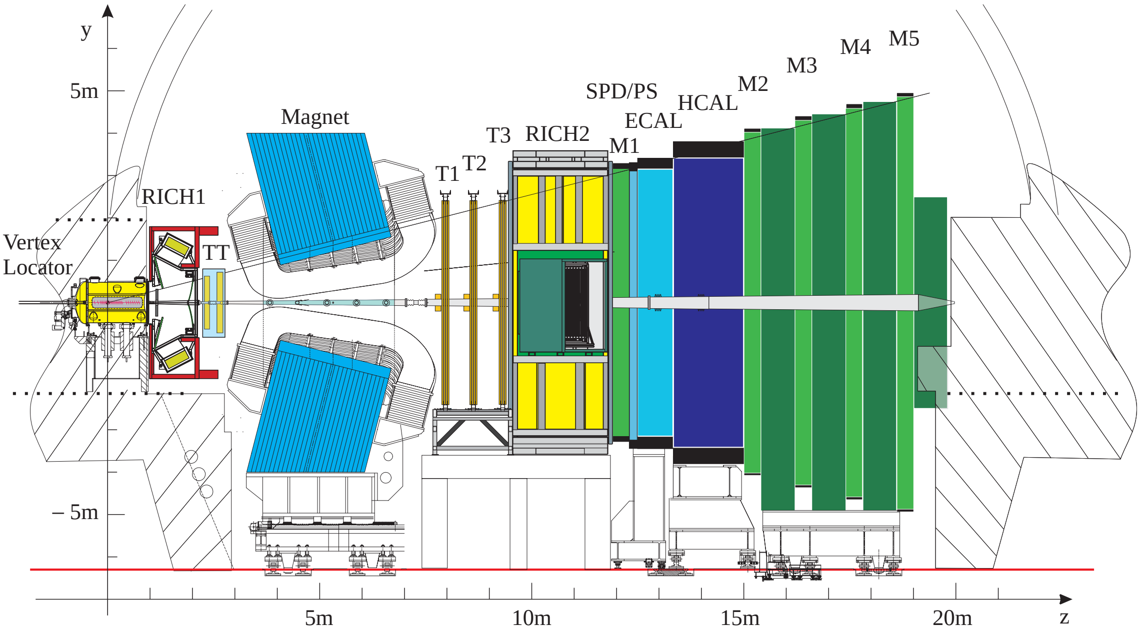

Figure 1.1: Reoptimized LHCb detector layout, showing the Vertex Locator (VELO), the dipole magnet, the two RICH detectors, the four tracking stations TT and T1–T3, the Scintillating Pad Detector (SPD), Preshower (PS), Electromagnetic (ECAL) and Hadronic (HCAL) calorimeters, and the five muon stations M1–M5. It also shows the direction of the y and z coordinate axes; the x axis completes the right-handed framework.

introduced compared to the TDR [4]. The material budget has been reduced by optimizing the thickness of the silicon sensors and the number of stations. The thickness of the sensors has been reduced from 300 to 220 μm, and the number of stations from 25 to 21 without significantly affecting its performance, as shown in this document.

The dipole magnet has not been modified from the TDR design [5] and its construction is advancing. Compared to the TP spectrometer layout, no shielding plate is placed upstream of the magnet. This change has been made in order to introduce magnetic field between the VELO and the magnet, i.e. in the region of RICH 1, for the Level-1 trigger improvement.

Compared to the TP, the number of tracking stations is reduced to four in order to reduce the material budget, without introducing performance losses, as demonstrated in this document[2]. The first station after the VELO, referred to as the Trigger Tracker (TT), is in front of the magnet and just behind RICH 1. It consists of four planes of silicon strip detectors. They are split into two pairs of planes separated by 30 cm. Together with the VELO, the TT is used in the Level-1 trigger. Large impact parameter tracks found in the VELO are extrapolated to the TT and the magnetic field in the RICH 1 region allows their momenta to be measured. The three remaining stations are placed behind the magnet with equal spacing. Each station consists of an Inner Tracker (IT) close to the beam pipe and an Outer Tracker (OT) surrounding the IT. The OT is made of straw tubes and the IT of silicon strip detectors. Their designs remain unchanged from those described in the corresponding TDR's [6, 2].

The RICH 1 material has been reduced, largely by changing the mirror material and redesigning the mirror support. The mirror will be made from either carbon-composite or beryllium. The mirror support has been moved outside of the acceptance. Further reduction of the material has been achieved by removing the entrance window, by connecting the front face of RICH 1 to the flange of the VELO exit window. Iron shielding boxes for the photon detectors have been introduced for two reasons. Firstly, they protect the photon detectors from the magnetic field. Secondly, they help to focus the magnetic field in the region where it is needed for the momentum measurement of the Level-1 trigger.

---

[2] In the track reconstruction the VELO is now used as an integral part of the the tracking system.

In order to accommodate the shielding boxes, the optics has been changed introducing an additional flat mirror to the TDR design [7].

No design changes have been introduced for RICH 2 and the calorimeter system compared to the designs given in the TDR's [7, 8], and their construction is advancing.

The muon system consists of five stations, M1 in front of the calorimeter system and M2–M5 behind the calorimeter, interleaved with iron shielding plates. In order to reduce the material budget seen by the calorimeter, M1 consists of two layers of Multi Wire Proportional Chambers, while the other four stations are made from four layers, as described in the TDR [9] and Addendum [10].

Figure 1.2 summarizes the material budget of the detector. The amount of material, as a fraction of radiation length, seen by a neutral particle from the nominal position of the primary vertex is plotted as a function of the pseudo-rapidity, η. The material is averaged over the azimuthal angle ϕ at three different z positions: 1) in front of the magnet, 2) in front of RICH 2 and 3) in front of the Calorimeter system. It shows that most of the particles see 20–30% of X_0 before entering the magnet. After the magnet, the three tracking stations lead to an additional ~10% of X_0. Before reaching the calorimeter system, RICH 2 and the first muon station add another ~30%. The fraction of interaction length in front of RICH 2 is now ~12% of λ_{I}.

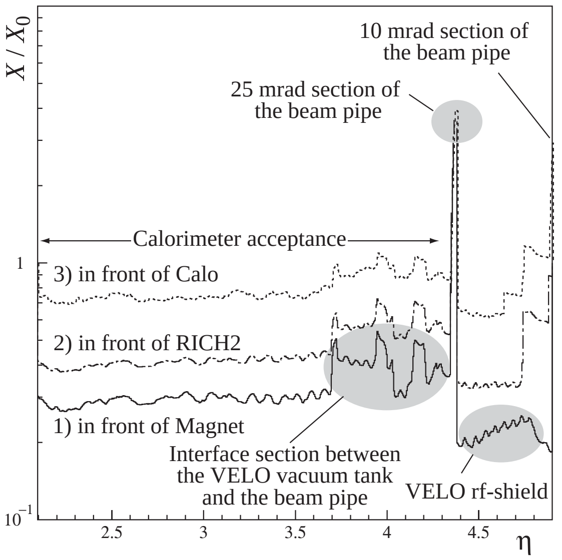

Figure 1.2: Material seen by a neutral particle from the nominal position of the primary vertex as a function of the pseudo-rapidity at three different z positions, averaged over the azimuthal angle.

1.3 Summary

Simulation studies have shown that the reoptimized LHCb detector fulfils the requirements given by the physics goals. Charged tracks are reconstructed with a high efficiency of ~ 95% with a low ghost rate, which does not introduce significant additional combinatorial background in the reconstructed B meson signals. With the excellent momentum and vertex resolutions, the proper time of B^0_s meson decays can be measured with a resolution of ~ 40 fs. The RICH system separates kaons from pions in the required momentum range. In addition, the decreased detector material helps in the reconstruction of photons, and the removal of material in the magnet allows a simpler reconstruction of electrons. Together with the improved trigger system, the LHCb detector maintains the high reconstruction yields for many interesting B meson decays described in the TP. As shown in this document, the quark flavour changing process in the Standard Model can be tested in a unique way using those reconstructed B mesons, beyond the capabilities of current experiments at the $\mathrm{e}^+\mathrm{e}^-$ B factories and the Tevatron. After the reoptimization, the cost of the detector is slightly lower than the original estimate. The updated construction schedule shows that the full physics programme can start when the LHC will become operational in 2007.

This document is organised in the following way: Firstly, the designs of the beam pipe, VELO, RICH 1 and TT, which have been modified as a result of the reoptimization process, are described. This is followed by a description of the LHCb simulation programme that was used for the performance studies. After presenting the track reconstruction and particle identification performance, the physics performance of the reoptimized detector is discussed. Finally the overall project plan and cost of the reoptimized LHCb experiment are given.

Chapter 2 Beam Pipe

2.1 Introduction

The beam pipe design is particularly delicate since the vacuum chamber is located in the high rapidity region of the LHCb detector where the particle density is high, and the number of secondary particles in the event depends on the amount of material seen by incident primary particles. The mass of the beam pipe and the presence of flanges or bellows has direct influence on the occupancy, in particular for the tracking chambers and the RICH detectors.

2.2 Evolution since the Technical Proposal

At the time of the TP [1], although a first detailed design of the beam pipe was under discussion, only a simplified description was used for the performance studies: the beam pipe consisted of a thin window sealed to the VELO vacuum tank followed by two conical sections; the first $\sim 1.5\,\mathrm{m}$ long with 25 mrad opening angle and the second $\sim 16\,\mathrm{m}$ long with 10 mrad opening angle. The whole chamber was of aluminium and no regions with flanges and bellows were included.

In the first realistic design two stainless-steel transitions[1] located upstream ($z = 2400$ to 2800 mm) and downstream ($z = 7040$ to 7500 mm) of the magnet were added to the basic layout described above. A third transition inside the calorimeter was also added.

Although satisfactory for vacuum and mechanical requirements, it became a major source of secondaries produced from $z \approx 850\,\mathrm{mm}$ (VELO exit window) to $z \approx 12\,\mathrm{m}$ (Muon station M1) [11]. The shape of the first realistic beam pipe is clearly visible in Fig. 2.1 (a), showing the origin of secondaries in the r-z plane. The detector layout in Fig. 2.1 (a) is that of the TP, with tracking stations present in the magnet. For comparison, Fig. 2.1 (b) shows the same for the current beam pipe design. The relative weight of the beam pipe as a source of secondaries has been considerably reduced.

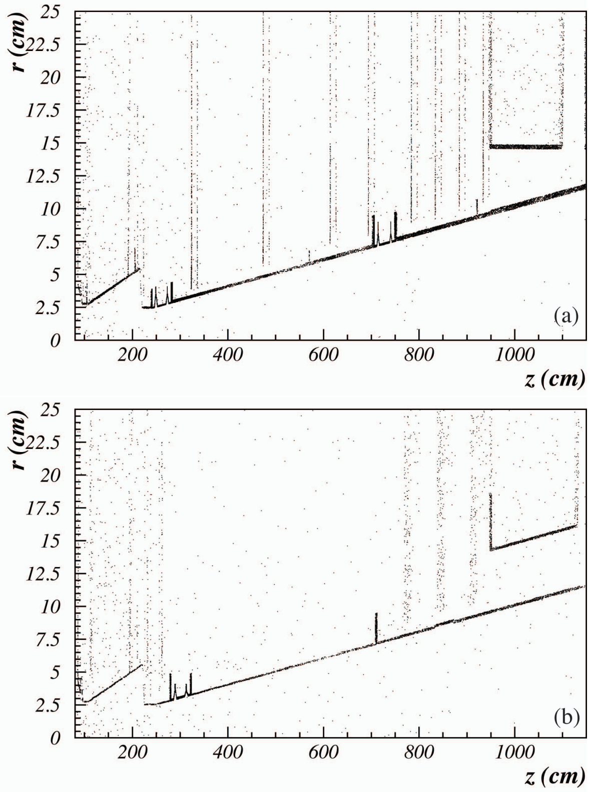

Figure 2.1: Origin of secondaries (a) for the first realistic beam pipe (aluminium with stainless-steel flanges and bellows), (b) for the current beam pipe (Be and Al-Be, with aluminium flanges and bellows).

In the last section of the detector where the calorimeters and Muon filter are located the material of the beam pipe is no longer a dominant effect.

Since the TP different designs have been studied taking into account particle background, vacuum and mechanical requirements. The material and thickness of the beam pipe as well as the number, material and location of bellows and flanges [11] have been optimized to keep the background levels as low as technically possible.

In order to reduce the material traversed by the particles, aluminium, an aluminium-beryllium alloy and beryllium have been considered. The me-

---

[1] A transition is a set of two bellows protected by flanges.

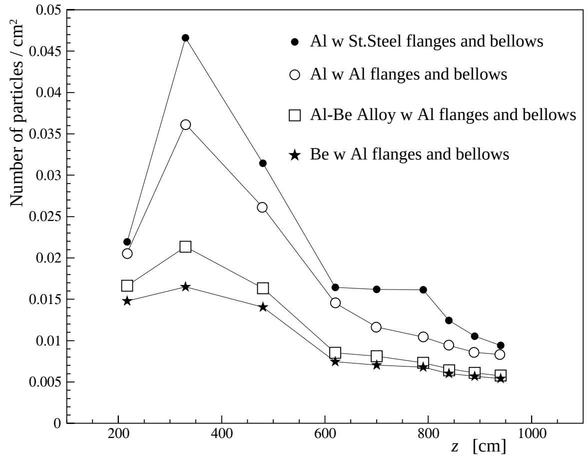

Figure 2.2: Effect of beam pipe materials on particle fluxes on the inner part of the tracking chambers. A simplified simulation of the chambers is used covering areas up to ±20 cm from the beam line. The detector layout is that of the TP with chambers present in the magnet.

chanical strength of both Be and Al-Be alloy being higher than that of Al, an additional gain in transparency can be achieved due to the reduced thickness. Figure 2.2 shows the particle flux in the tracking chambers (TP layout) for the different material options. The layout of the beam pipe is the same as that of the first realistic beam pipe design, with wall thicknesses adjusted according to the material used. The number of transitions has been reduced, replacing the transition at $z \approx 7040$ mm by a flange. As explained later in detail, all beam pipe sections will be coated, and this process limits the maximum length of a section to 7 m; consequently the 10 mrad cone has to be split into two pieces connected by a flange.

2.3 General layout

The current layout of the beam pipe (UX85) is shown in Fig. 2.3 [12]. The main features of the design are similar to that of the TP. The beam pipe consists of a thin exit window sealed to the VELO vacuum tank followed by two conical parts with apertures of 25 mrad and 10 mrad respectively.

The first section (UX85/1), of 1840 mm length, is made of 1 mm-thick beryllium and consists of a 25 mrad cone followed by a 10 mrad cone. The two cones are connected by a thin window followed by a short cylindrical section (250 mm in length) that constitutes the narrowest aperture of the beam pipe, with an inner diameter of 50 mm. This section is welded to the VELO exit window and ends with an optimized flange located at 2800 mm from the IP.

A transition connects UX85/1 with the second section of the vacuum chamber (UX85/2). This transition consists of a 10 mrad aluminium cone joining two aluminium bellows, terminated by aluminium flanges. Its position has been optimized to keep as low as possible the background induced by the beam pipe in the TT station, while keeping the length of UX85/1 manageable for mechanical reasons and for installation.

Sections UX85/2 and UX85/3 are long conical sections of 10 mrad aperture with a length of 3876 mm and 6000 mm respectively. They are formed from several pieces of increasing thickness (1.0 to 2.4 mm) welded together. The two conical sections are connected by optimized flanges located at 7100 mm from the IP.

Within the constraints imposed by the coating process, the length of UX85/3 has been chosen such as to locate the optimized flanges as far as possible upstream, thereby reducing the number of low energy secondaries produced in the flange that would reach the tracking stations.

A second transition connects UX85/3 with the last section of the beam pipe (UX85/4). It consists of a 10 mrad cone connecting two standard stainless-steel bellows, and has stainless-steel flanges.

Section UX85/4, surrounded by the calorimeters and the Muon system, will be made of stainless steel AISI 316L with thickness between 3 and 4 mm. It is connected by a thin window to a universal joint of shielded bellows at 20,088 mm from the IP. Ports for pumping are foreseen at the downstream end of this cone.

2.4 Vacuum

The vacuum system is designed for an average total pressure of 10^{-8} to 10^{-9} mbar inside the beam pipe during operation. With beam on, the vacuum is determined by dynamic pressure instabilities rather than by the static pressure.

The vacuum chamber will be pumped by a combination of lumped sputter ion pumps and distributed Non-Evaporable-Getter (NEG) pumps [13]. The NEG system consists of a few-μm-thick sputtered coating along the whole internal surface of the vacuum chambers. This coating has to be periodically reactivated by heating (bake-out) to 200°C for 24 hours. This temperature needs to be increased after several activations, however

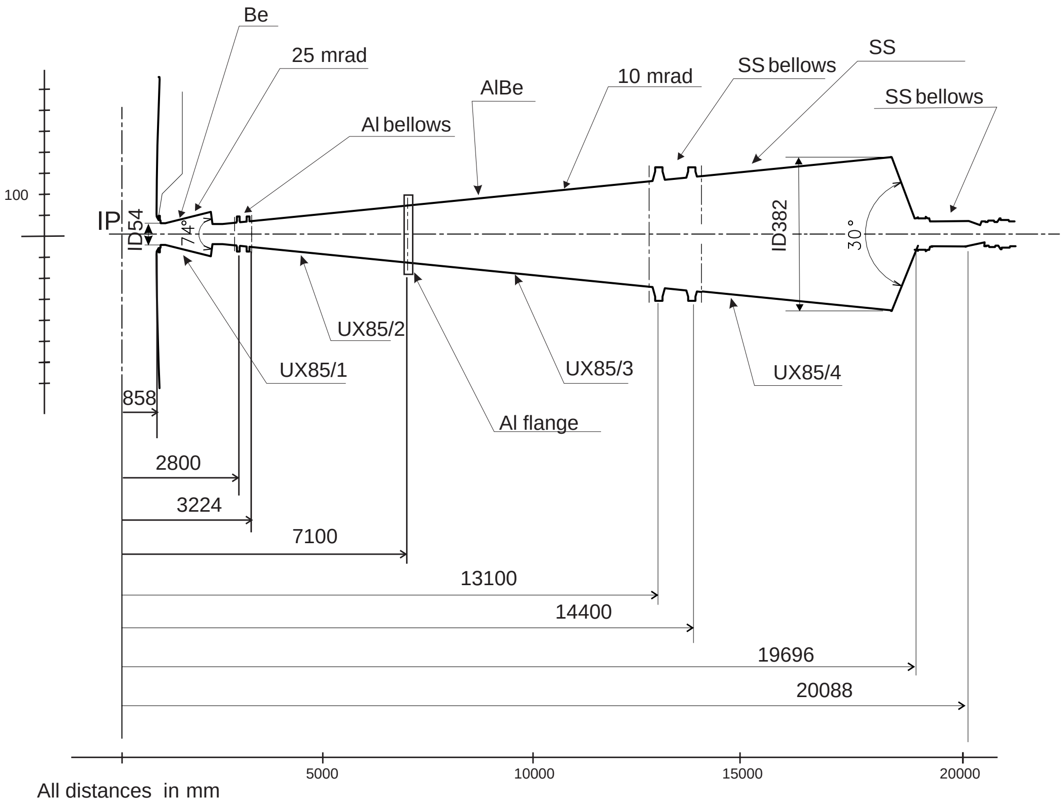

Figure 2.3: Layout of beam pipe.

mechanical considerations limit the bake-out temperature to 250°C.

Removable heating jackets are foreseen for the sections UX85/1, UX85/2 and UX85/3, whereas a permanent heating and insulation system will be installed in UX85/4. The heating system is still under design and a common approach with other experiments will be followed.

Final calculations for the vacuum will be available by the end of 2003.

2.5 VELO window

The VELO window consists of a 2 mm-thick foil covering 390 mrad. It is clamped to the VELO vacuum tank and leaves at the centre a circular aperture for the beam of 54 mm in diameter.

The vertex window will be machined from an aluminium alloy forging (Al6061 T652) [14]. This material has been chosen due to its higher transparency over the high temperature weldable aluminium alloy (Al2219), that contains about 8% Cu. Furthermore, the mechanical properties of Al6061 T652 will improve with the heating performed for the NEG activation.

The shape of the window has been optimized for minimal stresses using finite element (FE) analysis. The chosen shape of the window will withstand a

Figure 2.4: VELO window prototype.

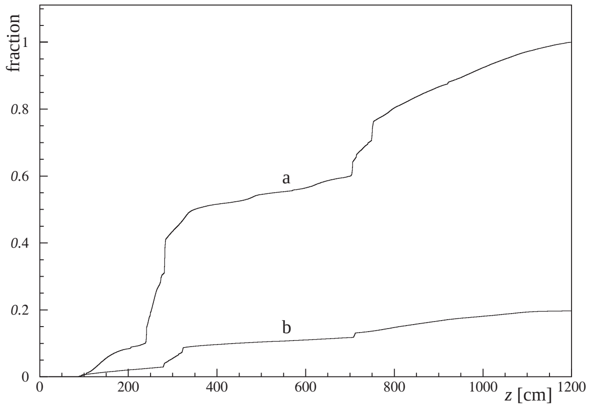

Figure 2.5: Cumulative histogram of origin of secondaries from the beam pipe for (a) the first realistic beam pipe design, and (b) the current design.

stress of 150 MPa at 150°C [15]. The creep performance of Al6061 T652 has been tested at 150 MPa and 150°C for a duration of 100 hours [16] and the results obtained confirm the data available in the literature. Stresses of 150 MPa are higher than those expected on the window even during bake-out, hence creep breaking is not a concern.

The window will be vacuum-sealed to the VELO tank by means of a Helicoflex joint HN200. The window includes four-convolution bellows, 0.4 mm-thick, that are machined together with the window from the same forging. The bellows will absorb the forces exerted by the beam pipe.

Five forgings have been purchased following detailed specifications drawn up with the collaboration of CERN metallurgists. No inclusion that could break the leak tightness or induce cracks were allowed in the forgings. This was measured and confirmed by ultrasonic testing of all forgings [17]. Only one had an inclusion of about 1 mm in a non-critical zone, and this forging has been used to machine the window prototype shown in Fig. 2.4, currently under test.

2.6 Aluminium bellows

A set of two bellows protected by rotatable flanges is needed between UX85/1 and UX85/2 to absorb the thermal expansion of the vacuum chambers during bake-out and minimize bending stresses on the VELO window due to misalignment.

Simulation studies showed that the stainless-steel transitions were the major source of secondaries produced by the beam pipe, as can be seen in Fig. 2.5, and consequently they were considered unacceptable.

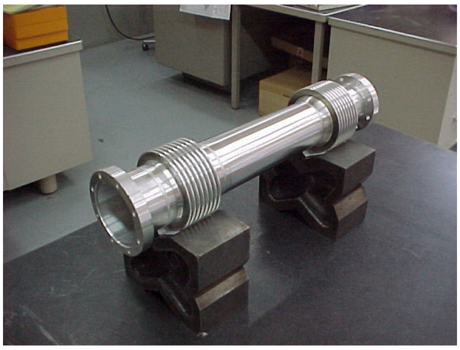

Figure 2.6: Prototype bellows machined at CERN.

It was therefore decided to develop and qualify aluminium bellows. Only one industrial partner showed interest in developing a prototype. However, the quality achieved was not sufficient for Ultra High Vacuum applications [18], cracks were present and the convolution shape was not uniform. In parallel, a process was developed at the CERN workshops to machine the bellows from an aluminium forging (Al2219). FE analysis showed that bellows with 16 convolutions of 0.4 mm thickness can absorb the expected thermal displacement of about 10 mm without exceeding the elastic limit. Figure 2.6 shows the prototype, that resulted in satisfactory leak tightness and mechanical performance close to the FE predictions.

2.7 Conical sections

High transparency to secondary particles is required up to the section UX85/3 [11]. The first section with the 25 mrad cone has the most impact on RICH 1 and TT occupancies. Since it is rather short, Be has been chosen. For the sections UX85/2 and UX85/3 both Be and Al-Be are being considered, the final choice will be made based on the price. For the physics simulation presented in this TDR the Al-Be option has been used. The alloy under consideration is AlBeMet162 HIP (Hot Isostatic Pressure) which has been qualified at the bake-out temperatures for the first time for LHCb. Table 2.1 gives some of the measured properties.

The creeping behaviour at two different bake-out temperatures, 200°C and 250°C, was measured with an applied stress of 100 MPa. Under these conditions, the creeping did not reach behaviour in the tertiary region after 1000 h at 200°C and 100 MPa. However, at 250°C it broke after ~ 70 h as seen in Fig. 2.7. FE analysis shows that the

Table 2.1: Mechanical properties of AlBeMet 162 at bake-out temperatures.

Temperature (°C)	200	250
Young's Modulus (GPa)	200	192
Ultimate Strength (MPa)	321	262
Yield Strength (MPa)	239	195
Elongation (%)	2	2

Table 2.2: Ultimate Tensile Strength (UTS) of AlBeMet welding measured at 250°C.

Welding material	UTS (MPa)
AlBeMet162 vs AlBeMet162	252
AlBeMet162 vs Al2219	290

stresses expected for the beam pipe due to atmospheric pressure are not higher than 30 MPa, indicating that no creep problem is to be expected.

The welding of beryllium and AlBeMet162 by two different processes, e-beam welding and TIG welding, is being studied for the first time for LHCb. A qualification at 250°C for the e-beam welding of AlBeMet62 HIP and with aluminium Al2219 has been performed [19], and the results are summarized in Table 2.2.

The ultimate tensile strength (UTS) of aluminium Al2219 at 250°C ranges between 185 and 200 MPa, i.e. the AlBeMet162–Al2219 e-beam welding is mechanically stronger. The welding of AlBeMet162–AlBeMet162 could not be qualified as quality-B following ISO 13919–2, due to a misalignment of the samples, but the quality of the welding was satisfactory. The TIG welding of Be to Be and Be to Al2219 is presently under qualification; the Yield Strength measured at room temperature for Be–Be is 150 MPa, and for Be–Al2219 is 256 MPa.

The determination of the mechanical properties of the AlBeMet162 allowed FE analysis to be made of the local buckling behaviour for different thicknesses of the beam pipe [20]. The minimal required wall thicknesses obtained are reported in Table 2.3, together with those of the initial design.

As indicated in the table, the thickness of several parts could be slightly reduced (by tenths of mm) with respect to the initially considered values that were used in the physics simulation presented in this TDR.

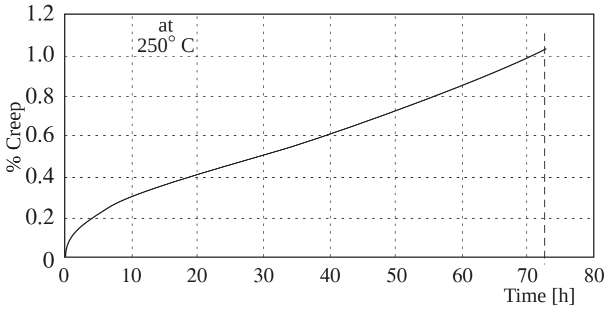

Figure 2.7: Creeping percentage as a function of time at 250°C.

Section UX85/4 consists of two stainless-steel cones AISI 316L of 3 and 4 mm thickness respectively, with an aperture of 10 mrad, that are welded together. The fabrication process will be the same as for the ALICE beam pipe that is presently in manufacture. Radiation activation studies of the complete beam pipe are planned to begin later this year.

The atmospheric pressure exerted on the conical beam pipe under vacuum leads to axial forces of about 0.58 N/mm [20]. Two fixed supports that prevent axial displacement will prevent the collapse of the bellows system. During bake-out additional axial forces will arise. The set of two stainless-steel bellows located at $z = 13\,100$ mm that connect UX85/3 and UX85/4 will be subject to a force of 1193 N. The column buckling calculations performed give a safety factor against buckling of 3.8, which is considered to be sufficiently high.

The beam pipe supports are currently under design and will take into account the transparency requirements. For the sections UX85/1, US85/2 and UX85/3 they will consist of stainless-steel wires attached to optimized rings made out of a material with high transparency (such as beryllium, aluminium or fibre-glass). A fixed support will be placed at $z = 4024$ mm in order to minimize the thermal expansion to be absorbed by the aluminium bellows and to protect the VELO window.

A spare beam pipe of identical design will be fabricated from aluminium Al2219, which will allow replacement of the beam pipe within 2 weeks if any accident occurs [21]. In case of necessity this beam pipe could also be used on a permanent basis.

2.8 Optimized flanges

The conical sections and transitions are connected with flanges, and the vacuum sealing will be achieved with Helicoflex joints. In the region between $z = 0.9$ and 12 m where high transparency is required, optimized flanges will be used. The alu-

Table 2.3: AlBe162 beam pipe minimum required segment thicknesses as obtained from buckling analysis. The thicknesses of the initial design, used in the simulation for this TDR, are also reported for comparison.

Seg. No.	$z_{\min}$ (mm)	Initial design Thickness (mm)	Initial design Mass (kg)	Optimal design Thickness (mm)	Optimal design Mass (kg)
1	3224	1.0	0.1915	1.0	0.1915
2	3624	1.1	0.2352	1.0	0.2136
3	4024	1.2	0.5928	1.0	0.4929
4	4824	1.3	0.7575	1.1	0.6398
5	5624	1.4	1.4558	1.3	1.3508
6	6824	1.7	1.1466	1.4	0.9423
7	7500	1.8	1.5844	1.6	1.4066
8	8300	1.9	0.9002	1.7	0.8045
9	8700	2.0	2.0271	1.9	1.9247
10	9500	2.1	2.3147	2.0	2.2033
11	10 300	2.2	1.2867	2.1	1.2276
12	10 700	2.3	2.8417	2.3	2.8417
13	11 500	2.4	3.1781	2.4	3.1781
14	12 300 ($z_{\max}$=13 100)	2.6	3.6749	2.4	3.3896
Total mass (kg)			22.1872		20.8070

minium bellows will have aluminium DN58 flanges at their ends. Similar flanges have already been qualified for the ATLAS experiment [22]. The mass of such a flange is reduced by a factor of three compared to the standard CF flange of similar dimensions. An optimized design of the flange joining UX85/2 and UX85/3 is under study, as well as the development of beryllium flanges.

2.9 Safety

The design, installation and operation of the beam pipe will follow CERN safety rules and safety codes. In particular, beryllium is the most toxic of all industrial metals, and its use at CERN is regulated by the safety document IS No. 25 [23].

Hazards include inhalation of dust, fume or vapour as well as ingestion. Furthermore, when involved in a fire, beryllium will rapidly oxidize and the oxide will spread in form of powder. Hence, all safety rules regarding the use of beryllium specified in the safety note IS No. 25 will be strictly applied.

2.10 Installation

The installation process has been studied in detail and no insurmountable problems have been found [24]. Dedicated tooling will be required and its design will be carried out in 2004.

Chapter 3 VELO Reoptimization

The Vertex Locator (VELO) has to provide precise measurements of track coordinates close to the interaction region. For this, the VELO features a series of silicon stations placed along the beam direction (Fig. 3.1). They are placed at a radial distance from the beam which is smaller than the aperture required by the LHC during injection and must therefore be retractable. This is achieved by mounting the detectors in a setup similar to Roman pots (Fig. 3.2). For minimizing the material between the interaction region and the detectors, the silicon sensors are inside a thin aluminium box with a pressure of less than 10^{-4} mbar (Fig. 3.3). The side of the box facing the beam also shields the sensors against RF pickup.

3.1 Evolution since the VELO TDR

In the VELO TDR [4], the material traversed in the VELO by particles in the LHCb acceptance added up to 17.1% of a radiation length on average, excluding the exit window. The dominant contributions came from the RF foil and from the silicon sensors. For the TDR, the VELO design was optimized to provide the best possible extrapolation to the interaction region. This is reflected in the corrugated shape of the RF foil, which minimizes the amount of material before the first measured point, and in the number of stations (25), which minimizes the extrapolation distance without adding too much dead material. The average material before the first measured point was 3.2% of an X_0. Since then, various studies have been made of how to reduce further the material:

- by re-designing the RF foil [25],
- by reducing the thickness of the silicon sensors,
- by reducing the number of detector planes.

In addition, we investigated beryllium instead of aluminium as the material for the RF foil [26].

On the other hand, we were forced to increase the material seen by the particles in some areas due to technological constraints. Prototype work on thin aluminium foils has shown limits of producing the double-corrugated shape. It was required to reduce the depth of the corrugations compared to the TDR design, which increases the average amount of material seen by particles. Full size prototypes have since been produced and new estimates of the material are now available (Sect. 3.2). The module design is now close to being finalised and its contribution to the material budget has been updated (Sect. 3.5).

A prototype of the 2 mm thin exit window [14] of the VELO is in production and is discussed in Chapter 2.

During the studies for the overall LHCb optimization, the VELO became an important part of

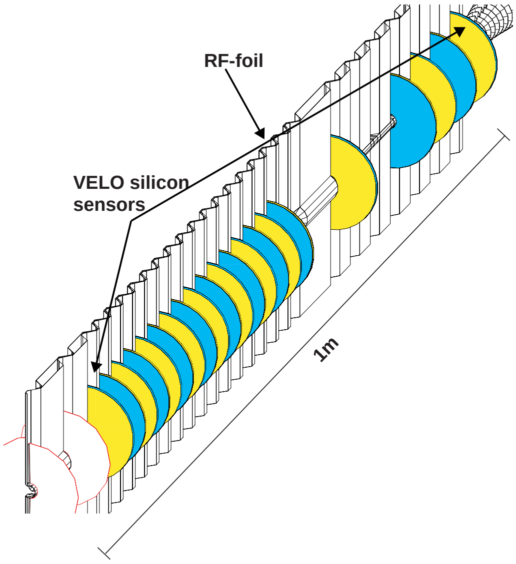

Figure 3.1: Arrangements of detectors along the beam axis. Only the silicon sensors on one side of the RF-foil, which separates the LHC vacuum from the detector vacuum, can be seen. The first two detectors (unshaded) belong to the Pile-Up system [3].

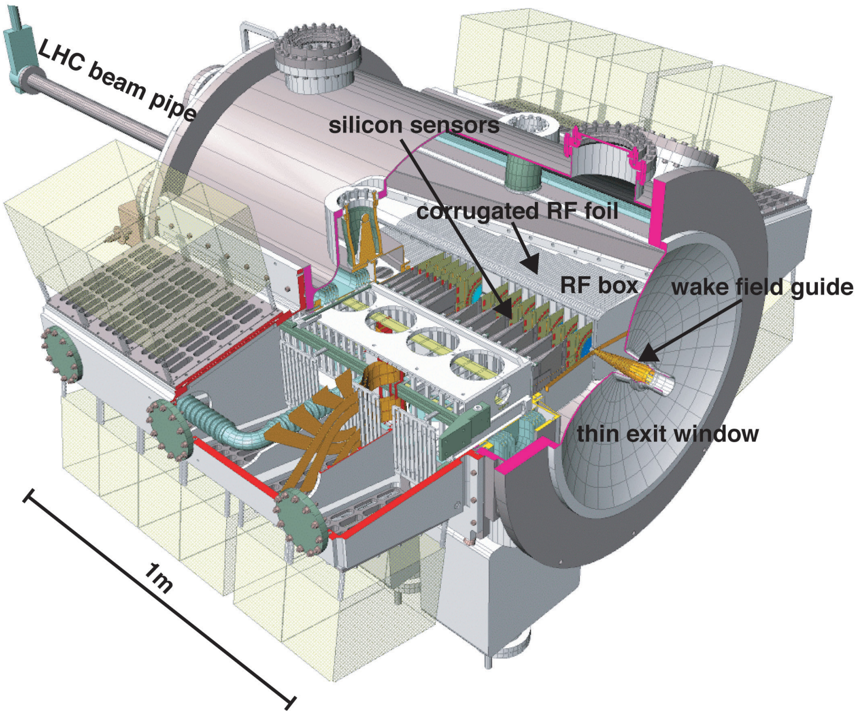

Figure 3.2: The VELO vacuum vessel with the silicon sensors (TDR layout with 25 stations), RF box, wakefield guides and exit window.

the overall tracking system. In addition to its original task of providing precise measurements of primary and secondary vertices, it is now the main tracking system before the magnet. As a result of this, the sensor design was slightly modified (Sect. 3.7) to give a better performance for the tracking and for the L1 trigger with only a small loss in vertex and impact parameter resolution.

The modifications to the VELO design compared to the TDR are summarized in the following sections. More details can be found in corresponding LHCb notes.

3.2 Mechanical aspects

The detector vacuum box equipped with corrugated foils, as proposed in the TDR, is shown in Fig. 3.3. The corrugated structure of the top foil was determined by the demand to limit the amount of material seen by the detected particles, and by the physical layout of the partially-overlapping silicon sensors. Background and multiple scattering considerations strongly favour low-Z materials. Properties like vacuum tightness, strength and electrical conductivity made aluminium or beryllium the obvious choices. In a separate LHCb note [26] we have investigated the comparison between the two materials.

Pure aluminium is quite soft, but the addition of a small amount of magnesium considerably increases its strength, while maintaining good welding properties. Aluminium can be deformed quite easily. Beryllium on the other hand cannot be pressed into the proposed shape, and machining

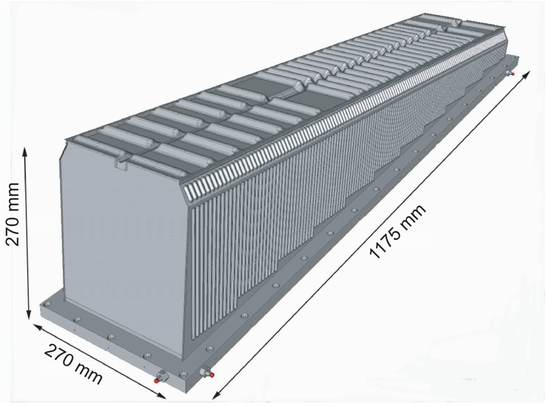

Figure 3.3: The detector vacuum box with corrugated foils.

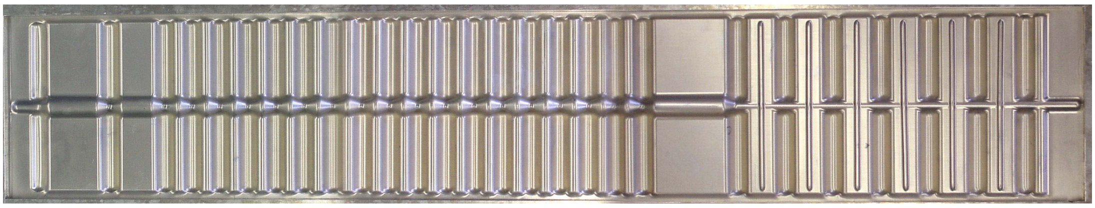

Figure 3.4: Top foil of the detector vacuum box, made from 0.3 mm thick AlMg3. The structure is 120 cm long, the width is 25 cm.

can easily damage the low-ductility material. As an alternative the use of a flat beryllium foil was also investigated. A flat foil results in a larger contribution to the material budget. Furthermore, the corrugations give the detector vacuum box significantly more stiffness; with flat foils a thicker foil has to be used, resulting in an even larger contribution to the material budget. In addition, a flat foil would no longer allow overlapping sensors. Sensor designs were studied which could minimize the loss in acceptance to about 1.5% per b-decay track. Their shape would be considerably different to the 180° disks proposed in the VELO TDR and would require additional R&D.

All these considerations have resulted in the choice of a corrugated aluminium foil. The material chosen is AlMg3, an aluminium alloy with 3% magnesium. The material properties used in these calculations are given in Table 3.1.

For the corrugated foil, several production methods were tried. The temperature and deformation speed are critical parameters since they have a large impact on the recrystallization of the material. Too high a temperature results in significant crystal growth, resulting in small vacuum leaks. The best results were obtained with hot gas forming, in which the material is heated to 350°C, and pressed into the desired shape. The minimal thickness for which a vacuum-tight foil could be produced was 300 μm. Foils with a thickness of 250 μm were not yet available from industry. Figure 3.4 shows a corrugated foil. Since the material is stretched considerably, the local thickness varies between 0.30 mm for the undeformed regions to 0.15 mm for the most-deformed ones, with an average value around 0.25 mm. The integrity of the dimensional structure has been verified on a 3D-measuring machine. The observed deviations from the design positions are less than 0.2 mm. R&D continues to work with thinner foils, 250 μm and 200 μm.

On the inside of the box a poly-amide-imide coating will be applied. This material is highly radiation resistant: it keeps its strength after a dose of 30 MGy. It will electrically isolate the sensors from the aluminium, and will also help to radiate away the heat that will be deposited in the detector vacuum foil by beam-induced effects. Desorption measurements have shown that the load from the outgassing of the material to the detector vacuum is small ($< 10^{-4}$ mbar ℓ/s at room temperature after 24 hours).

For the cables inside the vacuum a choice has been made for a design consisting of seven consecutive layers of Kapton and copper. A prototype is shown in Fig. 3.5. Desorption measurements have also been performed on these. They show that the outgassing can easily be handled by the detector vacuum system.

Table 3.1: Material properties of AlMg3.

Property	Value
Young's Modulus	70 GPa
Poisson ratio	0.33
Shear Modulus	27.3 GPa
Yield Strength	80 MPa (annealed)
Electrical conductivity	$1.9 \times 10^7\ \Omega^{-1}\text{m}^{-1}$

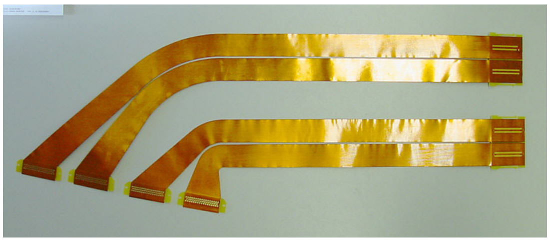

Figure 3.5: Prototype of the seven-layer Kapton-copper cables, that will be used inside the vacuum chamber.

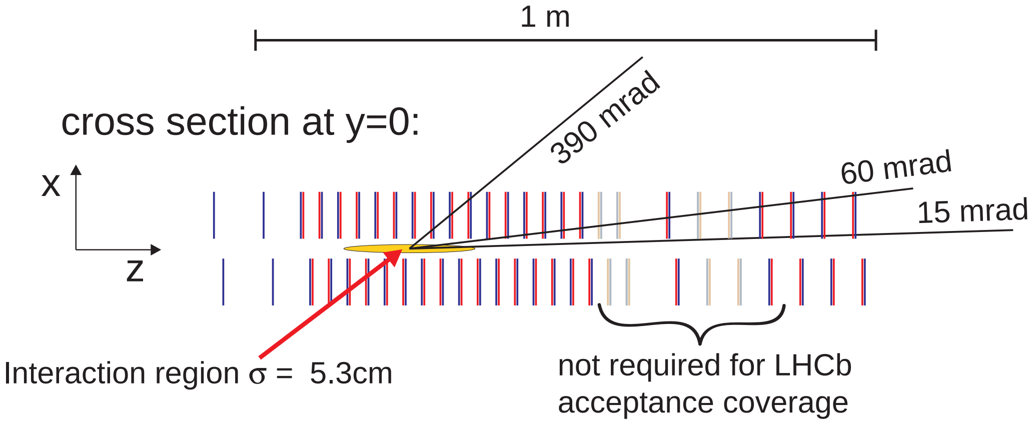

Figure 3.6: Station set-up. The stations which are not required for covering the LHCb acceptance are marked. The stations which have been removed in the new set-up are indicated with lighter shading.

3.3 Number of detector planes

For the TDR, the VELO was optimized for the best impact parameter resolution. For a track with a given momentum, the impact parameter error is smaller the shorter the extrapolation to the primary vertex. This requires detector stations as close as possible. However, the more detector stations, the more material and therefore increased multiple scattering. For the TDR, 25 stations turned out to be an optimum. For the LHCb reoptimization study, additional importance was given to the material after the first measured point. Given the dimensions of the sensors, their inner and outer radius, and the requirement to reconstruct tracks with angles of up to 390 mrad, it is not possible to reduce the number of stations close to the interaction region. The same is true for the most downstream stations which are required to reconstruct low angle tracks down to 15 mrad. However, there are about 6 stations in-between, which are not strictly required for covering the LHCb acceptance. They were inserted for minimizing the extrapolation distance of tracks towards their vertex and for redundancy reasons (Fig. 3.6). In the reoptimization study, it was found out that the VELO with four stations less has a very similar performance concerning robustness (Fig. 3.7) and resolution (Fig. 3.8) compared to the TDR design. The corrugations in the RF foil which accommodated those four stations will not be removed, since they are useful for minimizing on average the material traversed by particles in the acceptance, and also they add to the stiffness of the foil.

3.4 Thickness of sensors

For the VELO TDR, a silicon thickness of 300 μm was chosen as the baseline design for two reasons:

- wider range of manufacturers for the complicated double-metal n-on-n design;
- uncertainty about the noise performance of the final front-end chip.

Since then, the R&D with one of the manufacturers who is able to produce 220 μm thin sensors was suc-

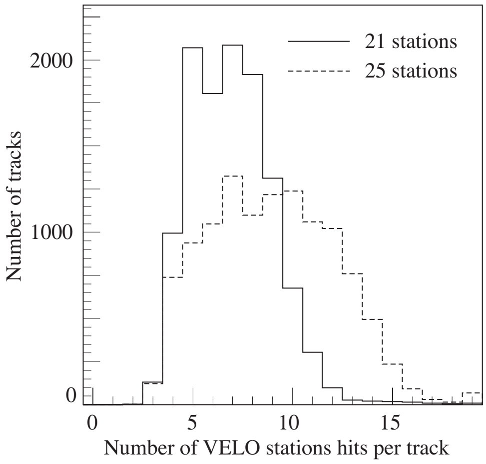

Figure 3.7: The number of VELO stations traversed by tracks in the LHCb acceptance for 25 stations (dashed line) and 21 stations (solid line). The number of tracks crossing less than four stations in the new setup is less than 0.1%; if a further station were to be removed, this fraction would increase to 0.5%. An average track crosses 7 stations.

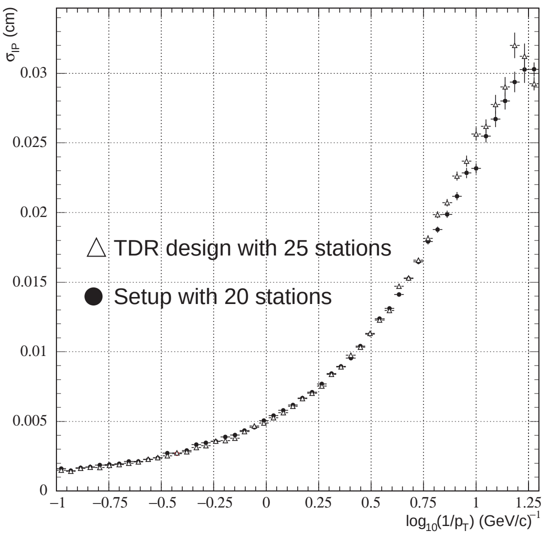

Figure 3.8: Impact parameter resolution as a function of $\log(1/p_{\mathrm{T}})$ for the TDR design with 25 stations and for a setup with 5 stations removed.

cessful. In addition, the current version of the Beetle chip (Beetle 1.2), which was recently selected as the front-end chip for the VELO, has a noise performance of about $\mathrm{N} = 500\,\mathrm{e}^- + 50\,\mathrm{e}^-/\mathrm{pF}$ (see also TT testbeam results in Sect. 5.4). This, together with the choice of an overall 45° sector design for the R-sensors (Sect. 3.7), which reduces considerably the capacitance for the strips at larger radii, enables the use of $220\,\mu$m thin sensors while still maintaining a signal-to-noise ratio $\mathrm{S/N} > 14$ [30].

3.5 Module and hybrid material

The design of the VELO module has been substantially modified [28] to allow low cost fabrication, to minimize the material and to provide high thermal conductivity. The two major differences compared to the TDR are:

- Removal of the module alignment system. The necessary accuracy will be achieved during fabrication.
- Reduction of material by adopting a “double sided” design, i.e. two hybrids on one substrate. This will however complicate the construction.

A schematic of an LHCb module is shown in Fig. 3.9. The key components are:

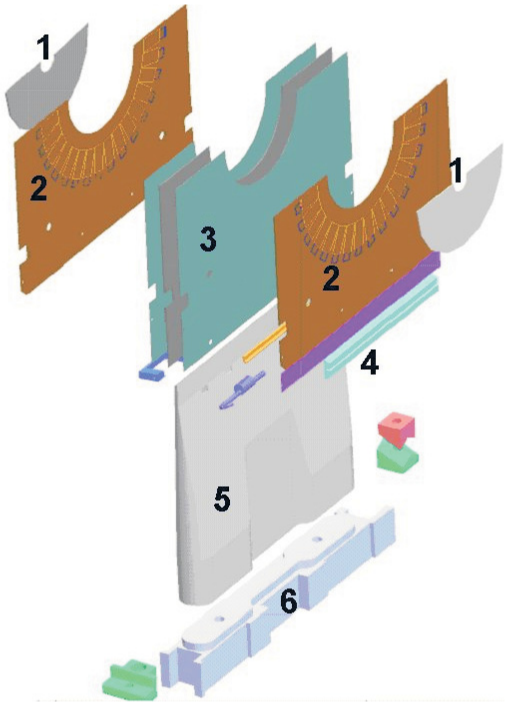

Figure 3.9: Schematic of the VELO module showing the key components. See the text for details.

1. The silicon sensors.
2. The front-end electronics mounted on a thin Kapton sheet.
3. The substrate which performs the dual role of a mechanical support and a thermal pathway; it is a complex carbon-fibre thermo-pyrolytic graphite composite.
4. The cooling block manufactured from carbon-carbon to match the coefficient of thermal expansion of the substrate, which provides the thermal linkage with the cooling system. Prototypes of aluminium have been made.
5. The low mass carbon-fibre paddle which is designed to rigidly hold the substrates and allow the sensors to be placed close to the interaction point.
6. The paddle base made of carbon-fibre. The base is connected via location inserts to the platform. The location inserts possess precisely machined surfaces which allow the precise placement of the base onto the (moveable) platform that supports the two halves of the VELO telescope. This design allows

Table 3.2: Average radiation and interaction length seen by tracks passing through the VELO detector. The numbers in brackets correspond to the material seen before the first measured hit.

	$2.0 < \eta < 5.0$		in ECAL acceptance $2.0 < \eta < 4.2$	
	X_0 [%]	λ_{I} [%]	X_0 [%]	λ_{I} [%]
Silicon	3.71 (0.30)	0.76 (0.06)	4.11 (0.29)	0.85 (0.06)
RF foil	9.28 (3.66)	2.10 (0.83)	8.00 (2.37)	1.81 (0.54)
RF box	0.88	0.19	1.00	0.22
Hybrids	1.50	0.51	2.05	0.69
Paddles	0.42	0.14	0.57	0.19
WF cone	0.70	0.08	0.02	0.01
Total	16.49 (3.96)	3.77 (0.89)	15.74 (2.70)	3.76 (0.60)

for the quick and repeatable insertion of the modules onto the platform with an accuracy of about 10 μm at 21°C.

The current design excluding the silicon sensors contributes about 1.9% of a radiation length to the average material traversed by particles in the LHCb acceptance.

Minor changes to the zero insertion force mechanism for the cooling block will be made before the 2004 pre-production, that will use the new assembly robot to be commissioned between June and August 2003.

3.6 Updated material budget

The numbers presented in Table 3.2 have been calculated using a detailed geometrical description of the VELO inside GEANT3 [27] with the final materials and thicknesses. A particle distribution which is flat in pseudorapidity η and azimuth angle ϕ is assumed for estimating an average radiation length X_0 and interaction length λ_{I}.

Summary of modifications which effectively reduced the material compared to the VELO TDR:

- Number of stations reduced from 25 to 21.
- Thickness of silicon reduced from 300 μm to 220 μm.
- Downstream corrugations of the RF foil removed.
- Reduced thickness in the stretched regions of the RF foil taken into account.

Summary of modifications which effectively increased the material compared to the TDR:

- Corrugations of RF foil reduced from 2 cm to 1.2 cm.
- More realistic estimate of module composition.

In the end, the total material is slightly less than that estimated in the TDR.

3.7 Sensor design

The strip layout in the VELO-TDR for the r-measuring sensor consisted of subdividing the strips at radii below 24.1 mm into four sectors of approximately 45° while for larger radii the strips were only subdivided in two sectors covering 91° degrees each. The aim was to save channels at larger radii, where the occupancy is low, and use these channels to decrease as much as possible the pitch at small radii to improve the impact parameter resolution.

A design that subdivides the strips in four sectors at all radii has advantages for the uniformity of the capacitance per channel, the execution time of the track reconstruction, and the number of clone and ghost tracks. Since the number of channels per sensor cannot be increased beyond 2048 for practical reasons, the strip pitch needs to be increased to cover the same area with four sectors at all radii. Four different designs for the layout of the R-sensors of the VELO were compared for their performance concerning the signal-to-noise ratio, the Pile-Up detector, the L1-tracking, the off-line tracking and the impact parameter resolution [29]. It was found that the loss in impact parameter resolution is in general small. The choice for the new design also takes into account fabrication risks. The strip pitch in the new design is given by the

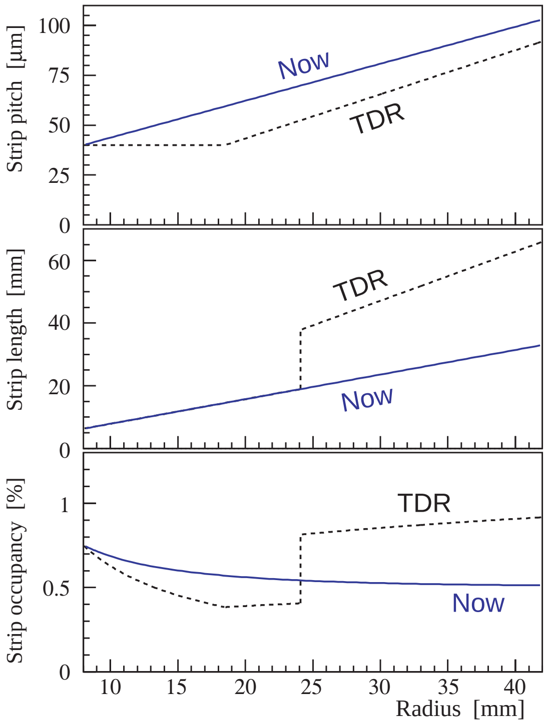

Figure 3.10: The strip pitch, length and occupancy as a function of the radius for two R-sensor strip designs.

following function of radius r (in μm):

$$40 + (101.6 - 40) \times \frac{r - 8190}{41949 - 8190} \ .$$

The resulting strip pitch, length and occupancy as a function of radius are compared to those of the TDR design in Fig. 3.10. The outer dimensions of the sensors are currently being finalized [30]. The measurements on the first full-size RF foil and measurements on the silicon cutting tolerances suggest an increase of the total tolerance between the RF foil and the silicon sensors from 1 mm to 1.2 mm.

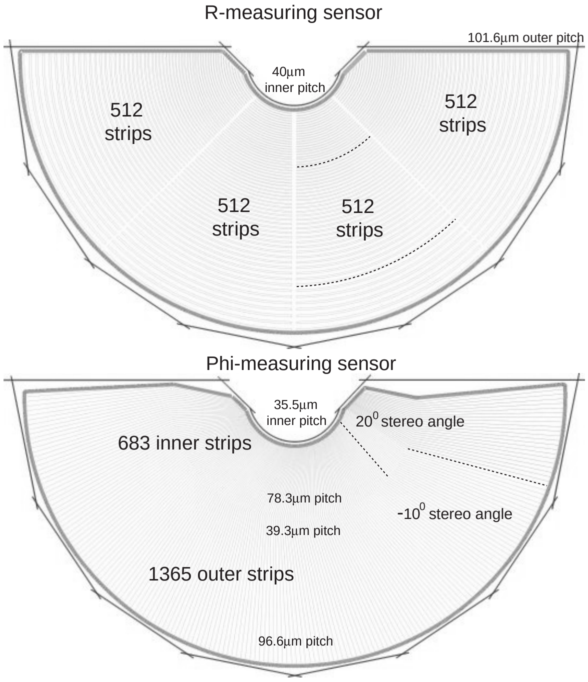

Figure 3.11: Sensor layout. Some strips are indicated with dotted lines for illustration.

To compensate for this, the RF foil has been moved a bit closer to the beam and the start of the sensitive area has been changed from $r = 8$ mm to $r = 8.17$ mm. In addition, the sharp inner corners of the TDR design needed to be smoothed in order that the sensors would fit within the RF-foil. A diagram of the present sensor layout is shown in Fig. 3.11. Increasing the inner radius of the sensitive area has only a small effect on the resolution [31].

Chapter 4 RICH 1 Reoptimization

4.1 Introduction

Hadron identification in LHCb is provided by two Ring Imaging Cherenkov detectors (RICH). High momentum particles (up to $\sim 100\,\mathrm{GeV}/c$) are identified by the RICH 2 detector, situated downstream of the spectrometer magnet and tracking stations. The RICH 2 design has undergone no significant change in the context of the LHCb detector optimization and is described in detail in the engineering design review [32]. Lower momentum particles, up to about $60\,\mathrm{GeV}/c$, are identified by the RICH 1 detector, located upstream of the magnet. RICH 1 has undergone a major redesign and differs significantly from that described in the RICH Technical Design Report (TDR) [7]. These changes are motivated by the need to reduce material within the spectrometer acceptance and to accommodate the magnetic bending power required for charged particle momentum determination at Level-1 in the LHCb trigger.

4.1.1 RICH 1 requirements

RICH 1 is designed to provide particle identification over the momentum range from 1 to $60\,\mathrm{GeV}/c$. It combines silica aerogel and fluorocarbon gas radiators with a polar angle acceptance from 25 to 300 mrad. The aerogel covers the low momentum tracks and plays an important role in tagging the flavour of the b-hadrons through the $\mathrm{b} \to \mathrm{c} \to \mathrm{s}$ quark decay chain.

An important requirement of the overall LHCb detector reoptimization is to minimize material within the spectrometer acceptance. The total material contributed by RICH 1 amounted to about 14% of a radiation length in the RICH TDR design. The design presented here reduces this significantly, mainly by reducing the contributions from the spherical mirrors and their supports.

In the LHCb reoptimization the Level-1 trigger [3] has been improved to yield better performance. An enhanced fringe field of the spectrometer magnet between the VELO and the Trigger Tracker (TT) station is required to determine the momenta of particles with a resolution of 20–40%. This has imposed strong constraints on the new RICH 1 design. In the TDR [5] design of the spectrometer magnet a large iron shielding plate was located upstream of the magnet. This reduced the magnetic field in the region of the RICH 1 photon detectors to a level that permitted their operation using simple magnetic shields made from high-permeability alloys[1]. The iron shield plate is incompatible with the Level-1 trigger requirement. Its removal results in a B-field of about 60 mT in the region of RICH 1. The consequence is that an iron shielding house is needed to attenuate the B-field by a factor ~ 25 to allow operation of the photon detectors, while at the same time providing adequate magnetic bending power for the Level-1 trigger. A bending power of 0.15 Tm between the interaction point and TT is required [3].

4.1.2 Evolution since RICH TDR

Material budget

Reduction of material is achieved by introducing the following features in the current RICH 1 design:

- Removal of RICH 1 entrance window and beam-pipe seal, by sealing directly to the VELO tank.
- Lightweight spherical mirrors. Prototype mirrors made from carbon-fibre composite, glass-coated beryllium and acrylic sheet[2] have been tested.
- Elimination of the contribution from the mirror supports, achieved by locating the support and adjustment mechanism outside the acceptance.

Level-1 magnetic-field requirements

The consequences of the magnetic field result in major design changes:

---

[1] Permalloy C or Mumetal.

[2] PERSPEX (a trademark of the Lucite International Group, Southampton, UK) with carbon-fibre honeycomb core.

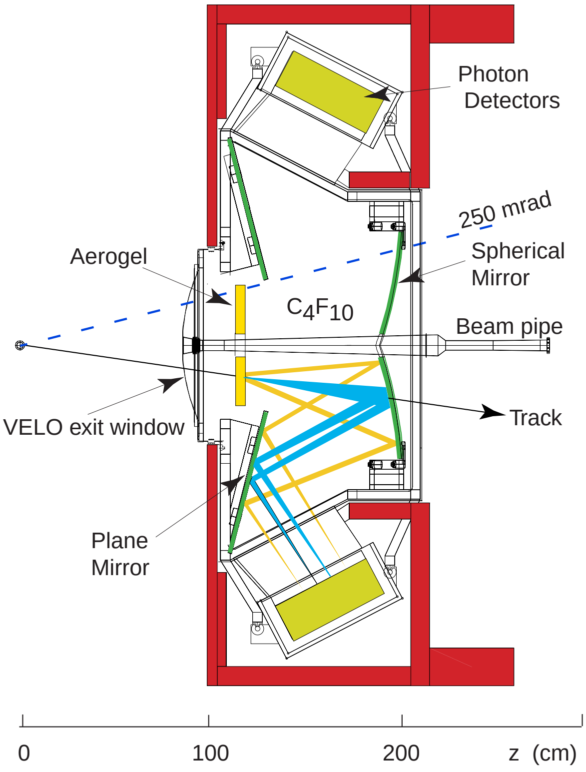

Figure 4.1: Layout of the vertical RICH 1 detector.

- Additional plane mirrors (as in RICH 2) are required so that the photon detectors can be located in a region where soft iron magnetic shielding can be used.
- Horizontally-located iron shields would steal the *B*-field away from where it is required by the trigger, so the photon detectors are located above and below the beam. Hence the new RICH 1 design has a vertical optical layout as shown schematically in Fig 4.1.

Gas system

The preferred RICH 1 gas Cherenkov radiator is C_4F_{10}. Concern over the future availability and cost of this gas has prompted the provision of additional features to the RICH 1 gas system that would allow mixing of C_3F_8 and C_5F_{12} to achieve the same refractive index as C_4F_{10}.

4.1.3 RICH photon detectors

Until June 2003 the baseline RICH photon detector was the Hybrid Photon Detector (HPD). The HPD is a 40 MHz high-resolution photon detector developed by LHCb together with several industrial partners[3]. Delay in the development of the solder-bump bonds that connect the silicon pixel sensor to its readout chip have resulted in a switch of baseline to the Hamamatsu M64 multianode photomultiplier tube (MaPMT). Nevertheless, HPD development within LHCb is on-going and the final technology choice for the RICH photon detector will be made by October 2003.

The MaPMT, equipped with a quartz lens to increase its active area coverage, has been tested [33] in charged particle beams as a Cherenkov photon detector, and shown to satisfy the LHCb RICH requirements. All physics performance studies reported in this document result from a simulation of the HPD. However, comparitive performance studies (including photon yield, Cherenkov angle precision, π–K separation and tagging efficiencies) carried out earlier [34] indicate that there is no change in the physics performance resulting from the use of either HPD or MaPMT. The baseline choice was made on the grounds of the lower cost (albeit higher risk) of the HPD. The design criterion for the overall magnetic shielding of the HPD's was set to < 1 mT. The MaPMT has a reduced sensitivity to magnetic field and the requirement is now set to < 2.5 mT. This has relaxed the constraints in the shielding and allowed a design that satisfies the opposing requirements for the photon detector shielding and the Level-1 trigger.

4.1.4 Contents of this chapter

We provide in the following section a description of the main components and the parameters of the new RICH 1 design. Section 4.3 summarizes results from prototyping carried out since the RICH TDR that is relevant to the new RICH 1 design. Measurements on prototype mirrors and the stability of their supports, together with laboratory and beam tests of aerogel radiators, are reported. Section 4.4 presents the basic performance parameters, photon yields and angular precision, that have been estimated from the simulation. Their influence on the particle identification and physics performance is reported in Chapter 8 of this document. The technical design is presented in Sect. 4.5. Institute responsibilities for RICH 1 are given in Sect. 4.6, and the rest of the project planning, including estimated costs, schedules and milestones, is discussed in Chapter 10.

In view of the recent switch of baseline pho-

---

[3] Delft Electronic Products, Netherlands; Kyocera, Japan; VTT, Tietotekniikka, Finland.

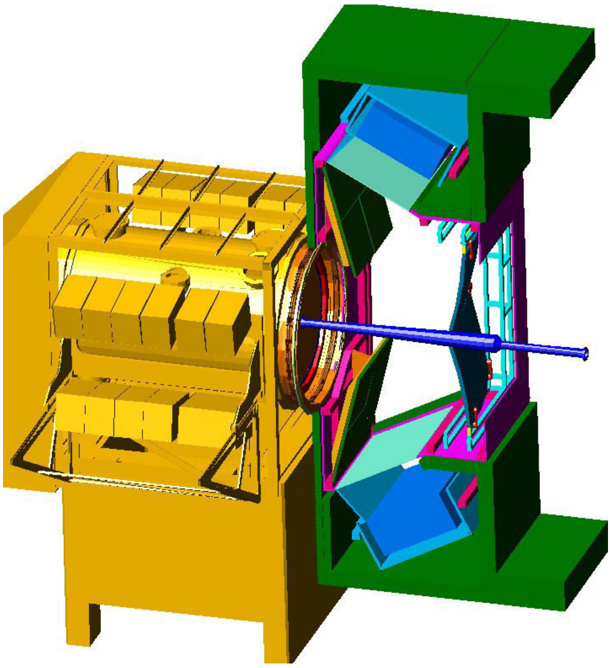

Figure 4.2: Cut-away 3D model of the vertical RICH 1 detector, shown attached by its gas-tight seal to the VELO tank.

ton detector technology, few details of the MaPMT integration into the RICH 1 design are presented in this document and all simulations relate to the HPD. As stated above, we expect only small differences in physics performance and the consequences following from the photon detector choice will be written in an addendum to the RICH TDR, to be submitted to the LHCC.

4.2 Detector description and specifications

In this section the principal features of the detector are described and their main parameters specified. Their optimization has been constrained by limits on the space available, on material within the spectrometer acceptance, on magnetic field requirements for the RICH photon detectors and for the Level-1 trigger and on the overall cost, to which the photon detectors contribute about 50%. Prototype tests and finite element modelling have been undertaken which demonstrate that the parameters listed can be achieved. The parameters have been used in the simulation studies reported in Sect. 4.4 and in Chapters 8 and 9.

4.2.1 Overall dimensions

RICH 1 is required to cover the full LHCb angular acceptance, so to reduce its physical size it is located upstream of the spectrometer magnet. The longitudinal space available, between the VELO and the TT station, limits the length of RICH 1 to about 1 m. The focusing of Cherenkov light is accomplished using spherical mirrors, tilted to bring the image out of the spectrometer acceptance. The light rays are again reflected using secondary plane mirrors to focus the ring images on the photon detectors, located above and below the beam, in a region where thay can be shielded from the B-field of the spectrometer magnet. The angular acceptance of 300 mrad (horizontal) × 250 mrad (vertical), and the optical system, result in a RICH 1 gas vessel with dimensions approximately $2 \times 3 \times 1\,\mathrm{m}^3$. The RICH 1 layout is illustrated in Fig. 4.1 and as a cut-away 3D model in Fig. 4.2. It has a 5 cm-thick aerogel radiator and a 85 cm-long fluorocarbon (C_4F_{10} or equivalent) gas radiator.

4.2.2 Cherenkov angle precision

The resolution on the reconstructed Cherenkov angle has the following contributions:

- *Emission point:* the tilt of the spherical mirror leads to a dependence of the image of a Cherenkov photon on its emission point on the track. In the reconstruction, all photons are treated as if emitted at the mid-point of the track through the radiator, leading to some smearing of the reconstructed angle.
- *Chromatic:* the chromatic dispersion of the radiators leads to a dependence of the Cherenkov angle on the photon energy.
- *Pixel:* due to the finite granularity of the photon detector.
- *Tracking:* due to errors in the reconstructed track parameters.

The effects of these contributions are discussed in Sect. 4.4.2. The effective granularity of the MaPMT photon detector is 3 mm×3 mm. This is a 20% increase compared with the HPD, but when combined with the other contributions results in a small effect on the overall Cherenkov angle precision.

4.2.3 Radiators

RICH 1 includes two radiators. A 5 cm-thick wall of aerogel with refractive index $n = 1.03$ provides positive kaon identification above 2 GeV/c and π–K separation up to about 10 GeV/c. The useful wavelength range of the Cherenkov light from aerogel is limited by Rayleigh scattering. The transmission T through a length L is given by

$$T = A\, e^{-CL/\lambda^4} \tag{4.1}$$

for wavelength λ, where C is the clarity coefficient. The value used in the simulations is $C = 0.008\,\mu\mathrm{m}^4/\mathrm{cm}$, however R&D is currently underway to reduce this (see Sect. 4.3.2) which would result in a higher fraction of unscattered photons. Alternatively, the material budget might be reduced for the same photon yield. Equation 4.1 indicates that the UV Cherenkov light is strongly scattered. To reduce the background due to this Rayleigh scattered light a 100 μm-thick glass filter is placed immediately downstream of the aerogel. The preferred gas radiator is C_4F_{10} at room temperature and atmospheric pressure, which occupies an $L = 85$ cm path length between the aerogel and the spherical mirror. The refractive index is $n = 1.0014$ for $\lambda = 260$ nm, and provides $3\,\sigma$ π–K separation up to about 50 GeV/c. An alternative radiator having similar refractive index and chromatic dispersion can be obtained by mixing C_3F_8 and C_5F_{12} with a 50:50 molar concentration and will be considered in the event of C_4F_{10} procurement problems. The number of focused and detected photon hits from $\beta \simeq 1$ tracks is given in Sect. 4.4.2.

4.2.4 Photon detectors

The baseline photon detectors are Hamamatsu M64 multianode photomultiplier tubes (MaPMT). The anodes are arranged in an 8×8 array of pixels, each 2 mm×2 mm, separated by 0.3 mm gaps. The vacuum tube envelope measures 25.7 mm×25.7 mm resulting in a sensitive area of 48%. This is increased by placing a plano-spherical quartz lens on the photocathode window of each MaPMT, resulting in close to full geometrical coverage with a demagnification of ×1.5 and an effective pixel size of 3 mm×3 mm.

The bialkali photocathode has a typical quantum efficiency of 24% at maximum (380 nm), with sensitivity extending from 600 nm down to 200 nm. Two versions of the M64 are considered: 7600-03-M64 with 12 dynodes and 7600-03-M64MOD with 8 dynodes. The latter has a gain $\sim 5 \times 10^4$, compatible with readout using the LHCb Beetle chip [35]. The 12-dynode tube has a gain $\sim 3 \times 10^5$ and requires a modified Beetle with reduced gain.

Using one 128-channel Beetle chip to read out two MaPMT's the subsequent readout chain can be very similar to that used by the silicon trackers [6]. Four multiplexed analogue signals from each Beetle, validated by the Level-0 trigger, are digitised using 8-bit FADC's then further multiplexed (×32) and transmitted on gigabit optical links to the Level-1 electronics in the counting room.

Each of the two RICH 1 photodetector planes covers an area of 120 cm×52 cm. With MaPMT's packed at 28 mm pitch in modules of 16, then 110 modules or 1760 MaPMT's are required. The use of MaPMT's in the RICH has been described in the Appendix to the RICH TDR [7]. More details will be presented in an addendum to the TDR.

4.2.5 Mirrors

Cherenkov light is focused onto the photon detector planes using tilted spherical mirrors and secondary plane mirrors, as shown in Fig. 4.1. The RICH 1 spherical mirrors have a radius of curvature of 2400 mm. The mirror surface is segmented into four rectangular quadrants each 820 mm×600 mm. Two technologies are considered for the spherical mirrors: 2 mm-thick carbon-fibre epoxy, coated with aluminium and a protective layer (SiO_2 and HfO_2) designed to optimize the reflectivity for the wavelength of the Cherenkov light, or 3 mm-thick beryllium, with a 0.3 mm glass skin on which aluminium is deposited, again with an appropriate protective layer. Each of the four mirrors can be individually adjusted in angle so that upper and lower pairs share a common centre of curvature. The secondary, plane mirrors are arranged in two halves above and below the beam. Each half has dimension 1500 mm×775 mm and is composed of eight rectangular units of 6 mm-thick polished glass with aluminium coating. The technology for the plane mirrors and their supports is the same as that described in the engineering design review for RICH 2 [32]. Their mounts have adjustment that allows the ring images to be centred on the detector plane.

The mean reflectivity of the mirrors over the wavelength range of interest ($200 < \lambda < 600$ nm) is expected to be above 85%.

4.2.6 Magnetic shielding

In the absence of shielding the magnetic field at the RICH 1 photon detectors is about 60 mT. The photoelectron detection efficiency of the MaPMT's is reduced by about 10% in an axial B-field of 2.5 mT [36]. The sensitivity to transverse fields is

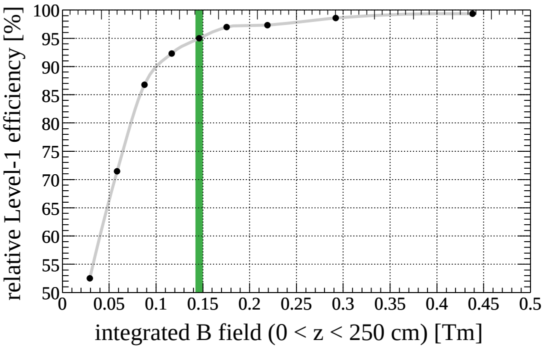

Figure 4.3: Dependence of the Level-1 trigger performance on the upstream magnetic bending. The vertical line corresponds to the integral of the field used in the performance studies.

much less. Magnetic shielding is needed to maintain a high photoelectron detection efficiency while at the same time boosting the magnetic bending in the region between the VELO and the Trigger Tracker. The dependence of the Level-1 trigger performance as a function of this bending is shown in Fig. 4.3, with further details in [37].

Specifications for the design of the shielding have been defined as follows:

- Maximum field at photon detector plane: $B_{\mathrm{max}} < 2.5\,\mathrm{mT}$.
- Field integral over $0 < z < 250\,\mathrm{cm}$: $B_{\mathrm{trig}} > 0.15\,\mathrm{Tm}$.

ARMCO[4] iron plates are assembled into boxes, above and below the beam, that shield the photon detectors as shown in Fig. 4.1. Finite element modeling has resulted in a design satisfying the criteria. The total weight of each box is about eight tonnes and the detail of their design is central to the overall mechanical design of RICH 1. In particular, access must be provided for photon detector maintenance, installation of the beam pipe and the optical components.

4.2.7 Gas vessel, seals and windows

Magnetic forces acting on the shielding iron result in displacements that are significant compared with the precision required for the RICH 1 optics. Hence the photon detectors and mirrors are mounted to a separate gas vessel, resulting in reduced mechanical distortion from the magnetic forces. At its upstream end the welded-aluminium gas vessel is sealed to the VELO tank. The downstream end is sealed by the RICH 1 exit window, made from 16 mm-thick rigid polymethylacrylimide foam sandwiched between 0.5 mm carbon skins.

To ensure the polar angle acceptance extends down to 25 mrad there is no inner wall surrounding the beam pipe and the exit window seals directly to the beam pipe using pre-formed corrugated kapton foils.

Quartz windows, 130 cm×60 cm×0.5 cm, seal the top and bottom of the vessel and transmit Cherenkov light to the photon detectors. These windows have the same design [32] as used in RICH 2. Finally each side of the gas vessel is fitted with removable plates for access to the optics and the beam pipe.

4.2.8 Alignment

The angular resolution of the RICH detector depends on the alignment of its optical components. To ensure that the precison in reconstruction of the Cherenkov angle, about 1.2 mrad in RICH 1, is not degraded by uncertainties in alignment the aim is to maintain alignment errors below 0.1 mrad. The alignment of the optical components will be achieved in stages. First an *in situ* survey of all mirrors and photon detectors will be performed to a level of 1 mrad. Final alignment parameters will be extracted from data. By reconstructing a large number of rings from $\beta \simeq 1$ tracks in which the ring image is formed via reflection from an unambigous combination of mirror segments, a precision ~ 0.1 mrad can be attained [38]. A laser system will be used to monitor the alignment parameters over time.

4.2.9 Beam pipe access

A common requirement for all LHCb sub-detectors is that provision has to be made for access to the LHC beam pipe [12] for maintenance procedures, and in particular, for bake-out. Most LHCb detectors are assembled in two halves, so that one side can be withdrawn, allowing access to the beam pipe. This solution is unacceptable for the RICH detectors as it would result in significant material to seal the vessel close to the beam and result in a loss of the light emitted into one side of the detector from tracks traversing the radiator on the other side. The solution adopted for RICH 2, a secondary beam pipe, would result in an unacceptable loss of low-angle acceptance. The seal of the RICH 1 vessel is therefore made directly to the beam pipe and

---

[4] Iron with purity > 99.8%, high magnetic saturation and low coercivity.

Table 4.1: Contributions (expressed as fractions of a radiation length and nuclear interaction length) to the material in RICH 1, that fall within the LHCb acceptance.

Item	X_0	λ_{I}
Aerogel	0.033	0.007
Gas radiator	0.026	0.016
Spherical mirror (CF)	0.011	0.005
Spherical mirror (Be)	0.008	0.007
Exit window	0.006	0.003
Total (with CF mirror)	0.076	0.031
Total (with Be mirror)	0.073	0.033

access for bake-out will be via the RICH 1 gas vessel, from which the gas, mirrors and possibly the seal would be removed. Providing the bonding of the flexible seal to the beam pipe can be qualified at 250°C it will remain in place, otherwise it would need to be replaced. The RICH 1 design ensures that all necessary access procedures can be carried within an acceptable time frame of less than one week.

4.2.10 Material budget

The contributions to the RICH 1 material budget that fall within the acceptance are listed in Table 4.1. The total amounts to less than 8% of a radiation length.

4.3 Prototype studies

4.3.1 Lightweight mirrors

Prototype mirrors and their mounts have been characterised and qualified. A quarter-size carbon-fibre/epoxy composite mirror prototype, shown in Fig. 4.4, has been purchased from CMA[5] who have supplied mirrors to NASA and the HERMES [39] experiment at DESY. Mirror specifications are being verified by measurement. The most critical specifications are the average values of radius of curvature, angular resolution and reflectivity. A mirror mount prototype is also being characterised in adjustment precision and stability. It is important to keep the variations in long term stability well below the requirements of the offline alignment procedure. This sets a stability requirement in the range of $\sigma < 0.1$ mrad. The effect of the radiator gas on the components is also being checked.

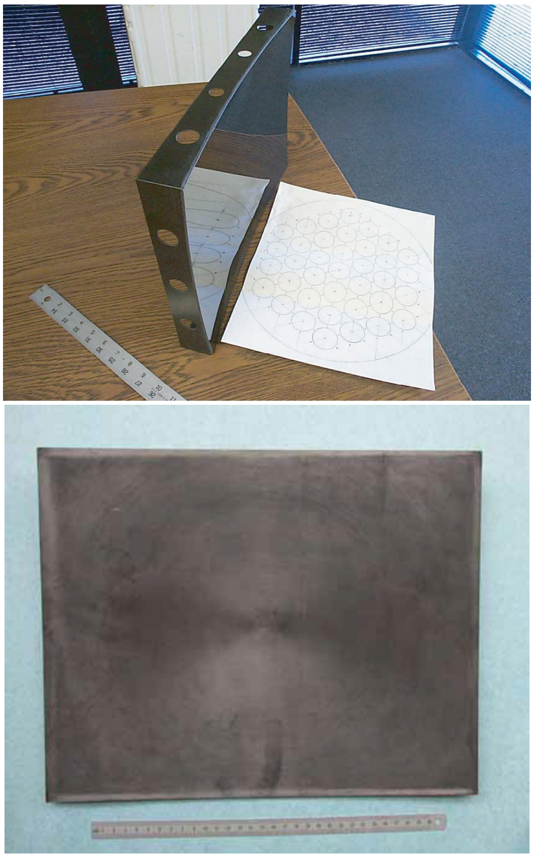

Figure 4.4: Prototype carbon-fibre/epoxy composite mirror (above), glass-coated beryllium mirror (below). The dimensions of these prototypes are approximately 40 cm× 30 cm.

If the carbon-fibre technology does not meet requirements, a solution using a 3 mm-thick beryllium substrate with 0.3 mm glass surface layer, coated with aluminium, SiO_2 and HfO_2, will be adopted. This technology has been proven to meet the optical specifications [40] and uses the same supports. It contributes less to the radiation length but more to the interaction length; however, the differences are very small as shown in Table 4.1. An R&D programme [41] on composite mirrors using acrylic sheet, backed with a carbon-fibre honeycomb structure, resulted in samples with satisfactory optical qualities but that were unstable in fluorocarbon gas.

Mirror quality

The prototype carbon-fibre mirror has been tested for radius of curvature and average angular preci-

---

[5] Composite Mirror Applications Inc, Tucson, USA.

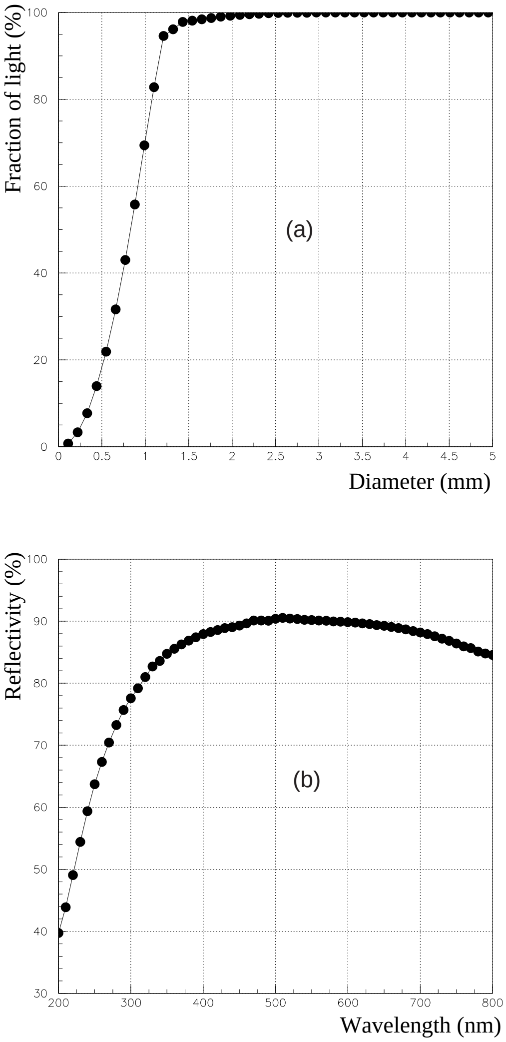

Figure 4.5: Light fraction inside circles of different diameter (a), and reflectivity as a function of wavelength (b), for the prototype mirror.

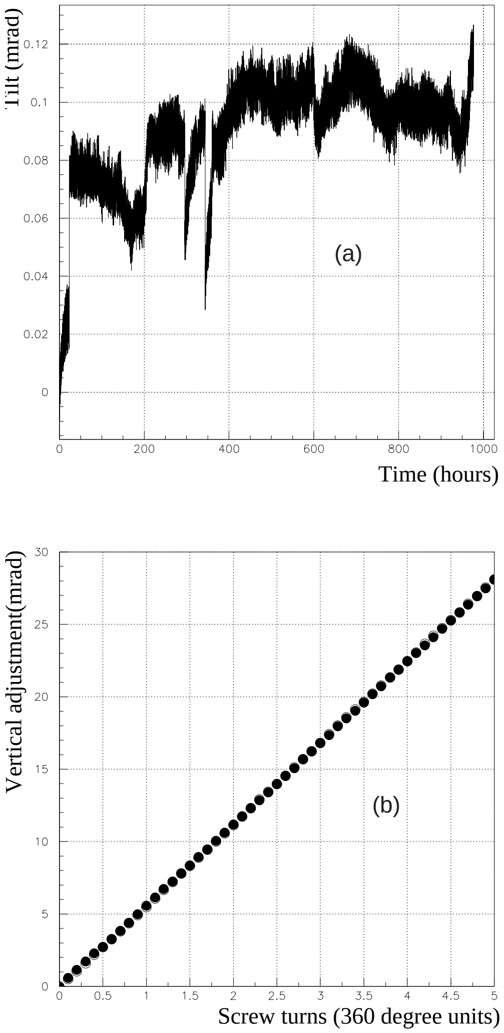

Figure 4.6: Long term stability (a), and linearity of adjustment (b), of the prototype mirror support.

sion. The measurement assesses the variation from an ideal spherical surface by imaging a point source reflected from the prototype and analyzing the size and shape of the resulting spot [40]. For a perfect spherical mirror of the size used in RICH 1 the diameter, D_0, containing 95% of reflected light is diffraction limited to $27\,\mu$m. For our purpose the parameter D_0 is required to be less than 2.5 mm in order not to dominate the Cherenkov angle resolution. In Fig. 4.5 (a) the fraction of light reflected from the prototype falling in circles of different diameter is shown. This indicates that carbon-fibre mirrors with a substrate thickness of 2 mm could satisfy the requirement of focusing 95% of reflected light into a circle with diameter $D_0 < 2.5$ mm at the plane defined by the mirror radius of curvature.

The reflectivity of the prototype mirror was found to be below the requirements of RICH 1 and a microscopic inspection identified the cause as surface crazing in the epoxy. Replacement samples of mirror substrate manufactured with a vacuum-deposited high purity aluminium reflective layer and SiO_2 protective overlayer have been measured at CERN with a calibrated light source and demonstrate that the problem is under control. The results shown in Fig. 4.5 (b) closely follow calculated predictions which indicate that a maximum reflectivity of 93% is obtainable without overcoating. These calculations also showed that attenuation of reflected light at lower wavelengths is dependent on the type and thickness of overcoating but that this can be minimised by careful selection of material and reflectivities approaching 90% can be maintained for the required angles of incidence and the wavelength range of interest ($200 < \lambda < 600\,\mathrm{nm}$).

It is encouraging that the HERMES experiment successfully uses a CMA carbon-fibre/epoxy composite mirror in a C_4F_{10} environment with no reported problems. However, the lower resolution of the HERMES RICH detector leaves the possibility that there might be effects not seen by that experiment but which may degrade the performance of LHCb. To exclude this possibility a sample is presently undergoing long term tests in a C_4F_{10} environment.

Mirror supports

Test facilities for the evaluation of the adjustment characteristics and the long term stability of mirror mounts have been developed [42]. A prototype mount has been produced that supports the mirror whilst keeping all material outside the spectrometer acceptance. The design also isolates the mirror from thermal expansion that could otherwise lead to deformation of the mirror profile. The details of the mount design are given in Sect. 4.5.3. In Fig. 4.6 (a) its long term stability is shown by means of monitoring its tilt over 1000 hours. After initial relaxation the fluctuations of vertical and horizontal tilts stay well within the 0.1 mrad required.

The precision of the tilt adjustment needs to be about 1 mrad, in order to allow the alignment parameters to be evaluated using Cherenkov ring data with a precision of 0.1 mrad. The mount adjustment precision is shown in Fig. 4.6 (b), where two datasets for positive and negative adjustment coincide to within 0.5 μrad after an integrated adjustment approaching 30 mrad. A tilt change of 0.56 mrad corresponds to a screw turn of 36°, which enables a sufficiently precise adjustment. The relationship between tilt and screw-turn is essentially linear.

4.3.2 Aerogel

Since the Technical Design Report [7], the R&D programme on aerogel produced a quality of aerogel with very high clarity and a thickness of 4 cm [43]. These aerogel tiles have been tested at the CERN-PS beam T7, and the results [44] are summarized here.

Possible ageing of the aerogel due to irradiation from different sources, or from absorption of humidity, has also been studied. Aerogel tiles were irradiated with intense γ, proton and neutron beams, or exposed to humid air flow, and their optical parameters were measured to monitor ageing, including the transmittance, clarity and index of refraction. Inside the RICH 1 detector, aerogel tiles will be positioned at a radial distance from the beam of about 5 cm and at about one metre downstream of the interaction point. As a consequence, they will be exposed to a significant particle flux [45].

Testbeam

The experimental setup consists of a light-tight black painted aluminium vessel, an aerogel radiator and a spherical mirror of 60 cm focal length. Nitrogen is flushed to preserve the quality of the hygroscopic aerogel tiles.

The results presented here concern two tiles of $7 \times 8 \times 4\ \mathrm{cm}^3$ and $10 \times 10 \times 4\ \mathrm{cm}^3$, produced by the Boreskov Institute of Catalysis in collaboration with the Budker Institute of Nuclear Physics in Novosibirsk [46]. They were tested separately and together to form a total thickness of 8 cm. The optical properties of these aerogel samples were measured in the laboratory. The tiles are hygroscopic with refractive index 1.0306 and 1.0298 respectively (at $\lambda = 400\,\mathrm{nm}$). From the curves of transmittance as a function of wavelength in the range 200–900 nm, the clarity coefficients $C = (72.2 \pm 0.1) \times 10^{-4} \mu\mathrm{m}^4/\mathrm{cm}$ and $(64.4 \pm 0.1) \times 10^{-4}\ \mu\mathrm{m}^4/\mathrm{cm}$ were determined for each tile, fitting Eq. (4.1). The clarity determined for the 8 cm stack was $C = (69.5 \pm 0.1) \times 10^{-4} \mu\mathrm{m}^4/\mathrm{cm}$. The A coefficients were $(92.0 \pm 0.1)\%$ and $(95.9 \pm 0.1)\%$ for the individual tiles and $(88.2 \pm 0.1)\%$ for the 8 cm thickness.

Data were taken under different conditions, changing the thickness of the aerogel (4 or 8 cm), the beam momentum (6, 8, 9, 10 GeV/c) and the particle charge. Highly relativistic charged particles ($\beta \simeq 1$) produce Cherenkov photons in aerogel with refractive index $n = 1.030$ at an angle of 242 mrad with respect to the particle direction. A 0.3 mm-thick glass filter[6], was added in some runs, at the exit wall of the aerogel radiatior, to absorb UV photons above $\sim$4 eV, which are most affected by Rayleigh scattering.

The detection of the Cherenkov photons produced inside the aerogel was performed using four Pad HPD's positioned in the focal plane of the mirror, providing a geometrical coverage of about 30% of the total ring. The design, fabrication and performance of the Pad HPD is described in [47].

---

[6] Schott D263 T borosilicate glass.

Table 4.2: Photoelectron yield, in the "on-ring" region, scaled to full ring coverage.

		No Filter	Filter D263
4 cm	Data	9.7±1.0	6.3±0.7
	MC	11.5±1.2	7.4±0.8
8 cm	Data	12.2±1.3	9.4±1.0
	MC	14.7±1.6	10.1±1.1

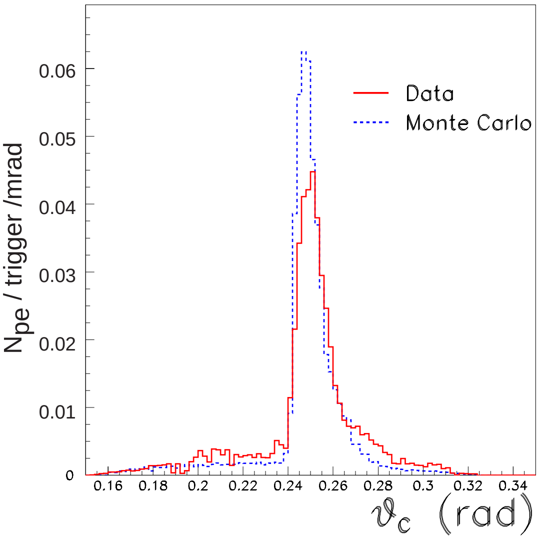

Figure 4.7: Distribution of the reconstructed Cherenkov angle for 4 cm-thick aerogel.

The number of detected photoelectrons has been evaluated separately in each HPD, summing over all the pads in the geometrical region defined as within three times the resolution around the fitted radius ("on-ring" region). The number of photoelectrons in each pad has been determined by analysing the corresponding ADC spectra. The same procedure has been applied to a Monte Carlo simulation. The comparison between data and Monte Carlo, for different thicknesses of aerogel and with or without the filter, is shown in Table 4.2. The measured yields are typically within 15% of the expectation.

The Cherenkov emission angle θ_C is extracted from the photoelectron hit coordinates and the knowledge of the geometry of the system using the re-tracking algorithm described in [48]. The measured θ_C distribution of detected photoelectrons is shown in Fig. 4.7, for a run of about 30k events taken using 4 cm of aerogel without filter.

The measured mean Cherenkov angles for the different samples, with or without filter, are in good agreement with the expectations. However the resolution on the Cherenkov angle was about 20% poorer than the value expected for this experimental setup. The source of this discrepancy is not believed to be the aerogel; it will be further investigated using a different photodetector setup in a test beam run later this year.

Radiation hardness

To investigate the effect of charged particle irradiation, one tile ($50\times50\times23$ mm^3) has been exposed to a proton source [49] using the CERN-PS T7 beam. The primary proton beam had momentum of 24 GeV/c, the beam spot was 2×2 cm^2 wide and fluxes were in the range 1–3 $\times$ 10^{13} p/cm^2/hour. Because of the small size of the beam, irradiation was concentrated only at the centre of the tile. The exposure was made in six steps, with a total fluence of 52×10^{12} p/cm^2. The first three steps correspond each to about one year of operation of LHCb, the last ones to larger doses that will not probably be reached in the lifetime of the detector.

Another tile of aerogel was exposed to neutrons, this time irradiating uniformly the whole tile [50]. Secondary particles in the irradiation cavity were neutrons (50–1000 keV), p, π^+, π^- (0.3–4 GeV) and γ (0.1–100 MeV). An energy cut at 100 keV was made to calculate the dose of neutrons. In order to separate effects due to the handling of the tiles, measurements were also made systematically on a reference tile which was not irradiated, with optical parameters A and C close to those of the irradiated ones at the start.

Figure 4.8 shows the results concerning the clarity. For proton irradiation, no evidence of degradation is visible: a linear fit has been superimposed on the data from both the irradiated and reference tiles, with slope consistent with 0. The data collected under the neutron exposure show an increasing trend for the clarity coefficient, but this is also seen in the reference tile, and may be due to humidity effects.

Tiles of hygroscopic and hydrophobic aerogel were also irradiated with γ from a radioactive ^{60}Co source used in a Gammacell[7] 220 unit [51] located at the Istituto Superiore di Sanita' in Rome. The source provides a uniform irradiation by gamma rays with an energy of 1.3 and 1.7 MeV. Seven irradiation steps provided a total dose of $\sim$230 kGy, corresponding to the dose absorbed by the innermost region of the aerogel radiator in $\sim$30 years of

---

[7] Gammacell 220 is a registered name of the Atomic Energy of Canada Limited (AECL) and MDS Nordion International.

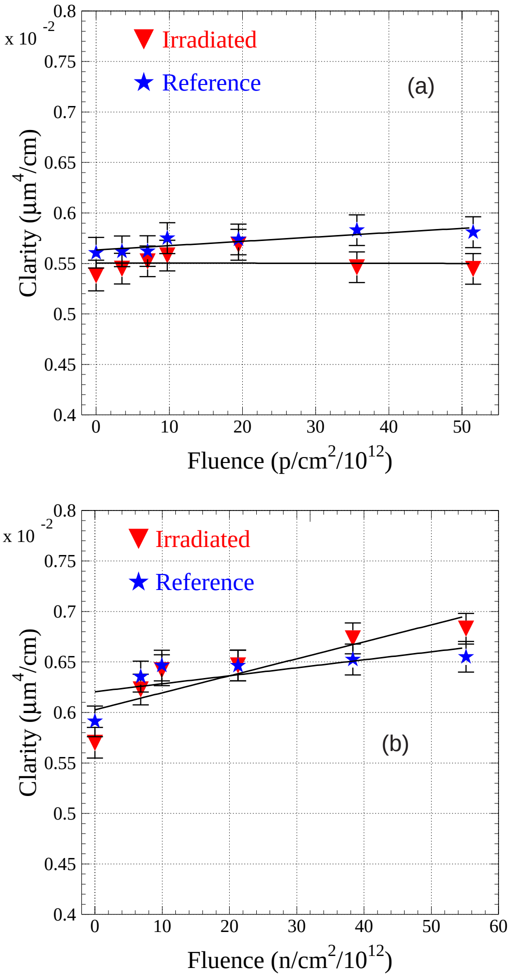

Figure 4.8: Clarity as a function of the absorbed dose with (a) protons and (b) neutrons, for both the irradiated and reference tiles. A linear fit is superimposed.

operation of LHCb. No detectable change of the clarity was observed.

Humidity absorption

An aerogel tile was exposed to humid air flow whilst placed on a balance. The absorption was then monitored by the change in weight of the tile, and the clarity C was measured as the water absorption increased. An increase of C as a function of the absorbed water is observed, as shown in Fig. 4.9. The initial conditions could, however, be restored, by baking the tile at a temperature of $\sim 500°\mathrm{C}$ for four hours.

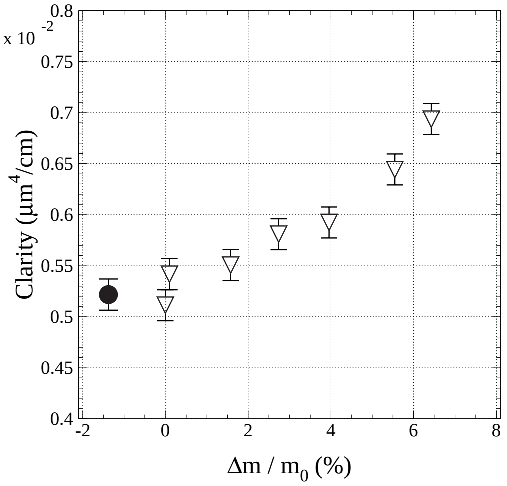

Figure 4.9: Clarity coefficient as a function of the relative change in mass due to water absorption; the round point shows the value obtained after baking the tile.

4.4 RICH 1 performance

4.4.1 RICH 1 simulation

Following the procedure established in the RICH TDR, the response of the RICH system has been modelled within the LHCb GEANT 3-based simulation program. The geometries and material of both RICH counters were updated to reflect the designs presented in this document.

The Cherenkov process itself and response of the photodetectors was described with “in house” code which had been verified against test-beam data. The transmissions, reflectivities and photodetector quantum efficiency were set to the nominal expectations. All known background sources were included, namely rings from secondary particles, photons from Rayleigh scattering in the aerogel, and the effects of charged particles striking the photodetector windows.

An improvement to the realism of the simulation with respect to that performed for the TDR was the inclusion of “spillover”. Late arriving photoelectrons from previous beam crossings falling within the time window of the event of interest were included in the digitisation. This was found to have little impact on the RICH performance.

In the Cherenkov angle calculations and event pattern recognition, only tracks found and reconstructed by the algorithms detailed in Chapter 7 were considered. This is in contrast to the TDR,

Table 4.3: The mean number of detected photoelectrons, N_{pe}, and the angular resolution, $\Delta\theta_C$, on the reconstruction of the Cherenkov angle for single photoelectrons for $\beta \simeq 1$ well measured tracks in physics events. The numbers in brackets are those values at the time of the RICH TDR.

	Radiator	
	Aerogel	C_4F_{10}
N_{pe}	6.8 (6.6)	30.3 (32.7)
$\Delta\theta_C$ [mrad]	1.89 (2.00)	1.27 (1.45)

where Monte Carlo truth information was used in the track finding. The pattern recognition and particle-identification performance is discussed in Chapter 8.

4.4.2 Photoelectron yield and angular precision

The intrinsic RICH performance can be quantified by N_{pe}, the number of photoelectrons detected per $\beta \simeq 1$ track, and the corresponding resolution for single photoelectrons on the Cherenkov angle, $\Delta\theta_C$. These are shown in Table 4.3 along with the equivalent numbers at the time of the TDR. Table 4.4 shows the component terms in the Cherenkov angle resolution: the emission point error, the chromatic error, the finite pixel size error and all these terms combined (“all RICH”). The resolution on the track direction (“tracking”) contributes a further uncertainty.

Not included in the standard simulation of the Cherenkov emission, and therefore absent from the table of resolution numbers, is the angular smearing introduced for the C_4F_{10} radiator by the curvature of the tracks in the magnetic field present in RICH 1. Dedicated studies have shown this effect to contribute a further 0.3 mrad, averaged over the track sample. For individual tracks it is given approximately by 4 mrad/p (for p in GeV/c), and is only significant at low momenta. In this regime it is the aerogel which dominates the particle identification, for which the bending in the radiator is negligible.

It can be seen that the re-design of RICH 1 has not impaired the detector performance. The new optics has resulted in a marginally improved resolution. The photoelectron yield from the C_4F_{10} radiator has fallen by 10%, mainly because of introduction of the additional plane mirror. No change is seen for the aerogel, because the geometrical acceptance of the photodetector plane has increased for these larger rings.

Table 4.4: The RMS widths (in mrad) of the contributions to the Cherenkov angle resolution, $\Delta\theta_C$, for single photoelectrons and $\beta \simeq 1$ well measured tracks in physics events. The pixel contribution of 0.62 mrad refers to the HPD; it increases to 0.75 mrad for the MaPMT.

Contribution	Aerogel	C_4F_{10}
Emission	0.29	0.69
Chromatic	1.61	0.81
Pixel	0.62	0.62
All RICH	1.77	1.22
Tracking	0.52	0.40
Total	1.89	1.27

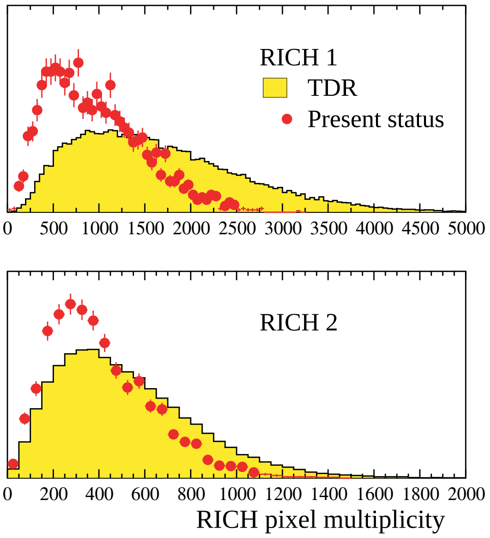

Figure 4.10: Hit pixel multiplicity in the RICH detectors, with the present simulation and at the time of the RICH TDR.

The resolution of RICH 2 has not changed significantly with respect to that at the time of the TDR. The photoelectron yield has increased as a result of the 20% increase in radiator length since the TDR [32].

4.4.3 Pixel multiplicities

Since the time of the RICH TDR the beampipe design has been optimised and the material changed from aluminium to beryllium in the first section, and Be-Al alloy for the second section. This, together with the new low-mass RICH 1, has led to a significant reduction in the number of photodetector hits from secondary particles. This is evident in Fig. 4.10 which shows the hit pixel multiplicity per event for the present simulation, compared with that at the time of the TDR. The reduction is less dramatic for RICH 2 because of the increase in its radiator length since the TDR.

This cleaner environment makes the task of the RICH pattern recognition simpler and reduces processing time.

4.5 RICH 1 design

The current status of the new RICH 1 design is presented in this section. Central to the mechanical design is the magnetic shielding of the photon detectors, so this comes first. Details of the mechanical design follow. The design of some components (e.g. the exit window) has reached an advanced stage, while others (e.g. the gas vessel) are likely to evolve before the final engineering design is completed. This will be reported in an engineering design review in 2004.

4.5.1 Magnetic Shielding

The bending of charged-particle tracks in the fringe field between the VELO (where the magnetic field must be small) and the TT station is an important requirement in the Level-1 trigger. The RICH 1 photon detector arrays sit in the fringe field of the magnet, from which they must be shielded to a level consistent with efficient operation of the MaPMT's.

The design goal for the shielding is to reduce the magnetic field everywhere in the plane of the photon detectors ($B_{\rm max}$) to < 2.5 mT while maintaining a field integral along the z-axis from 0 to 250 cm ($B_{\rm trig}$) of > 0.15 Tm. Further shielding will be provided using thin Mumetal sheet around each MaPMT, but this has not yet been included in the models described below.

The problem has been modeled extensively using the TOSCA/OPERA[8] finite element software and the effect of varying the parameters of the design are now rather well understood, although the absolute predictions of the models have yet to be confirmed experimentally. One global conclusion from the modeling is that the changes required to increase the field integral also increase the field inside the shielding. The resolution of these conflicting goals is only achieved by adding iron extension blocks between the shielding boxes and the magnet.

Each shield (top and bottom) basically consists of a 5-sided soft iron box that is open toward the beam line to allow the Cherenkov light to enter. The addition of blocks of iron mounted on the downstream vertical face channels the fringe field from close to the magnet poles to maximize $B_{\rm trig}$. The elements of these boxes can be seen in Fig. 4.11.

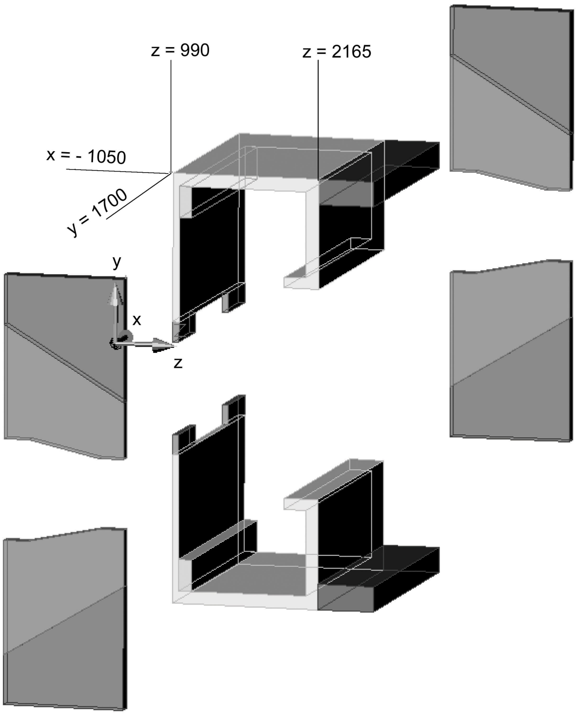

Figure 4.11: Exploded view of the components of the RICH 1 magnetic shielding. Coordinates are in mm.

The magnetic design is constrained by several other factors including the obvious need for an unobstructed light path to the photon detector. The available spatial envelope must be respected and the gravitational and magnetic forces must be accommodated in the final mechanical design. In particular the assembly of the beam pipe to the VELO and the subsequent sealing of the RICH 1 gas volume to the VELO window requires that the upstream vertical walls cannot approach closer than 55 cm to the beam pipe at $x = 0$, although some shaping around the aperture for the circular window is possible. The availability of raw ARMCO material may also restrict the thicknesses of the shielding wall to multiples of 5 cm.

In the absence of any shielding boxes in the magnetic model, the value of $B_{\rm trig}$ is about 10% below the target value whereas the field at the photon detectors is about 25 times too high. The required

---

[8] Vector Fields plc, Oxford, UK.

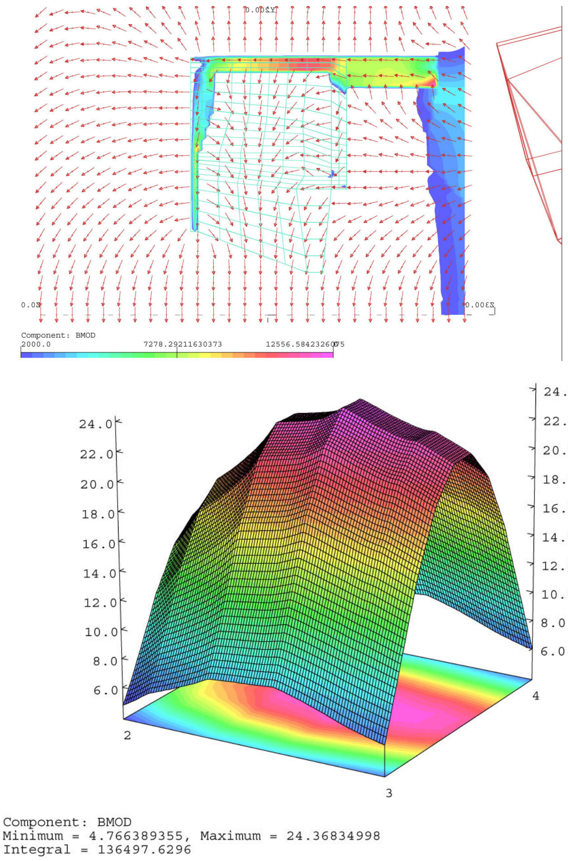

Figure 4.12: Results from the TOSCA model. The upper plot shows the B-field through the vertical cross section of the shield at $x = 0$. The magnet coils are seen at the right, from where flux is channelled via the extension block through the top of the shielding box and down the upstream pole. The arrows indicate the direction of the field, its magnitude (where it exceeds 2 kG) is indicated by the grey coding. Inside the box the MaPMT's experience a field whose main component is axial. The lower plot shows the magnitude (in gauss) of the B-field at the photodetector plane.

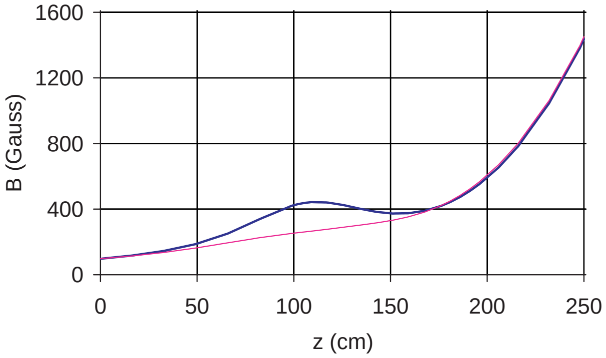

Figure 4.13: B-field along the beam line with upstream pole at $y = 37$ cm (upper curve) and $y = 65$ cm (lower curve).

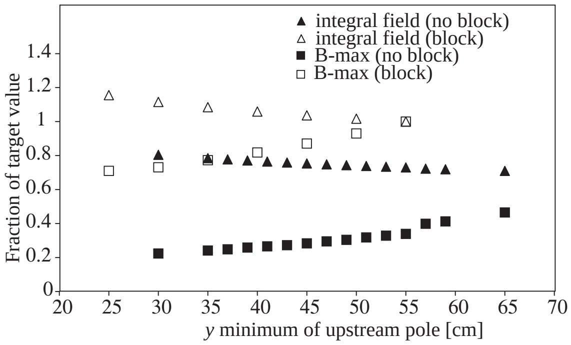

Figure 4.14: Sensitivity of B_{max} and B_{trig} to the vertical distance of the upstream pole from the beam line. Open (full) triangles refer to the field integral as a fraction of the target value with (without) the extension blocks. Open (full) squares refer to the field at the photon detector plane as a fraction of the target value with (without) the extension blocks.

increase in B_{trig} is obtained by routing the flux from close to the LHCb magnet down through the upstream vertical face of the shield, the *upstream pole*. The effect is demonstrated in Fig. 4.12, which shows the B-field (grey-coded) in a vertical section through one shield. The iron is not saturated.

The values of B_{trig} and B_{max} strongly depend on how close (y_{min}) the upstream pole approaches the beam line. Figure 4.13 shows how the B-field along the z-axis varies for values of y_{min} of 37 cm and 65 cm. The sensitivities of both B_{trig} and B_{max} to this parameter are shown in Fig. 4.14 where it becomes clear that the mechanical assembly constraints limit what can be achieved. However an acceptable solution is achieved for $y_{\mathrm{min}} = 55$ cm.

The other major factor is the design of the downstream blocks. The blocks are essential to reach the design goal for B_{trig}, but if their size is too large the limit of acceptability for the MaPMT shielding is exceeded. Figure 4.15 shows the sensitivities to the size of these blocks, including the result obtained with the blocks removed. The effect of the weight, shape and position of the blocks has been investigated taking into account that space must be left between upper and lower blocks to mount the TT station. Figure 4.15 (a) shows the sensitivity of B_{trig} to the weight of the blocks for three different values of the their z-dimension. It is clear that as the blocks approach closer to the mag-

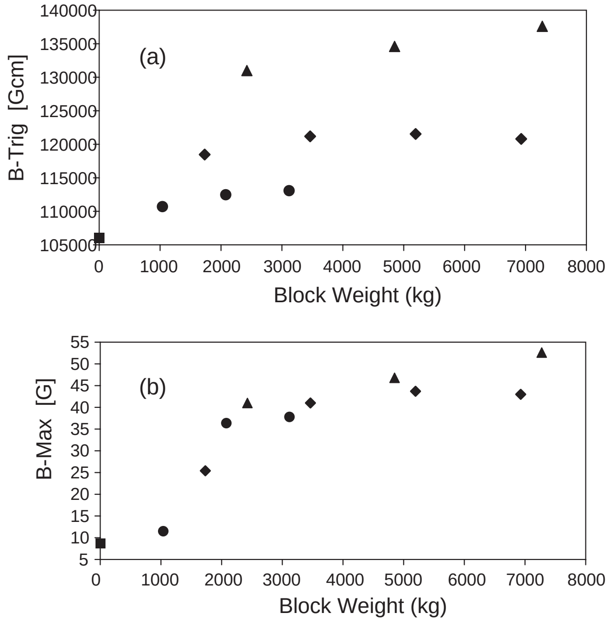

Figure 4.15: Sensitivity of (a) B_{trig} and (b) B_{max} to the weight of the extension blocks, for three different block lengths: 70 cm (triangles), 50 cm (diamonds), 30 cm (circles). (Note that the final values of other shielding parameters have not been imposed here.)

net more flux can be concentrated to increase the field integral (the magnetic forces also increase). The B_{max} sensitivity to the same parameters shows (Fig. 4.15 (b)) an increase correlated with B_{trig}, although with almost no sensitivity to the shape of the block. An optimal y-position has also been searched for and appears to be reached when the block is roughly in line with the horizontal surface of the boxes, although small improvements can be achieved by tilting the blocks in the y-z plane.

In a similar way the sensitivities to many other parameters have been investigated, including the x-dimension of the shields, the wall thicknesses, types of iron, extent of the side plates and the shape of the upstream pole.

A baseline design has been defined which satisfies the magnetic requirements and the constraints imposed by the mechanics. The shielding boxes will be constructed from ARMCO iron, all walls being 10 cm-thick apart from the upstream pole which will be limited to 5 cm, to provide space for the plane mirrors. The upstream wall begins at $z = 99$ cm and the downstream wall ends at $z = 216.5$ cm. The shape in the y-z plane is as shown in Fig. 4.12, although the addition of extra iron to the upstream pole is already foreseen to improve the shielding inside the box. The overall dimensions per box, excluding the extension blocks, are $x = 210$ cm, $y = 115$ cm and $z = 117.5$ cm and each box will weigh approximately 6 tonnes. The blocks will be 210 cm×20 cm×50 cm giving each block a weight of 1.7 tonnes. The total weight of the structure is 15 tonnes. The magnetic forces have been calculated by integrating the Maxwell stress tensor over the surface. The horizontal magnetic force on each box (towards the magnet) is about 70 kN and the vertical component, acting between the shielding boxes, is approximately 8 kN.

The mechanical design of the boxes allows for dismantling into smaller pieces. This may be necessary in any case depending on the load limit of the crane in the VELO/RICH 1 zone, but is also required by the beam pipe and RICH 1 optics installation and access constraints. The extension blocks are removable in order to allow the whole RICH 1 detector to move downstream in z during the beam pipe installation. Depending how the upper box is supported (it may be tied to the cavern wall), its downstream wall may have to be removed at that time. The sides are removable to allow access to the mirrors and photon detectors and a cabling slot must also be incorporated.

4.5.2 Mechanics

Support structure

To help describe how the RICH 1 shielding is positioned and supported, four separate components are defined:

1. The lower magnetic shield.
2. The gas enclosure with integral framework to support the optical components.
3. The upper shield.
4. The upper shield support system.

The lower shield is secured to the floor using a similar method to the superstructure of RICH 2 [32]. Adjustment mechanisms at the interface between the lower shield and the floor will allow it to be positioned, surveyed and fixed with respect to the VELO and the nominal beam line. Final adjustments follow the installation of the beam pipe, as described in Sect. 4.5.5.

The lower shield forms a support platform for the gas enclosure with its integral optics framework and also for the gravitational load of the upper shield. The gas enclosure and upper shield are essentially decoupled.

The upper shield is supported via four non-magnetic support pillars sitting outside, and independent of, the gas enclosure. When the magnet is not powered this structure is mechanically stable, and the attachment of the shielding side plates provides additional rigidity. However, further bracing to the walls and floor is necessary to balance the horizontal magnetic forces when the magnet is energized. A finite element analysis [52] of a similar structure has shown that deflections can be restricted to the required level.

During installation of the beam pipe, RICH 1 (with the optics and the photon detector arrays removed) is required to move 600 mm downstream on rails. Both the upper and lower shield will move together with the gas enclosure, which is positioned and fixed onto the lower shielding during the beam pipe installation.

Gas enclosure

The gas vessel shown in Fig. 4.17 is essentially an aluminium frame fitted with a skin of aluminium. The skin will add to the rigidity of the module. The frame provides the support for all RICH 1 optical sub-assemblies (aerogel, spherical mirrors, flat mirrors and photon detectors). The shape of the vessel is roughly cubic and all six faces have openings:

- The upstream face accommodates the seal to the VELO.
- The downstream face accommodates the RICH 1 exit window and its integral seal to the beam pipe flange and is described in detail below.
- Apertures in the top and bottom faces are sealed by quartz windows behind which sit the photon detector arrays.
- Access panels in both the vertical side-walls are required for installation, alignment and servicing of the mirrors. These access hatches are covered by parts of the side shielding walls, which will have to be removed to permit any operations inside the gas enclosure.

Some features of the above design are noted here:

- The apertures in the upstream and downstream vertical faces must be larger than the acceptance and sufficiently large to allow the VELO window to pass through during the beam pipe installation.

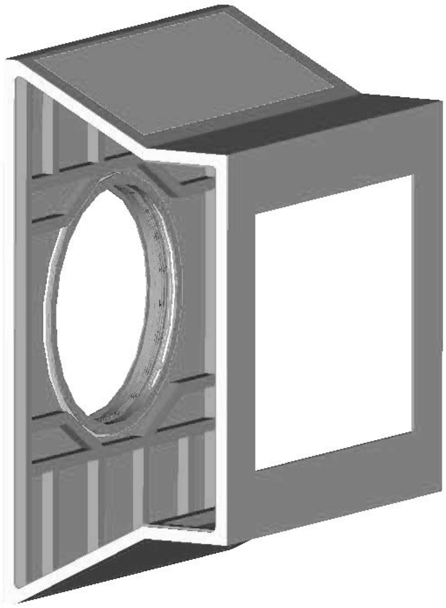

Figure 4.17: The RICH 1 gas vessel, with exit-window and side-access panels removed. The top and bottom panels are sealed with quartz windows that transmit Cherenkov light to the photon detector array.

- It is the diameter of the bellows (the seal to VELO) that sets the limit to which the upstream shielding pole can approach the beamline.
- All the gas seals will be implemented using O-rings made of Ethylene Propylene Diemo Monomer (EPDM), which has been shown to be unaffected by the fluorocarbon radiator gas.
- The inside of the enclosure and the bellows will be painted matt black to avoid unwanted reflections of scattered light.
- The framework that forms the skeleton of the gas enclosure will include adjustable fixing points for all the optical components (aerogel, spherical mirrors, flat mirrors and photon detectors).

Seal to VELO

A bellows assembly is used to seal RICH 1 to the VELO. It is attached in two stages, firstly by sealing the downstream flange of the bellows to the inside surface of the gas enclosure and secondly, by sealing the upstream flange of the bellows directly

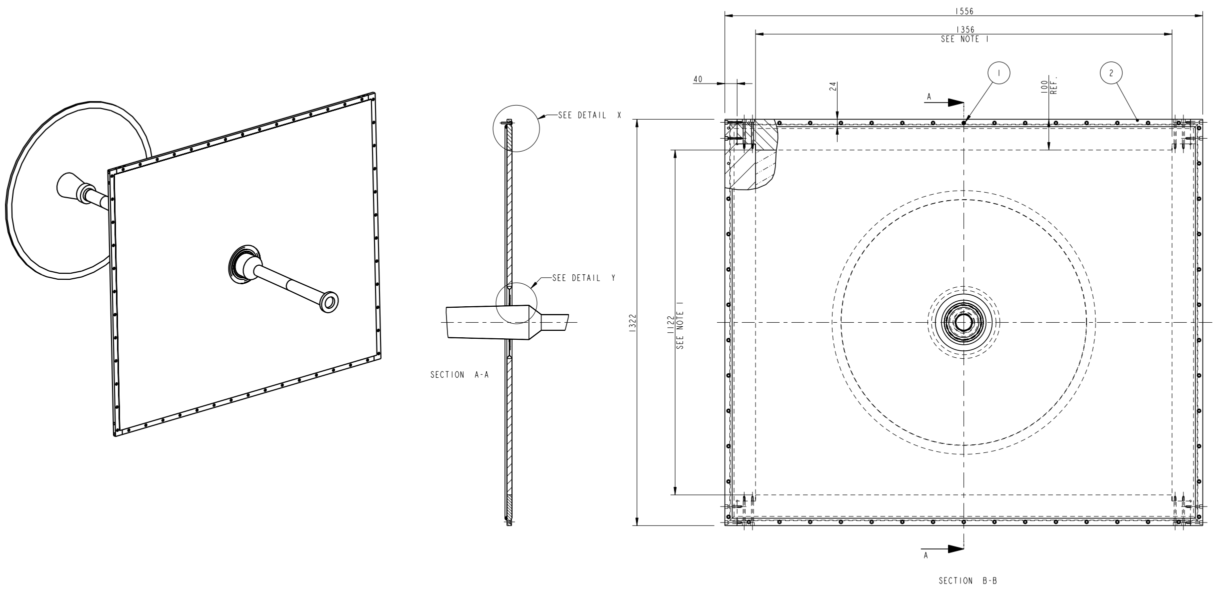

Figure 4.16: The RICH 1 exit window. Dimensions are in mm.

to the VELO tank. Although the bellows is a separate unit, the installation sequence dictates that it must be mounted within the gas enclosure so that the beam pipe can pass through it during its installation. All access to these seals is from within the RICH 1 gas volume.

Exit window and seal to beam pipe

The exit window is shown in Fig. 4.16. It has dimensions 1556 mm (horizontal) × 1322 mm (vertical) and is fabricated as a sandwich using a 16 mm-thick core of rigid polymethylacrilimide foam[9] with 0.5 mm-thick carbon-fibre skins. The downstream surface is at $z = 2155\,\mathrm{mm}$. Close to the beam pipe the window is bonded to a circular pre-formed polyimide foil, 225 mm diameter and 150 μm thick. This foil is used to seal to the beam pipe with an epoxy bond[10] to an annular fin, already machined into the beam pipe at $z = 2146\,\mathrm{mm}$. The foil is corrugated to reduce longitudinal forces on the beam pipe. Figure 4.18 illustrates the details. Finite element calculations on the composite structure show that a differential pressure of 500 Pa across the window exerts an acceptable force of about 6 N on the beam pipe.

Quartz windows

Two 5 mm-thick quartz windows, approximately 130 cm×65 cm, separate the radiator gas volume

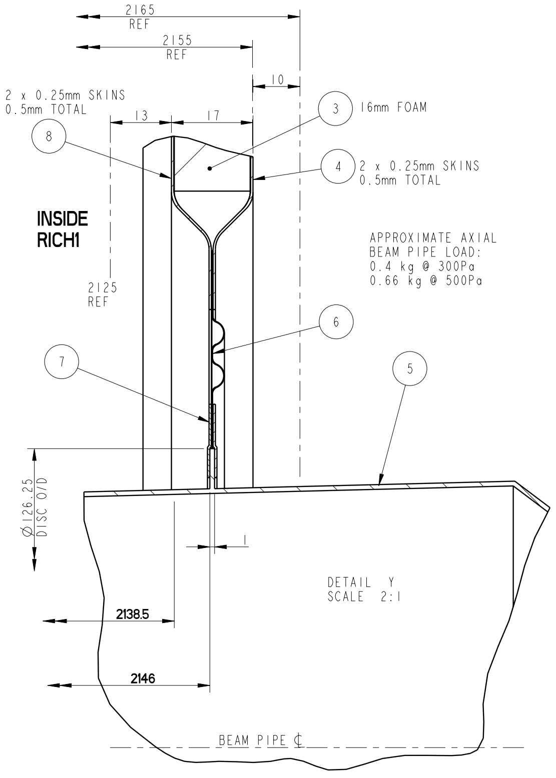

Figure 4.18: The RICH 1 exit window, showing detail of its seal to the beam pipe.

---

[9] ROHACELL IG51.

[10] The epoxy needs to be qualified at 250°C if it is to remain in place throughout the beam pipe bake-out.

from the photodetector assemblies. Each window is made from two separate pieces of quartz, bonded together via a narrow stainless steel I-section strip, and sealed into a frame. The joint between the two pieces is positioned to coincide with a boundary between MaPMT modules to minimise the reduction in active area. The windows are fastened and sealed to flanges incorporated into the gas vessel. The quartz will be coated with a multi-layer dielectric anti-reflection coating. A single layer of MgF_2 on a fused silica substrate reduces surface reflectance to less than 1.5% per surface over a broad spectral band. The design of these windows is very similar to those of RICH 2 and is described in the Engineering Design Review [32].

Photon detector mounting

The two photon detector assemblies, shown schematically in Fig. 4.1, each contain 880 MaPMT's. The MaPMT's are fitted with individual silica lenses and 1 mm-thick Mumetal shields and plug into a module carrying the dynode voltage divider and the Beetle chip. Each module carries 16 MaPMT's and eight Beetle chips. The power dissipation is expected to be about 800 W in each assembly and water cooling will be necessary. The photon detectors are accessed by removing the side walls of the magnetic shield and withdrawing the assembly laterally on rails.

A design study [53] for the mounting and cooling of MaPMT's in RICH 2 was carried out at the time of the RICH TDR. Features from this study are incorporated into the design of the RICH 1 system.

4.5.3 Optics

Mirror arrays and mirror supports

The focusing of Cherenkov light will be achieved using four spherical mirrors, one in each quadrant, each tilted to bring the image out of the spectrometer acceptance. Sixteen flat mirrors, arranged in arrays of four per quadrant, will reflect the image from the spherical mirror onto the photodetector plane outside the spectrometer acceptance. The spherical mirror support shown in Fig. 4.19 is designed to allow adjustment of the horizontal and vertical alignment of each mirror. It fixes to L-shaped frames mounted from the gas enclosure (see Fig. 4.20) such that the entire mounting system is situated outside the spectrometer acceptance.

The spherical mirrors are required to be as lightweight as possible and there is a possibility of deformation of the mirror during the processes of support and alignment. To minimise this risk each mirror is fixed to an L-shaped interface plate running along the two sides furthest from the beam pipe. This entire unit is located outside the spectrometer acceptance and is supported at the three corner points by threaded spindles received on the optical frame by threaded inserts. The spindles are terminated on the interface plate by ball joints so that rotating the threaded spindles adjusts the inclination about the horizontal, vertical and one diagonal axis. Only one of the three support points is fixed with the other two allowed motion in the plane of the mirror. This removes the effects of thermal expansion that could otherwise induce stress and deform the mirror.

In each quadrant the flat mirror array consists of 2×2 mirrors mounted to a 40 mm-thick aluminium honeycomb panel to form a continuous surface. The mounts have the same design as used for the RICH 2 mirrors. These are reported in the RICH 2 EDR [32] and consist of a polycarbonate ring glued to the back of each flat mirror with epoxy resin, and a corresponding polycarbonate tube insert fixed to the flat panel. This system has been demonstrated to be stable in the vertical and horizontal projections to within 0.04 mrad over 1500 hours. Once aligned the complete panel of mirrors is supported as a unit on the pivoting mount shown in Fig. 4.21, which itself is fixed to the optical frame. This allows adjustment of vertical and horizontal tilt to bring the image onto the photodetectors as well as an uncoupled motion along the

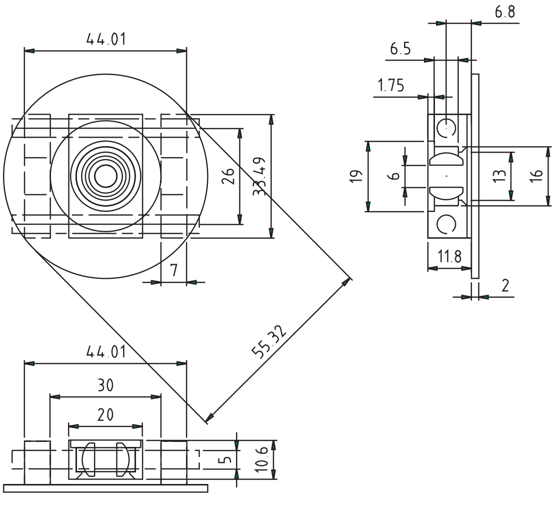

Figure 4.19: Details of the adjustment mechanism for the spherical mirrors. Dimensions are in mm.

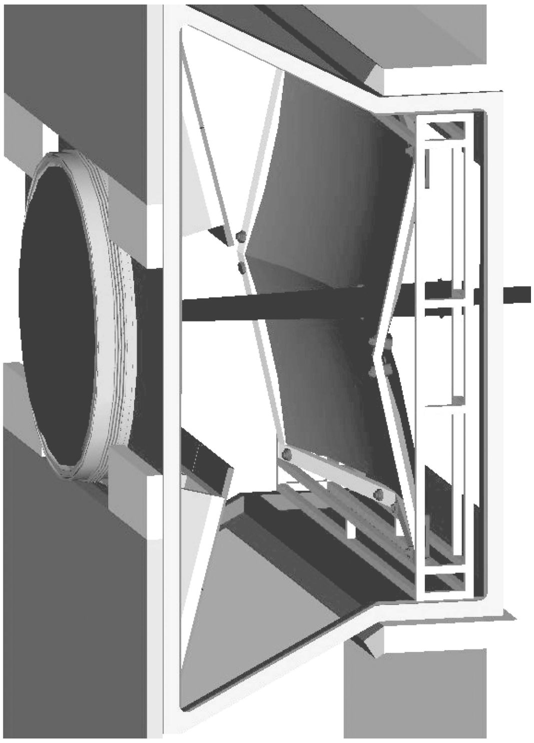

Figure 4.20: Spherical mirrors mounted in RICH 1 showing their L-shaped support frames and mounting structure located outside the LHCb acceptance.

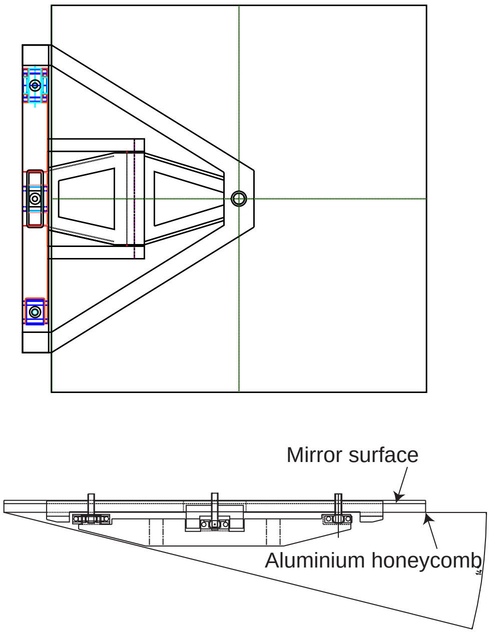

Figure 4.21: Support mechanics for one quadrant of flat mirrors. View along the beam line (above) and side view (below).

normal to the mirror surface to adjust the optical path length.

Mirror specifications

The spherical mirror surfaces have a radius of curvature of 2400 mm projected onto a 820 mm×600 mm rectangle. The mirrors are positioned so that the virtual point where the spherical surfaces intercept the z-axis is located at $z =$ 1930 mm. The centres of curvature of the upper and lower mirror assemblies are then positioned at $[x, y, z]$ = [0,±777.7, −340.5 mm] with respect to this point. The lightweight spherical mirrors will be manufactured either from a 2 mm-thick carbon-fibre/epoxy composite substrate coated by vacuum deposition with a high-purity aluminium reflective layer and a protective overcoating, or from 3 mm-thick beryllium, coated with a 0.3 mm glass skin on which the reflective coating is deposited. The thermal expansion coefficients of the glass and beryllium are well matched. Using these technologies the RICH 1 optical specifications can be achieved whilst maintaining a mirror material budget at the level of about 1%X_0.

The flat mirrors have dimensions 370 mm×387 mm, arranged in two 4×2 planar arrays above and below the beam. They are inclined in the y-z projection and the planes lie between $[y, z]$=[±350, 1310 mm] and [±1100, 1118.5 mm]. These arrays are outside the spectrometer acceptance so have no impact on material budget. The baseline design adopts the RICH 2 technology, reported in [32], of 6 mm-thick rectangular polished glass panels with an aluminium reflective layer.

4.5.4 Gas system

The RICH 1 gas radiator has a total volume of about 6 m^3 and C$_4$F$_{10}$ will be used as the Cherenkov medium. C$_4$F$_{10}$ has a vapour pressure of 1013 mbar at −1.9°C and the refractive index at room temperature and pressure is well described by a Sellmeier approximation:

$$(n-1) \times 10^6 = \frac{0.2375}{1/73.63^2 - 1/\lambda^2} , \qquad (4.2)$$

with the wavelength λ in nm. The basic philosophy of the gas system has not changed significantly from what was presented in the LHCb RICH TDR [7]. Although all possible precautions will be taken in the construction and in the operation of the RICH 1 detector, operational experience from the DELPHI

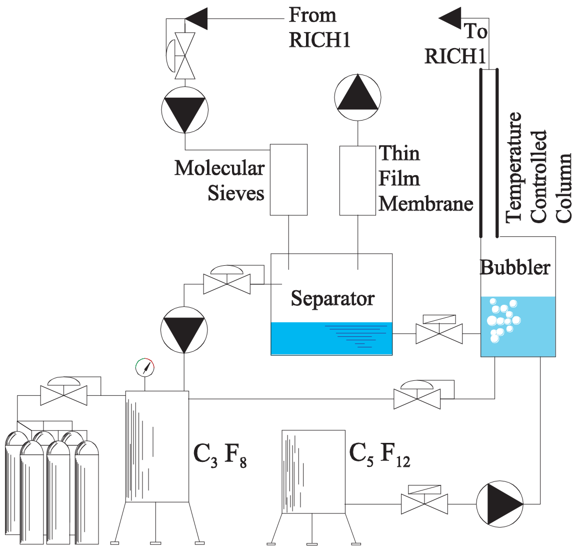

Figure 4.22: Sketch of the main components in a gas system with a mixture of C_5F_{12} and C_3F_8.

and the COMPASS experiments has indicated that it is prudent to anticipate a mean loss of 2 to 3 kg of fluid for each day of operation for these thin walled detectors with long O-ring connections. The main supplier [11] of C_4F_{10} has discontinued the production of this fluid and the price of the product has thereby increased by a factor of about 3, to more than 200 CHF/kg. We have therefore chosen to incorporate into the gas circulation system the possibility to work with a mixture of two perfluorocarbons, C_5F_{12} and C_3F_8. A 50/50 mixture of C_5F_{12} and C_3F_8 would have a refractive index at NTP given by

$$(n-1)\times 10^6 = \frac{0.1999}{1/79.86^2 - 1/\lambda^2}\ , \tag{4.3}$$

with the wavelength λ in nm. The chromatic aberration for this mixture is only slightly larger than for pure C_4F_{10}. Its dew point would be at $\sim 11.5°$C, well below the lowest temperature in the experimental cavern. The refractive index, light absorption and scintillation spectrum for the pure fluids are known; the proposed mixture will be tested in a beam in 2004. A sketch of the main components of the gas system is shown in Fig. 4.22. Thin-film membranes are used to remove molecules with small kinetic diameter like N_2 which is used as a pressure-stabilising gas. The efficiency of these membranes is shown in Fig. 4.23. The gas system can clearly also work with pure C_4F_{10}.

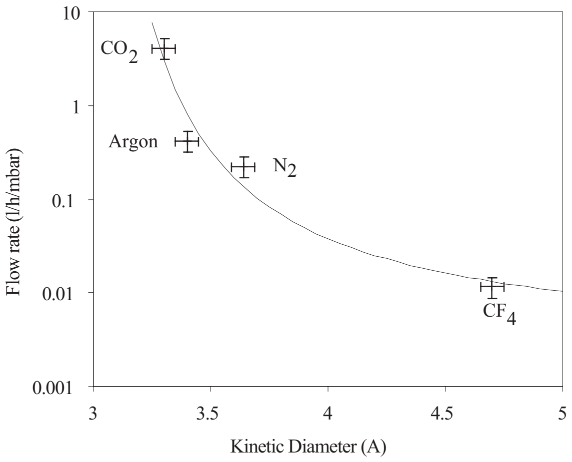

Figure 4.23: Flow rate through a thin-film membrane as function of the kinetic diameter of the molecule.

4.5.5 Installation

Installation of the RICH 1 detector is strongly coupled with the VELO, the beam pipe and the TT chamber, and the procedure is sequential. First the VELO vacuum tank has to be located at its final position, then RICH 1 is brought into the zone. The mirrors are removed and the beam pipe is installed and fixed to the VELO. Then RICH 1 is moved to its final location and the exit window fitted. Seals are made to the VELO tank and the beam pipe. Following the insertion of the optical components, aerogel and photon detectors, the gas vessel is sealed and the TT chamber is installed. The detailed sequence, listed below, has been prepared together with the technical coordination team and discussed with the LHCC installation review committee:

1. RICH 1 is lowered into the cavern and transported using temporary lifting gear to its position downstream of the VELO.

2. The structure is surveyed into position, then moved downstream by 600 mm on rails.

3. The beam pipe, fitted with a protective sheath and attached to the VELO exit window, is guided and surveyed into position using temporary supports located within the RICH gas enclosure. The VELO exit window is fitted to the vacuum tank.

4. RICH 1 is moved upstream on the rails to its final position and sealed using the bellows to the VELO tank.

---

[11] Performance Chemicals and Fluids, 3M Speciality Chemicals Division, 3M Center, Building 223-6S-04, St. Paul, MN 55144-1000, USA.

5. The exit window is fitted and sealed to the beam pipe.
6. Quartz windows are fitted and mirror assemblies installed and aligned to fixed locations.
7. The side panels of the gas vessel are fitted and the gas vessel tested.
8. The gas vessel is opened and mirrors removed.
9. The beam pipe is baked out.
10. Mirrors are re-installed and gas vessel closed.
11. Photon detectors are installed and aligned.

4.5.6 Safety aspects

The LHCb RICH detectors will follow the CERN safety rules and codes, CERN safety document SAPOCO 42 and European and/or international construction codes for structural engineering as described in EUROCODE 3. Specific risks and actions, as discussed in the Initial Safety Discussion (ISD) with the CERN Technical Inspection and Safety (TIS) Commission, were listed in the RICH TDR. With one exception, that concerning the high voltage and power specification of the photon detectors, all items remain valid. Instead of the 20 kV operating voltage of the HPD, the MaPMT will use 1 kV maximum, but the total power dissipation will be closer to 2 kW in each RICH detector. If beryllium mirrors are used safety precautions as specified in CERN safety document IS25 [23] will be applied. The requirement is not unique to RICH 1 as appropriate safety measures are already foreseen for the beryllium beam pipe, as discussed in Chapter 2.

Table 4.5: RICH 1 project: sharing of responsibilities for the mechanics and optical components.

Task	Institutes
Mechanics and optics	
Project management	Imperial
Gas vessel & superstructure	Imperial
Magnetic shielding	CERN, Imperial
Mirror supports, engineering and manufacture	Bristol
Mirror procurement, characterization & testing	Bristol, CERN
Exit windows and sealing of gas vessel	Rutherford
Photodetector mounting	Imperial
Radiators	
Gas system	CERN
Aerogel	Milano

4.6 Institute responsibilities

Institutes currently working on the LHCb RICH project are unchanged since the RICH TDR. The sharing of responsibilities for the main tasks associated with the reoptimized RICH 1 mechanics and optics is listed in Table 4.5.

Chapter 5 Trigger Tracker

5.1 Introduction

The Trigger Tracker (TT) is located downstream of RICH 1 and in front of the entrance of the LHCb magnet. It fulfills a two-fold purpose. Firstly, it will be used in the Level-1 trigger to assign transverse-momentum information to large-impact parameter tracks. Secondly, it will be used in the offline analysis to reconstruct the trajectories of long-lived neutral particles that decay outside of the fiducial volume of the Vertex Locator and of low-momentum particles that are bent out of the acceptance of the experiment before reaching tracking stations T1–T3.

The active area of the station will be covered entirely by silicon microstrip detectors with a strip pitch of 198 μm and strip lengths of up to 33 cm. Four detection layers amount to a total surface of approximately 8.3 m^2 of silicon and to approximately 180k readout channels.

The Trigger Tracker is part of the LHCb Silicon Tracker project, together with the Inner Tracker that covers the innermost part of tracking stations T1–T3. Readout electronics and infrastructure such as High Voltage and Low Voltage distribution and cooling system are a common development for Inner Tracker and Trigger Tracker and have been described in the Inner Tracker Technical Design Report [6]. In the present document, the discussion of these items will be limited to a description of relevant updates since the submission of the Inner Tracker TDR.

The remainder of this chapter is organized as follows. A concise description of the layout of the Trigger Tracker is given in Sect. 5.2 and the simulation of the detector response is described in Sect. 5.3. An overview of the R&D program that has been carried out in order to validate the layout is given in Sect. 5.4 and the detector design is described in Sect. 5.5. The project organization will be explained in Chapter 10.

5.2 Detector layout

The Trigger Tracker consists of four detection layers. The first and the fourth layer have vertical readout strips (x-layers), the second and the third layer have readout strips rotated by a stereo angle of $+5°$ and $-5°$, respectively (u/v-layers). The four layers are arranged in two pairs, with a gap of approximately 30 cm between the second and the third detection layers: the first two layers (TTa) are centered around $z = 232$ cm, the last two (TTb) around $z = 262$ cm.

The active area of the Trigger Tracker covers the nominal acceptance of the LHCb spectrometer, which is 300 mrad in the horizontal bending plane of the LHCb magnet and 250 mrad in the vertical plane. At the location of TTa, this corresponds to a width of 143.5 cm and a height of 118.5 cm, whereas at the location of TTb it corresponds to a width of 162.1 cm and a height of 133.8 cm.

In the forward direction, the active area is limited by the LHC beam pipe that passes through the detector and has an outer radius of 2.6 cm at $z = 232$ cm and of 2.72 cm at $z = 262$ cm. For safety reasons, a minimum clearance of 0.5 cm has to be maintained between beam pipe and any mechanical element of the detector. Taking into account in addition the wall thickness of the detector box, clearance between the detector box and the silicon ladders, dead space due to ladder mechanics, and the 0.1 cm-wide insensitive region due to HV protection features along the edge of the sensors, the width and height of the square-shaped central acceptance hole is 7.7 cm at the location of TTa and 8.0 cm at the location of TTb.

5.2.1 Layout of detection layers

A layout for the detection layers has first been described in [54]. It is based upon using 11 cm-long and 7.8 cm-wide silicon sensors with a readout strip pitch of 198 μm. These are the same sensor dimensions that are used in the Inner Tracker. The layout for the x-layers in TTa and in TTb are shown in Fig. 5.1. In TTa, the sensors are arranged in nine staggered 11-sensor-long ladders that cover the ac-

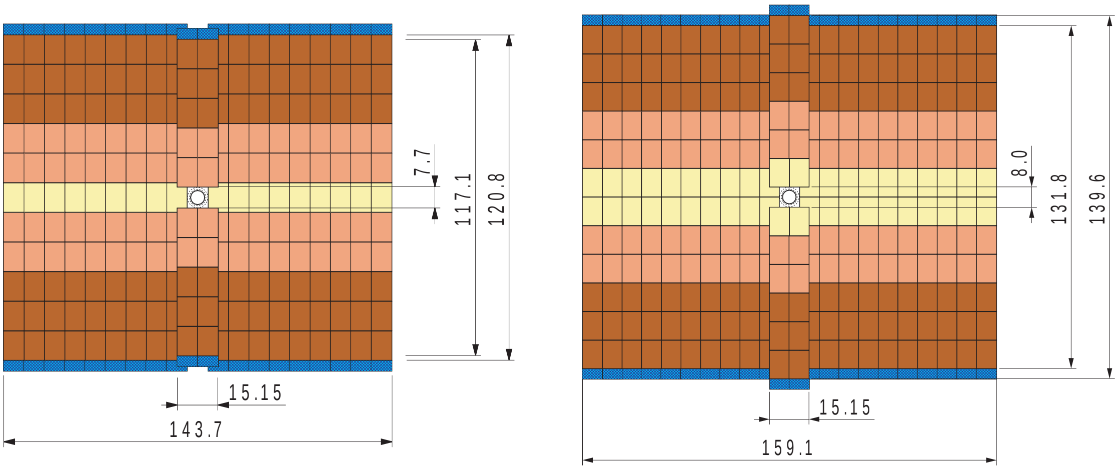

Figure 5.1: Layout of x-layer in TTa (left) and in TTb (right). Dimensions are in cm.

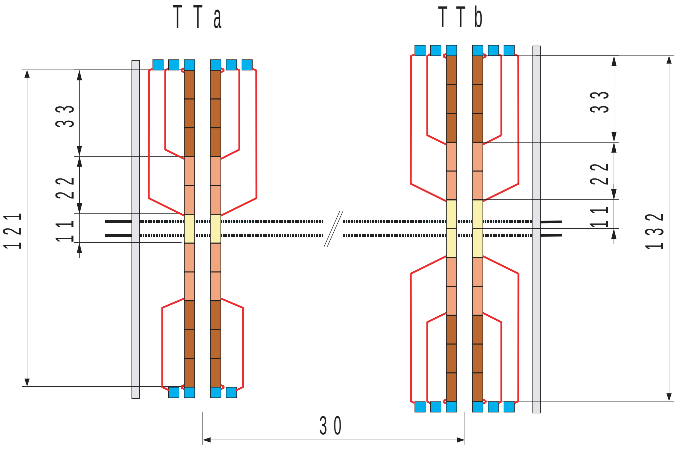

Figure 5.2: Sketch of readout scheme with interconnect cables. Dimensions are in cm.

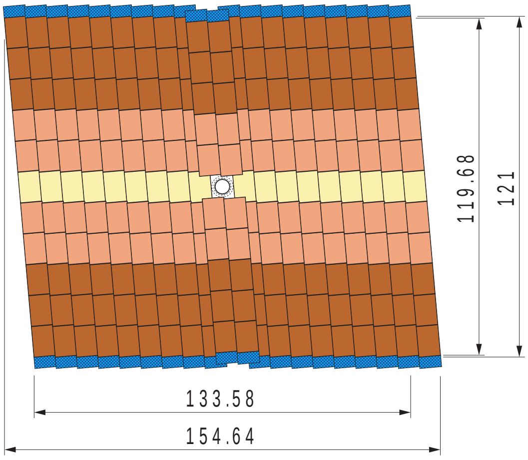

Figure 5.3: Sketch of stereo view in TTa. Dimensions are in cm.

tive area to the left and the right of the LHC beam pipe and in five-sensor-long ladders that cover the area above and below the beam pipe. In TTb, ten staggered 12-sensor-long ladders are employed to cover the active area to the left and the right of the LHC beam pipe and six-sensor-long ladders cover the area above and below the beam pipe. Electronically, each ladder is split into several readout sectors, as indicated by different shadings in Figs. 5.1 and 5.2. In Fig. 5.2, a sketch of the side view of the station is shown, illustrating the readout scheme for the different readout sectors. In order to minimize the dead material inside the acceptance of the LHCb detector, front-end hybrids for all readout sectors are located at the two ends of the ladder, outside the acceptance of the experiment. The inner sectors are connected to their front-end hybrids via 33 cm- and 55 cm-long interconnect cables. The layout of the u/v layers is similar to that of the x layers, except for the fact that all ladders are individually rotated clockwise, respectively anti-clockwise, by an angle of 5° as illustrated in Fig. 5.3.

Long readout strips and interconnect cables result in expected load capacitances of up to 50 pF at the input of the front-end readout amplifier. In order to maintain sufficiently high signal-to-noise ratios for full particle detection efficiency at a tolerable noise rate, thicker sensors have to be used for the Trigger Tracker than for the shorter ladders of the Inner Tracker. In [54], an estimate was given that used the measured noise performance of the Beetle 1.2 readout chip and the expected specific strip capacitances for silicon sensors and interconnect cables. It showed that 500 μm-thick silicon sensors should give sufficiently high signal-to-noise values if ballistic deficits can be neglected at the fast signal shaping times required for operation at the LHC. As described in Sect. 5.4, measurements on prototype ladders have demonstrated that sufficiently high signal-to-noise values can even be obtained using 410 μm-thick sensors.

In the layout described in [54], the areas above and below the beam pipe were each covered by a single ladder. However, in order to ensure full acceptance coverage, the ladders above and below the beam pipe have to overlap the adjacent ladders to the left and to the right of the pipe. This requirement defines an upper limit on the possible width of the beam pipe hole and it was found that the minimum required clearance to the beam pipe cannot be maintained using single ladders of the given sensor dimensions. Thus, two staggered ladders have to be employed to cover the areas above and below the beam pipe, as shown in Fig. 5.1.

5.2.2 Detector box

The expected radiation dose in the innermost region of the Trigger Tracker, close to the beam pipe, is similar to that expected for the Inner Tracker [45]. As for the Inner Tracker, the silicon sensors have to be kept at a temperature below 5°C in order to keep leakage currents at an acceptable level during several years of operation. The shot noise induced by these leakage currents should not cause a significant increase in the overall noise and thus deteriorate the signal-to-noise performance of the detector. All detector ladders will be housed in a common thermally-insulating housing that also provides electrical and optical insulation.

The design of the detector box is described in Sect. 5.5.3.

5.2.3 Silicon ladders

The silicon ladders employed to cover the areas to the left and to the right of the beam pipe consist of eleven or twelve silicon sensors and two or three readout hybrids that are attached to each end of the ladder. Mechanical stability is provided by carbon fibre rails that span the full length of the ladder and are mounted along the side edges of the sensors.

The short ladders above and below the beam pipe will be similar but consist of only five or six sensors and have hybrids attached only at one end of the ladder.

The design of the silicon ladders is described in Sect. 5.5.2.

5.2.4 Readout electronics

A sketch of the readout chain is shown in Fig. 5.4. It is identical for the Trigger Tracker and the Inner Tracker. The analogue output signals from the Beetle front-end readout chips will be transmitted via approximately 5 m-long copper cables to a service box that is located in regions of low radiation load, above and below the station.

In the service box, the signals from each Beetle will be digitised using four parallel 8-bit FADC channels and serialised by a CERN Gigabit Optical Link (GOL) chip [55]. The GOL chip is also used to drive a VCSEL diode and data from twelve VCSEL diodes, corresponding to four readout sectors, will be transmitted via a 100 m-long 12-fibre optical cable to the Level-1 electronics located in the LHCb counting room. Instead of the 12-fold parallel VCSEL transmitter that was described as

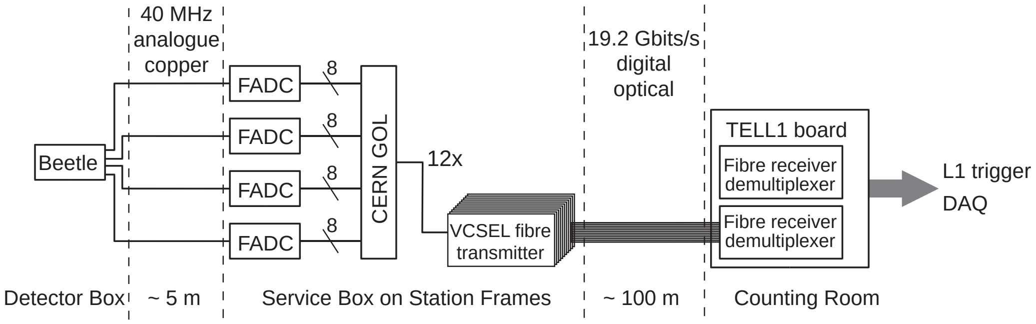

Figure 5.4: Sketch of readout chain.

baseline option in the Inner Tracker TDR, twelve single VCSEL diodes will be employed as these have been shown to be radiation tolerant [56].

The Level-1 electronics board (TELL1 board) is a common development for several LHCb subdetectors. In the Silicon Tracker, each board will receive the data from two 12-fibre optical cables, corresponding to eight readout sectors. It will perform synchronisation checks, run pedestal- and baseline-subtraction algorithms, perform zero-suppression and clustering, and provide an interface to the Level-1 Trigger and the data acquisition system.

5.3 Simulation of detector response

LHCb performance studies using the Trigger Tracker are described elsewhere in this document. For these performance studies, a detailed detector geometry according to the layout described in [54] has been implemented in the GEANT [57] simulation package of the LHCb detector. The amount of material implemented in the simulation corresponds to 500 μm-thick silicon sensors.

The simulation of the detector response in the reconstruction package is similar to that for the Inner Tracker, as described in the Inner Tracker TDR [6]. Three parameters have been adjusted in order to account for the thicker silicon sensors, and for the expected performance of the Beetle front-end readout chip for the larger load capacitances of the TT readout sectors:

- A Landau distributed signal corresponding to a most probable charge of 34,000 e^- for perpendicular tracks was generated along the particle trajectory. This value was obtained assuming a ballistic deficit of 10% for a most probable charge of 37,500 e^- generated by a minimum-ionizing particle in 500 μm of silicon.
- A Gaussian noise with a sigma of 2700 e^- was generated for each hit readout strip. This value corresponds to an earlier measurement of the noise performance of the Beetle 1.2 readout chip for a discrete load capacitance of 50 pF.
- The pulse shape of the Beetle has been adjusted to give a 50% signal remainder 25 ns after the maximum of the pulse.

The signal and noise parameters used in the simulation correspond to a signal-to-noise ratio of 12.6 for the most probable energy loss. It should be noted that the testbeam measurements described below have shown that a most probable signal-to-noise ratio greater than this can be achieved for signal remainders well below 50%, using 410 μm-thick silicon sensors.

5.4 Summary of R&D and prototyping

The R&D program for the Trigger Tracker has concentrated mainly on the particle detection performance of the 33 cm-long readout sectors and on the design of the interconnect cables that connect the inner readout sectors of the station to their readout hybrids at the two ends of the ladder. In addition, new measurements on a full prototype of the digital optical readout link is presented below.

With readout strips of up to 33 cm in length, load capacitances of up to 50 pF at the input of the front-end readout amplifier are expected in the Trigger Tracker. These large load capacitances will give rise to significant Johnson noise in the front-end readout amplifier, since fast electronics with shaping times of the order of 25 ns have to be em-

Table 5.1: Geometry parameters of prototype ladders.

	LHCb3	GLAST	CMS
Sensor thickness	$320\,\mu$m	$410\,\mu$m	$500\,\mu$m
Overall strip length	330 mm	268.5 mm	283.2 mm
Strip pitch	$198\,\mu$m, $237.5\,\mu$m	$228\,\mu$m	$183\,\mu$m
implant width (w/p)	0.25–0.35	0.25	0.25

ployed in order to avoid overlapping events from consecutive LHC bunch crossings.

This front-end amplifier noise determines the thickness of the silicon sensors that is required in order to obtain a sufficiently high signal-to-noise ratio for full particle detection efficiency at acceptably low noise hit rates. R&D for the Inner Tracker has demonstrated that a most probable signal-to-noise ratio in excess of ten is required in order to ensure full particle detection efficiency. On the other hand, the silicon sensors should be as thin as possible in order to minimise multiple scattering of particles traversing the detector. For the sensor thicknesses under consideration, the amount of charge generated in the silicon scales linearly with the thickness of the sensor. Ballistic deficits could, however, become significant with increasing sensor thickness since the charge collection time in the silicon bulk is of the same order of magnitude as the shaping time of the front-end amplifier.

Earlier measurements on Inner Tracker prototype ladders [58] had shown that a significant loss of charge collection efficiency occurs for particles that pass through the central region in between two readout strips. A careful optimisation of the readout strip geometry is thus required in order to optimise the detector performance.

Finally, the shaping time of the Beetle front-end readout chip can be adjusted within certain limits, by programming an internal register (parameter V_{fs}). Increasing the shaping time, the noise performance of the chip can be improved, albeit at the expense of longer pulse shapes. The relevant pulse-shape parameter for operation at the LHC is the signal remainder 25 ns after the signal maximum, i.e. at the time of the next bunch crossing. If this signal remainder is large enough to pass the clustering algorithm cuts, signals created by particles from the previous bunch crossing can cause "fake" hits, increasing detector occupancy and creating ghost tracks. One aim of the R&D for the Trigger Tracker was to measure the signal-to-noise performance and particle detection efficiency as a function of the signal remainder.

Several long prototype ladders using silicon sensors of different thickness have been constructed and tested in a laser setup, using a 1064 nm laser to generate charge in the silicon bulk, and in a beam test using 120 GeV charged pions in the CERN X7 test beam. All ladders were equipped with the Beetle 1.2 readout chip.

5.4.1 Prototype ladders

Prototype ladders have been constructed from the $320\,\mu$m-thick multi-geometry prototype sensors developed for the LHCb Inner Tracker, from $410\,\mu$m-thick GLAST2000 sensors [59] and from $500\,\mu$m-thick CMS-OB2 sensors [60]. Each prototype ladder consisted of three sensors bonded in series. The relevant geometry parameters of the ladders are summarized in Table 5.1. In the following, they will be referred to as the LHCb3, GLAST and CMS ladders, respectively. The LHCb prototype sensors contained five regions of different strip geometries. In the following, results will be shown only for a strip pitch of $p = 198\,\mu$m and an implant width w corresponding to $w/p = 0.35$. In addition to the ladders described here, two additional ladders consisting of two LHCb sensors and of a single LHCb sensor, respectively, were included in all tests. Results from all prototype ladders and all strip geometry regions of the LHCb ladders are described in [61] and [62].

All sensors were characterised in detail before being assembled into ladders. The results of these measurements are summarised in [63]. Measured CV curves for all sensors are shown in Fig. 5.5. They demonstrate that all LHCb and GLAST sensors reach full depletion at a bias voltage of 60–70 V, whereas the full depletion voltage of the CMS sensors varied significantly from sensor to sensor and lay between 100 V and 200 V.

Total specific strip capacitances (inter-strip capacitance plus backplane capacitance) for all sensors are shown in Fig. 5.6. Although the measurement errors for the GLAST sensors are comparatively large, the measured capacitances agree well with calculated values from a finite-element model of the sensors and show the expected dependence

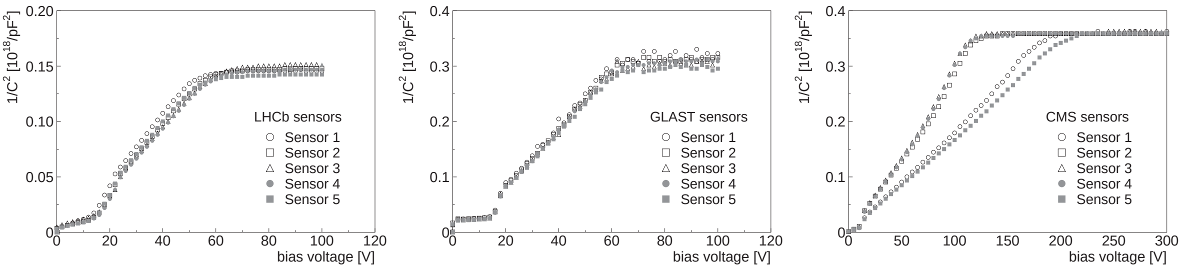

Figure 5.5: Backplane capacitances as a function of the bias voltage V_{bias} (CV curves).

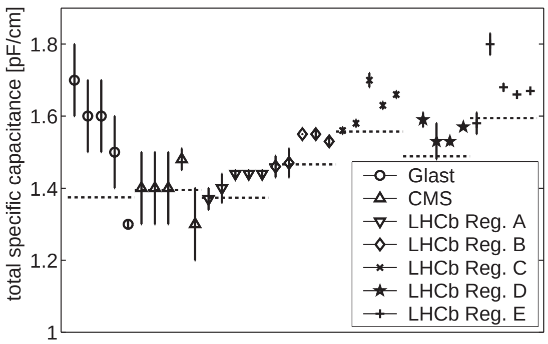

Figure 5.6: Measured (points) and calculated (lines) total specific strip capacitances for the different prototype sensors.

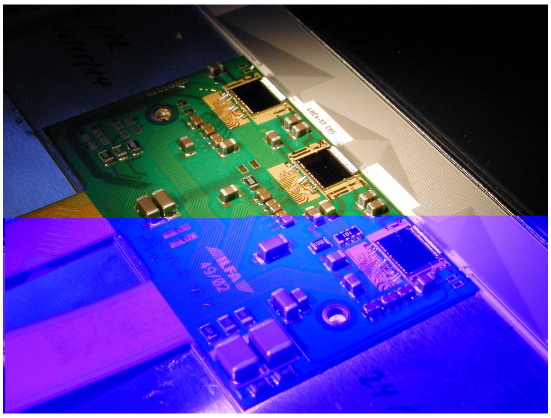

Figure 5.7: Photograph of a readout hybrid carrying three Beetle 1.2 chips.

on the ratio w/p.

5.4.2 Readout chip and hybrid

All prototype ladders were equipped with the Beetle 1.2 readout chip, which contains an improved front-end amplifier compared to the Beetle 1.1 chip that was used in the R&D program described in the Inner Tracker TDR [6]. The readout hybrid was similar to that used in the earlier measurements. Minor modifications of the layout of the hybrid were necessary since the pad layout of the Beetle 1.2 chip was not compatible with that of the Beetle 1.1. A photograph of a readout hybrid carrying three Beetle 1.2 chips and bonded to one of the prototype ladders is shown in Fig. 5.7.

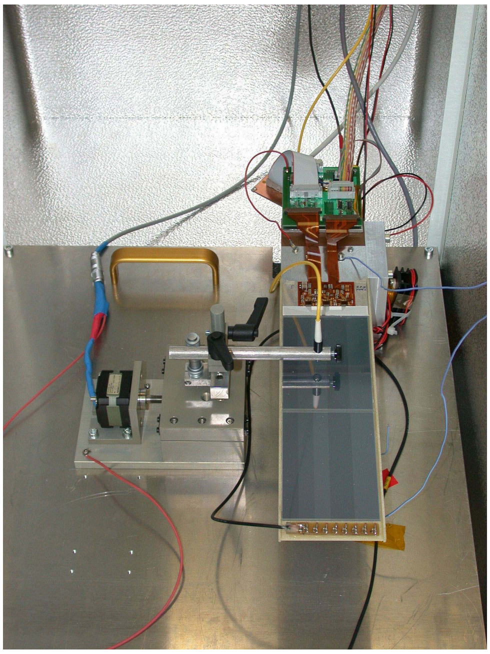

Figure 5.8: Photograph of the laser test setup.

5.4.3 Laser tests

Initial measurements on the prototype ladders were performed in a laboratory setup using a pulsed 1064 nm laser to generate a well-defined amount of charge inside the silicon bulk. At this wavelength, the laser beam penetrates the full thickness of the silicon sensor. The laser beam was focussed to better than 20 μm and could be moved across the silicon sensor in steps of 5 μm. A photograph of the

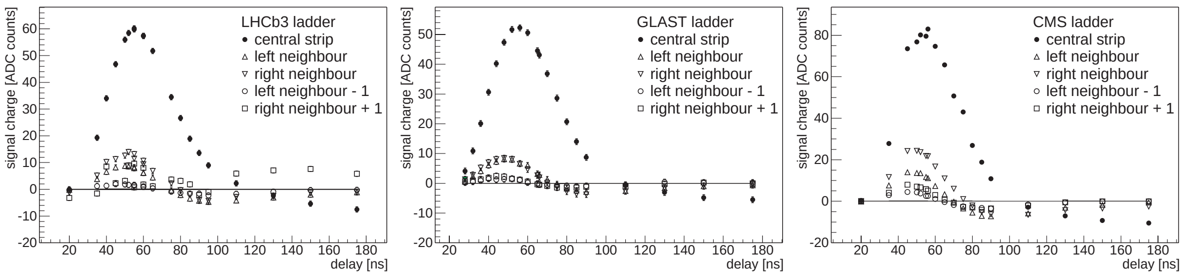

Figure 5.9: Beetle 1.2 pulse shapes on central strips, their neighbours and their next-but-one neighbours, measured in the laser setup for $V_{fs} = 400\,mV$.

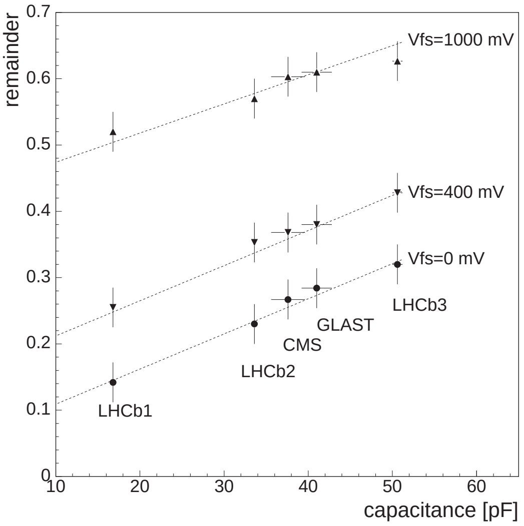

Figure 5.10: Signal remainder 25 ns after the maximum for the three prototype ladders and for different settings of the signal shaping parameter V_{fs}.

test setup is shown in Fig. 5.8. A detailed description of the setup and the results obtained in the laser tests is given in [61].

In Fig. 5.9, pulse shapes for each of the three prototype ladders are shown for a setting of $V_{fs} = 400\,mV$ and for a laser position close to a readout strip. These measurements were performed by varying the time delay between the laser pulse and the sampling time of the Beetle chip. Also shown in the figure are the induced signals on the direct neighbours and the next-but-one neighbours of the strip closest to the laser beam. These induced signals are due to capacitive coupling between the strips and can be accurately reproduced in a simulation that takes into account the charge collection in the silicon sensor, the capacitive network formed by the readout strips and a SPICE simulation of the Beetle front-end response [64].

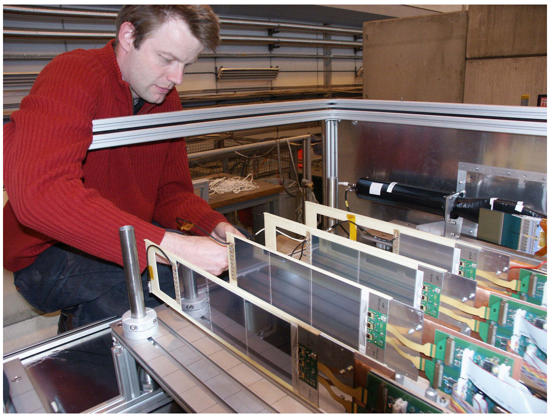

Figure 5.11: Photograph of the beam test setup.

In Fig. 5.10, the measured signal remainder after 25 ns is shown for the different prototype ladders and for different values of the parameter V_{fs}. For $V_{fs} = 400\,mV$, the signal remainder for all prototype ladders is comfortably lower than 50%, which is the value used in the simulation of the detector response for all LHCb performance studies (see Sect. 5.3).

5.4.4 Beam test

A photograph of the setup at the CERN-X7 testbeam is shown in Fig. 5.11. All prototype ladders were installed in a common detector box, together with a beam telescope consisting of four double-sided silicon detectors that was provided by the HERA-B vertex detector group. The beam telescope allowed the reconstruction of track coordinates at the position of the prototype ladders with a spatial resolution of better than $14\,\mu m$ and thus allowed the study of the detector performance as a function of the particle impact point relative to the readout strips. A detailed description of the setup and of the results obtained in the beam test is given in [62].

In Fig. 5.12, pulse shapes for the three pro-

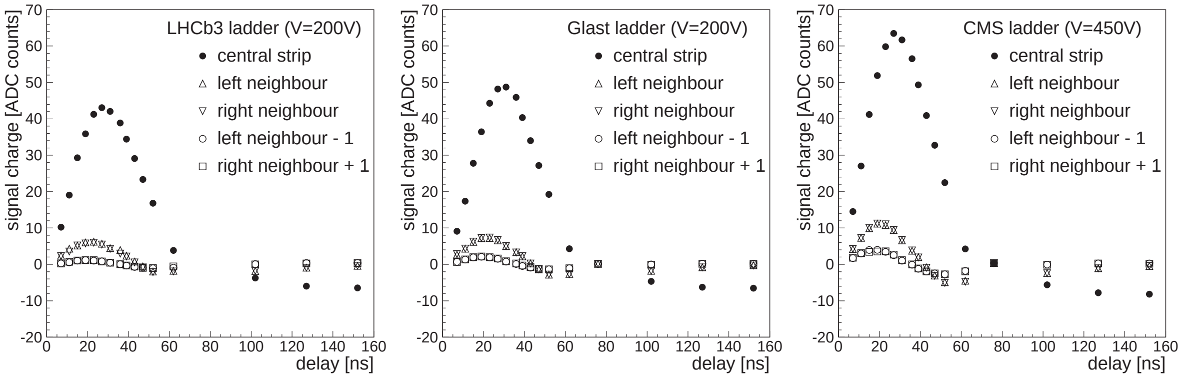

Figure 5.12: Beetle 1.2 pulse shapes on central strips, their neighbours and their next-but-one neighbours, measured in the testbeam for $V_{fs} = 400\,\mathrm{mV}$.

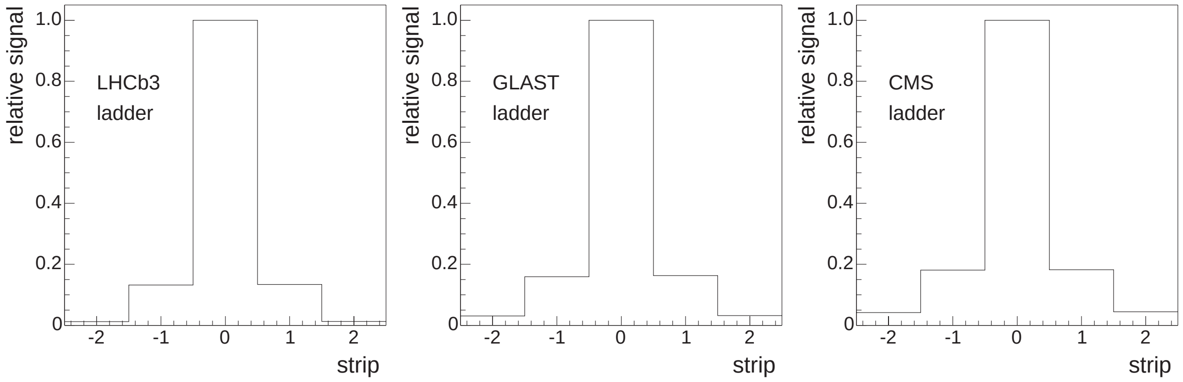

Figure 5.13: Relative amplitudes on central strip, neighbours and next-but-one neighbours for particles passing through a readout strip.

totype ladders are shown for a setting of $V_{fs} = 400\,\mathrm{mV}$ and for reconstructed track coordinates at the position of a readout strip. These measurements were performed by varying the time delay between the trigger signal and the sampling time of the Beetle chip. Pulse shapes on the central strip, the neighbouring strips and the next-but-one neighbours reproduce those measured in the laser setup. For all following measurements, the sampling time of the Beetle was adjusted to the time of the signal maximum.

The induced signals on the neighbouring strips reach their maximum earlier than the signal on the central strip, but still have a non-zero pulse height at the time of the maximum on the central strip. This gives rise to the cluster shapes illustrated in Fig. 5.13. As expected from the increasing ratio of interstrip capacitance to backplane capacitance, the relative amplitude on the neighbouring strips increases with the thickness of the sensors. This cross-talk can give rise to larger cluster sizes, if the signal amplitudes on the neighbouring strips are large enough to pass clustering algorithm cuts.

The collected charges on the two closest strips to a track are shown in Fig. 5.14 as a function of the relative track position in between the strips. For the small w/p value of the GLAST ladder, significant charge sharing occurs over almost the full interstrip gap, improving the spatial resolution of the detector. A typical residual distribution of reconstructed cluster positions and extrapolated track positions from the beam telescope is shown in Fig. 5.15. The RMS of the distribution of 0.23 strip pitches includes the contribution from the beam telescope resolution and corresponds to a spatial resolution of approximately $50\,\mu$m for the strip pitch of $228\,\mu$m of the GLAST ladder.

Signal-to-noise distributions for the three prototype ladders are shown in Fig. 5.16. In all three plots, full histograms are for clusters associated to a track ("signal clusters") and dashed histograms are for clusters not associated to a track ("noise clusters"). The curves show a fit of a Landau distribution folded with a Gaussian to the distribution for

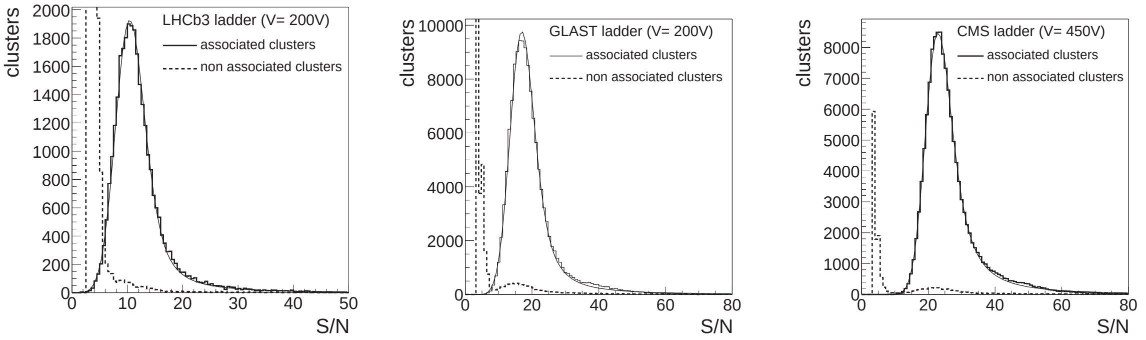

Figure 5.16: Signal-to-noise distributions measured for $V_{fs} = 400\,\mathrm{mV}$.

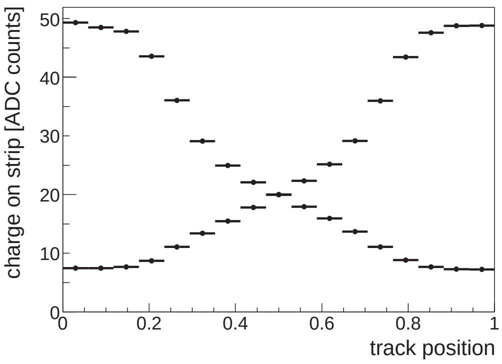

Figure 5.14: Charges collected on the two strips closest to a track as a function of the relative track position in between the strips, measured for the GLAST ladder.

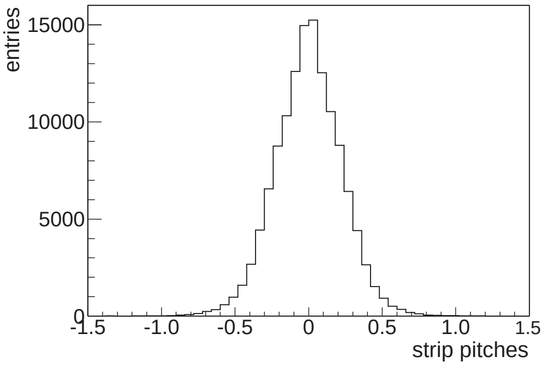

Figure 5.15: Residual distribution for the GLAST ladder.

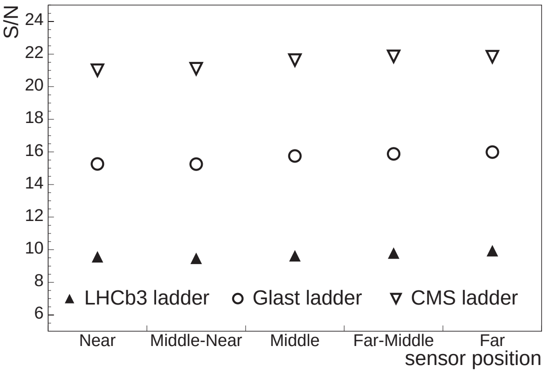

Figure 5.17: Most probable signal-to-noise ratios as a function of the beam position along the three prototype ladders, measured for $V_{fs} = 400\,\mathrm{mV}$.

signal clusters. The fit yields most probable signal-to-noise ratios of approximately 9.6 for the LHCb ladder, 15.8 for the GLAST ladder and 21.6 for the CMS ladder. As expected, the signal-to-noise performance of the LHCb3 ladder is not satisfactory, whereas for both the GLAST ladder and the CMS ladder signal clusters can be clearly separated from noise clusters.

As was shown in Table 5.1, the readout strips on the GLAST and CMS ladders are approximately 20% shorter than the 33 cm-long readout strips foreseen for the Trigger Tracker. This fact has to be taken into account when interpreting the signal-to-noise performance measured on these ladders. However, from earlier measurements of the noise performance of the Beetle readout chip as function of the load capacitance, the expected reduction of the signal-to-noise ratio is less than 15%.

A cluster finding algorithm was applied to the data in order to evaluate the particle detection efficiency of the prototype ladders. The algorithm is described in [62]. Clustering cuts were adjusted to give less than 0.1% noise clusters per readout strip and event. With these cuts, an average cluster finding efficiency of 96.2% was found for the LHCb3 ladder, whereas efficiencies in excess of 99.8% were found for the GLAST and CMS ladders.

The signal-to-noise distributions shown in Fig. 5.16 were measured for a beam position in the centre of the sensor closest to the readout chip.

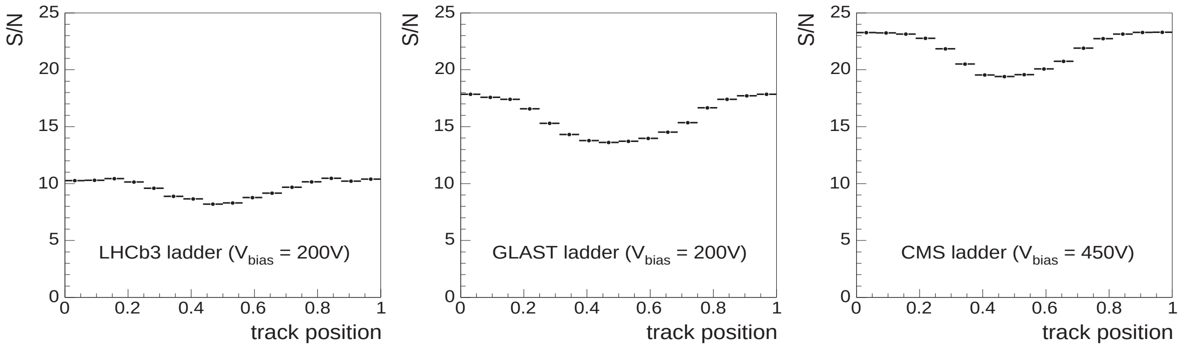

Figure 5.18: Most probable signal-to-noise ratios as a function of the relative interstrip position of the extrapolated track, measured for $V_{fs} = 400\,\text{mV}$.

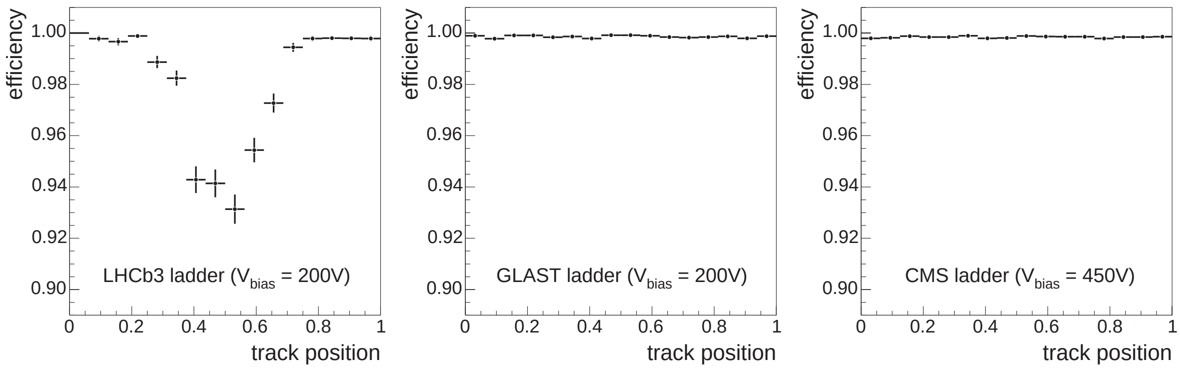

Figure 5.19: Cluster finding efficiencies as a function of the relative interstrip position of the extrapolated track, measured for $V_{fs} = 400\,\text{mV}$.

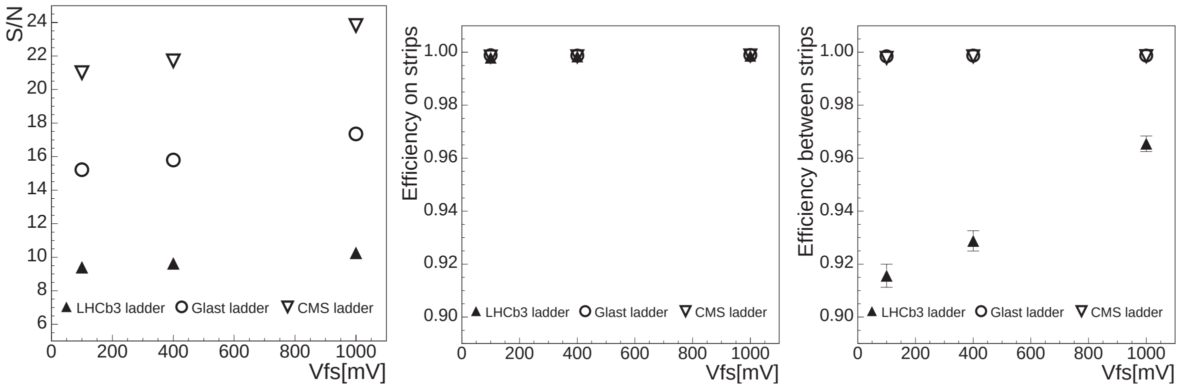

Figure 5.20: Most probable signal-to-noise ratios (left), average cluster finding efficiencies (middle) and cluster finding efficiencies in the central region between two strips (right) as a function of V_{fs}.

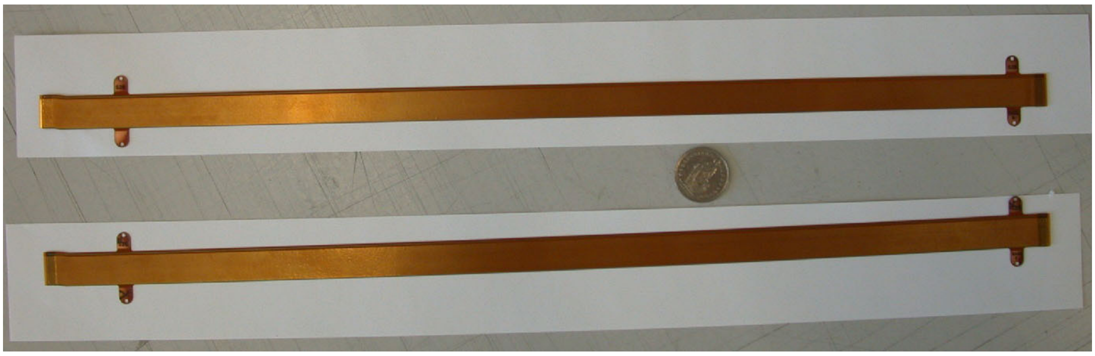

Figure 5.21: Photograph of prototype Kapton interconnect cables.

Measurements were also performed for beam positions on the middle sensor and the sensor furthest from the readout chip. The most probable signal-to-noise ratios obtained for the three different beam positions are shown in Fig. 5.17. For all prototype ladders the detector performance is constant over the full length of the ladder.

In Fig. 5.18, most probable signal-to-noise ratios are shown as a function of the relative interstrip position of the extrapolated track. For all three prototype ladders a significant drop of the signal-to-noise ratio is observed in the central region in between two readout strips. The same effect had already been observed in the laser tests on these ladders [61] and in earlier measurements on Inner Tracker prototype ladders [6]. It can also be reproduced in the detector simulation [64] and is mainly attributed to a loss of charge carriers at the boundary between the silicon bulk and the silicon oxide layer between the two strips.

Cluster finding efficiencies as a function of the relative interstrip position of the extrapolated track are shown in Fig. 5.19. For the LHCb3 ladder, the efficiency drops below 93% in the central region in between two strips, whereas for the GLAST and CMS ladders full efficiency is maintained over the full interstrip gap.

All results shown so far were measured for a Beetle shaping time corresponding to a setting of $V_{fs} = 400\,mV$. Most probable signal-to-noise ratios, average cluster efficiencies and cluster efficiencies in the central region in between strips for different settings of the parameter V_{fs} are shown in Fig. 5.20. As expected from the noise performance of the Beetle chip, signal-to-noise ratios for all ladders increase with increasing shaping time (increasing value of V_{fs}). For the LHCb3 ladder, this leads to an improved cluster finding efficiency, whereas for the GLAST and CMS ladders signal-to-noise ratios are so high that full cluster finding efficiency is found for all settings of the shaping time.

In conclusion, measurements have demonstrated that the signal generated in $320\,\mu$m-thick silicon sensors is not sufficiently large to ensure full particle detection efficiency for the 33 cm-long readout sectors employed in the Trigger Tracker. For both the GLAST ladder using $410\,\mu$m-thick sensors and the CMS ladder using $500\,\mu$m-thick sensors, full particle detection efficiency was obtained over the full active area of the silicon sensor and for an LHCb compatible shaping time of the Beetle front-end readout chip. Measured signal-to-noise ratios on both ladders are sufficiently high that the less than 15% reduction expected due to the slightly longer readout strips of the Trigger Tracker compared to the prototype ladders will not effect this conclusion. Due to material budget considerations, $410\,\mu$m-thick sensors are the preferred option for the Trigger Tracker.

5.4.5 Interconnect cable

As explained in Sect. 5.2, low-mass interconnect cables of 33 cm and 55 cm in length will be employed in order to connect the inner readout sectors on a ladder to their front-end readout hybrid. R&D on these interconnect cables is ongoing. Up to 54.5 cm-long prototype cables using $15\,\mu$m-wide copper traces with a pitch of $91\,\mu$m on a $50\,\mu$m-thick Kapton substrate were produced and tested in the laboratory. A photograph of two of these prototype cables is shown in Fig. 5.21. They are similar to those under development for the Run IIb upgrades of the CDF and D0 silicon trackers [65].

One relevant parameter for operation in LHCb is the specific strip capacitance of the cable. It should be as small as possible as it adds to the load capacitance at the input of the front-end readout chip and thus deteriorates the noise performance of the chip. A specific interstrip-capacitance of

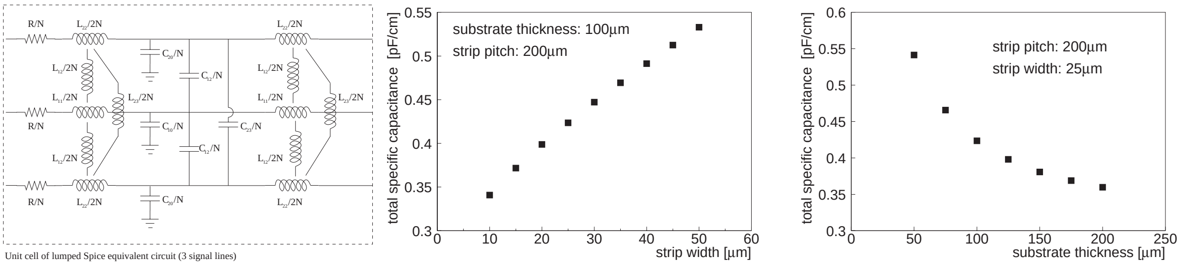

Figure 5.22: SPICE model of Kapton interconnect cable (left) and calculated total specific strip capacitance as a function of trace width (middle) and substrate thickness (right).

0.17 pF/cm has been measured on the prototype cable [63]. This result compares well to the value of 0.154 pF/cm that is obtained in an electrostatic calculation using the Maxwell [66] code.

The prototype cables tested so far have no backplane and use single strip lines to provide bias voltage and ground connection to the sensor. Measurements on these cables have demonstrated that pick-up noise can be kept small in the laboratory. Nevertheless, a more solid ground connection between front-end hybrids and sensors may be desirable in order to reduce the risk of pick-up noise in the LHC environment. Additional prototypes that are equipped with a backplane consisting of a thin copper mesh have been received recently and will be tested soon. As illustrated in Fig. 5.22, electrostatic calculations demonstrate that total strip capacitances smaller than 0.5 pF/cm can be obtained using a 100 μm-thick substrate with backplane.

Measurements of signal integrity on a prototype ladder equipped with a 55 cm-long interconnect cable are currently under way, using the laser setup described in Sect. 5.4.3.

In addition, a SPICE [67] model of the readout cable has been programmed. The model is shown in Fig. 5.22 and will be used in order to obtain additional input for the optimisation of the strip geometry.

5.4.6 Readout link

The optical part of the readout link was already shown to work satisfactorily in tests for the Inner Tracker TDR [6]. Those tests did not, however, yet include the 5 m copper link that connects the Beetle chip to the service box, as described in Sect. 5.2.4. Measurements on a full prototype readout link, including up to 15 m-long copper cables to transmit the fully differential analogue output signals of the Beetle 1.2 chip, are described in [68]. These tests have demonstrated that signal integrity can be fully preserved using off-the-shelf unshielded twisted-pair cable (AWG30UTP). This is illustrated in Fig. 5.23, in which a Beetle output signal is shown at the input of the FADC. For this measurement, a differential line receiver was employed to convert the differential Beetle signal. Although some increase of the signal risetime is seen, due to the capacitance of the 15 m-long twisted pair cable, the full information is transmitted. The observed noise on the signal is dominated by a coherent 80 MHz clock noise generated by the Beetle 1.2 chip[1] and was shown to be independent of the length of the cable used for transmission. In LHCb, all twisted pair cables will be housed in a common shielding in order to suppress pick-up from external noise sources.

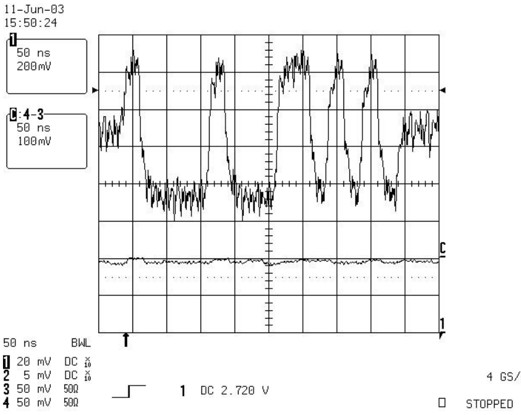

Figure 5.23: Beetle output signal measured at the input of the FADC, using a 5 m-long CAT6 cable plus a 10 m-long AWG30UTP cable to connect the Beetle 1.2 output to the digitiser board.

Furthermore, neutron irradiation of critical components that will be located in the service box

---

[1] The source of this clock noise is expected to have been eliminated in the next iteration of the chip, the Beetle 1.3. Furthermore, any noise contribution that has a stable phase with respect to the LHC clock would be corrected for by pedestal subtraction algorithms.

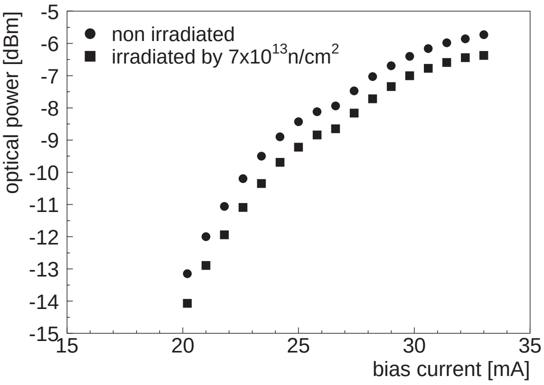

Figure 5.24: Optical power of the VCSEL diode as a function of the applied bias current, for a non irradiated diode and for a diode irradiated by 7×10^{13} 1-MeV-equivalent neutrons/cm^2.

close to the detector was performed at the Prospero Reactor at CEA Valduc, France. A detailed description of the irradiation study and the results obtained is given in [69]. In particular, a VCSEL diode and optical fibres were irradiated by neutron fluences corresponding to 50, respectively 350, years of operation at the location of the service box. As shown in Fig. 5.24, the optical power of the VCSEL diode was reduced by 0.6 dB after irradiation, which is negligible compared to the power margin of the optical link of 11.5 dB. Similarly, the radiation-induced additional attenuation of the optical fibre was shown to be negligible.

5.5 Detector design

The technical design of silicon sensors, ladders and station mechanics shown in this section is based upon the station layout illustrated in Figs. 5.1 and 5.2 and relies on the R&D program described in Sect. 5.4.

5.5.1 Silicon Sensors

The layout of the Trigger Tracker suggests the use of 11 cm-long and 7.8 cm-wide silicon sensors. The measurements on prototype ladders described in Sect. 5.4.4 have demonstrated that 410 μm-thick sensors provide for full particle detection efficiency. The geometry parameters and technology specifications for the silicon sensors are summarised in Table 5.2.

Table 5.2: Silicon sensor geometry and technology specifications.

Wafer size	6”
Wafer thickness	(410±15) μm
Bulk material	n type
Bulk resistivity	(3–8) kΩ·cm
Crystal orientation	<100>
Implant	p^+ type
Bias resistors	(1.5±0.5) MΩ polysilicon
Readout coupling	AC SiO_2 / Si_3N_4 multilayer
Coupling capacitance	> 125 pF/mm^2
Overall dimensions	110 mm × 78 mm
Active area	108 mm × 76 mm
Strip pitch	198 μm
Implant width	$\sim$ 58 μm ($w/p = 0.35$)
Readout metal width	$\sim$ 66 μm

5.5.2 Silicon ladders

The design of the silicon ladders follows the layout described in Sect. 5.2.3. The long ladders that cover the area to the left and to the right of the beam pipe will be constructed from two half-ladders, each of which consists of either six silicon sensors with three readout hybrids attached to one of its ends, or of five silicon sensors with two readout hybrids attached to one of its ends. Each hybrid carries three Beetle chips to read out the 384 strips of one readout sector on the ladder. Silicon sensors are mounted edge-to-edge without overlaps, in order to simplify the design of the ladder and to avoid hot spots of material budget. Mechanical stability of the half-ladders will be provided by 2 mm-wide and 6.5 mm-high carbon fibre rails that run along the side edges of the sensors. The two half-ladders will be joined together by an additional 1 mm-wide carbon fibre strip that is glued onto these rails. A sketch of the construction is shown in Fig. 5.25.

On each half-ladder, the three sensors closest to the readout hybrids are wire-bonded together and to a pitch adapter that connects to one the hybrids. The fourth and fifth sensors on the half-ladder will be wire-bonded together and to an approximately 33 cm-long Kapton interconnect cable that connects to the second hybrid. At the sensor

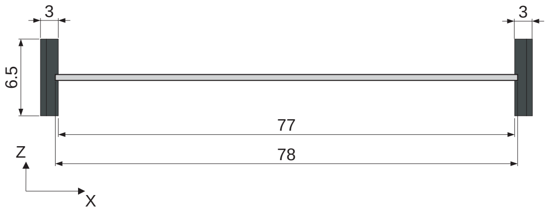

Figure 5.25: Cross section of silicon ladder showing carbon fibre support rails. Dimensions are in mm.

end, the Kapton interconnect cable will be glued onto a thin AlN support plate that in turn will be glued onto the sensor as illustrated in Fig. 5.26. At the hybrid end, the cable will be glued onto a pitch adaptor that connects to the hybrid. The last sensor on the six-sensor-long half-ladder will be connected to the third readout hybrid in a similar way, using an approximately 55 cm-long interconnect cable.

The interconnect cables will consist of approximately 100 μm-thick Kapton, carrying 384 copper strips on one side and a copper ground mesh on the other side. The exact geometry of strips and ground mesh is still subject to optimisation studies.

In order to remove the heat generated by the front-end readout chips, the readout hybrids will be mounted onto a copper cooling balcony that also fixes the ladder mechanically. The balcony will in turn be mounted onto a cooling plate that is integrated into the station frame described in Sect. 5.5.3 below.

The short laddders above and below the beam pipe will be similar to the half-ladders described above.

5.5.3 Station mechanics

An isometric drawing of the TT station is shown in Fig. 5.27. All ladders are housed in a common thermally, electrically and optically insulating housing. They are mounted at both ends onto one of two C-shaped stainless-steel support frames. Since these support frames are located outside the acceptance of the experiment, no special care has to be taken with respect to the radiation length of the selected materials. Ladders within a detection layer are pairwise staggered in order to allow for a small overlap of the sensitive surfaces of adjacent ladders and avoid acceptance gaps in between the ladders.

The two support frames are mounted onto precision rails that are fixed to the extension blocks of the RICH 1 magnetic shielding, above and below the station. They can thus be retracted from the beam pipe for detector maintenance and for bake-out of the beam pipe. The frames include a cooling plate through which liquid C_6F_{14} at $-20°C$ is circulated as cooling agent. Additional cooling ribs are integrated into the side walls of the support frame in order to keep the ambient temperature inside the box at the desired value of 5°C. The detector box will be continuously flushed with cold, dry nitrogen in order to avoid condensation on the cold surfaces.

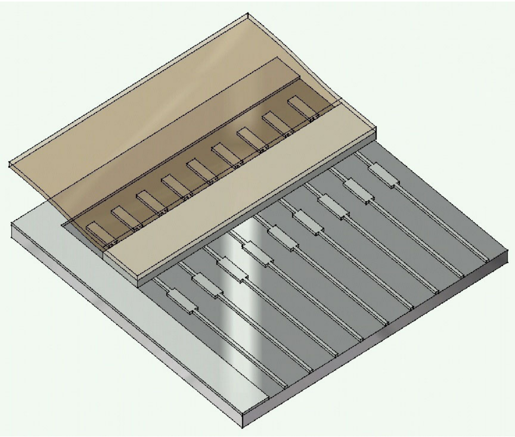

Figure 5.26: Illustration of interface between silicon sensor and Kapton interconnect cable.

Thermal insulation to the environment is provided by 2 cm-thick sheets of non-inflammable polyurethane foam, similar to those used for the Inner Tracker boxes. In order to provide electrical insulation, the polyurethane sheets are clad on both sides with 25 μm thin aluminium foils. A detail of the region around the beam pipe is shown in Fig. 5.28. Here, insulation is provided by two conical pieces of polyurethane foam that are mounted onto the front walls of the half boxes and slide into each other as the two detector halves are moved together. At the position of the detection layers, the thickness of the thermally insulating layer is reduced to 3 mm in order to allow for the silicon ladders to approach the beam pipe as close as possible.

The overall height of the detector box is 218 cm and the total mass of each half station is estimated to be approximately 350 kg.

Inside the acceptance of the experiment, the Trigger Tracker is estimated to correspond to 3.5% of a radiation length and 1.14% of a nuclear interaction length. A breakdown of the material budget is given in Table 5.3.

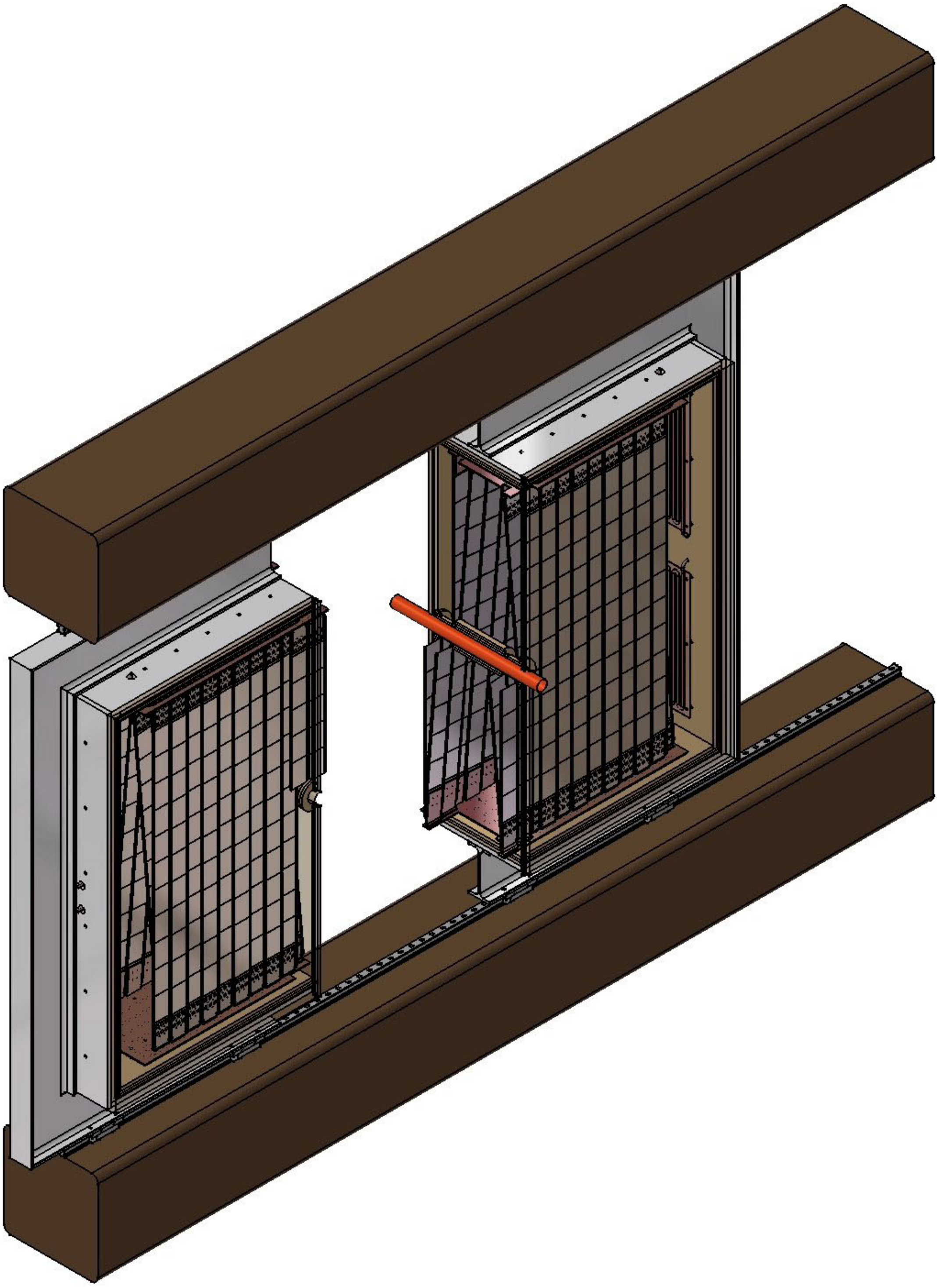

Figure 5.27: Isometric view of the TT station. One detector half is shown retracted from the beam pipe and the downstream wall of the enclosure is not shown in order to display the interior of the detector box.

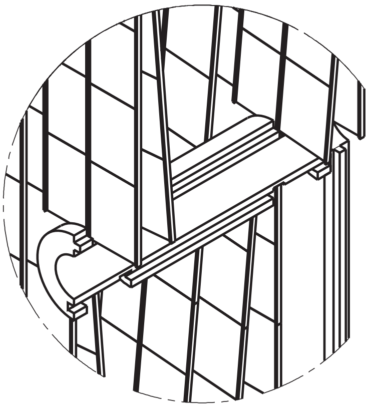

Figure 5.28: Detail of insulation around the beam pipe.

	X/X_0	$\lambda/\lambda_{\mathrm{I}}$
Silicon sensors	1.71%	0.35%
Support rails	0.66%	0.31%
Interconnect cables	0.30%	0.08%
Box enclosure	0.83%	0.40%
Sum	3.50%	1.14%

Table 5.3: Breakdown of material budget.

5.5.4 Readout electronics

The readout electronics will be identical for Trigger Tracker and Inner Tracker. They have been described in detail in the Inner Tracker TDR [6] and its supporting notes. The service boxes for the Trigger Tracker will be located above and below the extension blocks of the RICH 1 magnetic shielding shown in Fig. 4.11. From a FLUKA simulation of the LHCb radiation environment, a radiation dose of less than 10 krad after ten years of operation is expected at this location. This value is similar to the radiation dose expected at the location of the service boxes for the Inner Tracker.

5.5.5 Infrastructure

High-voltage and low-voltage distribution and cooling systems will be identical for the Trigger Tracker and the Inner Tracker. They have been described in the Inner Tracker TDR [6] and its supporting notes.

5.6 Safety aspects

In accordance with CERN's safety policy as described in the document SAPOC042, the Silicon Tracker project will follow the CERN safety codes which also allow the use of international construction codes for structural engineering as described in EUROCODE 3.

In the Initial Safety Discussion (ISD) with the CERN Technical Inspection and Safety Commission (TIS) the following risks and actions have been discussed:

1. The electrical circuits of the Silicon Tracker will be subject to an electrical reception prior to operation (Code C1).
2. Electrical protection will be assured by the ECS/DSS that will be able to cut the power source when necessary.
3. Interventions on the circuits will require the primary power source to be switched off by means of the DSS.
4. Detector boxes will be cooled with C_6F_{14} and interlocks to the electronic equipment will be activated by over-temperature.

No risks other than electrical and material safety were identified during the Initial Safety Discussion.

Task	Institutes
Silicon sensors	Zürich
L0 electronics	MPI Heidelberg
Beetle chip and hybrid	
Readout link	Zürich
digitization and optical link	
L1 electronics	Lausanne
common Level-1 board	
DAQ and L1 interface	
Mechanics	Zürich
ladder & station mechanics	
Infrastructure	Santiago
HV, LV and ECS	
Station assembly	Zürich
Installation & commissioning	all
Software	all

Table 5.4: Trigger Tracker project: sharing of responsibilities.

5.7 Institute responsibilities

The institutes currently working on the LHCb Silicon Tracker project are as listed in the Inner Tracker TDR. The sharing of responsibilities for the main tasks associated with the Trigger Tracker is described in Table 5.4. The project schedule and the project costs are given in Chapter 10.

Chapter 6 Simulation

The software programs used for the performance studies execute the following tasks:

- generation of the event;
- tracking of particles through the detector;
- simulation of the detector response;
- simulation of the trigger decision (described in [3]);
- reconstruction of the event, including track finding and particle identification (described in Chapters 7 and 8 respectively);
- offline selection of specific B-meson final states (described in Sect. 9.3).

For the last three steps, the simulated events are processed as if they were from real data, i.e. without using any information from the Monte Carlo truth. This information is only used, at the end of a given step, to assess the performance of the different reconstruction and selection algorithms.

We discuss in this chapter some relevant features concerning the first three steps of the software chain. We then give the main characteristics of the Monte Carlo samples used to derive the performance shown in the following chapters.

6.1 Event generation

Minimum bias proton-proton interactions at $\sqrt{s} =$ 14 TeV are generated using the PYTHIA 6.2 program [70] with the predefined option `MSEL=2`: this includes hard QCD processes, single diffraction, double diffraction, and elastic scattering[1]. Other samples of events are obtained by filtering a large minimum bias data-set. For example, $\mathrm{b\overline{b}}$ events are obtained by selecting events with at least one b- or $\bar{\mathrm{b}}$-hadron. The total inelastic and $\mathrm{b\overline{b}}$ production cross sections obtained in this way are 79.2 mb and 633 μb respectively[2].

The decay of all unstable particles is performed with the QQ program [71], originally developed by the CLEO collaboration, using a decay table from CDF which includes also $\mathrm{B^0_s}$ and b-baryon decays. The $\mathrm{B^0}$ and $\mathrm{B^0_s}$ oscillation parameters are set to $x_\mathrm{d} = 0.755$ and $x_\mathrm{s} = 20$ respectively.

In the following, we explain how some of the PYTHIA parameters have been tuned based on the available published data, and how bunch crossings are described at the LHCb interaction point.

6.1.1 Tuning of PYTHIA

Several parton-parton interactions can occur in a single proton-proton collision. In PYTHIA, the average number of such interactions, and hence the average particle multiplicity in a proton-proton collision, is controlled by a parameter $p_\mathrm{T}^\mathrm{min}$ that represents the minimum transverse momentum of the parton-parton interaction. Different multiple parton-parton interaction models are available in PYTHIA, which mainly affect the shape of the particle multiplicity distribution. One of these models, called Model 3 in PYTHIA (`MSTP(82)=3`) and originally developed [72] to reproduce the UA5 data, assumes a varying impact parameter between the two colliding protons that is described with a Gaussian distribution. Figure 6.1 shows that the UA5 data [73] indeed favour such a model over another PYTHIA model (Model 1, i.e. `MSTP(83)=1`) which assumes that all the proton-proton collisions have a fixed impact parameter. Studies performed by the CDF collaboration [74, 75] also conclude that a varying impact parameter model is preferred to describe the minimum-bias events and the underlying particles in $\mathrm{b\overline{b}}$ events produced in $\mathrm{p\overline{p}}$ collisions at $\sqrt{s} = 1.8\,\mathrm{TeV}$. Model 1 is the default in PYTHIA and was used for the performance studies reported in the Technical Proposal; however, all simulation studies for subsequent Technical Design Reports have been performed with Model 3.

In Fig. 6.2 (a) the densities of charged particles at $\eta = 0$, where η is the pseudo-rapidity, are plotted for non single-diffractive events measured at six different center-of-mass energies ranging from 50 to 1800 GeV [76, 77]. The figure also shows the result

---

[1] Elastic scattering practically never produces tracks reconstructible in the detector.

[2] A $\mathrm{b\overline{b}}$ production cross section of 500 μb has been assumed for the yield calculations given in Sect. 9.4.

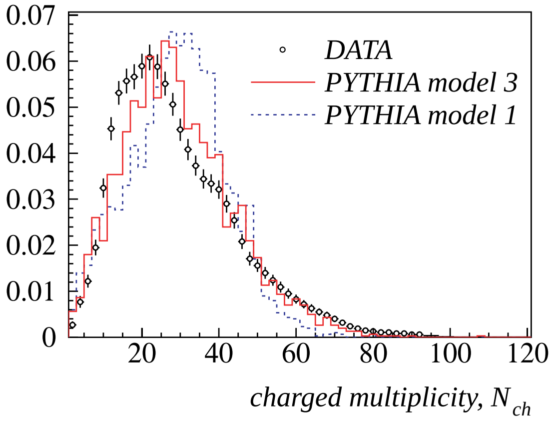

Figure 6.1: Charged multiplicity distribution for non single-diffractive events in $p\bar{p}$ collisions at $\sqrt{s} = 546\,\text{GeV}$ as measured by UA5 [73], compared with PYTHIA predictions using the CTEQ4L parton distribution functions and either Model 1 (dashed) or 3 (solid histogram) for multiple interactions. In each case the $p_{\rm T}^{\rm min}$ parameter has been tuned to reproduce the mean multiplicity of the data.

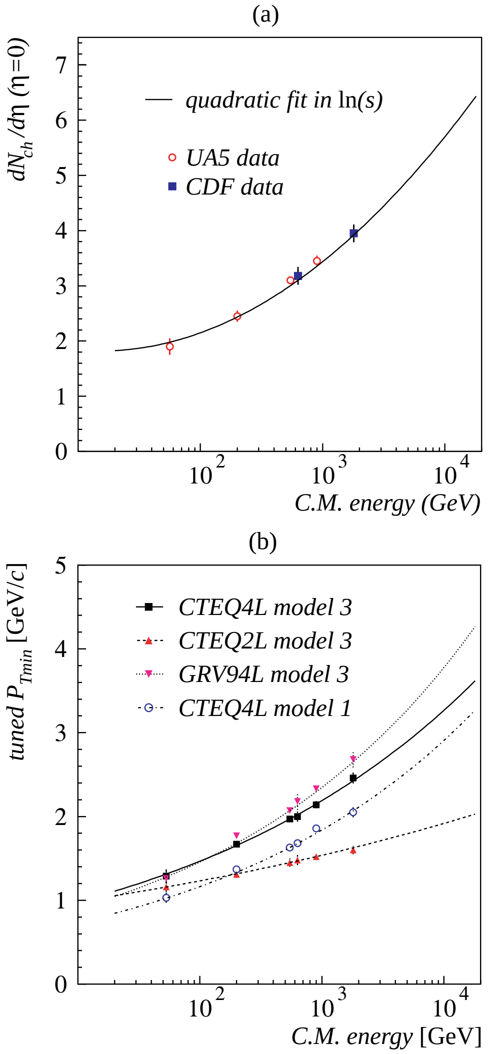

Figure 6.2: (a) Average charged multiplicity at $\eta = 0$ measured at different energies by UA5 and CDF. (b) Corresponding values of $p_{\rm T}^{\rm min}$ which allow PYTHIA to reproduce these data, using different multiple interaction models or parton distribution functions. Details can be found elsewhere [78].

of a quadratic fit in $\ln(s)$ [77] to the data. From the extrapolation of the fit, we obtain

$$(dN_{\rm ch}/d\eta)^{\text{direct fit}}_{\eta=0} = 6.11 \pm 0.29 \quad \text{at } \sqrt{s} = 14\,\text{TeV}\,, \tag{6.1}$$

where the quoted error is due to the statistical uncertainty of the fit.

Using PYTHIA Model 3, the value of the $p_{\rm T}^{\rm min}$ parameter has been tuned [78] so as to reproduce those measured charged particle densities at $\eta = 0$ for different parametrizations of the structure functions. The tuned $p_{\rm T}^{\rm min}$ values, displayed in Fig. 6.2 (b), show an energy dependence which is well described by a power law, as advocated in recent PYTHIA versions. Although the values of $p_{\rm T}^{\rm min}$ themselves strongly depend on the assumed set of structure functions, the predicted charged particle density at $\eta = 0$ obtained at the LHC energy using the extrapolated values of $p_{\rm T}^{\rm min}$ depends only weakly on the choice of the structure functions. Choosing the CTEQ4L parton distribution functions together with Model 3, as PYTHIA settings for the LHCb simulation study, an extrapolated value of

$$p_{\rm T}^{\rm min} = 3.47 \pm 0.17\,\text{GeV}/c \quad \text{at } \sqrt{s} = 14\,\text{TeV} \tag{6.2}$$

is obtained, which leads to

$$(dN_{\rm ch}/d\eta)^{p_{\rm T}\ \text{fit}}_{\eta=0} = 6.30 \pm 0.42 \quad \text{at } \sqrt{s} = 14\,\text{TeV}\,.$$

This is in good agreement with Eq. (6.1), the direct fit of Fig. 6.2 (a), supporting the validity of the PYTHIA prediction at the LHC energy. A central value of $3.47\,\text{GeV}/c$ is therefore used as default to generate collisions in LHCb.

Contrary to Model 1, a model for multiple parton-parton interactions with varying impact parameter results in significantly different multiplicities for minimum-bias and $b\bar{b}$ events. This is illustrated in Fig. 6.3, where various predictions are shown for the distribution of the number of charged particles produced in hard pp collisions at LHC energy in the pseudo-rapidity region $1.8 < \eta < 4.9$, corresponding roughly to the LHCb acceptance. The mean charged multiplicity is higher in $b\bar{b}$

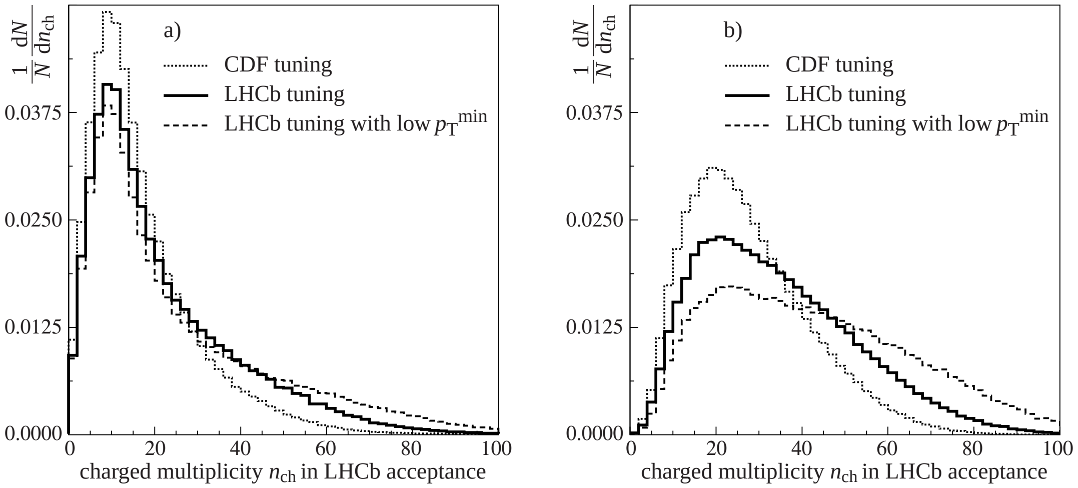

Figure 6.3: Charged multiplicity distributions in the LHCb acceptance ($1.8 < \eta < 4.9$) for (a) minimum-bias collisions and (b) collisions producing b-hadrons, as predicted by PYTHIA 6.2 with `MSEL=1` (hard collisions) and different settings for multiple parton-parton interactions. The plain histograms are obtained with the nominal LHCb settings, the dashed histograms with modified LHCb settings where $p_T^{\min}$ of Eq. (6.2) is lowered by three times its uncertainty, and the dotted histograms with a recent tuning from CDF [79]. Decay products of K_S^0 mesons and Λ baryons are not counted.

events than in minimum-bias events. With the nominal LHCb settings for PYTHIA (i.e. Model 3 tuned as explained above) these averages are 33.9 and 21.3 respectively; they increase by 26% and 19% respectively if the value of $p_T^{\min}$ from Eq. (6.2) is lowered by three times its uncertainty.

The CDF collaboration has recently published [75] their tuning of PYTHIA 5.7 which reproduces best the soft and hard interactions they observe in $p\overline{p}$ collisions at $\sqrt{s} = 630$ and 1800 GeV; it involves Model 4 for multiple parton-parton interactions, a variant of Model 3 with a double-Gaussian parametrization of the matter distributions of the colliding hadrons. Using an updated version of this tuning [79], valid for PYTHIA 6.2 and claimed to reproduce minimum-bias data and the "underlying event" in hard scattering processes at the two Tevatron energies, the average multiplicities predicted in LHCb would be approximately 20% lower than those obtained with the nominal LHCb settings (see Fig. 6.3).

6.1.2 Bunch-crossing description

The two proton beams of 7000 GeV each are assumed to have a horizontal (vertical) crossing half-angle of 285 μrad (0 μrad), with an angular spread corresponding to an emittance of 0.503 m and a β^* of 10 m. The luminous region is assumed to be a Gaussian ellipsoid with $\sigma_z = 5$ cm and $\sigma_x = \sigma_y = 70\,\mu$m, truncated at $\pm 4\sigma$ in all dimensions.

Several inelastic proton-proton collisions may occur in the same bunch crossing. This "pile-up" phenomenon is simulated assuming that the number of inelastic pp interactions in one bunch crossing follows a Poisson distribution with a mean given by $L\sigma_{\rm inel}/\nu$, where L is the instantaneous luminosity, $\sigma_{\rm inel}$ is the inelastic cross section taken to be 80 mb, and $\nu = 29.49$ MHz is the average non-empty bunch crossing frequency at the LHCb interaction point. The luminosity L is assumed to decrease exponentially with a 10-hour lifetime in the course of 7-hour fills, with an average value of 2×10^{32} cm^{-2}s^{-1} (implying a maximum value of $\sim 2.8 \times 10^{32}$ cm^{-2}s^{-1} at start of fill). In practice, only "visible" collisions contribute to the pile-up; we define such collisions as the ones producing at least two charged particles reconstructible as long tracks in the detector (according to the definition of Sect. 7.3), corresponding to $(79.1\pm0.2)\%$ of $\sigma_{\rm inel}$. Pile-up characteristics, averaged over a fill and considered for visible collisions only, are given in Table 6.1 for minimum-bias and $b\overline{b}$ events.

6.2 Detector simulation

Generated particles are tracked through the detector material and surrounding environment using

Table 6.1: Average probabilities F_i to produce i visible pp collisions and average number $\sum_{i=1}^{\infty} iF_i$ of such collisions in bunch crossings producing at least one visible collision. This table effectively gives the pile-up distribution and average in the generated minimum-bias sample (first line) and $b\overline{b}$ sample (second line). Absolute uncertainties from MC statistics are approximately 0.001.

	F_1	F_2	F_3	F_4	F_5	$\sum_{i=1}^{\infty} iF_i$
All bunch crossings	79.9%	17.2%	2.6%	0.3%	0.0%	1.234
Crossings producing b-hadrons	64.9%	27.8%	6.2%	1.0%	0.1%	1.420

the GEANT 3 package [57]. The geometry and material of the LHCb detector are described in detail. The description includes not only the active detection components and their front-end electronics, but also passive material such as the beam-pipe, frames, supports and shielding elements. Low-energy particles, mainly produced in secondary interactions, are also traced, down to an energy cut-off of 10 MeV for hadrons and 1 MeV for electrons and photons. These values were shown to be appropriate in a dedicated study [80] of the detector response with 10 times lower energy thresholds.

In the simulation program the entrance and exit points of each particle traversing a sensitive detection layer are registered, together with the energy loss in that layer and the time-of-flight of the particle with respect to the primary interaction time. These informations are then used to generate digitized "raw data", taking into account the details of the sensitivity and response of each detector. Detection efficiencies and resolutions of the individual sub-systems are adjusted using results from beam tests of prototypes. Electronics noise and cross-talk effects are also included.

The detector response is simulated as a function of the arrival time of each particle and, depending on the detection technology and electronics, may span more than the time interval between two consecutive bunch crossings at 40 MHz. This effect is referred to as "spill-over". In order to take it properly into account, the generated "event" fed into the detector simulation consists not only of the particles produced in a specific bunch crossing ($t = 0$), but also of those, if any, produced in the two preceeding ($t = -50, -25$ ns) and in the following ($t = +25$ ns) bunch crossings. The instantaneous luminosity is used to determine the probability that the neighbouring bunch crossing produce particles (but the fact that some bunches are empty, due to the LHC beam structure, is conservatively neglected here).

In the Muon system, the number of hits generated by charged particles is rather low, and the neutron-induced background thus becomes relevant. Since the time structure of this background is very different from that due to the charged particles, special studies have been made to find a suitable parametrization to include the effect in the response of the Muon system [81].

Background from the LHC machine is presently expected to contribute less than one extra particle per bunch crossing, once stable beam conditions are reached [82]. Such background has not been considered in the studies presented here, as its relative effect is clearly negligible. However, dedicated studies have been performed to assess the effect of the beam halo muons on the trigger performance [3].

To demonstrate the level of detail of the detector simulation, the part related to the tracking, which is the system most affected by the detector optimization, is described below at some length. For the tracking detectors the response simulation can be classified into two categories: silicon detector response (VELO, TT and IT) [83] and straw detector response (OT) [84].

6.2.1 Silicon detector response

The number of primary electron-hole pairs corresponding to the energy loss inside the silicon are distributed along the particle trajectory. This trajectory is subdivided into parts, in each of which the number of electrons is sampled from a Landau distribution. Subsequently, the charge signals of each part are collected on the readout strips by applying a charge sharing function, which is tuned to describe test-beam data. For each strip a noise signal is added according to a Gaussian distribution corresponding to a signal-to-noise ratio of 14 (VELO) or 12 (TT and IT). A 5% (VELO) and 10% (TT/IT) cross-talk between neighbouring strips is also implemented to simulate capacitive coupling and cross-talk effects in the front-end chip. A strip causes a hit if the signal surpasses a threshold that is a multiple of the noise. Standard settings are given in Table 6.2. The effective efficiency for a layer to observe a traversing particle is $> 99\%$ (VELO) and between 97.5% and 98% for TT and IT. The reasons for the lower TT/IT efficiencies are the assumption that 1% of the silicon strips are inoperative, the presence of small insensitive regions between the silicon sensors of the TT/IT ladders (such as guard rings), and the slightly reduced efficiency due to the imperfect charge collection in the region between two strips for the large TT/IT strip pitch [6].

The analog front-end pulse shape has a remaining amplitude of approximately 30% for VELO and IT, and 50% for TT, after 25 ns. This is taken into account by applying the same procedure as mentioned above to all hits caused by the previous bunch-bunch collisions at -25 ns (and -50 ns in the case of TT and IT) after reducing the amplitudes accordingly.

6.2.2 Straw detector response

The path length of a traversing track in each straw is calculated as is its distance of closest approach to the wire. A hit efficiency is assigned based on the calculated trajectory length l and effective primary ionization density ρ, using the parametrization [2]

$$\eta(l) = \eta_0\,(1 - e^{-\rho l})\,,$$

where $\eta_0 = 0.99$ and $\rho = 1.47\,\mathrm{mm}^{-1}$ have been tuned to reproduce OT test-beam results [84], leading to an integrated cell efficiency of 97%. If a hit is registered, a detector response time is generated according to

$$t_{\mathrm{TDC}} = t_{\mathrm{bunch}} + t_{\mathrm{tof}} + t_{\mathrm{drift}} + t_{\mathrm{delay}}\,,$$

where t_{bunch} is the bunch time ($-50, -25, 0, 25$ ns), t_{tof} is the time-of-flight of the track as it passes through the straw, t_{drift} is the drift time in the cell and t_{delay} is the additional time delay due to signal propagation along the wire. A measurement resolution of $200\,\mu$m, again based on test-beam measurements [2], is implemented by smearing t_{drift} accordingly.

Since the front-end readout works with a 50 ns sensitive time gate, a hit is only registered if it falls in a time window $t_0 < t_{\mathrm{TDC}} < t_0 + 50$ ns. The value t_0 is calibrated for each station as the rising edge of the time spectrum of all hits from the bunch at $t = 0$. In case two or more tracks pass through a single straw only the one with the earliest t_{TDC} is registered, for the others the straw is inefficient. Finally, cross-talk between straws is implemented such that in 5% of the cases a signal in a neighbouring straw is generated (with identical t_{TDC}).

The overall efficiency to produce at least one hit in a double layer depends on the momentum of a track;[3] for $p > 2\,\mathrm{GeV}/c$ the overall efficiency is 98%. The measurement resolution also depends on the track momentum,[4] however for tracks with $p > 2\,\mathrm{GeV}/c$ it is close to $200\,\mu$m.

6.3 Monte Carlo samples

Several samples of Monte Carlo events have been generated and simulated to assess the performance of the reconstruction, trigger and offline selection with the reoptimized LHCb detector:

- samples of specific signal B decays, with typically between 50k and 200k events for each channel under study;
- other samples of specific b-hadron decays identified as physics backgrounds for the channels under study;
- a sample of approximately 10^7 inclusive $\mathrm{b\overline{b}}$ events, used for the estimation of the combinatorial background in the offline selections;
- two special background samples of approximately 380k events each with a prompt J/ψ produced at the primary vertex and decaying to $\mu^+\mu^-$ and $\mathrm{e}^+\mathrm{e}^-$;
- a large sample of approximately 3×10^7 minimum-bias events (needed for the simulation of spill-over for all the other samples), used for the trigger studies.

No cut is imposed at generator level for the minimum-bias sample. In all other cases, the particle of interest (i.e. the signal b-hadron, or one of the b-hadron in inclusive $\mathrm{b\overline{b}}$ events, or the prompt J/ψ) is required to have a true polar angle smaller than 400 mrad. This avoids tracking and reconstructing many events where not all interesting decay products are in the detector acceptance. The sample sizes mentioned above are given after this requirement, which has an efficiency of 34.7% for signal B events and 43.2% for inclusive $\mathrm{b\overline{b}}$ events. All these samples are produced using a nominal set of simulation parameters, corresponding to the expectations and assumptions from today's knowledge.

---

[3] Due to the fact that very low momentum tracks (often secondaries) have significantly longer time-of-flight, the digitization time t_{TDC} can occasionally fall outside the sensitive time gate, resulting in inefficiency.

[4] The longer time-of-flight for low momentum tracks leads to a biased drift time measurement after t_0 subtraction, which results in a worse resolution for very low momentum tracks.

Table 6.2: List of all simulation parameters that have been varied simultaneously for the "global robustness test", compared to nominal settings.

Subsystem(s)	Parameter	Nominal value	Test value
PYTHIA	$p_{\mathrm{T}}^{\mathrm{min}}$ of multi-parton interactions	3.47 GeV/c	2.96 GeV/c
VELO	cluster resolution		nominal $\oplus$ 5 μm
VELO	inefficient channels	0.0%	1.5%
VELO	noise (RMS/threshold)	1500 e^- / 4680 e^-	1900 e^- / 6240 e^-
TT, IT	cluster resolution		nominal $\oplus$ 30 μm
TT, IT	inefficient channels	1.0%	1.5%
TT	noise (RMS/threshold)	2700 e^- / 8640 e^-	3600 e^- / 11520 e^-
IT	noise (RMS/threshold)	2000 e^- / 6400 e^-	2700 e^- / 8640 e^-
OT	hit resolution	200 μm	250 μm
OT	single channel efficiency	97%	94%
OT	noise hit rate per straw	0 kHz	10 kHz
OT	cross-talk	5%	8%
RICH1, RICH2	p.e. detection efficiency		nominal × 80%
RICH1, RICH2	random noise per pixel (HPD)	0.0%	0.3%
RICH1	emission point error	0.7 mrad	1.2 mrad
PS	coherent noise	0.0 ADC	0.5 ADC
PS	incoherent noise	1.0 ADC	1.5 ADC
ECAL, HCAL	coherent noise	0.3 ADC	0.5 ADC
ECAL, HCAL	incoherent noise	1.2 ADC	1.5 ADC
SPD, PS	dead channels	0.0%	1.0%
ECAL, HCAL	dead channels	0.0%	0.2%
SPD	gain error	0.0%	1.5%
PS, ECAL, HCAL	gain error	1.0%	1.5%
MUON	low-energy background		nominal × 2
MUON	single-gap efficiency	95%	90%
MUON	wire readout cross-talk	8%	20%
MUON	cathode readout cross-talk	8%	30%
MUON	electronics noise per channel	0.1 kHz	1 kHz
MUON	channel dead-time	50 ns	80 ns

In addition, samples of minimum-bias events and selected signal B decays have been generated under special conditions to test the stability of the performance with respect to our nominal assumptions.

In a first test, referred to as the "global robustness test", several simulation parameters are changed simultaneously in the direction of degraded performance, by a relatively large amount, but still judged to be plausible. This primarily concerns the efficiency, noise and cross-talk of the various sub-detectors. In the silicon detectors, an additional smearing of the resolution is introduced, as a simple way to simulate possible misalignment effects. In addition, a more conservative value of $p_{\mathrm{T}}^{\mathrm{min}}$ is used for the PYTHIA generator (see Sect. 6.1.1 and Fig. 6.3) leading to an increase in track multiplicity, and hence detector occupancy. The overall result corresponds to a rather unlikely worse-case scenario, where several of the expectations would turn out to be too optimistic, and none to be too pessimistic. The list of all parameter changes considered in this global test is given in Table 6.2.

As a second test, the detector is kept at its nominal performance and only the PYTHIA parameters are modified. We use here the settings obtained from a recent tuning on CDF data [79], after extrapolation to LHC energy. As explained in Sect. 6.1.1 and Fig. 6.3, this leads to a lower track multiplicity than we assume by default.

The results of these tests are discussed in Sects. 7.4, 8.9, and 9.4.

Chapter 7 Track Reconstruction

7.1 Introduction

In the track reconstruction program the registered hits of the VELO, the TT, the IT and the OT detectors are combined to form particle trajectories from the VELO to the calorimeters. The program aims to find all tracks in the event which leave sufficient detector hits, not only possible B-decay products. After fitting the reconstructed trajectory a track is represented by state vectors (x, y, dx/dz, dy/dz, Q/p) which are specified at given z-positions in the experiment.

The performance of the reconstruction is expressed using the following quantities:

- the efficiency of the track finding procedure and the corresponding ghost rate;
- the precision of the reconstructed momentum parameter;
- the precision of the reconstructed impact parameter;
- the precision of the track slopes in the RICH detectors.

The first three items are most important for the B-decay products, while the last item is also of importance for all tracks which traverse the RICH detectors and have a momentum high enough to emit Cherenkov light.

Depending on their generated trajectories inside the spectrometer the following classes of tracks are defined, illustrated in Fig. 7.1:

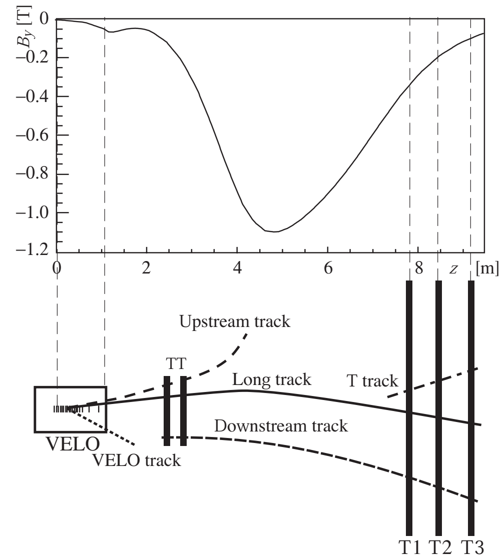

Figure 7.1: A schematic illustration of the various track types: long, upstream, downstream, VELO and T tracks. For reference the main B-field component (B_y) is plotted above as a function of the z coordinate.

1. **Long tracks:** traverse the full tracking set-up from the VELO to the T stations. They are the most important set of tracks for B-decay reconstruction.
2. **Upstream tracks:** traverse only the VELO and TT stations. They are in general lower momentum tracks that do not traverse the magnet. However, they pass through the RICH 1 detector and may generate Cherenkov photons. They are therefore used to understand backgrounds in the particle-identification algorithm of the RICH. They may also be used for B-decay reconstruction or tagging, although their momentum resolution is rather poor.
3. **Downstream tracks:** traverse only the TT and T stations. The most relevant cases are the decay products of K^0_S and Λ that decay outside the VELO acceptance.[1]
4. **VELO tracks:** are measured in the VELO only and are typically large angle or backward tracks, useful for the primary vertex reconstruction.
5. **T tracks:** are only measured in the T stations. They are typically produced in secondary interactions, but are useful for the global pattern recognition in RICH 2.

---

[1] In $B^0 \rightarrow J/\psi\, K^0_S$ events in which the K^0_S decay products traverse the T stations, about 25% of the K^0_S decays occur in the VELO acceptance, 50% outside the VELO acceptance but before the TT station, and 25% downstream of TT.

The overall strategy to reconstruct all of the above-mentioned track types with good performance is discussed in the following section. The sections thereafter describe the actual performance of the track reconstruction algorithms.

7.2 Reconstruction strategy

The input of the tracking pattern recognition are the simulated detector signals of the tracking detectors (VELO, TT and T stations), discussed in Sect. 6.2. The track reconstruction starts with a search for track "seeds", the initial track candidates. Both the VELO region and the T stations are well suited for such a search. As can be seen in Fig. 7.1 the magnetic field in these regions is low and a search for almost straight lines is possible.

- **VELO seeds:** are reconstructed as straight segments in the VELO using the r and ϕ coordinates of the VELO clusters. A VELO seed provides an initial track state without momentum information.
- **T seeds:** are reconstructed using the IT clusters and OT hits after applying the drift time corrections. A T seed is parametrized as a parabola since the magnetic field in this region is low but not negligible. An initial momentum estimate can be assigned to the track seed either from the measured curvature or by assuming that the track originates from the nominal interaction point. For long tracks the latter provides a momentum estimate with a precision of approximately 1%.

Proceeding from these seeds, the following strategy of consecutive steps has been adopted for optimal performance:

1. **Long track search.** Starting from a VELO seed an attempt is made to form a track with each hit in the T stations in turn. A combination of a VELO seed and a single T-station hit determines the momentum of the track candidate and hence the particle's trajectory across the measurement planes. Around this trajectory a search for hits in other stations, including the TT station, is performed. When enough hits have been collected along a trajectory, a track is reconstructed. This method is referred to as the "forward tracking" algorithm [85]. About 90% of all long tracks are reconstructed using this algorithm.

   After this procedure has been applied to all VELO seeds, the hits in the T stations that have been used are discarded and the T-seed search is performed [86]. An additional 5% of the long tracks can be reconstructed by extrapolating the track state of T seeds to the VELO region and by requiring that they have position and slope parameters that match to a VELO seed [87].

   All used VELO and T seeds are discarded before searching for other track types.

2. **Upstream and Downstream search.** Two separate algorithms search for upstream [88] and downstream [89] tracks by associating the remaining VELO and T seeds to TT clusters. In order to reduce the number of ghost tracks in the upstream track search algorithm, hits in both TTa and TTb detectors are required. The hits in TTa define, together with the VELO seed, the momentum of the track candidate while the hits in TTb confirm the track. For downstream tracks this requirement does not apply since an initial momentum estimate is available, assuming that the track originates from the nominal vertex.

3. **VELO and T track search.** Remaining VELO and T seeds that have not been associated with any of the above mentioned tracks are also stored as tracks, either with no (VELO tracks) or a poor (T tracks) momentum estimate.

After tracks have been found their trajectories are refitted with a Kalman filter fit [90]. An initial state is obtained from the pattern recognition algorithms and taken at the most downstream measurement position. The fit then proceeds in the upstream direction, updating the state vector at each measurement plane. As it traverses the detector the fit retrieves from the geometry database any (inactive) layers of material encountered. This allows for "kinks" in the trajectory due to multiple scattering and in addition corrects for dE/dx energy loss. As soon as the most upstream measurement is reached the fit reverses direction in order to update the downstream state vectors with the full information of all measurements.

The quality of the reconstructed tracks is monitored by the χ^2 of the fit and with the "pull" distribution of the track parameters. The assigned errors of the fitting procedure of the position and slope parameters are correct within 5%, while the assigned momentum error is correct within 15%. The latter is mainly attributed to non-Gaussian multiple scattering effects.

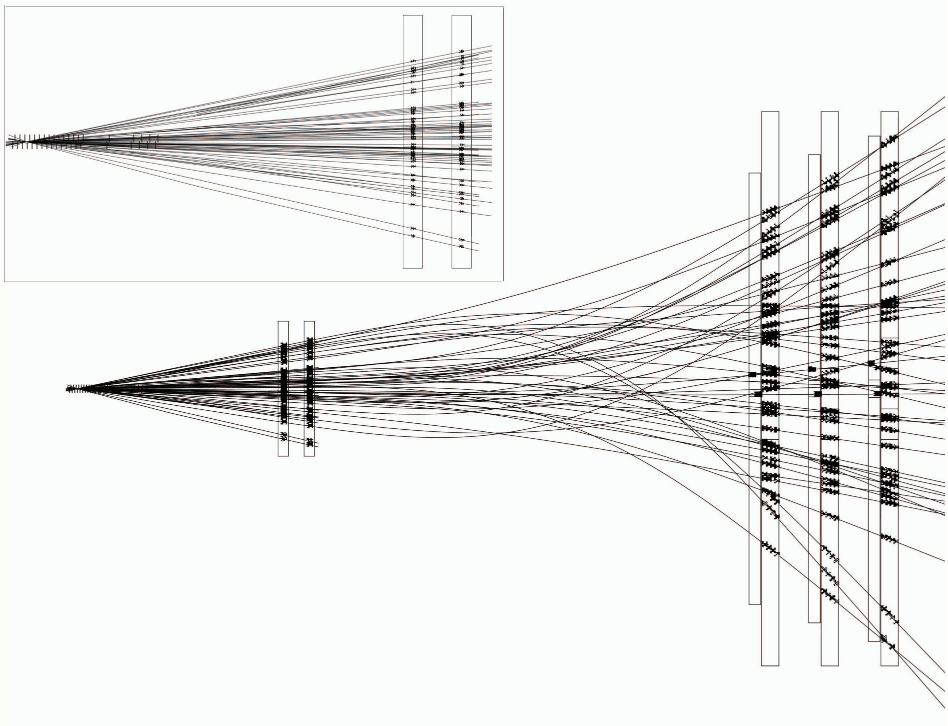

Figure 7.2: Display of the reconstructed tracks and assigned hits in an event. The insert shows a zoom in of the VELO and TT region. This particular event contains 50% more hits than average.

7.3 Performance

The pattern recognition performance is evaluated in terms of efficiencies and ghost rates. The efficiencies are normalized to the different reconstructible track samples. To be considered reconstructible, the requirements for each track type are as follows:

- for VELO tracks the particle must give at least 3 r and 3 ϕ hits;
- for T tracks the particle must give at least 1 x and 1 stereo hit in each station T1–T3;
- for long tracks the particle must be reconstructible as a VELO and T track;
- for upstream tracks the particle must be reconstructible as a VELO track and give at least 3 hits in TT;
- for downstream tracks the particle must be reconstructible as a T track and give at least 3 hits in TT.

To be considered as "successfully reconstructed" a VELO or T track must have at least 70% of its associated hits originating from a single Monte Carlo particle, an upstream or downstream track must have in addition a correct TT hit assigned, and a long track must have both correctly found VELO- and T-track segments. The reconstruction efficiency is defined as the fraction of reconstructible particles that are successfully reconstructed, and the ghost rate is defined as the fraction of found tracks that are not matched to a true Monte Carlo particle.

The results quoted in this section are obtained from a sample of $\mathrm{B}^0 \rightarrow \mathrm{J}/\psi\,\mathrm{K}^0_\mathrm{S}$ events. Particle tracks originating from either decays of the signal B^0 or the other b-hadron in the event are referred to simply as B tracks in the text.

The average number of successfully reconstructed tracks in $\mathrm{b}\bar{\mathrm{b}}$ events is 72, which are distributed among the track types as follows: 26 long tracks, 11 upstream tracks, 4 downstream tracks, 26 VELO tracks and 5 T tracks. The track finding performance is summarized for the most important cases: the long tracks, the low momentum (upstream) tracks and K^0_S decay (downstream) tracks. An example of a reconstructed event is displayed in Fig. 7.2.

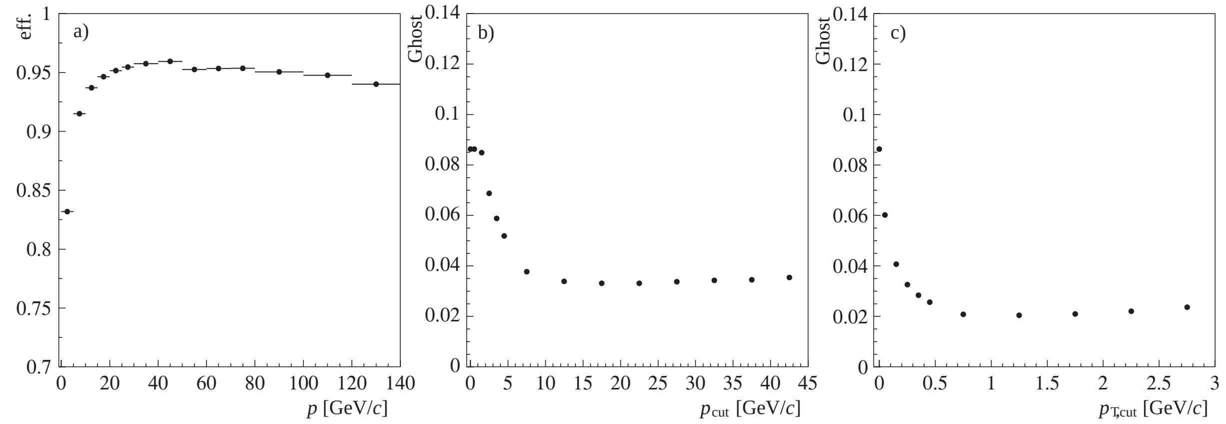

Figure 7.3: Performance of the long track finding: (a) efficiency as a function of the momentum of the generated particle; (b) ghost rate, for tracks with reconstructed momentum greater than p_{cut}; (c) ghost rate, for tracks with reconstructed transverse momentum greater than $p_{\mathrm{T,cut}}$.

7.3.1 Long tracks

The efficiency of long track reconstruction is plotted in Fig. 7.3 (a) as function of the track momentum. For tracks with momentum higher than 10 GeV/c the average efficiency is 94%. For final state particles of specific B decays even higher efficiencies are observed (95–96%) as can be deduced from Table 9.4 in the physics performance chapter. The corresponding ghost rates are plotted in Fig. 7.3 both as function of the track momentum and transverse momentum. Although the average ghost rate is 9%, most of the reconstructed ghost tracks have a low reconstructed transverse momentum. Since the majority of B tracks have $p_{\mathrm{T}} > 0.5\,\mathrm{GeV}/c$, the effective ghost rate for physics reconstruction is approximately 3%.

The plots show that the search for low momentum particles is more difficult than that for high momentum particles. The main reason lies in the fact that multiple-scattering angles are inversely proportional to the particle momentum, requiring relatively large search windows in the pattern recognition algorithms for low momentum tracks. However, large search windows lead to a higher ghost rate. The choice of the search window sizes follows from an optimization of efficiency and ghost rate. For low momentum tracks both a reduced efficiency and a higher ghost rate is observed.

Distributions of the total number of hits on a track, as well as the fraction of correctly assigned hits, are shown in Fig. 7.4 for tracks which have been successfully reconstructed. The small peak in the left plot is due to tracks traversing the IT, the larger peak is due to tracks passing through the OT. On average a reconstructed long track contains 13.3 VELO hits, 3.7 TT hits, and 11.7 (22.0) IT (OT) hits. Of these, on average 98.7% are correct, which in practice implies one wrongly assigned hit in two tracks.

The momentum and impact parameter resolutions of the reconstructed track parameters are shown in Fig. 7.5. The momentum resolution is plotted as a function of the track momentum and is seen to be increasing from $\delta p/p = 0.35\%$ for low momentum tracks to $\delta p/p = 0.55\%$ for tracks at the high end of the spectrum. In the same figure the momentum spectrum for B-decay tracks is also illustrated. The impact parameter resolution is plotted as function of $1/p_{\mathrm{T}}$ of the track. The linear dependence can be parametrized as $\sigma_{\mathrm{IP}} = 14\,\mu\mathrm{m} + 35\,\mu\mathrm{m}/p_{\mathrm{T}}$ with p_{T} in GeV/c. For comparison the momentum and $1/p_{\mathrm{T}}$ spectra of B-decay

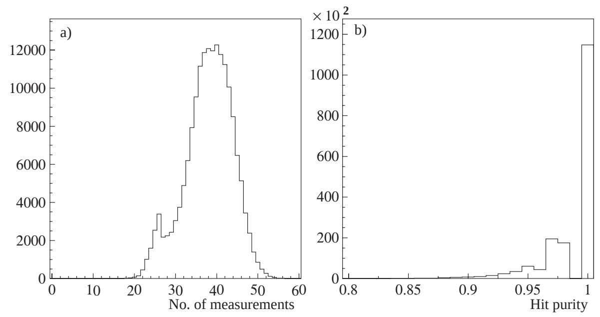

Figure 7.4: (a) The number of detector measurements assigned to reconstructed long tracks, (b) the fraction of correctly assigned hits.

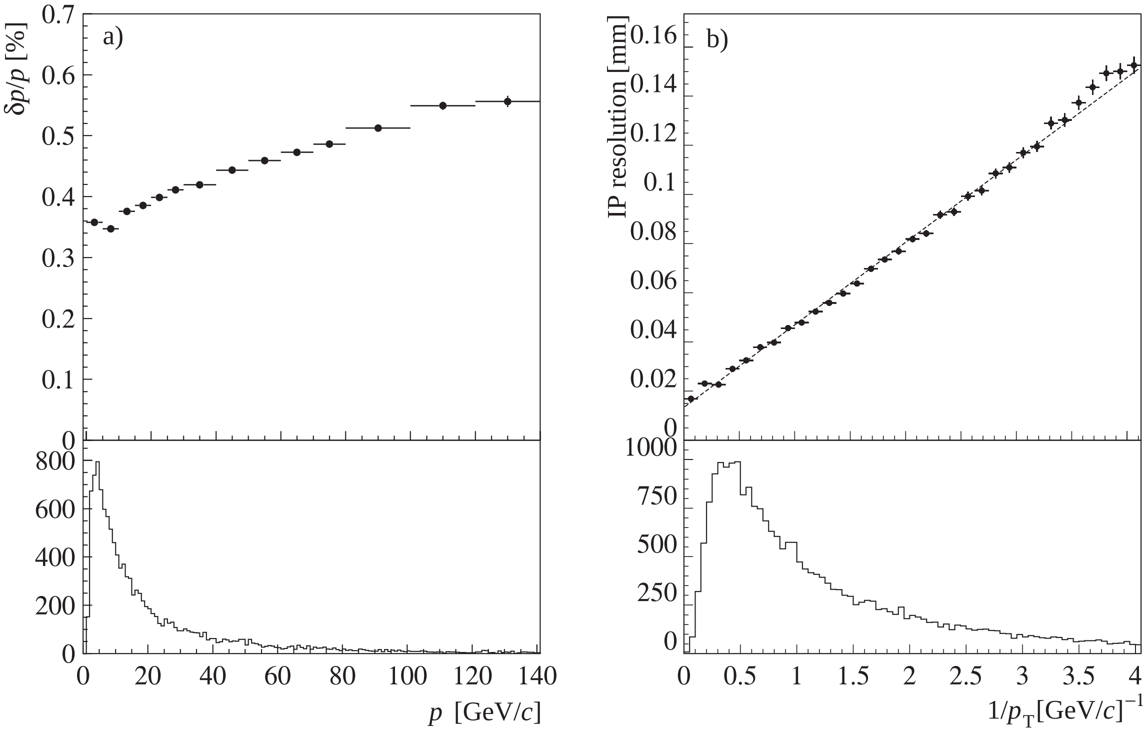

Figure 7.5: Resolution on the reconstructed track parameters at the production vertex of the track: (a) momentum resolution as a function of track momentum, (b) impact parameter resolution as a function of $1/p_{\mathrm{T}}$. For comparison, the momentum and transverse-momentum spectra of B-decay particles are shown in the lower part of the plots.

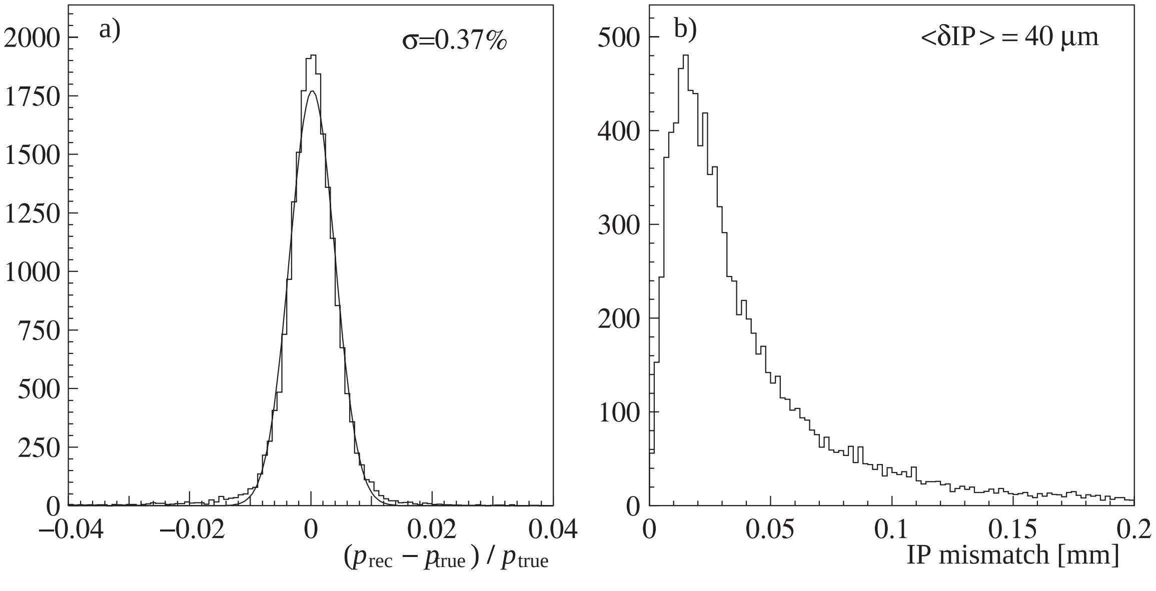

Figure 7.6: (a) momentum resolution with single Gaussian fit, and (b) impact parameter precision, for B-decay tracks.

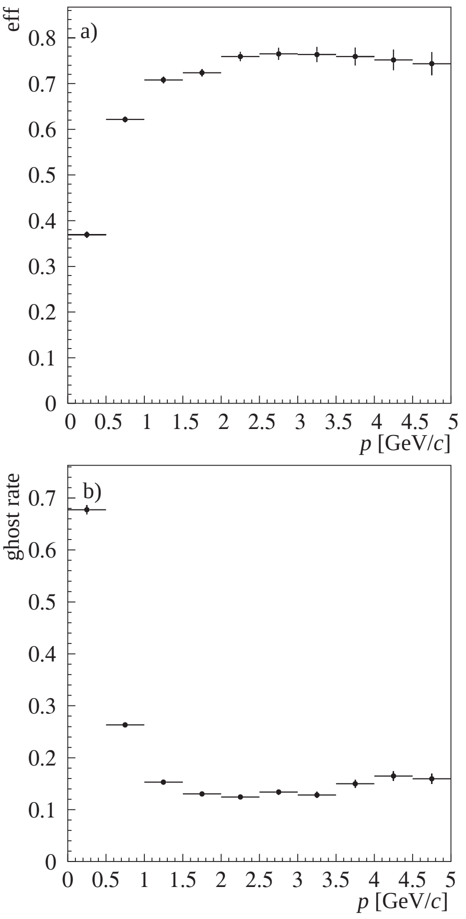

Figure 7.7: (a) Efficiency and (b) ghost rate, as a function of momentum, for upstream tracks.

particles in the detector acceptance are plotted in the same figure.

Figure 7.6 shows the resolutions for generic B-decay tracks. In the left plot the reconstructed momentum is compared to the true particle momentum for reconstructed B-decay tracks. The average momentum resolution is seen to be $\delta p/p = 0.37\%$. In the right part of the figure the impact parameter distance is plotted for B-decay tracks. The distribution peaks at a value of $\delta(IP) = 20\,\mu$m, while the average value is $\langle\delta(IP)\rangle = 40\,\mu$m.

7.3.2 Short tracks

The reconstruction procedure of the long tracks profits from the fact that robust track segments are measured at both sides of the dipole magnet. The reconstruction of the short upstream and downstream tracks either misses a T or a VELO segment and is therefore more difficult.

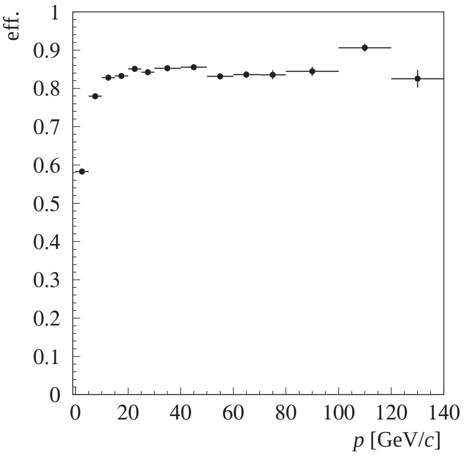

Figure 7.8: Downstream track finding efficiency as function of momentum.

Upstream tracks

The dependence of the efficiency and ghost rate on the momentum of upstream tracks is shown in Fig. 7.7. As for the long tracks, the search for low momentum tracks suffers from reduced efficency and leads to an increased number of low momentum ghost candidates. Since most tracks with $p < 1$ GeV/c are below threshold in RICH 1 the relevant efficiency for this procedure is approximately 75% with a corresponding ghost rate of 15%. Since the upstream tracks only see a small fraction of the total B-field integral they have a relatively poor momentum resolution: $\delta p/p \sim 15\%$.

Downstream tracks

As they have no hits in the VELO detector the downstream tracks are mainly used to reconstruct long-lived decays such as $\mathrm{K^0_S}$. Downstream tracks of low momentum are relatively difficult to find due to a long lever arm in the magnetic field between the T and TT stations. In order to maintain high efficiency the reconstruction allows for typically two or three track candidates in TT to be linked to a single track seed in the T stations. The ghost tracks introduced by this procedure are easily eliminated at a later stage when the pion track pairs are combined into $\mathrm{K^0_S}$ decays, as is shown in Chapter 8.

The efficiency for finding downstream tracks is plotted as a function of track momentum in Fig. 7.8. For tracks above 5 GeV/c the reconstruction efficiency is about 80%. Since the downstream tracks traverse most of the magnetic field, the momentum resolution is relatively good with an aver-

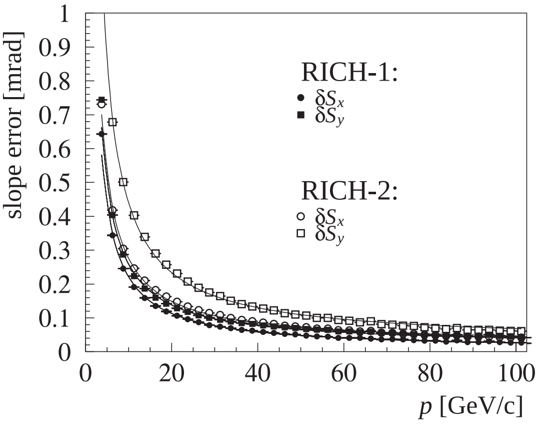

Figure 7.9: The precision of the reconstructed track slopes δS_x and δS_y in RICH 1 and RICH 2.

age of $\delta p/p = 0.43\%$ for pions originating from $\mathrm{K^0_S}$ decays in $\mathrm{B^0} \rightarrow \mathrm{J}/\psi\, \mathrm{K^0_S}$ events.

7.3.3 Track slopes in the RICH

The particle-identification algorithms of the RICH assume that the angle of the tracks as they traverse the RICH are known. The precision in the reconstruction of the Cherenkov photon angle is about 1.2 mrad in RICH 1 and 0.6 mrad in RICH 2 [7]. In order to not limit the particle-identification performance the track slopes should be known with better precision.

The particle-identification algorithm of the RICH 1 uses as input the reconstructed long, upstream and downstream track types with an average efficiency of 92%; the algorithm in RICH 2 uses the long, downstream and T tracks types, also with an average efficiency of 92% ($p > 4\,\mathrm{GeV}/c$). The precision of the angle of the track segment in the RICH detectors for these track types is plotted as function of the track momentum in Fig. 7.9, both for the slopes $S_x = dx/dz$ and $S_y = dy/dz$. A parametrization of the error on the slopes is given in Table 7.1. Due to the stereo angle set-up of the TT and T stations a difference is observed between the S_x and S_y angular precision. This difference is small in RICH 1 as the VELO track extrapolation has equal precision for both angles.

From the parametrizations given in Table 7.1 it can be concluded that the precision requirement is met for most of the spectrum of tracks emitting Cherenkov light: for RICH 1 for tracks with $p > 2.5\,\mathrm{GeV}/c$ and in RICH 2 for tracks with $p > 8\,\mathrm{GeV}/c$.

Table 7.1: The slope resolution parametrizations δS_x and δS_y (p in GeV/c) for tracks in RICH 1 and RICH 2.

	δS_x (mrad)	δS_y (mrad)
RICH 1	$2.16/p + 0.005$	$2.42/p + 0.017$
RICH 2	$2.55/p + 0.017$	$4.14/p + 0.027$

7.4 Global robustness test

As discussed in Sect. 6.2 the robustness of the detector has been tested with a dedicated simulation in which each of the detectors is assumed to be operating under conservatively estimated parameter settings. For the tracking detectors this implies: a reduced hit detection efficiency, a higher noise level and cross-talk rate, and reduced measurement resolution. The exact parameters used are compared to those of the standard simulation in Table 6.2.

The same track reconstruction program has been run on these Monte Carlo events and the results are compared below. It should be noted that this study reflects an unlikely scenario since not only all detector parameters are of lower quality than expected, but in addition the pattern recognition algorithms have not been retuned to adapt to the worse parameter settings.

Long Tracks

The efficiency and ghost rate in the robustness test are compared to that of the standard simulation program in Fig. 7.10. On average the track finding efficiency is reduced by 2.5% while the ghost rate is approximately 3% higher.

It is observed that a track reconstructed in the robustness test has on average 0.7 reconstructed hits less than a track reconstructed with the standard program, which is consistent with the detector efficiency degradation assumed in the program. A priori, a reduction of the fraction of correctly assigned hits is expected due to the fact that the algorithms have not been re-tuned to adapt to the worse resolution parameters. However, the purity of the assigned hits is reduced only to 97.8% (from 98.7%) and is still very comfortable.

The momentum and impact parameter resolutions are compared in Fig. 7.11. A degradation of the momentum resolution in the robustness test is only seen for tracks with very high momenta. The impact parameter resolution is slightly reduced and can be parametrized as: $\sigma_{\mathrm{IP}} = 18\,\mu\mathrm{m} + 36\,\mu\mathrm{m}/p_{\mathrm{T}}$,

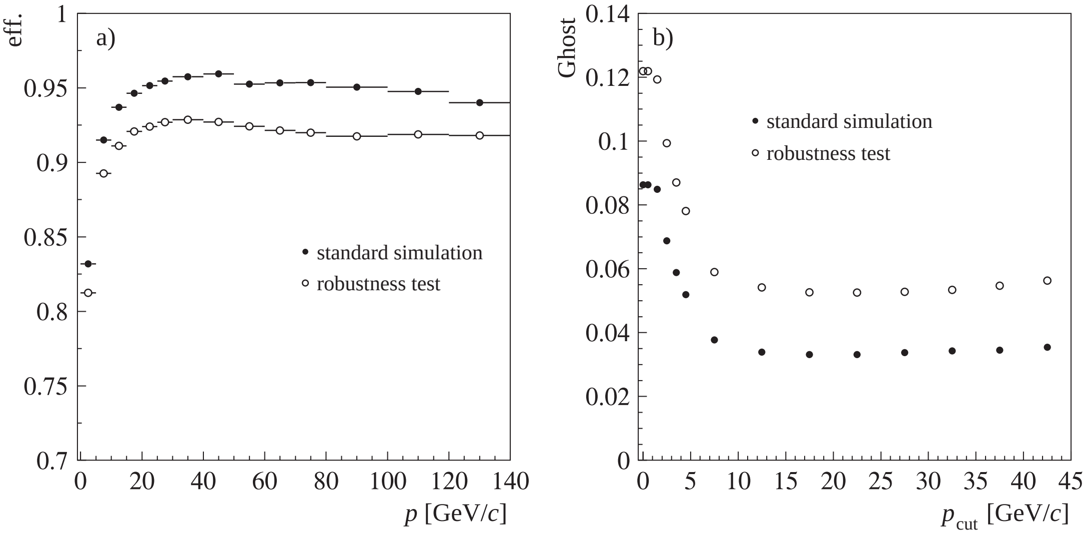

Figure 7.10: Comparison of pattern recognition performance between the standard simulation and the global robustness test: (a) track finding efficiency, (b) ghost rate.

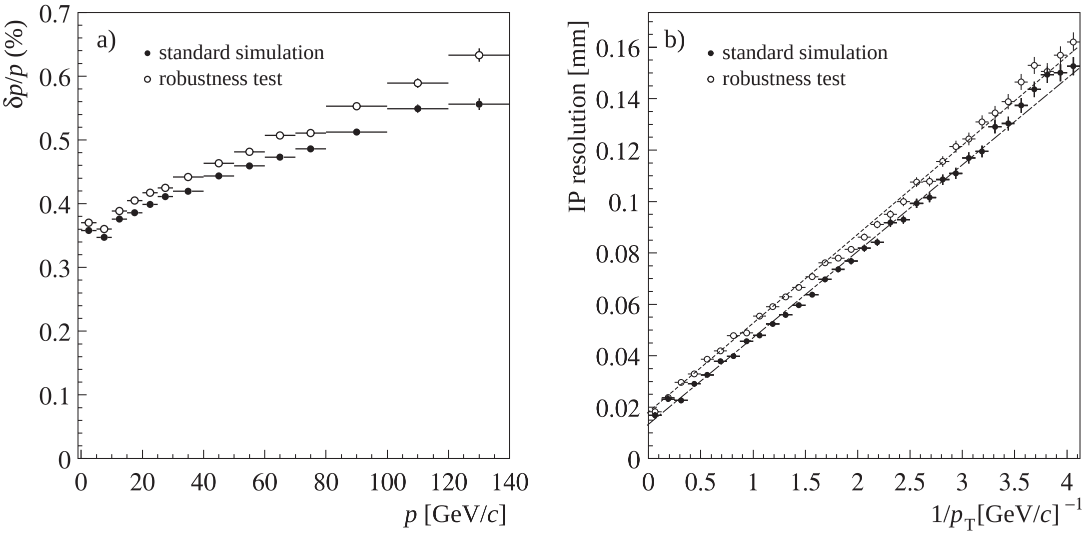

Figure 7.11: Comparison for long tracks between the standard simulation and the global robustness test: (a) reconstructed momentum resolution, (b) reconstructed impact parameter resolution.

which is consistent with the reduced cluster resolution in the VELO.

The slope precision in the RICH 1 and RICH 2 detectors remains unchanged in the global robustness test.

Upstream and Downstream tracks

The efficiency of the search algorithms for the upstream tracks is reduced, similarly to the long tracks, by 2.5% while the efficiency to find downstream pion tracks of K^0_S decays is reduced by 7%. The resolutions for these tracks are not significantly affected.

7.5 Other robustness tests

To test the reconstruction performance as a function of the hit occupancy in the detectors a sample of 50k $B^0 \to J/\psi K^0_S$ events has been subdivided in bins of hit-multiplicity using a "relative multiplicity" quantity:

$$n_{\mathrm{rel}} = \frac{1}{4}\left(\frac{n_{\mathrm{VELO}}}{\langle n_{\mathrm{VELO}}\rangle} + \frac{n_{\mathrm{TT}}}{\langle n_{\mathrm{TT}}\rangle} + \frac{n_{\mathrm{IT}}}{\langle n_{\mathrm{IT}}\rangle} + \frac{n_{\mathrm{OT}}}{\langle n_{\mathrm{OT}}\rangle}\right)$$

where n_i is the number of hits in the corresponding subdetector. Figure 7.12 shows the track reconstruction efficiency and ghost rate for events classified according to this quantity for long tracks with $p > 5\,\mathrm{GeV}/c$. For multiplicity variations within a factor of two the track reconstruction efficiency and ghost rate are seen to depend linearly on the total number of hits in the tracking detectors, according to the following parametrizations:

$$\begin{aligned} 1 - \text{efficiency} &= 0.048 + 0.026\, n_{\mathrm{rel}} \\ \text{ghost rate} &= 0.040\, n_{\mathrm{rel}} \end{aligned}$$

These parametrizations imply that a multiplicity increase of a factor of two would lead to a 30% increase in track reconstruction inefficiency and a ghost rate increase of a factor of two.

Apart from the global robustness test, additional dedicated simulation studies reported in [91] and [92] have been made to study the tracking performance as function of individual detector parameters (such as detector efficiency, noise and cross-talk). From these studies the following conclusions have been drawn:

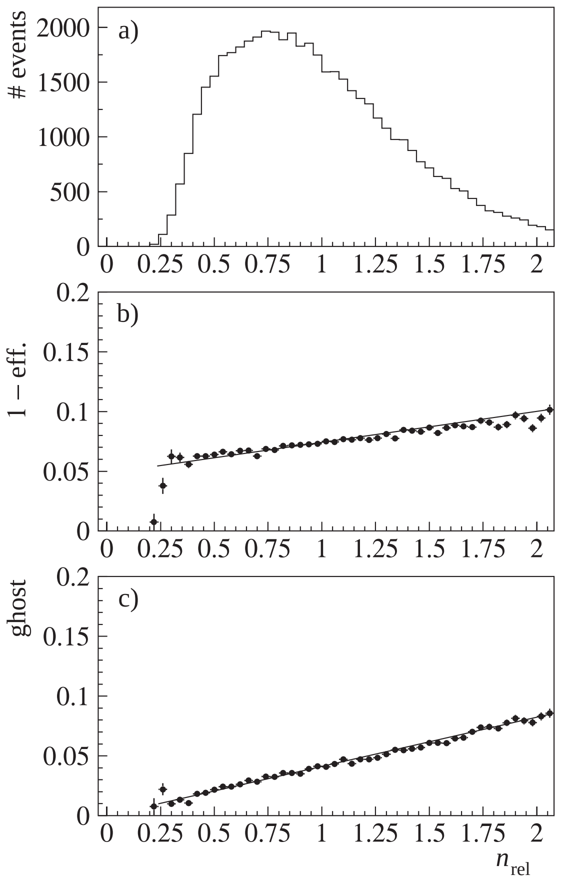

Figure 7.12: Track reconstruction performance as a function of the number of hits in the tracking detectors. (a) Distribution of the quantity n_{rel}, (b) track reconstruction efficiency for tracks with $p > 5\,\mathrm{GeV}/c$ versus n_{rel}, (c) ghost rate as function of n_{rel}.

1. The track reconstruction efficiency depends relatively mildly on the hit detection efficiency of the tracking detectors. The VELO track reconstruction efficiency is observed to reduce by 0.7%, 1.5%, 2.5% or 4.7% if the detection efficiency of the silicon detectors is reduced by 1%, 2%, 3%, 5% respectively. For the reconstruction of long tracks the performance is stable for additional detector inefficiencies in the Inner Tracker and Outer Tracker up to ∼ 10% [91, 92].

2. The effect of additional detector hits in the Outer Tracker due to electronic noise or cross-talk has little effect on tracking, even for relatively high values of 1 MHz noise rate per straw and 20% cross-talk. [92].

3. Degrading the detector resolution in the Outer Tracker from 200 μm to 300 μm does not significantly affect the reconstruction efficiency, while it leads to a 20% relative increase in the ghost rate [92].

Chapter 8 Particle Identification

8.1 Introduction

Particle identification within LHCb is provided by the two RICH detectors, the Calorimeter system and the Muon Detector. For the common charged particle types $(\mathrm{e}, \mu, \pi, \mathrm{K}, \mathrm{p})$, electrons are primarily identified using the Calorimeter system, muons with the Muon Detector, and the hadrons with the RICH system. However, the RICH detectors can also help improve the lepton identification, so the information from the various detectors is combined. Neutral electromagnetic particles (γ, π^0) are identified using the Calorimeter system, where the $\pi^0 \rightarrow \gamma\gamma$ may be resolved as two separate photons, or as a merged cluster. Finally $\mathrm{K_S^0}$ are reconstructed from their decay $\mathrm{K_S^0} \rightarrow \pi^+\pi^-$. These various particle identification techniques are described in this chapter.

8.2 RICH reconstruction

Details of the RICH system can be found in its TDR [7]. The design of RICH 1 has been modified as a consequence of the reoptimization of LHCb, and the new design is described in Chapter 4. The performance results presented here, and used for the physics analyses in this document, have been produced using a simulation that includes the modified design of RICH 1. Local magnetic shielding has to be provided for the RICH photon detectors, and this has been achieved by adjusting the optics, introducing a second (flat) mirror in a similar fashion to RICH 2. This new optical layout leads to a slight reduction in the number of detected photoelectrons per track from the gas radiator of RICH 1, as shown in Table 8.1. This is due to the ~ 90% reflectivity of the extra mirror. A similar effect is not seen in the number of detected photoelectrons from aerogel, as the reoptimized optical layout has allowed a larger fraction of the aerogel image to be covered for the same overall size of photodetector plane. For RICH 2 the expected increase is observed from the 20% extension of the radiator length that was introduced between the TDR and EDR [32]. The angular resolution per photoelectron has not changed significantly since the RICH TDR.

Table 8.1: Average number of detected photoelectrons per saturated track in the three RICH radiators, compared to the number in the RICH TDR, and resolution on the Cherenkov angle per photoelectron.

Radiator	N_{pe}	N_{pe} (TDR)	$\sigma(\theta_{\mathrm{C}})$
Aerogel	6.8	6.6	1.9 mrad
$\mathrm{C_4F_{10}}$ gas	30.3	32.7	1.3 mrad
$\mathrm{CF_4}$ gas	23.2	18.4	0.7 mrad

Particle identification with the RICH system is performed as follows. The pattern of hit pixels observed in the RICH photodetectors is compared to the pattern that would be expected under a given set of mass hypotheses for the reconstructed tracks passing through the detectors, using the knowledge of the RICH optics. A likelihood is determined from this comparison, and then the track mass-hypotheses are varied so as to maximise the likelihood. In the high track multiplicity environment typical of LHCb events, the main source of background photons in the RICH detectors is from neighbouring tracks. By maximising the global likelihood for all found tracks, this background is optimally controlled. Details of the method can be found elsewhere [93].

Full pattern recognition is now in place for all steps of the event reconstruction. Thus the quality of the reconstructed tracks includes the effects of imperfect assignment of hits to tracks and of ghost tracks. All expected backgrounds have been included in the simulation of the RICH system response. These include the effect of Rayleigh scattering of light generated in the aerogel, hits from tracks that point towards the photodetector plane, and Cherenkov light produced by tracks that traverse the windows of the photodetectors. The response of the photodetectors themselves is simulated in detail. For the results presented here, the HPD photodetector was used [94]. However it has been verified that the multianode photomulti-

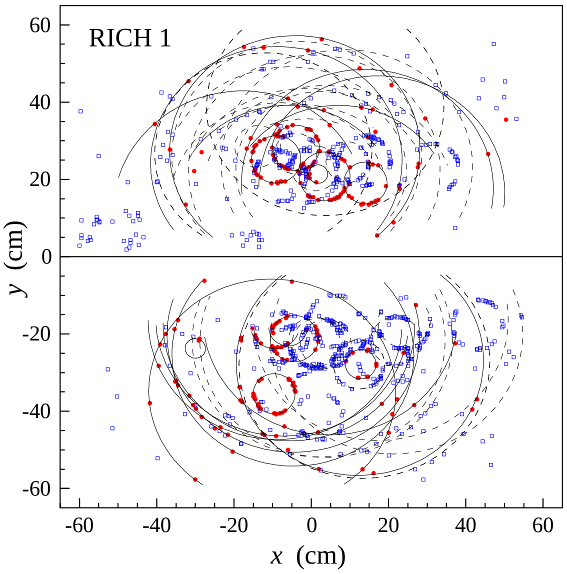

Figure 8.1: Event display of the detected photoelectrons for a typical event in RICH 1, with all background sources included and with detailed photodetector simulation. The two detector plane halves are drawn next to each other, and fitted rings are superimposed, indicated by solid lines for rings from long tracks and dashed lines for other tracks.

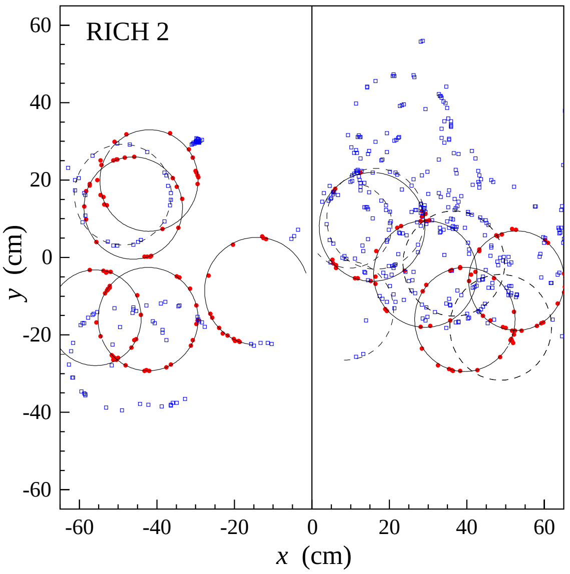

Figure 8.2: Event display of the detected photoelectrons for a typical event in RICH 2, for the same event as in Fig. 8.1.

plier [95] gives equivalent physics performance [34]. An event display of the photodetector hits in a typical event is shown for RICH 1 in Fig. 8.1 and for RICH 2 in Fig. 8.2. For RICH 1, densely-populated small diameter rings can be seen from the C_4F_{10} gas radiator, as well as the more sparsely-populated large diameter rings from the aerogel.

To study the performance of the RICH system, “long” tracks (passing through the full spectrometer, as defined in Chapter 7) have been studied in a sample of $B_s^0 \to D_s^- K^+$ events. The ratio of likelihoods between assuming the pion and kaon hypothesis in the RICH analysis is determined. This is equivalent to a difference in log-likelihood:

$$\begin{aligned} \Delta \ln \mathcal{L}_{K\pi} &= \ln \mathcal{L}(K) - \ln \mathcal{L}(\pi) \qquad (8.1) \\ &= \ln [\mathcal{L}(K)/\mathcal{L}(\pi)] \ , \end{aligned}$$

which is plotted in Fig. 8.3 for tracks that have been matched to true kaons and pions. As can be seen, $\Delta \ln \mathcal{L}_{K\pi}$ tends to have positive values for kaons, with a double-peaked structure that is due to the momentum-dependence of the π–K separation of the RICH system, whilst pions tend to have negative values. The log-likelihood difference can be converted into the significance of π–K separation, $N_\sigma = \sqrt{2\,|\Delta \ln \mathcal{L}|}$, signed according to $\Delta \ln \mathcal{L}$. The distribution of this significance can be seen as a function of momentum in Fig. 8.4, for tracks matched to true pions. The few negative entries correspond to tracks for which the kaon hypothesis was preferred over the pion hypothesis. The average of this distribution is superimposed, and illustrates that substantial π–K separation is achieved over most of the momentum range of interest, $2 < p < 100\,\mathrm{GeV}/c$.

Care should be taken when interpreting such π–

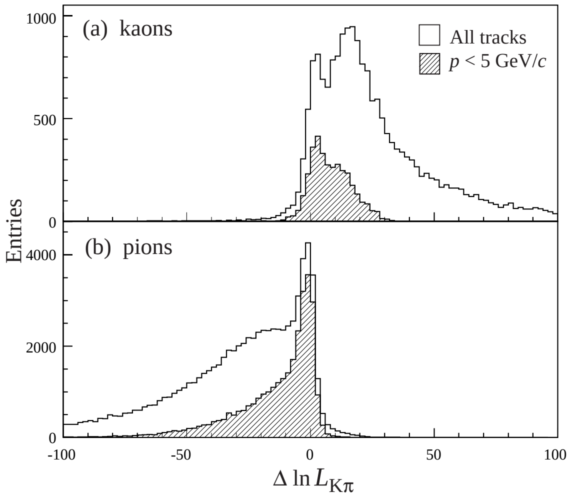

Figure 8.3: Difference in log-likelihood between the kaon and pion hypotheses from the RICH system, for (a) kaons and (b) pions, in a sample of $B_s^0 \to D_s^- K^+$ events; the shaded histograms are for low momentum tracks.

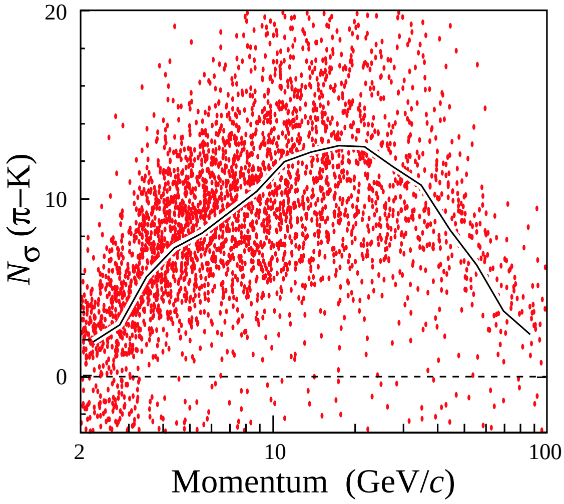

Figure 8.4: π–K separation in sigma as a function of momentum for true pions, for each track in a sample of $\mathrm{B}^0 \to \pi^+\pi^-$ events. The average π–K separation is superimposed as a line.

K separation figures, as the behaviour is not Gaussian, as is evident from Fig. 8.4. More relevant is the performance expressed as the efficiency for reconstructing kaons, viewed in conjunction with the misidentification rate for pions. Tracks are identified here according to their maximum-likelihood hypothesis. For the kaon efficiency, shown in Fig. 8.5, the effect of crossing the thresholds for Cherenkov light production in the three radiators is evident at $p \sim 2$, 9 and 16 GeV/c. The average efficiency for kaon identification between 2 and 100 GeV/c is 88%. The pion misidentification rate, $\epsilon(\pi \to \mathrm{K})$, is also shown in Fig. 8.5. The average pion misidentification rate between 2 and 100 GeV/c is 3%.

By changing the cut on $\Delta \ln \mathcal{L}_{\mathrm{K}\pi}$ used to separate kaons from pions, the misidentification rate of pions can be reduced (thus improving the purity of the selected sample) at the cost of reduction of the kaon identification efficiency. As an example, the efficiency and misidentification rates are shown in Fig. 8.6, for a tighter cut of $\Delta \ln \mathcal{L}_{\mathrm{K}\pi} > 4$, illustrating that the misidentification rate can be reduced by a factor of 3 for a modest loss of efficiency ($\sim 6\%$, averaged over momentum). The trade-off between efficiency and purity can be adjusted according to the needs of the individual physics analyses. Representative values are listed in Table 8.2. Tuning the cut in each bin of momentum to reproduce the pion misidentification rate that was quoted at the time of the RICH TDR [34], the kaon efficiency is now 5–10% lower than at that time. This is ascribed to the greater realism that is now present in the simulation.

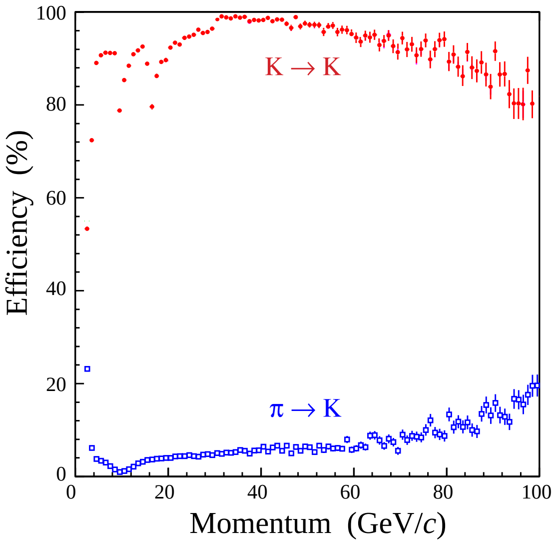

Figure 8.5: Kaon identification efficiency (solid points) and pion misidentification rate (open points) as a function of momentum. For this figure tracks are selected as kaons if their maximum-likelihood hypothesis kaon or heavier, and as pions if it is pion or lighter.

Applying a cut of $\Delta \ln \mathcal{L}_{\mathrm{K}\pi} > 2$ to the long tracks in a sample of $\mathrm{B}_s^0 \to \mathrm{D}_s^- \mathrm{K}^+$ events, the selected sample comprises 62% kaons, 10% pions and 22% protons (the remainder being leptons or ghosts). To suppress the proton background, a cut

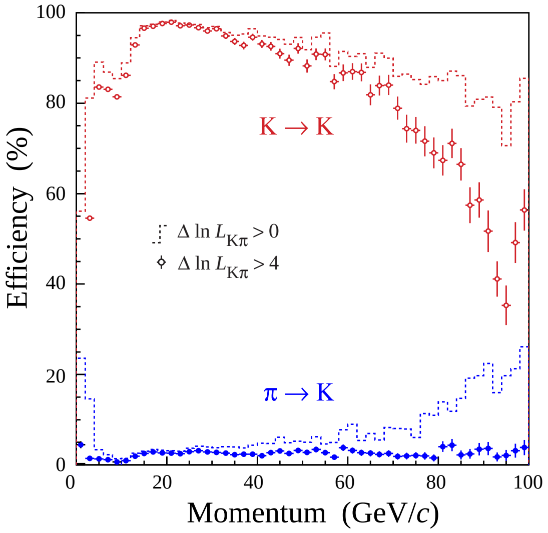

Figure 8.6: Kaon identification efficiency and pion misidentification rate as a function of momentum, for two different values of the $\Delta \ln \mathcal{L}_{\mathrm{K}\pi}$ cut, indicated by the histograms and points respectively.

Table 8.2: Effect of varying the cut on $\Delta \ln \mathcal{L}_{\mathrm{K}\pi}$ on the average kaon selection efficiency and pion misidentification rate.

$\Delta \ln \mathcal{L}_{\mathrm{K}\pi}$	$\epsilon(\mathrm{K})$	$\epsilon(\pi \to \mathrm{K})$
> 0	91%	5.6%
> 2	88%	2.9%
> 4	85%	1.7%
> 8	79%	0.8%

can be made on $\Delta \ln \mathcal{L}_{\mathrm{Kp}}$, shown in Fig. 8.7. Requiring $\Delta \ln \mathcal{L}_{\mathrm{Kp}} > -2$ reduces the proton contamination by a factor two, for only a 3% loss of kaon efficiency.

This performance is achieved with the use of all classes of tracks discussed in Chapter 7, including in particular the upstream tracks that do not have hits in stations T1–T3: these help in the description of the observed photon distributions in RICH 1. The particle identification performance is quoted for long tracks, though, as these are the tracks which are of most interest for physics studies, and the RICH reconstruction was tuned for these tracks.

The RICH reconstruction programme used for the analyses presented in this document, written in FORTRAN, has been rewritten in object-oriented C^{++}. The performance of the new reconstruction code [96] now matches that of the original, and in addition particle identification is now available for the upstream tracks, as shown in Fig. 8.8. Although less powerful than the identification of long tracks, this is expected to give significant improvement in those analyses which should profit from upstream tracks, such as kaon tagging and D* reconstruction.

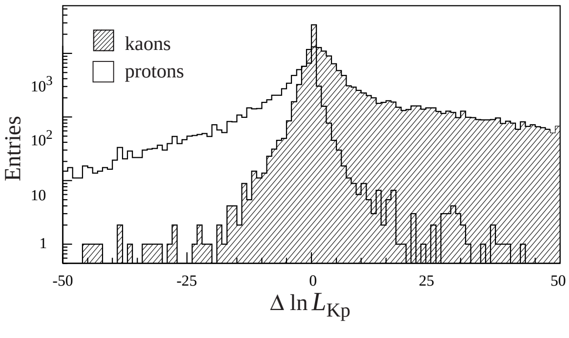

Figure 8.7: Difference in log-likelihood between the proton and kaon hypotheses from the RICH system, for kaons and protons in a sample of $\mathrm{B_s^0} \to \mathrm{D_s^- K^+}$ events.

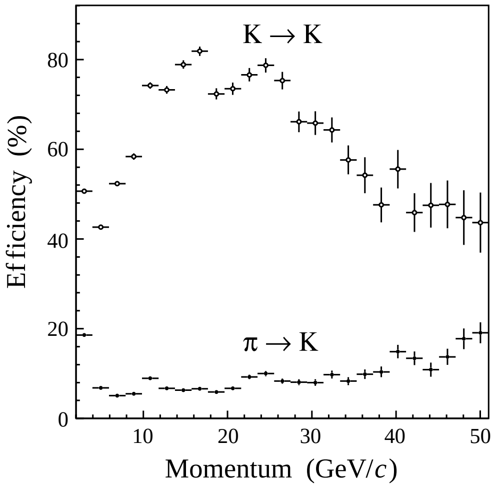

Figure 8.8: Kaon efficiency (open points) and pion misidentification rate (solid points) as a function of momentum, for upstream tracks for which the maximum-likelihood hypothesis is kaon.

8.3 Combined particle identification

Lepton identification with the Muon and Calorimeter systems will be described in the following sections. However, the RICH system also provides some separation between leptons and hadrons, which can be used to improve the overall particle identification performance. This is illustrated in Fig. 8.9, which shows the value of $\Delta \ln \mathcal{L}_{\mathrm{e}\pi}$ from the RICH for electron candidates that have been selected using the Calorimeter information. The true electrons predominantly have positive values of this log-likelihood difference. To utilise this information in the combined particle identification, all the Calorimeter and Muon system estimators for lepton identification are now also expressed as likelihood ratios. In the case of electron identification in the Calorimeter system, it is the ratio of likelihood between the electron and background (non-electron) hypotheses that is determined, whilst for the Muon Detector it is the ratio between muon and non-muon hypotheses. Then the likelihoods from the various detectors are simply combined as follows:

$$\begin{aligned}
\mathcal{L}(\mathrm{e}) &= \mathcal{L}^{\mathrm{RICH}}(\mathrm{e})\,\mathcal{L}^{\mathrm{CALO}}(\mathrm{e})\,\mathcal{L}^{\mathrm{MUON}}(\mathrm{non}\,\mu) \\
\mathcal{L}(\mu) &= \mathcal{L}^{\mathrm{RICH}}(\mu)\,\mathcal{L}^{\mathrm{CALO}}(\mathrm{non\,e})\,\mathcal{L}^{\mathrm{MUON}}(\mu) \\
\mathcal{L}(h) &= \mathcal{L}^{\mathrm{RICH}}(h)\,\mathcal{L}^{\mathrm{CALO}}(\mathrm{non\,e})\,\mathcal{L}^{\mathrm{MUON}}(\mathrm{non}\,\mu)\ ,
\end{aligned}$$

where h represents a hadron. Furthermore, if there is more than one estimator from a given detector, they can be simply combined by taking the product of their individual likelihoods.

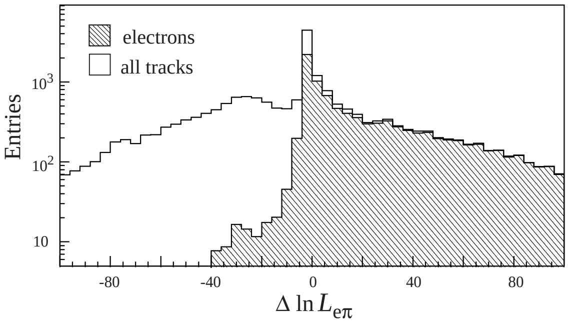

Figure 8.9: $\Delta \ln \mathcal{L}_{e\pi}$ from the RICH system for electron candidates selected using the Calorimeter system, in a sample of $B^0 \to J/\psi(e^+e^-)\,K^0_S$ events.

8.4 Muon identification

Muons are identified by extrapolating well reconstructed tracks with $p > 3$ GeV/c into the Muon stations. The tracks must be within the M2 and M5 acceptance. For details see the Muon Detector TDR [9].

Muon Detector hits are searched within fields of interest (FOI) around the extrapolation point in each station, parametrized as function of momenta for each station and region. A track is considered a muon candidate when a minimum number of stations have hits in their corresponding FOI's, as shown in Table 8.3. This number was optimized to maintain high efficiency.

Using single muons generated with a flat distribution both in momentum (between 1 and 200 GeV/c) and in polar angle, the FOI were parametrized from plots of $(x(y)_{\mathrm{MC}} - x(y)_{\mathrm{hit}})/d$ for x and y in each station region, where d is the pad size, according to the parametrization FOI $= a + b\,\mathrm{e}^{(-cp)}$ [97]. The strategy used to tune the FOI's was based on maximising the efficiency while maintaining reasonable levels of pion misidentification. Those remaining pions can then be eliminated with discriminating variables or analysis cuts. Using a sample of $B^0 \to J/\psi\,K^0_S$ the performance was measured to be $\epsilon(\mu) = 94.3 \pm 0.3\%$ and $\epsilon(\pi \to \mu) = 2.9 \pm 0.1\%$. The efficiency is a flat function of the momentum, above 10 GeV/c, as shown in Fig. 8.10.

Table 8.3: Stations that must have hits in their FOI, for the selection of a muon candidate, as a function of the track momentum.

Momentum (GeV/c)	Muon stations
$3 < p < 6$	M2 + M3
$6 < p < 10$	M2 + M3 + (M4 or M5)
$p > 10$	M2 + M3 + M4 + M5

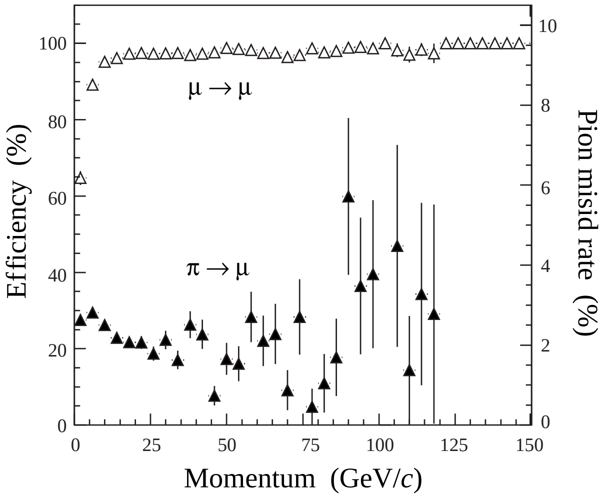

Figure 8.10: Muon efficiency (open triangles), and the pion misidentification rate (solid triangles, with scale on the right) as a function of track momentum.

Discriminating variables to help further improve the muon selection purity are constructed from the comparison of slopes in the muon system and the main tracker, and from the average track-hit distance of all hits in FOI's associated to the track. The probability distributions of these variables are shown in Fig. 8.11. For each track the difference in log-likelihood between the muon hypothesis and pion hypothesis is determined, and summed with the values from the RICH and Calorimeter systems (if available). The

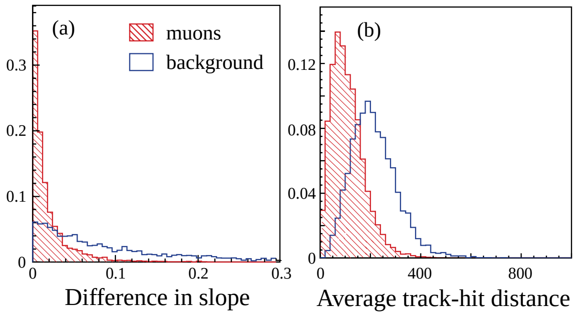

Figure 8.11: Variables used to construct the muon identification estimators: (a) the comparison of slopes in the Muon Detector and the main tracker, (b) the average track–hit distance for all hits in FOI's; the distributions are shown for muons (shaded) and pions (open histogram).

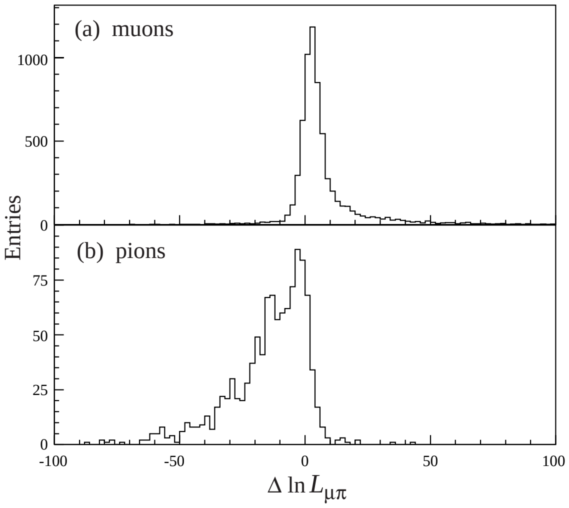

Figure 8.12: Difference in log-likelihood between muon and pion hypotheses, for tracks with Muon Detector information in a sample of $B^0 \rightarrow J/\psi(\mu^+\mu^-)\,K^0_S$ events: (a) muons, (b) pions.

resulting distributions of $\Delta \ln \mathcal{L}_{\mu\pi}$ are shown in Fig. 8.12. Requiring $\Delta \ln \mathcal{L}_{\mu\pi} > -8$ reduces the pion misidentification rate to 1%, whilst maintaining a muon efficiency of 93%, for muons above $3\,\mathrm{GeV}/c$ inside the Muon Detector acceptance. Averaged over all long tracks matched to muons from $B^0 \rightarrow J/\psi(\mu^+\mu^-)\,K^0_S$ decays, the efficiency is 80%.

The high purity that can be achieved with such cuts is illustrated in Fig. 8.13 (a), where the $\mu^+\mu^-$ mass plot is shown at the first step in the analysis of $B^0_s \rightarrow J/\psi\,\phi$ events, taking all oppositely-charged pairs of tracks from signal events that pass the muon identification requirements. As can be seen, a clean J/ψ mass peak is reconstructed with a resolution of about $13\,\mathrm{MeV}/c^2$.

8.5 Electron identification

The electromagnetic calorimeter, ECAL, plays an important role in electron identification [98]. The major ECAL estimator χ^2_e is constructed as a χ^2 of a global matching procedure, which includes the balance of track momentum and the energy of the charged cluster in the ECAL, shown in Fig. 8.14, and the matching between the corrected barycenter position of the cluster with the extrapolated track impact point. Charged clusters are defined as those for which the estimator χ^2_γ defined in Sect. 8.6 satisfies $\chi^2_\gamma < 49$. The distribution of χ^2_e is shown in Fig. 8.15 (a).

A second estimator provided by ECAL is related to the Bremsstrahlung photons emitted by electrons before the magnet. As there is little material within the magnet, such neutral clusters are expected in a well defined position given by the electron track extrapolation from before the magnet, as illustrated in Fig. 8.16. A χ^2 is calculated of the track extrapolation from before the magnet to ECAL and the neutral cluster matching, shown in Fig. 8.15 (b). This estimator is also used in the Bremsstrahlung photon recovery.

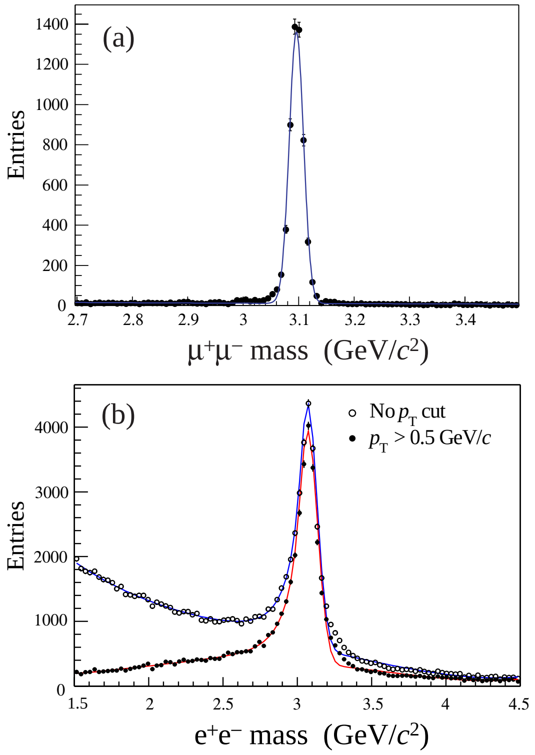

Figure 8.13: Invariant mass plots for the reconstruction of $J/\psi \rightarrow \ell^+\ell^-$ decays in $B^0_s \rightarrow J/\psi\,\phi$ signal events: (a) for $\ell = \mu$, (b) for $\ell = e$, where the open points are before any p_T cut, and the solid points are after requiring $p_T > 0.5\,\mathrm{GeV}/c$ for the $e^\pm$ candidates.

Further improvement in electron identification is made by using the track energy deposition in the Preshower detector, as shown in Fig. 8.15 (c), and the deposition of the energy along the extrapolated particle trajectory in the hadronic calorimeter, HCAL, shown in Fig. 8.15 (d).

To combine these various sources of information, likelihood distributions are constructed. Reference two-dimensional histograms are filled with the variables described above, versus momentum, using samples containing a selection of physics channels, and inclusive $b\bar{b}$ events. Two histograms are filled, one for tracks that are matched to true electrons and the other for non-electron tracks

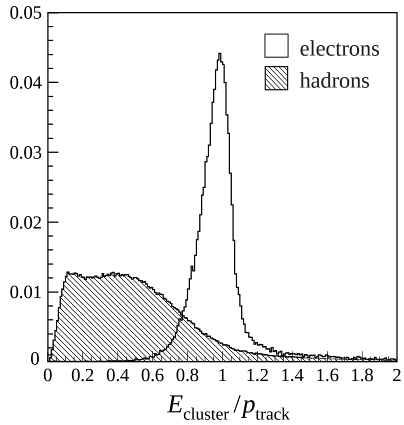

Figure 8.14: The ratio of uncorrected energy of the charged cluster in ECAL to the momentum of reconstructed tracks for electrons (open histogram) and hadrons (shaded histogram).

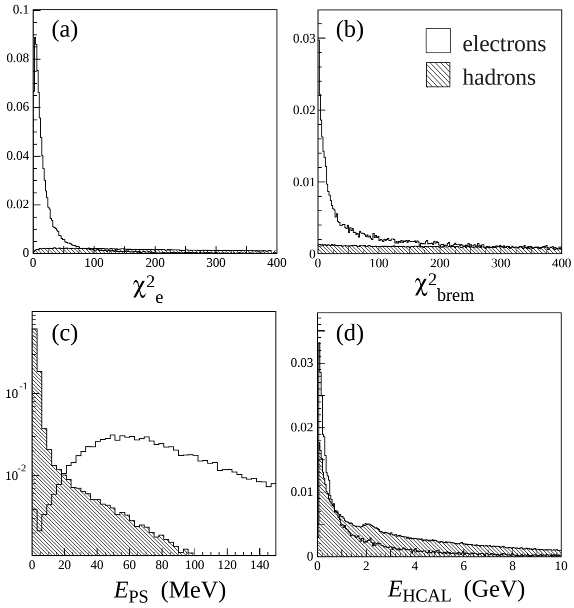

Figure 8.15: Electron identification estimators: (a) the value for the χ^2_{e} estimator for track-cluster energy/position matching procedure for reconstructed tracks and charged clusters in ECAL, (b) the value of the χ^2_{brem} estimator, (c) the energy deposited in the Preshower, and (d) the deposition of the energy along the extrapolated particle trajectory in the hadron calorimeter. The track sample for these plots was taken from a selection of B-decay channels, and the shaded component labelled "hadrons" also includes the muons from that sample; the electron and hadron distributions are normalised (including overflows).

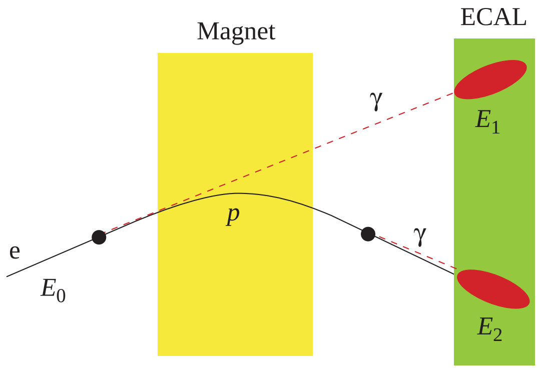

Figure 8.16: Schematic illustration of Bremsstrahlung correction. An electron may radiate photons when passing through material before or after the magnet: in the first case, a well defined cluster is seen in the ECAL, with energy E_1, whilst in the second case the Bremsstrahlung energy forms part of the electron cluster with energy E_2; for electron identification $E_2 = p$, the momentum measured in the spectrometer, while the energy of the electron at the origin, $E_0 = E_1 + E_2$.

(ghosts are ignored). After normalisation the histograms provide the likelihood distributions for electrons and background. For a given track, the difference of log-likelihood for the electron and non-electron hypotheses are computed, and summed for the different variables. Finally, the Calorimeter information is combined with the RICH and Muon detectors, as described Sect. 8.3, significantly improving the electron identification performance. The log-likelihood difference $\Delta \ln \mathcal{L}_{e\pi}$ is shown in Fig. 8.17, for tracks that have information available from the Calorimeter system.

To illustrate the performance of electron identification, the J/ψ mass plot is shown as the open points in Fig. 8.13 (b). The signal is fit with a function including a radiative tail, to account for the imperfect correction of Bremsstrahlung. The background is larger than in the muon channel, and is either due to real (secondary) electrons, or due to one of the pair of tracks being a ghost track; the contribution from misidentified hadrons is very small. These background tracks are dominantly of low p_{T}, and can be efficiently rejected by applying the requirement $p_{\mathrm{T}} > 0.5\,\mathrm{GeV}/c$ for the electron candidates, as shown by the solid points in Fig. 8.13 (b).

The average efficiency to identify electrons in the calorimeter acceptance from $J/\psi \rightarrow e^+e^-$ decays in $B^0 \rightarrow J/\psi K^0_S$ events is 95%, for a pion misidentification rate of 0.7%, as shown in

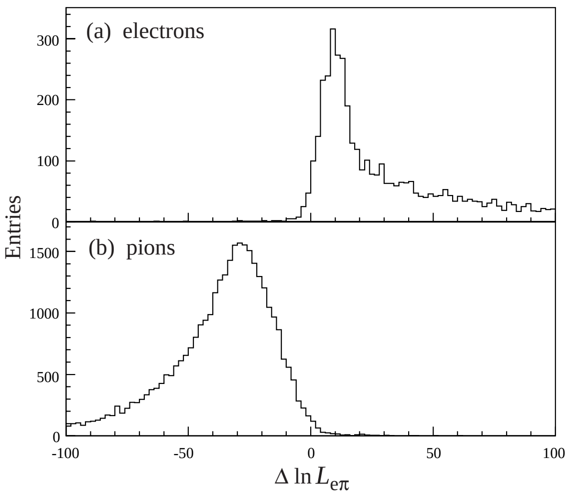

Figure 8.17: Difference in log-likelihood between the electron and pion hypotheses, for tracks with Calorimeter information in a sample of $B^0 \to J/\psi(e^+e^-)\,K^0_S$ events: (a) electrons, (b) pions.

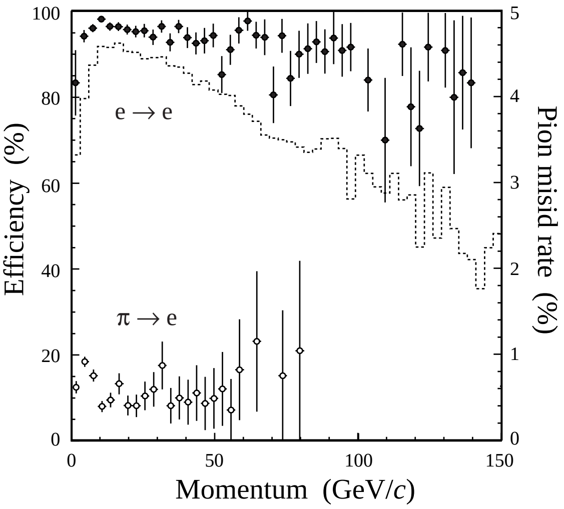

Figure 8.18: Efficiency for electron identification, after requiring $\Delta \ln \mathcal{L}_{e\pi} > 0$, as a function of momentum. The solid points are for electrons within the Calorimeter acceptance, the dotted histogram for all electrons from J/ψ decays. The pion misidentification rate is indicated by the open points, with scale on the right.

Fig. 8.18. Without the requirement that the electron is within the calorimeter acceptance, the average efficiency drops to 81%, as indicated by the histogram in the figure; this is largely due to the inner hole around the beam pipe, which leads to a drop of efficiency with momentum as high-momentum tracks tend to be at low angle.

8.6 Photon identification

Photons are reconstructed and identified with the electromagnetic calorimeter, ECAL, as neutral clusters [8]. ECAL clusters are created with a "Cellular Automaton" algorithm [99] and are tested for matching with all reconstructed tracks. The tracks are extrapolated to the ECAL face, and the positions of the track impact point and cluster barycenter, together with the track's covariance matrix and the matrix of second-order cluster moments, are used to construct a cluster-track position matching estimator, χ^2_γ. The minimal value of the χ^2_γ estimator for each cluster is shown in Fig. 8.19. The clusters due to charged tracks are clearly identified as a peak at a small value of χ^2_γ. Clusters with $\chi^2_\gamma > 4$ are selected as photon candidates. The background (mainly hadrons) is large, and this cut removes a large part of it. The remaining photon background has low p_T and in the cases of the $B^0 \to \pi^+\pi^-\pi^0$ and $B^0 \to K^*\gamma$ analyses no other photon identification criteria are required. In $B^0 \to \pi^+\pi^-\pi^0$ decays the incorrect π^0 reconstruction is due to combinatorial background of real photons or fragmentation π^0, rather than the pairing of background clusters.

For the precise evaluation of the energy and position of photon candidates at the ECAL face several effects are taken into account [100]:

1. The energy losses in the material before the ECAL face, in particular in the lead absorber of the Preshower detector.
2. The energy losses in the passive material between ECAL modules. The correction is estimated using the evaluated position of photon candidate within the ECAL cell.
3. The longitudinal and transversal shape of the electromagnetic shower is used for evaluation of energy and position corrections.

The identification of photons converted in the passive material of the apparatus after the magnet, e.g. RICH 2 or M1, is based on whether there is a hit in the SPD cell that lies in front of central cell of the ECAL cluster. Seventy percent of reconstructed photons from $B^0 \to K^*\gamma$ decays are selected as non-converted photons, while the remaining photons are identified as converted photons, with correct assignment fractions of 90% and 79% respectively.

A cut on the energy deposition in the Preshower detector can improve the purity of selected samples both for converted and non-converted photons [100]

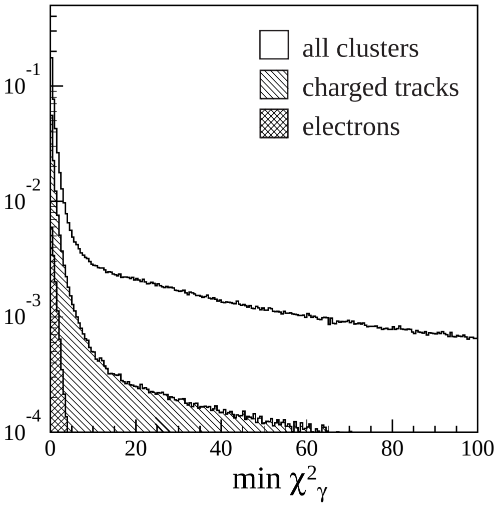

Figure 8.19: The minimal value of the χ^2_γ estimator from the track-cluster position matching procedure for ECAL clusters. The peak at small values of χ^2_γ corresponds to clusters due to charged particles, as indicated by the hatched distribution; the distribution for electrons is shown cross-hatched.

and could be used for analyses requiring reconstruction of medium p_{T} photons or π^0, where part of the background comes from hadron clusters.

8.7 π^0 reconstruction

Neutral pion reconstruction has focussed on the $B^0 \to \pi^+\pi^-\pi^0$ decay channel, for which the mean transverse momentum of the π^0 is about $3\,\mathrm{GeV}/c$. Below this value the π^0 are mostly reconstructed as a resolved pair of well separated photons, while for higher p_{T} a large fraction of the pairs of photons coming from the decay of the π^0 cannot be resolved as a pair of clusters within the ECAL granularity. About 30% of the reconstructible π^0 from $B^0 \to \pi^+\pi^-\pi^0$ lead to a single cluster, referred to as a merged π^0.

8.7.1 Resolved π^0

Photon candidates with $p_{\mathrm{T}} > 200\,\mathrm{MeV}/c$ are paired to reconstruct resolved π^0. Figure 8.20 shows the mass distributions obtained in the cases where both photon candidates reached the calorimeter (a), or one converted before the calorimeter (b), according to the SPD signal. The contributions of true π^0 is roughly 20% of the distribution in the range $105 < m_{\pi^0} < 165\,\mathrm{MeV}/c^2$, the remaining contribution being due to background cluster pairings and γ combinatorial background.

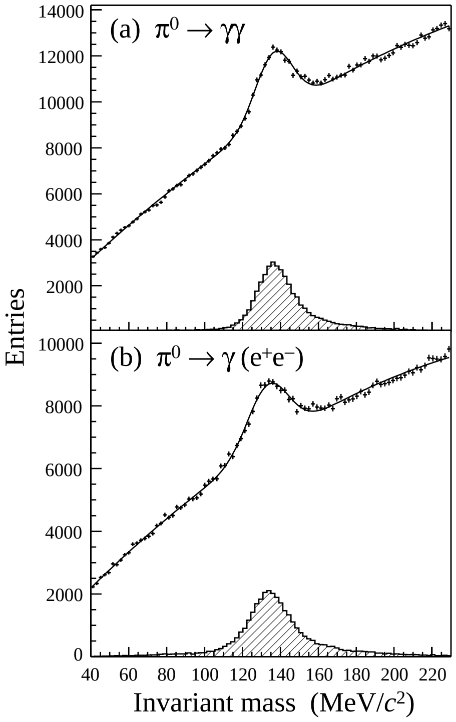

Figure 8.20: π^0 mass distributions, where (a) neither photon has converted, (b) one γ converted before the calorimeter. The separation converted/not-converted is obtained from the SPD information. The contributions of true π^0 are indicated by the shaded histograms.

The distributions are fitted with the sum of a Gaussian and a polynomial function, giving a resolution for the π^0 mass of $\sigma = 10\,\mathrm{MeV}/c^2$.

8.7.2 Merged π^0

An algorithm has been developed to disentangle a potential pair of photons merged into a single cluster. The energy of each cell of the cluster is shared between two virtual sub-clusters according to an iterative procedure based on the expected transverse shape of photon showers. Each of the two sub-clusters is then reconstructed as coming from a photon, as for isolated photons. This method allows the photons' energy and direction to be corrected for detector effects, and has been shown to perform better than an analytical method based on the moment analysis of the cluster shape, which relies on shower symmetries.

The reconstructed invariant mass obtained from all single clusters in $B^0 \to \pi^+\pi^-\pi^0$ events is shown in Fig. 8.21 (a). The bump around the π^0 mass is from merged pairs of photons. The same distribution for the clusters associated to the π^0 from B^0

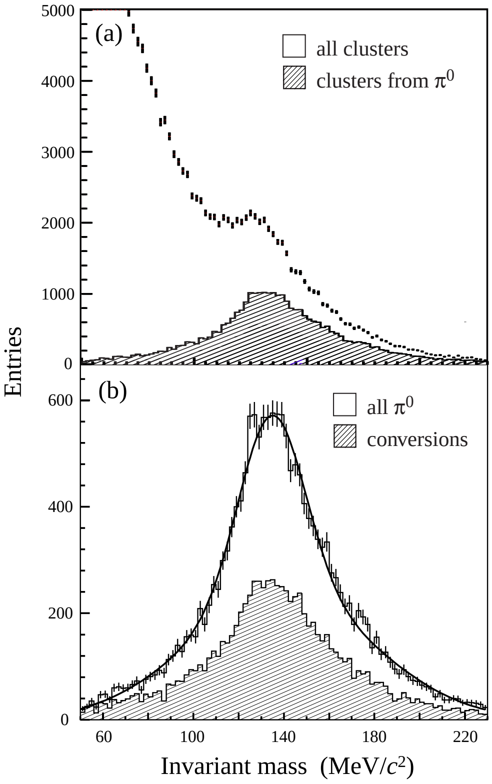

Figure 8.21: Invariant mass obtained with the merged π^0 algorithm (a) for all clusters in $\mathrm{B}^0 \to \pi^+\pi^-\pi^0$ events, where the shaded histogram indicates the contribution from true π^0, and (b) for clusters associated to true π^0 from B^0 decays, where the shaded histogram indicates the contribution from pairs of photons with at least one conversion.

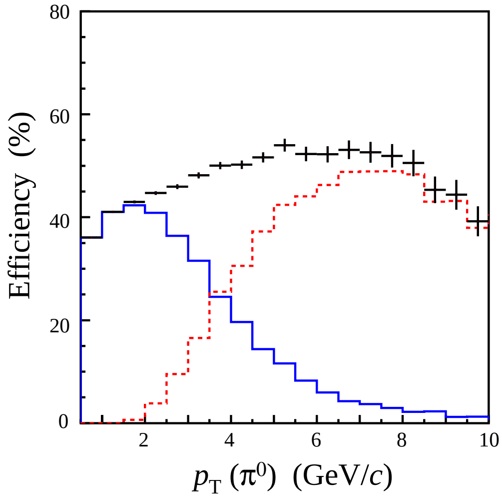

Figure 8.22: The reconstruction efficiency for π^0 that give photons inside the geometrical acceptance with $p_\mathrm{T} > 200\,\mathrm{MeV}/c$, versus the π^0 transverse momentum. The separate contributions from resolved and merged π^0 reconstruction are indicated by the solid and dashed histograms, respectively.

decay is shown in (b). The distribution is fit with two Gaussians, to account for the broadening of the resolution due to photon conversion. A core resolution of about $15\,\mathrm{MeV}/c^2$ is obtained. The reconstruction of the 4-momentum of merged π^0 is competitive with the resolved configuration, with an angular resolution of better than 1 mrad for merged π^0 above 20 GeV.

As seen in Fig. 8.21 (a), the merged π^0 have to be identified within a large combinatorial background. This is achieved by applying the following criteria:

1. The cluster has to be neutral, i.e. its position is required not to coincide with a charged track. The χ^2_γ of the cluster-track matching is required to be greater than unity.

2. The π^0 energy is required to be compatible with a pair of merged photons. A cut is applied on the minimal distance kinematically allowed between the impact on ECAL of the two photons: $d_{\gamma\gamma} = 2\,z_\mathrm{ECAL}\,m_{\pi^0}/E_{\pi^0} < 1.8\,D$, where D is the cell size. This cut is equivalent to an energy cut of 45, 30 and 15 GeV in the inner, middle and outer parts of calorimeter, respectively, and is roughly equivalent to a cut of $p_\mathrm{T} > 2\,\mathrm{GeV}/c$.

3. The invariant mass of merged photons is required to be compatible with the π^0 mass. Due to the fact that the combinatorial continuum decreases with mass, an asymmetric window is applied around the nominal π^0 mass, between 95 and $215\,\mathrm{MeV}/c^2$.

The identification of merged π^0 benefits from several features with respect to the resolved case: the large transverse energy required for the π^0 to be merged; the much lower combinatorial background (~ 60 clusters per event, compared to ~ 2000 pairs); and the fact that identification criteria such as cluster neutrality are applied to a single cluster, while a pair of clusters is involved for resolved π^0 and the corresponding efficiency is then squared. As a consequence of the intrinsic purity of the merged π^0, a reasonably high efficiency can be maintained, as shown in Fig. 8.22.

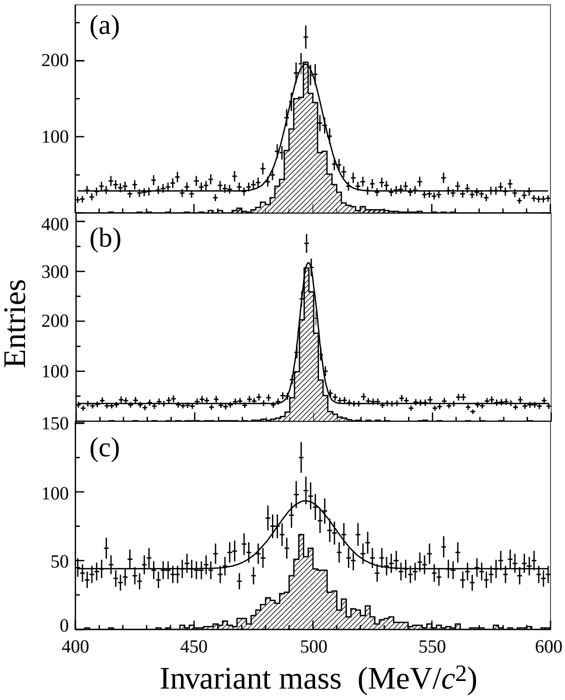

Figure 8.23: Reconstruction of $K^0_S \to \pi^+\pi^-$. The $\pi^+\pi^-$ invariant mass is shown in $B^0 \to J/\psi K^0_S$ signal events, using different categories of tracks for the pion candidates: (a) downstream-downstream, (b) long-long, (c) long-upstream. Combinations coming from a K^0_S are indicated by the shaded histograms.

8.8 K^0_S reconstruction

K^0_S are reconstructed through their decay to $\pi^+\pi^-$. For K^0_S from $B^0 \to J/\psi K^0_S$ decays, about 25% decay inside the active region of the VELO, 50% decay outside the active region of the VELO but upstream of TT, and the rest decay after TT (and will therefore be difficult to reconstruct).

The K^0_S that decay outside the active region of the VELO but before TT are reconstructed using pairs of oppositely-charged downstream tracks, which are found using the hits in the TT and T1–T3 tracking stations, as described in Chapter 7. The tracks are required to be well reconstructed, with $\chi^2/\text{ndf} < 5$, to have an impact-parameter significance greater than 3 with respect to all reconstructed primary vertices, and a cut is applied on the combined particle-identification variable $\Delta \ln \mathcal{L}_{\pi e} > 0$ for each track, to reject electrons. A vertex is formed between the pair of tracks, required to have $\chi^2 < 50$, and the transverse-momentum of the pair is required to exceed 250 MeV/c. The mass of the pair is then calculated, under the assumption that they are both pions, giving the distribution shown in Fig. 8.23 (a).

Table 8.4: Number of reconstructible $K^0_S \to \pi^+\pi^-$ decays N_1, number with both tracks reconstructed N_2, number of K^0_S decays after selection cuts N_3, efficiency $\epsilon = N_3/N_1$, and mass resolution σ, for different categories of track pairs from a sample of 10,000 $B^0 \to J/\psi K^0_S$ decays generated with the B^0 polar angle less than 400 mrad.

Cat.	N_1	N_2	N_3	ϵ (%)	σ (MeV)
DD	1728	1135	927	54	7
LL	704	578	527	75	4
LU	341	248	208	61	12

The pions from K^0_S that decay within the VELO acceptance give either a long track or an upstream track, depending on whether they pass through the magnet to give hits in the downstream tracking stations. They are reconstructed using pairs of oppositely-charged tracks, either long-long or long-upstream, with similar cuts to the downsteam category [101]. The corresponding mass plots are shown in Fig. 8.23 (b) and (c).

The number of reconstructed K^0_S in the various categories from a sample of $B^0 \to J/\psi K^0_S$ decays are listed in Table 8.4. As can be seen in Fig. 8.23 there is some combinatorial background from other tracks in the signal events, particularly for the long-upstream category, but this background is removed by the additional requirements that are imposed when reconstructing the B meson, as will be demonstrated in Chapter 9.

8.9 Robustness studies

Studies have been performed to verify that the particle identification will not be severely degraded in case the event complexity is more severe than suggested by the simulation, or if the intrinsic detector performance is poorer than anticipated.

8.9.1 RICH robustness

The higher the number of rings in the event, the harder it is for the RICH pattern recognition to make the correct association between rings and tracks, leading to a degradation in the particle identification. This dependency has been quantified by evaluating the performance as a function of the track multiplicity in the event. The results are shown in Fig. 8.24, which shows the efficiency of correctly identifying pions and kaons as light or

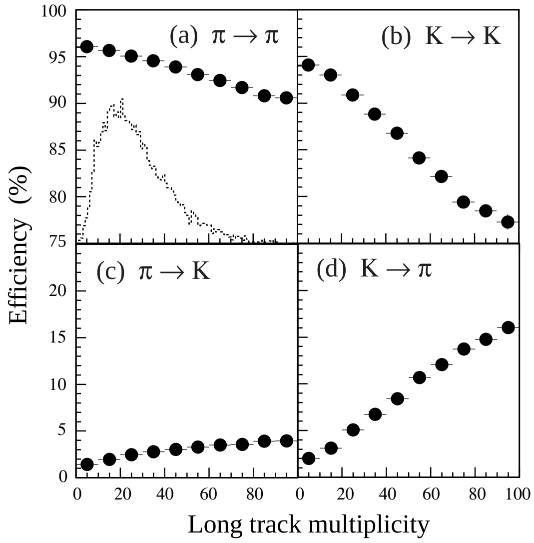

Figure 8.24: Robustness of RICH reconstruction versus long track multiplicity: (a) pion efficiency, (b) kaon efficiency, (c) pion misidentification rate, (d) kaon misidentification rate. The distribution of long track multiplicity for the nominal simulation is superimposed on (a) as a dotted histogram.

heavy particles respectively, and the corresponding misidentification probabilities, as a function of the number of long tracks in the event. As expected, the identification efficiencies are lower for the events with more tracks, with the π efficiency falling by 5% and the K efficiency by 16% over the considered range of 1–100 tracks. In physics events the mean (RMS) number of long tracks is 26 (16). Therefore it can be seen that a factor of two increase in track multiplicity above expectation will induce a loss in kaon efficiency of 5%, with a few percent increase in the pion misidentification rate.

The photoelectron yields shown in Table 8.1 assume that the photodetectors and mirrors work to specification. The consequences of an inferior performance were probed by varying in the simulation the number of detected photons from all three radiators by a common scale factor. The change in performance can be seen in Fig. 8.25 for tracks of low momentum ($2 < p < 10\,\mathrm{GeV}/c$), which are found to be most sensitive to changes in this parameter. In these plots a scale factor of 1 represents the nominal photoelectron yield. A lower yield results in a worse performance as expected, but the dependence is not severe.

Finally, in order to ascertain the global effects on the LHCb physics reach of a degraded detector performance and a more pessimistic set of generator parameters, a special Monte Carlo “global

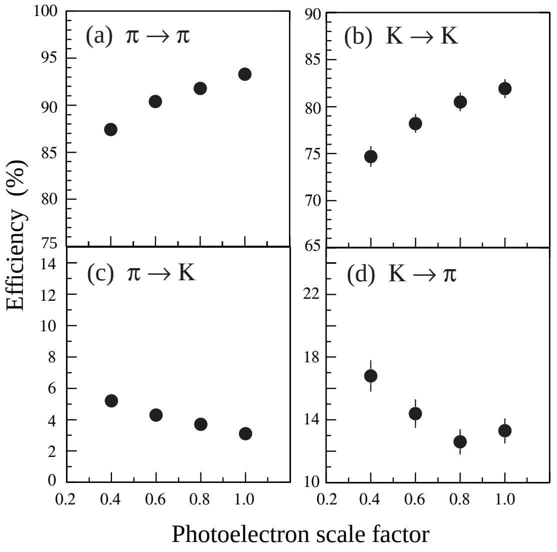

Figure 8.25: Robustness of RICH reconstruction against the scale factor on the number of detected photoelectrons, for low momentum tracks: (a) pion efficiency, (b) kaon efficiency, (c) pion misidentification rate, (d) kaon misidentification rate.

robustness” production was performed. Details of these settings are given in Table 6.2. The modifications specific to the RICH simulation were as follows:

1. A decrease of 20% in efficiency for all photodetectors;
2. The introduction of random noise at the rate of 0.3% per pixel;
3. The smearing of the emission-point error for the RICH 1 gas from 0.7 mrad to 1.2 mrad, to represent the effect of a less optimal layout of the mirrors and photodetector plane.

The particle-identification performance in this simulation was inferior to that of the standard production, but not dramatically so. Figure 8.26 shows, for example, the kaon identification and the pion misidentification as a function of momentum, for the standard and robustness productions. The most significant effect is seen at low momentum, where the kaon efficiency is 5–10% lower in the robustness production.

8.9.2 Muon Detector robustness

The effect of the low-energy background in the Muon Detector has been studied, increasing it by a factor of five in stations M2–M5. Applying

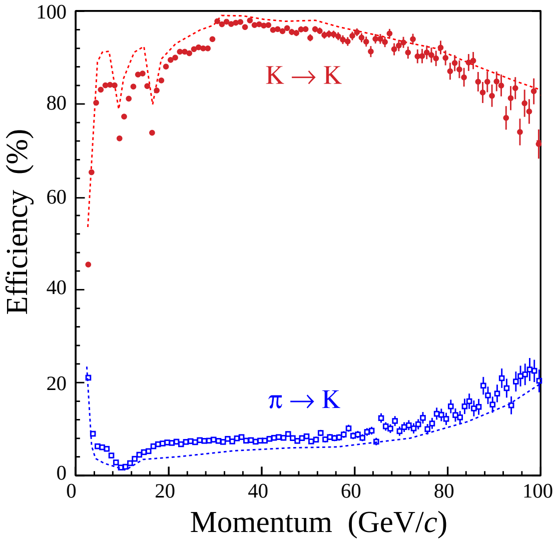

Figure 8.26: RICH reconstruction performance in the global robustness test: the kaon efficiency (solid points) and pion misidentification rate (open points) as a function of momentum. The distributions seen with the nominal parameters, as shown in Fig. 8.5, are indicated by the dotted lines.

the standard muon identification algorithm to this sample leads to an increase of the pion misidentification rate to 11.7% (from the nominal 2.9%), whilst the muon identification efficiency remains unaffected at 94%. Retuning the fields of interest in the algorithm, the pion misidentification rate can be reduced. Applying a reduction factor of 2.5 for the FOI in Region 1 of the stations (the busiest region), and a factor of 1.5 in the other regions, reduces the misidentification rate back to the nominal value, for a loss of 7% of muon identification efficiency.

8.9.3 Calorimeter robustness

For the global robustness test the level of coherent and incoherent noise was varied for calorimeter channels, and conservative estimates of the percentage of dead channels were used. In addition the unknown detector and calibration imperfections were combined into an effective parameter, referred to as "gain error" which appears as an additional constant term in the energy resolution of the channel. The nominal values of these parameters and their setting for the global robustness test are listed in Table 6.2.

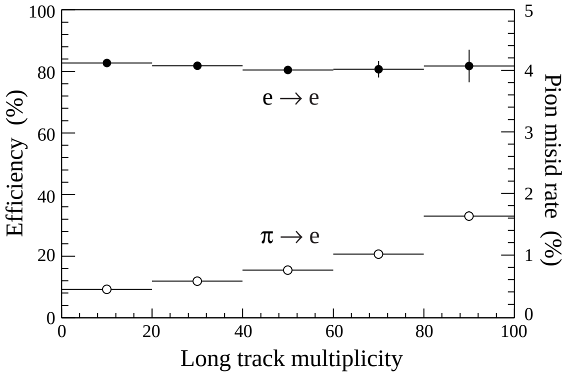

Figure 8.27: Robustness of electron identification versus track multiplicity: electron identification efficiency (solid points) and hadron misidentification rate (open points, with scale on the right).

For the evaluation of estimators used for electron identification the same reconstruction and identification procedure and parameters were used without re-tuning, such that the nominal estimators of uncertainties were used for evaluation of χ^2_γ, χ^2_e, and $\chi^2_{\rm brem}$; the reference histograms obtained with nominal parameter settings were used for the log-likelihood difference estimation. For a sample of 50,000 $B^0_s \to J/\psi\,(e^+e^-)\,\phi$ events a 2.5% loss of efficiency of electron identification was observed, with an increase of hadron misidentification rate from 0.7% to 1%. For the $B^0 \to K^*\gamma$ decay a 7% degradation in B^0 mass resolution and 5% loss of overall reconstruction efficiency were seen [102].

Events with high occupancy have an increased hadron misidentification rate, as illustrated in Fig. 8.27. A factor of two increase in track multiplicity above the expectation leads to no significant loss of electron identification efficiency, but an increase in the hadron misidentification rate to 1%.

Concerning π^0 reconstruction, the global robustness test gave a degradation of the core mass resolution of ~ 14% and ~ 19% for the resolved and merged configurations, respectively [100]. No significant change in the π^0 reconstruction efficiency was observed, but an overall ~ 10% loss of efficiency was seen for the selection of $B^0 \to \pi^+\pi^-\pi^0$ events (before applying the trigger) [103].

Chapter 9 Physics Performance

9.1 Introduction

In the Standard Model, flavour-changing processes between the quarks are solely due to charged current interactions with couplings given by a 3×3 unitary matrix, usually referred to as the Cabibbo-Kobayashi-Maskawa (CKM) matrix [104, 105]:

$$V = \begin{pmatrix} V_{\rm ud} & V_{\rm us} & V_{\rm ub} \\ V_{\rm cd} & V_{\rm cs} & V_{\rm cb} \\ V_{\rm td} & V_{\rm ts} & V_{\rm tb} \end{pmatrix} .$$

The matrix can be parametrized with four independent parameters, including one phase, which introduces CP violation. One of the commonly used parametrizations, introduced by Wolfenstein [106], is based on the λ, A, ρ and η parameters. In this parametrization, V can be approximated as

$$V \approx \begin{pmatrix} 1-\lambda^2/2 & \lambda & A\lambda^3\,(\rho - i\,\eta) \\ -\lambda & 1-\lambda^2/2 & A\lambda^2 \\ A\lambda^3\,(1-\rho-i\,\eta) & -A\lambda^2 & 1 \end{pmatrix} + \delta V ,$$

where

$$\delta V = \begin{pmatrix} 0 & 0 & 0 \\ -i\,A^2\lambda^5\eta & 0 & 0 \\ A\lambda^5(\rho+i\,\eta)/2 & A\lambda^4(1/2-\rho-i\,\eta) & 0 \end{pmatrix} .$$

CP violation is present if $\eta \neq 0$. Note that λ is identical to the sine of the Cabibbo angle [104]. It is measured to be 0.2229 ± 0.0022 from nuclear, kaon and hyperon decays [107].

Among the nine unitarity relations of the CKM matrix, the following two are the most relevant for B physics:

$$\begin{aligned} V_{\rm ud}V^*_{\rm ub} + V_{\rm cd}V^*_{\rm cb} + V_{\rm td}V^*_{\rm tb} &= 0 , \\ V_{\rm tb}V^*_{\rm ub} + V_{\rm ts}V^*_{\rm us} + V_{\rm td}V^*_{\rm ud} &= 0 . \end{aligned}$$

Using the approximation introduced above, the two relations can be drawn as triangles (see Fig. 9.1). Although the imaginary part of $V_{\rm cd}$ plays an important role in CP violation in K^0–$\overline{\mathrm{K}}^0$ oscillations, it can be neglected in the first triangle. The second triangle has a particular relevance to the $\mathrm{B}^0_{\rm s}$ meson system. The parametrization implies

$$\arg V_{\rm td} = -\beta,\ \ \arg V_{\rm ub} = -\gamma,\ \ \arg V_{\rm ts} = \chi + \pi ,$$

and that all the other elements are real.

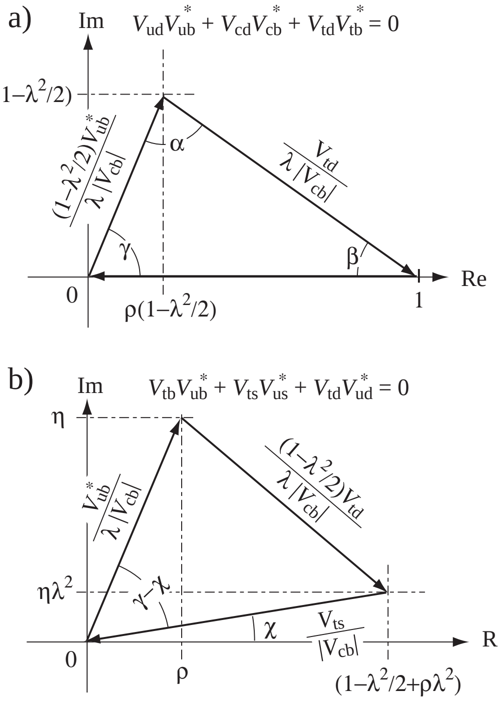

Figure 9.1: Two unitarity relations drawn in the complex plane: (a) for $V_{\rm ud}V^*_{\rm ub} + V_{\rm cd}V^*_{\rm cb} + V_{\rm td}V^*_{\rm tb} = 0$, and (b) for $V_{\rm tb}V^*_{\rm ub} + V_{\rm ts}V^*_{\rm us} + V_{\rm td}V^*_{\rm ud} = 0$.

The quantities $|V_{\rm cb}|$ and $|V_{\rm ub}|$ can be determined from the various B-meson decays generated by tree diagrams. Assuming that B^0–$\overline{\mathrm{B}}^0$ and $\mathrm{B}^0_{\rm s}$–$\overline{\mathrm{B}}^0_{\rm s}$ oscillations are given only by the Standard Model box diagrams shown in Fig. 9.2, $|V_{\rm td}|$ and $|V_{\rm ts}|$ can be calculated from the respective oscillation frequencies. Currently, the B^0–$\overline{\mathrm{B}}^0$ oscillation frequency is very well measured but only a lower limit is known for the $\mathrm{B}^0_{\rm s}$–$\overline{\mathrm{B}}^0_{\rm s}$ oscillation frequency. From Fig. 9.1, it is clear that those measurements are sufficient to establish the triangles and extract A, ρ and η. With the currently known values of $|V_{\rm cb}|$, $|V_{\rm ub}|$, $|V_{\rm td}|$ and $|V_{\rm ts}|$, the phase of $V_{\rm td}$ is determined to be [107]

$$\sin 2\beta_{\rm side} = 0.695 \pm 0.055 . \tag{9.1}$$

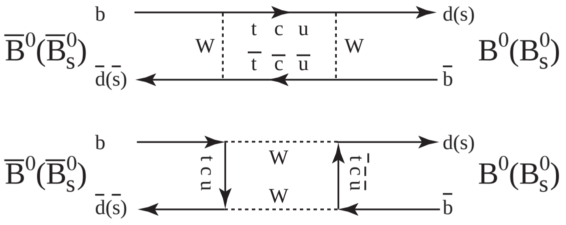

Figure 9.2: The Standard Model box diagrams which generate B^0–$\overline{B}^0$ and B^0_s–$\overline{B}^0_s$ oscillations.

In 2001, long awaited CP asymmetries outside of the neutral kaon system were measured for various CP eigenstates generated by the $b \to c + W^-$ and $\overline{b} \to \overline{c} + W^+$ tree diagrams in B^0 decays, such as $J/\psi K^0_S$ and $\eta_c K^0_S$, by the BABAR [108] and BELLE [109] collaborations. Assuming these decays are dominated by the Standard Model processes, CP asymmetries from those final states yield [110]

$$\sin\phi_{\rm d} = \begin{cases} 0.741 \pm 0.075 & \text{BABAR} \\ 0.719 \pm 0.082 & \text{BELLE} \end{cases} ,$$

where $\phi_{\rm d}$ is identical to the phase of the B^0–$\overline{B}^0$ oscillation amplitude, since the B^0 and $\overline{B}^0$ decay amplitudes are real with the phase convention of the Wolfenstein parameterization used here. As done for the extraction of $|V_{\rm td}|$ from the B^0–$\overline{B}^0$ oscillation frequency, if only the Standard Model box processes contribute to the B^0–$\overline{B}^0$ oscillation, $\phi_{\rm d}$ is identical to $-2\arg V_{\rm td} = 2\beta$, i.e.

$$\phi_{\rm d} = 2\beta\,. \tag{9.2}$$

Averaging the two results, one obtains

$$\sin 2\beta_{\rm CP} = 0.731 \pm 0.055\,. \tag{9.3}$$

This is in very good agreement with the prediction of β from the absolute values of CKM elements given in Eq. (9.1), and shows that the Standard Model can give a very consistent picture.

Results from the $B^0 \to \pi^+\pi^-$ decays are less consistent. BABAR [111] and BELLE [112] fit the two CP violation parameters $\mathcal{A}^{\rm dir}_{\pi^+\pi^-}$ and $\mathcal{A}^{\rm mix}_{\pi^+\pi^-}$ to the measured time-dependent CP asymmetries between $\overline{B}^0$ and B^0 decaying into $\pi^+\pi^-$ with the function

$$\mathcal{A}^{\rm CP}_{\pi^+\pi^-}(t) = \mathcal{A}^{\rm dir}_{\pi^+\pi^-}\cos(\Delta m_{\rm d}t) + \mathcal{A}^{\rm mix}_{\pi^+\pi^-}\sin(\Delta m_{\rm d}t)\,,$$

where $\Delta m_{\rm d}$ is the oscillation frequency. The results are

$$\mathcal{A}^{\rm dir}_{\pi^+\pi^-} = \begin{cases} 0.30 \pm 0.25 & \text{BABAR} \\ 0.77 \pm 0.28 & \text{BELLE} \end{cases}$$

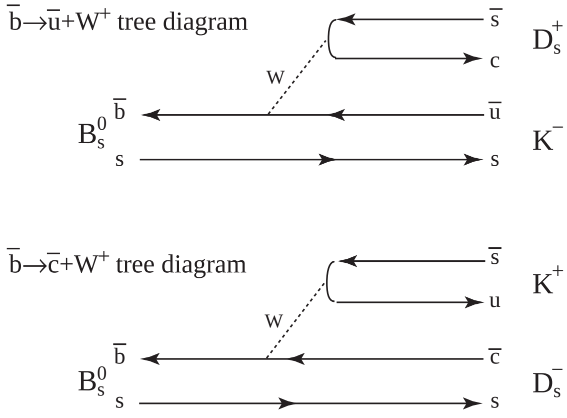

Figure 9.3: The two tree diagrams which generate $B^0_s \to D^+_s K^-$ and $B^0_s \to D^-_s K^+$ decays.

and

$$\mathcal{A}^{\rm mix}_{\pi^+\pi^-} = \begin{cases} +0.02 \pm 0.34 & \text{BABAR} \\ -1.23 \pm 0.42 & \text{BELLE} \end{cases} ,$$

which do not allow us to draw a clear conclusion.

Unlike for the case of the $J/\psi K^0_S$ decays, a theoretical interpretation of $\mathcal{A}^{\rm dir}_{\pi^+\pi^-}$ and $\mathcal{A}^{\rm mix}_{\pi^+\pi^-}$ is not simple. In addition to the $\overline{b} \to \overline{u} + W^+$ tree process, the $\overline{b} \to \overline{d} + g(\gamma, Z^0)$ penguin process is expected to make a sizeable contribution to the decay. Since the two processes have different phases, γ and $-\beta$ respectively, we cannot extract γ and β without knowing the exact relative contributions of the two processes.

For many other $B^\pm$, B^0 and $\overline{B}^0$ decay modes, no further evidence of CP violation has been seen so far with the current statistics of the BABAR and BELLE experiments.

If indeed new physics such as SUSY is just around the corner, it must contribute to B^0–$\overline{B}^0$ oscillations and various decay modes which are generated by the loop diagrams, e.g. penguins and boxes. Since CP violation is sensitive to the phases of couplings, it gives a unique opportunity to probe not only the strengths but also the phases of the new couplings.

If new particles contribute to B^0–$\overline{B}^0$ oscillations, $|V_{\rm td}|$ cannot be determined from the oscillation frequency. Similarly, Eq. (9.2) is no longer valid and β cannot be determined from the CP asymmetry in $J/\psi K^0_S$ decays. Therefore, neither $\beta_{\rm side}$ of Eq. (9.1) nor $\beta_{\rm CP}$ of Eq. (9.3) will give the phase of $V_{\rm td}$.

For a comprehensive study of CP violation including possible contributions from new physics,

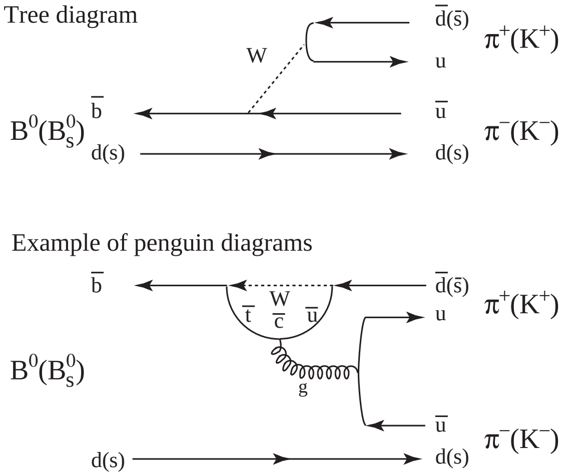

Figure 9.4: The tree diagram and an example of the penguin diagrams which generate $B^0 \to \pi^+\pi^-$ and $B^0_s \to K^+K^-$ decays.

the B^0_s meson plays an essential role, as shown in the following example. The phase of V_{ub} can be measured in several ways:

I. A theoretically clean way to extract γ is to mix the two tree diagrams, $\bar{b} \to \bar{u} + W^+$ and $\bar{b} \to \bar{c} + W^+$. This can be done by studying the time-dependent rates of B^0_s decaying into $D^+_s K^-$ and $D^-_s K^+$ and their CP-conjugated processes [113]. Figure 9.3 illustrates the corresponding diagrams. From them, one can extract $\phi_s + \gamma$ without any theoretical ambiguity. Here, ϕ_s is the phase of B^0_s–$\overline{B}^0_s$ oscillations, which can be obtained from the time-dependent CP asymmetry of B^0_s and $\overline{B}^0_s$ decaying into $J/\psi\phi$ (or other CP eigenstates produced by the $b \to c + W^-$ and $\bar{b} \to \bar{c} + W^+$ tree processes). Combining the two results, γ can be determined.

II. As already discussed, both $\bar{b} \to \bar{u} + W^+$ tree and $\bar{b} \to \bar{d} + g(\gamma, Z^0)$ penguin processes contribute to the decay of B^0 into $\pi^+\pi^-$. By replacing all the d and $\bar{d}$ quarks by s and $\bar{s}$ quarks, respectively, the tree and penguin processes generate K^+K^- decays for the B^0_s meson. Figure 9.4 illustrates the relevant diagrams. If we assume that the strong interaction dynamics remains invariant under this interchange (U-spin symmetry) [114], the relative contributions of the penguin process with respect to the tree process are identical for the $B^0 \to \pi^+\pi^-$ and $B^0_s \to K^+K^-$ decays. Under this assumption, γ can be determined from the time-dependent CP asymmetry for B^0 and $\overline{B}^0$ decaying into $\pi^+\pi^-$ and that for B^0_s and $\overline{B}^0_s$ decaying into K^+K^-. Using the ϕ_d and ϕ_s values obtained from the CP asymmetries measured with $B^0, \overline{B}^0 \to J/\psi K^0_S$ and $B^0_s, \overline{B}^0_s \to J/\psi\phi$ respectively, the assumed U-spin symmetry can be tested as well.

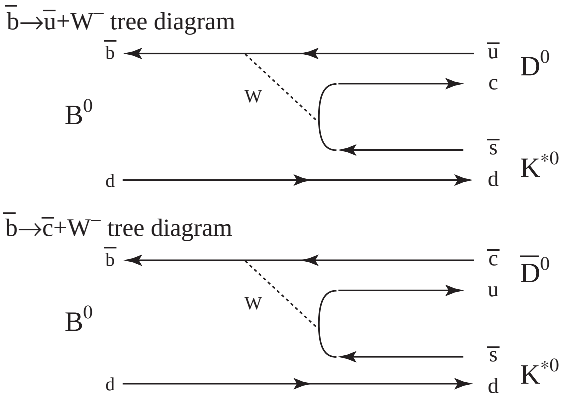

Figure 9.5: The two tree diagrams which generate $B^0 \to D^0K^{*0}$ and $B^0 \to \overline{D}^0K^{*0}$ decays.

III. Another opportunity for observing the interference between the two tree processes, $\bar{b} \to \bar{u} + W^+$ and $\bar{b} \to \bar{c} + W^-$, and thus extracting γ, is given by D^0–$\overline{D}^0$ mixing [115]. This can be done by measuring the time-integrated decay rates for $B^0 \to D^0K^{*0}$, $B^0 \to \overline{D}^0K^{*0}$, $B^0 \to D^0_{CP}K^{*0}$ and for their CP-conjugated processes, where $D^0_{CP} = (D^0 + \overline{D}^0)/\sqrt{2}$ denotes the CP-even eigenstate of the D^0–$\overline{D}^0$ system. Figure 9.5 shows relevant diagrams.

It is important to note that the phase γ measured in the first method will not be affected by the possible existence of new particles. The second method makes an explicit use of the penguin processes where new particles can contribute to the loops. Therefore, the extracted value of γ could be affected by new physics. Equally for the third method, new physics in D^0–$\overline{D}^0$ mixing could affect the extracted value of γ. From these three γ measurements, we can

- determine γ and, together with the $|V_{ub}|$ measurements, extract the CKM parameters, A, ρ and η even in the presence of new physics, and

- extract the contribution of new physics to the oscillations and penguins.

Note that the Standard Model analysis using the present knowledge of $|V_{\mathrm{ub}}|$, $|V_{\mathrm{cb}}|$, $|V_{\mathrm{td}}|$ and $\sin 2\beta$ predicts $\gamma \sim 65^\circ$ [107].

There are many other CP-violating decay modes where the extracted phases of V_{td}, V_{ub} and V_{ts} are affected differently by new physics. Studies of those decay modes with high accuracy will give us a different insight to the properties of the new physics, compared to what could be obtained from the direct search at ATLAS and CMS. As demonstrated, $\mathrm{B_s^0}$ mesons play a crucial role here. This gives a distinct advantage to hadron machines over $\mathrm{e^+e^-}$ B factories operating at the $\Upsilon(4\mathrm{S})$. Similarly, $\mathrm{B_c^+}$ mesons and b baryons are also an exclusive domain of hadron machines. For interesting CP-violating $\mathrm{B^0}$ decay modes such as $\pi^+\pi^-$, $\mathrm{K}^\pm\pi^\mp$ and $\mathrm{K}^{*0}\ell^+\ell^-$, the LHCb experiment will be able to collect several times more statistics in one year than that obtained by BABAR and BELLE by the time LHC becomes operational.

The purpose of the rest of this chapter is to show, within the physics scope outlined above, the potential of the reoptimized LHCb detector for the reconstruction and selection of interesting B channels. We include in this discussion fully hadronic decays (involving also neutrals like $\mathrm{K_S^0}$, π^0, η), decays with leptons, and radiative decays. Emphasis is put on the offline selections, whereas trigger aspects are discussed in detail elsewhere [3]. We also present a few "toy Monte Carlo" studies of the statistical sensitivity to interesting physics parameters and CP observables.

9.2 Primary vertex reconstruction

The primary vertex search and fit is performed using the following iterative procedure:

- One builds an histogram of the z-coordinate of the point of closest approach to the beam line for all tracks measured in the VELO (long tracks, upstream tracks and VELO tracks). The bin width is 1 mm. The highest bin of this histogram is used, together with its 4 neighbours on each side, to define a cluster of tracks. The mean value computed from these tracks is used as the z of an original vertex (located on the beam axis).
- Tracks with a large χ^2 contribution to the vertex (> 225 for the first iteration, > 9 afterwards) are eliminated from the cluster, and the remaining tracks in the cluster are fitted to a new common vertex. This step is iterated until no tracks are rejected anymore.
- If at least 6 tracks were used in the last iteration, their vertex is kept as a primary vertex, these tracks are removed from the overall set of tracks, and the whole search procedure is restarted to find additional primary vertices.
- Otherwise, the current vertex is discarded and the search is stopped. In case no primary vertex has been found, the original vertex obtained from the histogram peak is kept as the only primary vertex of the event.

Table 9.1: Efficiency for finding the $\mathrm{b\overline{b}}$ production vertex as a function of the number of collisions producing at least two long tracks in the detector.

No. of collisions	1	2	3	4
Efficiency (%)	99	96	90	81

The cuts have been chosen in order to optimize the efficiency for finding the $\mathrm{b\overline{b}}$ production vertex, which is 98% on average. In the other 2% of the cases, the search is disturbed by another primary vertex from a minimum-bias interaction close to the $\mathrm{b\overline{b}}$ production vertex. This is illustrated in Table 9.1 which shows the efficiency for finding the $\mathrm{b\overline{b}}$ production vertex as a function of the number of visible pp collisions in the event (defined as producing at least two long tracks in the detector).

The resolution on the $\mathrm{b\overline{b}}$ production vertex in the directions longitudinal (z) and transverse (x, y) to the beam are shown in Figs. 9.6 and 9.7, for $\mathrm{b\overline{b}}$ events passing the trigger in which a b hadron was produced forward within 400 mrad of the beam axis. The distributions are fitted with a double Gaussian with a common central value. The core resolutions are 44 μm and 7.8 μm respectively with about 25% of events in the second Gaussian, 2 to 3 times wider. The z-resolution is slightly better (41.7 μm) in single-interaction events. A small but significant 8 μm bias in z is caused by decay products of b- or c-hadrons that cannot be separated from the primary vertex by the χ^2 cut. This shift is not present in minimum-bias events.

In the offline selections of B decays, the $\mathrm{b\overline{b}}$ production vertex is chosen as the primary vertex with respect to which the fully reconstructed B candidate has the smallest impact parameter or impact parameter significance (and a positive decay length). This implies that all cuts with respect

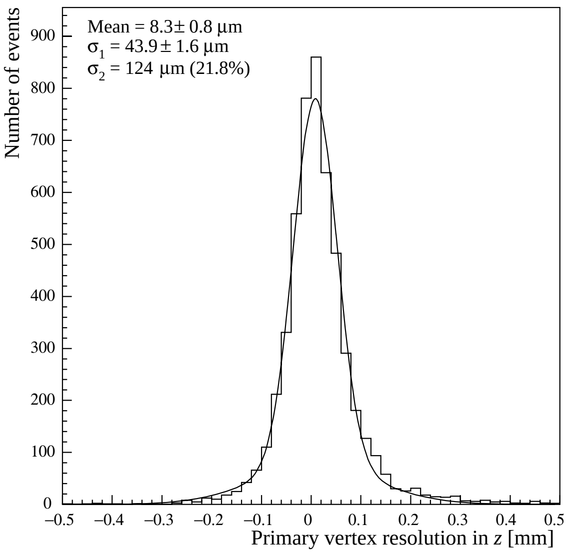

Figure 9.6: z resolution of the b$\overline{\text{b}}$ production vertex in forward b$\overline{\text{b}}$ events passing the trigger.

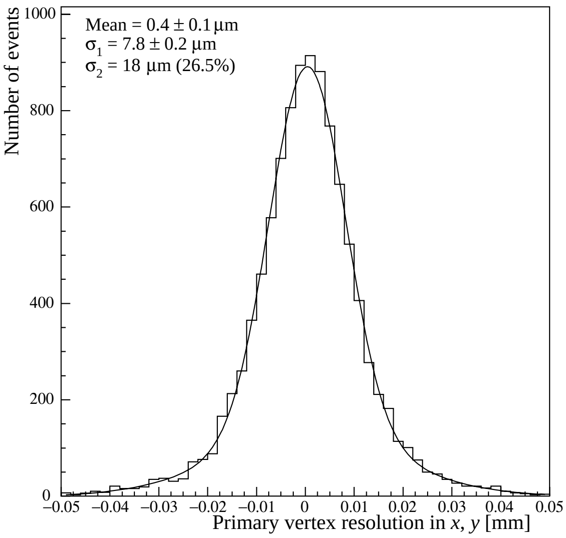

Figure 9.7: x and y resolution of the b$\overline{\text{b}}$ production vertex in forward b$\overline{\text{b}}$ events passing the trigger.

to this vertex (which will be referred to as "the" primary vertex), e.g. on track impact parameters, can only be applied once a B candidate has been formed. Unless specified otherwise, this procedure is applied in the analyses described below.

9.3 Reconstruction of specific B final states

The main challenge in the offline selection of B final states is to maintain high efficiency for the signal while providing a very large rejection factor for the combinatorial background. The combinatorial background events surviving the selection cuts are highly biased and non-typical of minimum-bias events, sitting for example in the far tails of p_{T}, impact parameter and vertex χ^2 distributions which are not known sufficiently well to be parametrized. The studies are therefore performed with fully simulated events (generated as described in Chapter 6), with the drawback that only a limited statistics of background events can be generated. We have therefore chosen to focus on what is very likely to be the dominant and therefore most dangerous source of combinatorial background, namely b$\overline{\text{b}}$ events where at least one b-hadron is emitted forward within 400 mrad of the beam axis (called forward b$\overline{\text{b}}$ events). Tracks from inclusive b-hadron decays are displaced from the primary vertex and, after minimum p_{T} requirements, have a much larger probability to form fake secondary vertices than tracks in c$\overline{\text{c}}$ or light-flavour events. Even with these assumptions, the Monte Carlo background statistics available currently is not sufficient to obtain a precise estimate of the background levels (except for channels with a relatively large visible branching ratio), so upper limits are derived.

The offline selections of a few fully reconstructed B^0 and $\mathrm{B}^0_{\mathrm{s}}$ channels are presented below. They represent examples of what can be done with the LHCb detector. Each selection was developed independently, without attempting so far to define a common selection strategy. Charged conjugate reactions are implied throughout. Unless mentioned otherwise, only long tracks are used.

9.3.1 $\mathrm{B}^0_{(\mathrm{s})} \to \mathrm{h}^+\mathrm{h}^-$

We outline here the selection of $\mathrm{B}^0 \to \pi^+\pi^-$, $\mathrm{B}^0 \to \mathrm{K}^+\pi^-$, $\mathrm{B}^0_{\mathrm{s}} \to \mathrm{K}^+\mathrm{K}^-$ and $\mathrm{B}^0_{\mathrm{s}} \to \pi^+\mathrm{K}^-$ decays [116]. Due to the large penguin amplitude, $\mathrm{B}^0 \to \pi^+\pi^-$ alone does not provide a clean way to determine CKM phases. However, the combination of the $\mathrm{B}^0 \to \pi^+\pi^-$ and $\mathrm{B}^0_{\mathrm{s}} \to \mathrm{K}^+\mathrm{K}^-$ CP measurements provides an interesting strategy to extract the γ angle [114], as will be discussed in Sect. 9.6.4.

The selection starts with the reconstruction and identification of tracks as charged pions or kaons. Each track must have a momentum p in the range $p_{\mathrm{min}} < p < p_{\mathrm{max}}$, a transverse momentum p_{T} larger than $(p_{\mathrm{T}})_{\mathrm{each}}$ and an impact parameter significance $\mathrm{IP}/\sigma_{\mathrm{IP}}$ larger than $(\mathrm{IP}/\sigma_{\mathrm{IP}})_{\mathrm{each}}$ with respect to the primary vertex.

Pairs of tracks with opposite charges are formed

Table 9.2: Summary of the offline selection cuts and estimates of the remaining background levels for the different $\mathrm{B}^0_{(\mathrm{s})} \to \mathrm{h}^+\mathrm{h}^-$ analyses. The meaning of each cut is described in the text.

	$\mathrm{B}^0 \to \mathrm{h}^+\mathrm{h}^-$		$\mathrm{B}^0_\mathrm{s} \to \mathrm{h}^+\mathrm{h}^-$	
Channel	$\pi\pi$	$\mathrm{K}\pi$	KK	$\pi\mathrm{K}$
Selection cuts				
p_{min} [GeV/c]	2.50	2.75	2.75	2.75
p_{max} [GeV/c]	100	200	125	100
$(p_T)_{\mathrm{each}}$ [GeV/c]	1.2	1.2	0.8	1.4
$(p_T)_{\mathrm{one}}$ [GeV/c]	3.2	3.0	2.6	3.4
$(\mathrm{IP}/\sigma_{\mathrm{IP}})_{\mathrm{each}}$	6	6	5	7
$(\mathrm{IP}/\sigma_{\mathrm{IP}})_{\mathrm{one}}$	12	11	9	14
χ^2_{max}	4	5	5	4
$(p_T^{\mathrm{B}})_{\mathrm{min}}$ [GeV/c]	1.6	1.4	1.0	1.6
$(\mathrm{IP_B}/\sigma_{\mathrm{IP_B}})_{\mathrm{max}}$	2.25	2.50	2.75	2.25
$(L/\sigma_L)_{\mathrm{min}}$	19	17	14	20
δm [MeV/c^2]	50	50	50	40
B/S ratios				
two-body	0.13	0.04	0.04	0.41
combinatorial ($\mathrm{b\bar{b}}$)	< 0.72	< 0.22	< 0.51	< 1.28

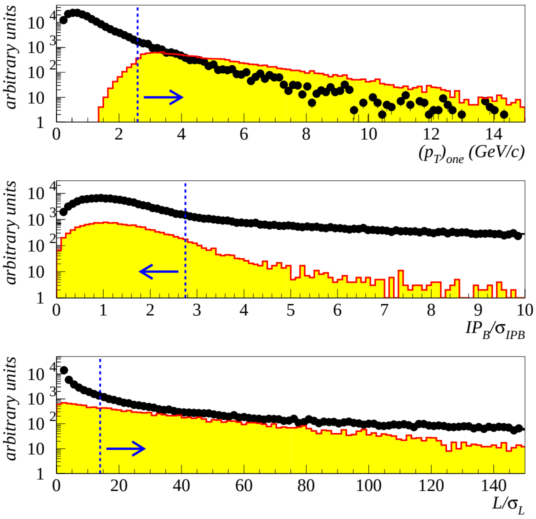

Figure 9.8: Distributions of some of the selection variables for true $\mathrm{B}^0_\mathrm{s} \to \mathrm{K}^+\mathrm{K}^-$ events (shaded histogram) and $\mathrm{b\bar{b}}$ combinatorial background (black dots). The meaning of each variable is described in the text. The plots are obtained after track reconstruction and particle identification, but before trigger and offline selection. Vertical dashed lines indicate the cut value, while the arrows indicate the accepted region.

requiring at least one track with $p_\mathrm{T} > (p_\mathrm{T})_{\mathrm{one}}$ and at least one track with $\mathrm{IP}/\sigma_{\mathrm{IP}} > (\mathrm{IP}/\sigma_{\mathrm{IP}})_{\mathrm{one}}$. Each pair surviving these cuts is fitted to a common vertex and used to form a B^0 candidate, which must pass the following criteria:

- the vertex χ^2 must be smaller than χ^2_{max};
- the p_T of the $\mathrm{B}^0_{(\mathrm{s})}$ must exceed $(p^\mathrm{B}_\mathrm{T})_{\mathrm{min}}$;
- the direction of flight must point to the primary vertex, with an impact parameter significance smaller than $(\mathrm{IP_B}/\sigma_{\mathrm{IP_B}})_{\mathrm{max}}$;
- the distance L between the primary and the secondary vertices must have a significance exceeding $(L/\sigma_L)_{\mathrm{min}}$;
- the invariant mass of the pair must lie within $\pm\delta m$ of the true $\mathrm{B}^0_{(\mathrm{s})}$ mass.

The selection cuts have been optimized separately for each of the decays under study, in order to reject the backgrounds and maximize the signal efficiency. The best cuts identified for each channel are shown in Table 9.2, together with the estimates of the background-to-signal (B/S) ratios after selection. The distributions of signal and $\mathrm{b\bar{b}}$ background for some of the selection variables are shown in Fig. 9.8.

A crucial requirement for these selections is the ability to suppress other b-hadron decays with the same two-track topology. This is particularly important since such backgrounds may exhibit their own CP asymmetries, thus biasing the CP measurements of the channel under consideration. The rejection of these backgrounds relies on the performance of the RICH particle identification and on the invariant mass resolution, which is about 17 MeV/c^2. As an example, Fig. 9.9 shows $\mathrm{K}^+\mathrm{K}^-$ mass distributions after the trigger and the $\mathrm{B}^0_\mathrm{s} \to \mathrm{K}^+\mathrm{K}^-$ selection. As is clearly visible, the specific two-body backgrounds can be kept small.

The combinatorial background is estimated from a sample of 10^7 forward $\mathrm{b\bar{b}}$ events, with a relaxed δm mass cut of ± 0.6 GeV/c^2 (± 1.2 GeV/c^2 in the case of $\mathrm{B}^0_\mathrm{s} \to \pi^+\mathrm{K}^-$); only a handful of $\mathrm{b\bar{b}}$ events survive the offline selection, leading to the 90% CL upper limits quoted in Table 9.2.

Finally, an important quantity is the resolution on the proper decay time. This is particularly relevant for the fast-oscillating B^0_s meson, where a bad resolution would dilute the sensitivity to the CP measurements. Figure 9.10 shows the proper-time resolution for triggered and reconstructed $\mathrm{B}^0_\mathrm{s} \to \mathrm{K}^+\mathrm{K}^-$ decays, which has a width of about 40 fs.

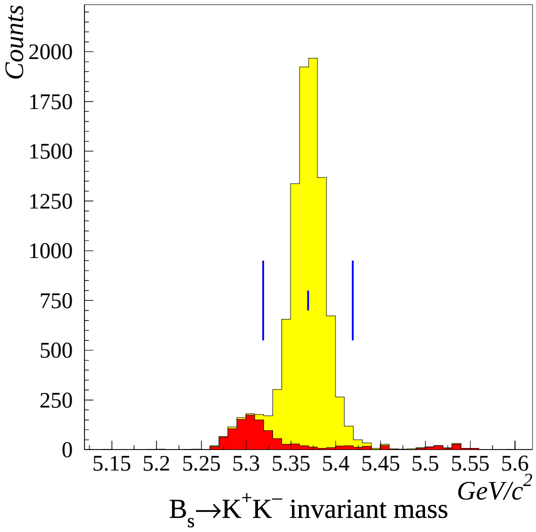

Figure 9.9: Invariant mass distribution of triggered and offline-selected $\mathrm{B_s^0} \to \mathrm{K^+K^-}$ candidates. The light-shaded (yellow) histogram is the signal and the dark (red) one represents the background from $\mathrm{B^0} \to \pi^+\pi^-$, $\mathrm{B^0} \to \mathrm{K^+}\pi^-$, $\mathrm{B_s^0} \to \pi^+\mathrm{K^-}$, $\Lambda_\mathrm{b} \to \mathrm{pK^-}$ and $\Lambda_\mathrm{b} \to \mathrm{p}\pi^-$ decays. The vertical lines indicate the mass cut applied in the selection.

9.3.2 $\mathbf{B_s^0 \to D_s^- h^+}$

We summarize here the $\mathrm{B_s^0} \to \mathrm{D_s^- h^+}$ selections [117], where $\mathrm{h^+}$ refers to a "bachelor" $\mathrm{K^+}$ or π^+ coming directly from the $\mathrm{B_s^0}$ decay. The $\mathrm{B_s^0} \to \mathrm{D_s^\mp K^\pm}$ decays involve two tree amplitudes (see Fig. 9.3) and can be used, together with $\mathrm{B_s^0} \to \mathrm{J}/\psi\phi$, to extract the angle γ in a theoretically clean way, even in presence of new physics in loop diagrams. With its large branching ratio and flavour-specific final state, the $\mathrm{B_s^0} \to \mathrm{D_s^-}\pi^+$ mode can be used to measure the $\mathrm{B_s^0}$ oscillation frequency, but also constitutes both a background channel and a control channel for the $\mathrm{B_s^0} \to \mathrm{D_s^\mp K^\pm}$ analysis.

All charged tracks used in this $\mathrm{B_s^0}$ reconstruction are required to have a track fit χ^2 less than 4 per degree of freedom, $p > 2\,\mathrm{GeV}/c$, $p_\mathrm{T} > 0.3\,\mathrm{GeV}/c$, and an impact parameter significance larger than 1 with respect to the $\mathrm{B_s^0}$ production vertex, taken as the primary vertex with the highest track multiplicity. These tracks are assumed to be kaons if $\Delta \ln \mathcal{L}_{\mathrm{K}\pi} > -5$ and pions if $\Delta \ln \mathcal{L}_{\pi\mathrm{K}} > -5$, based on the RICH information. There is an overlap region, $-5 < \Delta \ln \mathcal{L}_{\mathrm{K}\pi} < 5$, were a single track can be considered both as a kaon or a pion.

The $\mathrm{D_s^-}$ is reconstructed in the $\mathrm{K^+K^-}\pi^-$ final state. The three tracks must have $\sum p_\mathrm{T} > 2.2\,\mathrm{GeV}/c$, an invariant mass within $\pm 15\,\mathrm{MeV}/c^2$ of the true $\mathrm{D_s^-}$ mass, and a vertex with $\chi^2 < 10$.

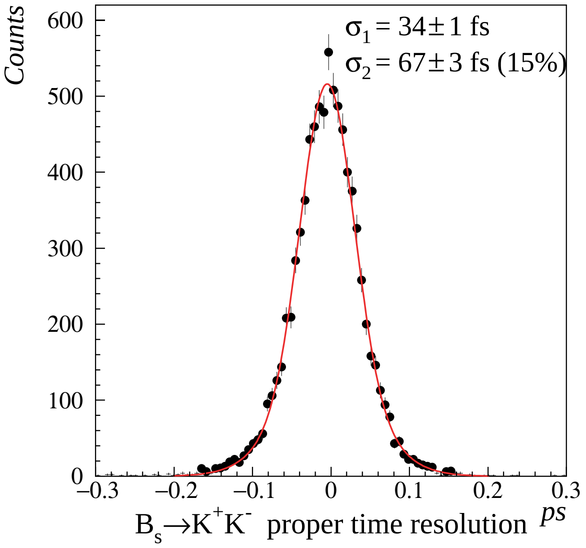

Figure 9.10: Proper-time resolution for triggered and offline-selected $\mathrm{B_s^0} \to \mathrm{K^+K^-}$ decays. The fit is a double Gaussian. A fit with a single Gaussian gives $\sigma \sim 40\,\mathrm{fs}$.

$\mathrm{B_s^0}$ candidates are formed by combining the $\mathrm{D_s^-}$ with remaining $\mathrm{K^+}$ and π^+ tracks (bachelor $\mathrm{h^+}$), and the following criteria are applied:

- the bachelor track must have $p_\mathrm{T} > 0.7\,\mathrm{GeV}/c$ and an impact parameter significance in excess of 4 with respect to the $\mathrm{B_s^0}$ production vertex;
- the $\mathrm{D_s^-}$ vertex must be separated from the $\mathrm{B_s^0}$ production vertex by at least 4.5σ in the downstream direction;
- the $\mathrm{D_s^-}$ candidate must have an impact parameter significance larger than 2 with respect to the $\mathrm{B_s^0}$ production vertex;
- the $\mathrm{D_s^- h^+}$ pair must form a vertex with $\chi^2 < 4$, between the $\mathrm{D_s^-}$ and the primary vertices;
- the significance of the impact parameter of the $\mathrm{B_s^0}$ candidate with respect to its production vertex must be smaller than 3;
- the angle θ between the reconstructed $\mathrm{B_s^0}$ momentum and the line of flight determined by its production and decay vertices must be less than 8 mrad;
- the reconstructed $\mathrm{B_s^0}$ mass must be within $\pm 50\,\mathrm{MeV}/c^2$ of the true mass.

The only difference between the $\mathrm{B_s^0} \to \mathrm{D_s^\mp K^\pm}$ and $\mathrm{B_s^0} \to \mathrm{D_s^-}\pi^+$ selections is in the treatment of the bachelor particle. Kaons must have

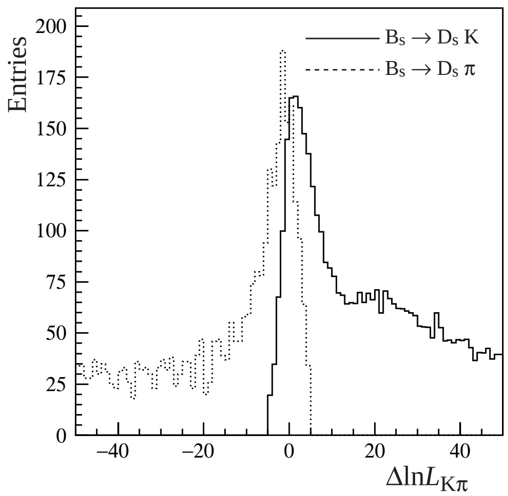

Figure 9.11: Distribution of $\Delta \ln \mathcal{L}_{K\pi}$ showing the separation achieved between the $B^0_s \to D^-_s \pi^+$ and $B^0_s \to D^{\mp}_s K^{\pm}$ samples based on the particle-identification information of the bachelor particle. The relative normalization is arbitrary.

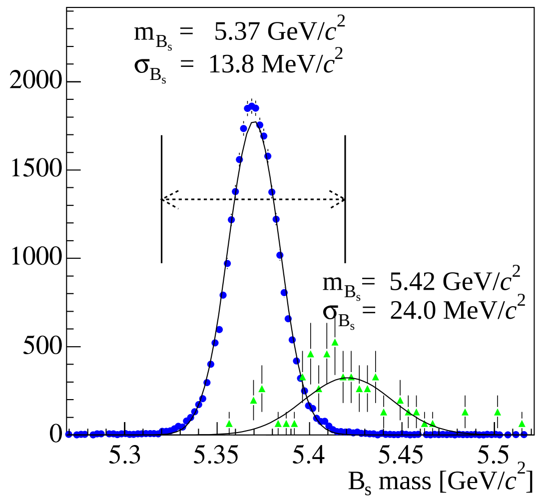

Figure 9.12: B^0_s mass distribution for selected $B^0_s \to D^{\mp}_s K^{\pm}$ candidates. The Gaussian fit gives a resolution of 14 MeV/c^2 for the signal. Also shown are the misidentified $B^0_s \to D^-_s \pi^+$ events normalized to the branching ratios given in Table 9.5. Their mass is shifted up due to the misidentification of the bachelor π as a K.

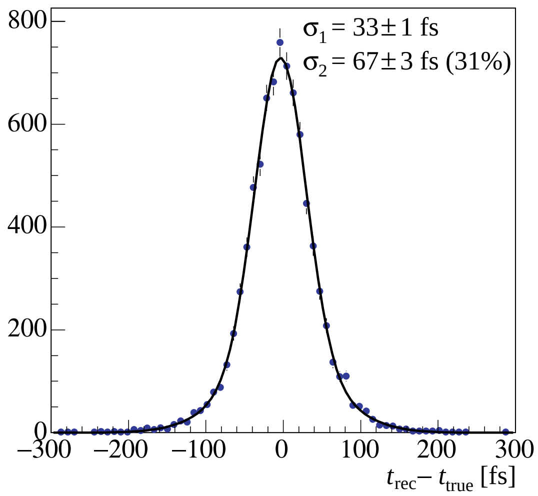

Figure 9.13: B^0_s proper-time resolution for $B^0_s \to D^{\mp}_s K^{\pm}$ decays in selected and triggered events. The fit is a double Gaussian with a core (69%) $\sigma = 33 \pm 1$ fs. The resolution of $B^0_s \to D^-_s \pi^+$ decays is very similar.

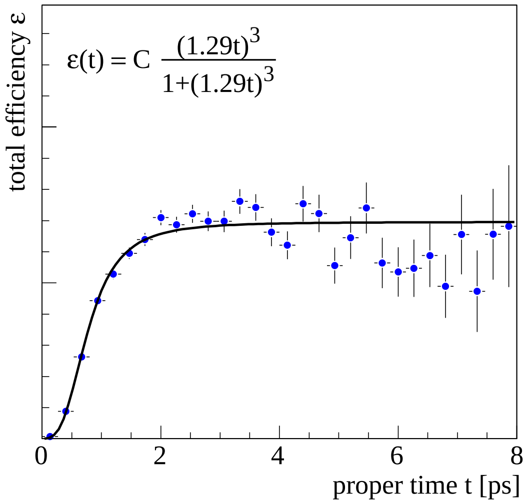

Figure 9.14: Total $B^0_s \to D^-_s h^+$ selection and trigger efficiency as function of proper time, in arbitrary units. The expression of the fitted parametrization is shown.

$\Delta \ln \mathcal{L}_{K\pi} > 2$ and $\Delta \ln \mathcal{L}_{Ke} > 2$ while pions must have $\Delta \ln \mathcal{L}_{\pi K} > -5$. This separation can be seen in Fig. 9.11. These cuts greatly reduce the $B^0_s \to D^-_s \pi^+$ pollution of the $B^0_s \to D^{\mp}_s K^{\pm}$ channel, which is estimated to correspond to $B/S = 11\%$ with the cuts presented here, while retaining the pions for the $B^0_s \to D^-_s \pi^+$ selection ($B^0_s \to D^{\mp}_s K^{\pm}$ pollution of $B^0_s \to D^-_s \pi^+$ is negligible due to the difference in branching ratios).

Figure 9.12 shows the mass resolution for selected $B^0_s \to D^{\mp}_s K^{\pm}$ candidates from signal events along with the background from misidentified $B^0_s \to D^-_s \pi^+$ decays. Correctly selected $B^0_s \to D^-_s \pi^+$ events show a similar mass resolution.

The combinatorial background is estimated from a sample of 10^7 forward $b\overline{b}$ events, with a relaxed B^0_s mass window of ± 0.5 GeV/c^2. Only 10 (1) combinatorial background events survive the selection criteria with a bachelor pion (kaon) leading to the 90% CL upper limit $B/S < 0.5$ (1.0).

The $\mathrm{B_s^0}$ proper-time resolution, after a $\mathrm{B_s^0}$ mass constrained fit of the $\mathrm{B_s^0}$ vertex, is shown in Fig. 9.13. The combined efficiency of the selection and trigger has the proper-time dependence shown in Fig. 9.14.

9.3.3 $\mathrm{B^0} \to \mathrm{J}/\psi(\mu\mu)\mathrm{K_S^0}$

$\mathrm{B^0} \to \mathrm{J}/\psi\mathrm{K_S^0}$ is the best decay for the measurement of the angle β. In addition to its physics interest, we use it as a benchmark for our performance on $\mathrm{J}/\psi \to \ell^+\ell^-$ and $\mathrm{K_S^0} \to \pi^+\pi^-$ reconstruction. We summarize here the dimuon case [118], while electrons will be discussed in the following section.

Muon candidates are identified with the requirement $\Delta \ln \mathcal{L}_{\mu\pi} > -8$ (see Sect. 8.4). Pairs of muons with opposite charges are required to come from a common vertex with $\chi^2 < 20$ and to have an invariant mass within $\pm 50\,\mathrm{MeV}/c^2$ of the true J/ψ mass (the core resolution is $\sim 10\,\mathrm{MeV}/c^2$). After a mass-constrained vertex fit with $\chi^2 < 50$, the vertex resolution along z has a core of $165\,\mu$m.

The $\mathrm{K_S^0} \to \pi^+\pi^-$ decays are reconstructed with different types of tracks, as described in Sect. 8.8. The J/ψ and $\mathrm{K_S^0}$ candidates are combined to form $\mathrm{B^0}$ candidates and the following requirements are applied; cut values are given for the most frequent case where the $\mathrm{K_S^0}$ is formed with two downstream tracks, and the values in parentheses apply to the category with two long tracks:

- the significance of the displacement in z between the J/ψ vertex and the primary vertex must be greater than 1.2;
- the significance of the displacement in z between the $\mathrm{K_S^0}$ vertex and the primary vertex must be greater than 0.0 (5.7);
- the impact parameter significance of the $\mathrm{K_S^0}$ with respect to the J/ψ must exceed 8 (3.5);
- the impact parameter significance of each $\mathrm{K_S^0}$ leg with respect to the primary vertex must be larger than 2 (3), and similarly for each J/ψ leg with a cut at 1.2 (1.4);
- the impact parameter significance of the $\mathrm{B^0}$ with respect to the primary vertex must be smaller than 5.0, and that of the $\mathrm{K_S^0}$ must be larger than 0.0 (1.0);
- the $\mathrm{B^0}$ transverse momentum of must be larger than $0\,\mathrm{MeV}/c$ ($200\,\mathrm{MeV}/c$);
- the $\mathrm{J}/\psi\mathrm{K_S^0}$ vertex χ^2 must be less than 16;
- the $\mathrm{J}/\psi\mathrm{K_S^0}$ mass must be within $\pm 60\,\mathrm{MeV}/c^2$ of the true $\mathrm{B^0}$ mass.

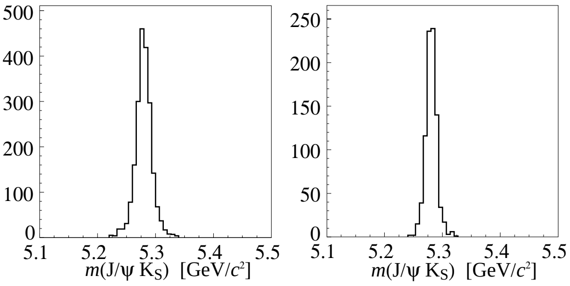

Figure 9.15: Invariant mass distribution for $\mathrm{B^0} \to \mathrm{J}/\psi(\mu\mu)\mathrm{K_S^0}$ signal events where the $\mathrm{K_S^0}$ is reconstructed as two downstream (left) or two long (right) tracks.

The $\mathrm{B^0}$ mass distribution obtained after this selection has a core resolution of $12\,\mathrm{MeV}/c^2$ ($9\,\mathrm{MeV}/c^2$) and is shown in Fig. 9.15. Core resolutions are $150\,\mu$m ($120\,\mu$m) for the z coordinate of the $\mathrm{B^0}$ vertex, and 41 fs (46 fs) for the $\mathrm{B^0}$ proper time.

$\mathrm{B^0}$ candidates are also reconstructed and selected using $\mathrm{K_S^0}$ formed with one long track and one upstream track. These events have somewhat worse $\mathrm{B^0}$ mass resolution, which can however be recovered by applying a mass-constrained fit to the $\mathrm{K_S^0}$. The relative contributions of the various $\mathrm{K_S^0}$ categories in the final $\mathrm{B^0}$ sample are 65% (downstream-downstream), 26% (long-long) and 9% (long-upstream).

No forward $\mathrm{b\overline{b}}$ event pass the selection out of 10^7 generated events. If the $\mathrm{B^0}$ mass window is enlarged to $\pm 600\,\mathrm{MeV}/c^2$, 37 candidates are accepted, which are mainly formed using a true J/ψ originating away from the primary vertex. The decay modes $\mathrm{B^0} \to \mathrm{J}/\psi(\mu\mu)\mathrm{K^{*0}}$, $\mathrm{B_s^0} \to \mathrm{J}/\psi(\mu\mu)\phi$ and prompt $\mathrm{J}/\psi \to \mu^+\mu^-$ have been studied as a source of background, and were found to give a negligible contribution.

9.3.4 $\mathrm{B^0} \to \mathrm{J}/\psi(\mathrm{ee})\mathrm{K_S^0}$

Oppositely-charged pairs of reconstructed and identified electrons are used to reconstruct $\mathrm{J}/\psi \to \mathrm{e^+e^-}$ candidates (see Sect. 8.5). In order to suppress ghosts, both electron tracks in a pair are required to have $p_\mathrm{T} > 0.5\,\mathrm{GeV}/c$ and at least one of them $p_\mathrm{T} > 1.5\,\mathrm{GeV}/c$. Only pairs which form a common vertex with $\chi^2 < 8$ and have an invariant mass (after the Bremsstrahlung correction explained in Fig. 8.16) between $2.7\,\mathrm{GeV}/c^2$ and

3.2 GeV/c^2 are kept as J/ψ candidates. This mass window is asymmetric to take into account the fact that some Bremsstrahlung photons are not recovered. The sample of J/ψ selected in this way has a mass resolution of 59 MeV/c^2 and a core vertex resolution along z of 148 μm.

The K^0_S candidates are again selected in three different categories. In the following we only describe the cuts applied on $B^0 \to J/\psi(ee)K^0_S$ candidates involving K^0_S formed with two downstream tracks, and the values in parentheses apply to the category with two long tracks (see [119] for details):

- the p_T of the K^0_S must exceed 0.8 (0.5) GeV/c;
- the B^0 vertex χ^2 must be less than 30 (16);
- the significance of the distance between the B^0 vertex and the primary vertex must be greater than 3.5 (5);
- the impact parameter significance of each pion from the K^0_S with respect to the primary vertex must be larger than 3 (4), and that each electron from the J/ψ larger than 2 (1.5);
- the impact parameter significance of the B^0 with respect to the primary vertex must be smaller than 4;
- the significance of the distance between the K^0_S vertex and the B^0 vertex must be greater than 12 (10);
- the unsigned impact parameter significance of the K^0_S with respect to the primary vertex must be greater than 0 (1);
- the difference between the reconstructed masses of the B^0 and J/ψ candidates must be within ±100 (80) MeV/c^2 of its true value.

The latter cut is designed to compensate for the electron Bremsstrahlung losses, and is more effective than a simple cut on the reconstructed B^0 mass.

Figure 9.16 shows the distribution of the reconstructed mass after all cuts, with a core resolution of 20 MeV/c^2 (17 MeV/c^2). The B^0 proper-time core resolution is found to be 50±3 fs (51±3 fs).

The $B^0 \to J/\psi(ee)K^{*0}$, $B^0_s \to J/\psi(ee)\phi$, $B^0_s \to J/\psi(ee)\eta$ decay modes were studied as source of background and found to give a negligible contribution. All prompt J/ψ events in a sample of 350k events are eliminated. This selection was also applied to a 10^7 forward $b\bar{b}$ and 2 background events pass the cuts. This number goes up to 23 in a B^0 mass window which is 10 times wider.

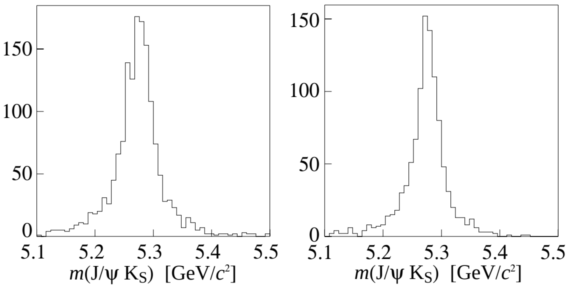

Figure 9.16: Invariant mass distribution for $B^0 \to J/\psi(ee)K^0_S$ signal events where the K^0_S is reconstructed as two downstream (left) or two long (right) tracks.

9.3.5 $B^0_s \to J/\psi\phi$

The reconstruction and selection of $B^0_s \to J/\psi\phi$ has been studied for both the dimuon and dielectron channels [120]. We describe here only the former.

The J/ψ candidates are formed by taking opposite sign charged tracks, with a transverse momentum larger than 0.5 GeV/c, identified as muons by the muon system. The pair is required to have an invariant mass within ±50 MeV/c^2 of the J/ψ mass and the fit to a common vertex must have a χ^2 of less than 9. Similarly, for ϕ candidates, we again require two charged tracks with a transverse momentum of at least 0.5 GeV/c, but which are identified by the RICH as kaons, have an invariant mass within ±20 MeV/c^2 of the ϕ mass, and form a common vertex with $\chi^2 < 40$. In addition, we require that the ϕ candidate has a momentum in excess of 12 GeV/c. Finally we combine the J/ψ and ϕ into a B^0_s candidate, requiring that the four charged tracks form a common vertex with a χ^2 of less than 20. The impact parameter of the B^0_s candidate with respect to the primary vertex has to be less than 0.4 cm.

To reduce the large background from prompt J/ψ and ϕ production, we determine the proper time (and its resolution) from a fit which requires consistency between the proper time, the momentum and the vector between the production and decay vertices of the B^0_s candidate. We require that the χ^2 of this fit be less than 100, the proper-time resolution less than 100 fs, and the proper-time significance larger than five. These cuts remove all events from a simulated sample of 350k events with a prompt J/ψ in the forward direction.

The B^0_s meson mass peak obtained from signal Monte Carlo after this selection is shown in Fig. 9.17 (a). The 15 MeV/c^2 width, obtained from a single Gaussian fit, could be reduced with a con-

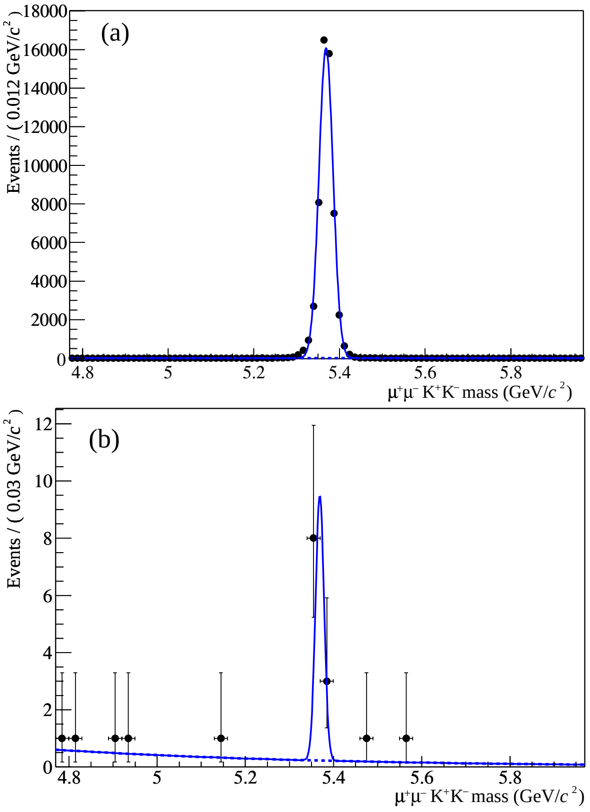

Figure 9.17: Invariant mass distribution of offline-selected $B_s^0 \to J/\psi(\mu\mu)\phi$ candidates in (a) signal events, and (b) inclusive $b\overline{b}$ events.

straint on the J/ψ mass. Conservatively, we assume a signal mass window of $\pm 50\,\mathrm{MeV}/c^2$ around the true B_s^0 mass.

The inclusive $b\overline{b}$ background mass distributions, applying the same cuts is presented in Fig. 9.17 (b). Eleven events out of 10^7 forward $b\overline{b}$ events passed the selection, all of which contain a true signal decay. Enlarging the mass window to $\pm 600\,\mathrm{MeV}/c^2$, we find 7 additional (background) events, from which we determine the $b\overline{b}$ background-to-signal ratio to be less than 0.3.

Figure 9.18 shows the proper-time resolution for selected signal decays. The width obtained from a single Gaussian fit is 38 fs. The curve superimposed on the figure is a parametrization using the event-by-event uncertainty on the proper time estimated from the track covariance matrices. It corresponds to the projection onto the proper-time residual of a pull distribution described by a double Gaussian with widths of 1.02 (90%) and 2.3 (10%) respectively, showing that the uncertainty is properly estimated for the majority of the events.

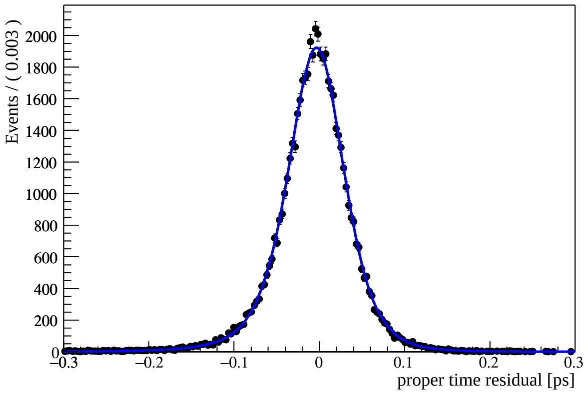

Figure 9.18: Proper-time resolution of offline-selected $B_s^0 \to J/\psi(\mu\mu)\phi$ signal events.

9.3.6 $\mathbf{B^0 \to K^{*0}\gamma}$ and $\mathbf{B_s^0 \to \phi\gamma}$

Radiative B decays like $B^0 \to K^{*0}\gamma$ and $B_s^0 \to \phi\gamma$ involve the $b \to s\gamma$ quark transition which is loop-suppressed in the Standard Model. New physics could therefore show up in these decays, for example with sizeable CP violation effects.

For the reconstruction of the $B^0 \to K^{*0}\gamma$ ($B_s^0 \to \phi\gamma$) decay [102], we look for two oppositely-charged tracks to form the $K^{*0} \to K^+\pi^-$ ($\phi \to K^+K^-$) decay, and combine them with an energetic photon candidate. Requesting a high transverse energy photon suppresses drastically the dominant background from low energy photons. However, the two photons from an energetic π^0 can produce a single merged cluster in the electromagnetic calorimeter, and thus fake an energetic photon. In particular, the decay $B^0 \to K^{*0}\pi^0$ ($B_s^0 \to \phi\pi^0$) could constitute a potentially dangerous background. This background can be evaluated and discriminated using the different polarization of the vector meson.

The offline selection criteria for the $B^0 \to K^{*0}\gamma$ ($B_s^0 \to \phi\gamma$) reconstruction are the following:

- the two charged tracks must be identified, satisfying $\Delta \ln \mathcal{L}_{\pi K} > 0$ for the pion hypothesis, and $\Delta \ln \mathcal{L}_{K\pi} > 1$ (2) and $\Delta \ln \mathcal{L}_{Kp} > 1$ (2) for the kaon hypothesis;

- the significance of the impact parameter of each of the two tracks with respect to each primary vertex must exceed 4 (2);

- the χ^2 of the two-track vertex fit must be less than 49;

- the invariant mass of the two-track combination must be within $\pm 60\,\mathrm{MeV}/c^2$ ($\pm 10\,\mathrm{MeV}/c^2$) of the true K^{*0} (ϕ) mass;

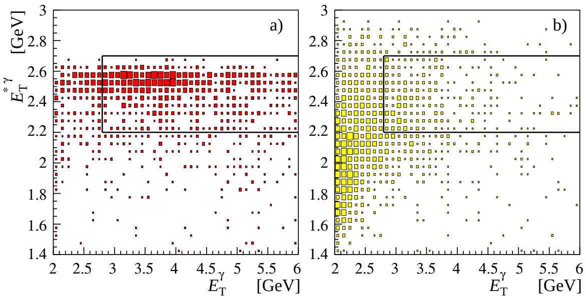

Figure 9.19: Transverse energy of the photon candidate $E_T^{*\gamma}$ with respect to the B^0 momentum direction versus the transverse energy of the photon candidate E_T^{γ}: (a) for $B^0 \to K^{*0}\gamma$, (b) for $b\overline{b}$ events; the selection cuts are superimposed.

- the transverse energy of the photon candidate E_T^{γ} must exceed of 2.8 GeV;
- the transverse energy of the photon candidate $E_T^{*\gamma}$ with respect to the flight direction of the B candidate must be between 2.2 (2.0) and 2.7 GeV;
- the angle between the B-candidate momentum and the direction defined by B-production and B-decay vertices must be less than 6 mrad (15 mrad);
- the polarization angle θ_{hel} between the B and the K^+ candidates in the K^{*0} (ϕ) rest frame must satisfy $|\cos\theta_{\mathrm{hel}}| < 0.7$;
- the reconstructed B mass must be within $\pm 0.2\,\mathrm{GeV}/c^2$ of the expected value.

The cuts were chosen to maximize the signal significance, estimated with the $S/\sqrt{B}$ ratio. To illustrate the discriminating power between signal and background, Fig. 9.19 shows the distributions of the transverse energies E_T^{γ} versus $E_T^{*\gamma}$ of the photon candidates for $B^0 \to K^{*0}\gamma$ signal and inclusive $b\overline{b}$ events.

The mass distribution of selected and triggered $B^0 \to K^{*0}\gamma$ candidates is shown in Fig. 9.20. The B^0 (B_s^0) mass resolution is $64 \pm 2\,\mathrm{MeV}/c^2$ ($65 \pm 4\,\mathrm{MeV}/c^2$).

The contribution from $B^0 \to K^{*0}\pi^0$ ($B_s^0 \to \phi\pi^0$) background is estimated to be less than 2.2% (4.0%) of the signal, assuming a ratio of branching fractions of $\mathrm{BR}_{\pi^0}/\mathrm{BR}_{\gamma} < 8\%$ [121]. The combinatorial background was studied with a sample of 10^7 forward $b\overline{b}$ events; none of them passes the selection cuts, even when the B mass window is enlarged to span the interval from 4.5 to 6.0 GeV/c^2.

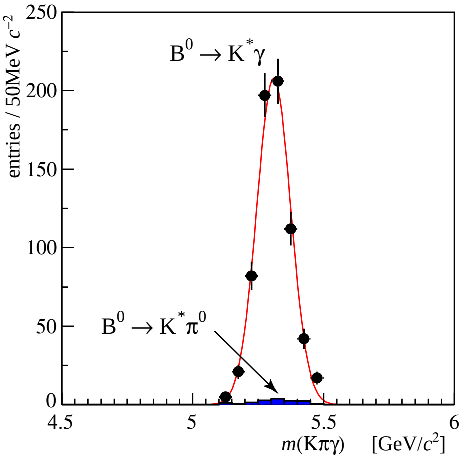

Figure 9.20: B^0 mass after selection and trigger for $B^0 \to K^{*0}\gamma$ signal and $B^0 \to K^{*0}\pi^0$ background.

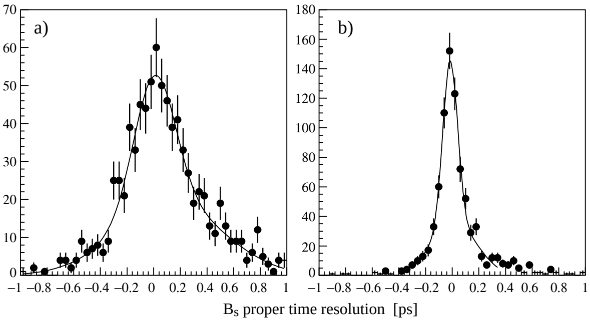

Figure 9.21: $B_s^0 \to \phi\gamma$ proper-time resolution: (a) simple vertex fit, (b) direction vertex fit (see text).

CP violation studies with $B_s^0 \to \phi\gamma$ require a proper-time analysis, since the final state is not flavour-specific. However, the $\phi \to K^+K^-$ decay provides a rather poor B_s^0 vertex and proper-time determination, because of the small opening angle between the two kaons. This can be improved by a special choice of selection cuts and vertex fitting procedure. Figure 9.21 (a) shows the proper-time resolution after removing the cut on $E_T^{*\gamma}$ and requiring $E_T^{\gamma} > 3.2\,\mathrm{GeV}$, while Fig. 9.21 (b) shows the additional improvement obtained when applying a vertex fit where the B_s^0 is constrained to originate from the primary vertex (“direction” fit). After this, the resolution can be described as a double Gaussian with widths of 62 ± 6 fs (60%) and 200 ± 30 fs (40%). Furthermore the core component can be nicely isolated by requiring $\cos\theta^* < -0.4$, where θ^* is the B_s^0 decay angle.

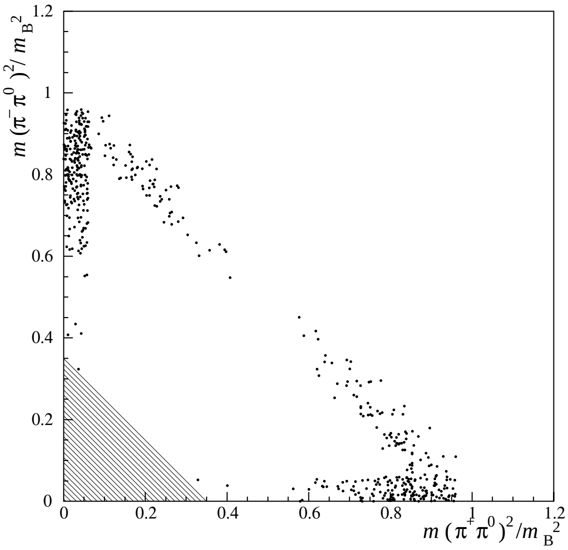

Figure 9.22: Normalized Dalitz plot for the signal events after all selection cuts, involving both resolved π^0 and merged π^0. The hatched region is excluded from the analysis.

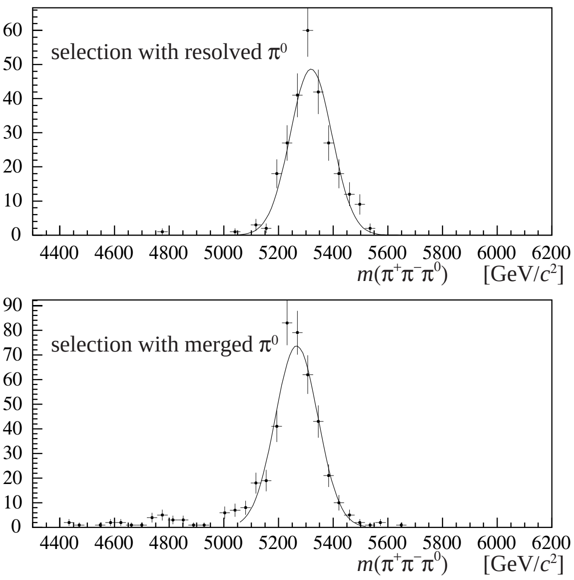

Figure 9.23: The $B^0 \to \pi^+\pi^-\pi^0$ mass distributions obtained with signal Monte Carlo for the selection involving resolved π^0 (top) and merged π^0 (bottom). The B^0 mass resolutions are both $\sim 75\,\mathrm{MeV}/c^2$.

9.3.7 $B^0 \to \rho\pi$

In order to be able to extract unambiguously the angle $\alpha \equiv \pi - \beta - \gamma$ of the unitarity triangle, it is important to have access to the ρ-interference regions of the $B^0 \to \pi^+\pi^-\pi^0$ Dalitz plot. These regions correspond to different kinematical regimes. The region where $m^2_{\pi^+\pi^0} + m^2_{\pi^-\pi^0} > 10\,\mathrm{GeV}^2/c^4$ is characterized by the presence of an energetic π^0, one fast charged track and a slow one (in the interference region itself, one of the charged tracks is almost at rest in the B^0 center-of-mass frame). The other part of the Dalitz plot, defined by $m^2_{\pi^+\pi^0} + m^2_{\pi^-\pi^0} < 10\,\mathrm{GeV}^2/c^4$ and corresponding to the hatched area of Fig. 9.22, is populated by events with two fast charged tracks and a slow π^0. This region has a large combinatorial background from soft π^0's and is not included in the selection presented here [103].

Only events with exactly one reconstructed primary vertex are used. The π^0 candidates are reconstructed either as "resolved π^0" or as "merged π^0" (see Sect. 8.7), and selected in the mass regions $105 < m_{\pi^0} < 165\,\mathrm{MeV}/c^2$ and $105 < m_{\pi^0} < 175\,\mathrm{MeV}/c^2$ respectively. In order to reduce the combinatorial background, their transverse momenta are required to be larger than $1.5\,\mathrm{GeV}/c$. They are combined with charged pions of transverse momenta greater than $150\,\mathrm{MeV}/c$ to form $\pi^+\pi^-\pi^0$ combinations which are selected as B^0 candidates under the following conditions:

- the vertex formed by two charged tracks must be displaced by more than $500\,\mu$m with respect to the primary vertex;

- the slowest (fastest) track should have an impact parameter significance $\mathrm{IP}_1/\sigma_{\mathrm{IP}_1}$ ($\mathrm{IP}_2/\sigma_{\mathrm{IP}_2}$) in excess of 2 (3) with respect to the primary vertex;

- the angle θ_{B} between the B^0 line of flight and the B^0 momentum should be smaller than 20 mrad;

- the distances in space d_1 and d_2 between the charged-pion tracks and the B^0 direction should be smaller than $100\,\mu$m;

- one of the three two-pion invariant masses should be less than $1.2\,\mathrm{GeV}/c^2$.

In addition, in order to reject as much as possible of the large $b\overline{b}$ combinatorial background while keeping a reasonable signal efficiency, a combined variable has been designed. It is constructed as the ratio of the product of the probability density functions for the signal and background of the following discriminating variables: $\mathrm{IP}_1/\sigma_{\mathrm{IP}_1}$, $\mathrm{IP}_2/\sigma_{\mathrm{IP}_2}$, d_1, d_2, θ_{B}, the π^0 transverse momentum, the B^0 transverse momentum and the arithmetic sum of the transverse momenta of the three pions with respect to the B^0 direction. This combination does not take into account the correlations between the variables and as such cannot be seen as a true probability. However it offers an easy way to optimally reduce the large combinatorial background which is due to the presence of a low momentum track in conjunction with the absence of tight mass constraints. It has been designed keeping in mind the need to preserve the ρ-interference regions in the Dalitz plot. After cutting on this combined variable (computed separately for the selection involving resolved and merged π^0) the normalized Dalitz plot and the B^0 mass plots obtained with signal Monte Carlo are shown in Figs. 9.22 and 9.23 respectively. The proper-time resolution is approximately 80 fs. After all cuts including trigger, 64% of the selected signal events are reconstructed with a merged π^0.

Monte Carlo signal events were generated with a $\rho^+\pi^-$:$\rho^-\pi^+$:$\rho^0\pi^0$ mixture of 1.00:0.39:0.39. The proportion of $\rho^0\pi^0$ is therefore inflated compared to model estimates [122]. This could lead to the efficiency of the analyses described above being optimistic by as much as 12%. To compensate for this we assume a $B^0 \to \rho\pi$ branching ratio of 2×10^{-5}, to be compared to $BR(B^0 \to \rho^\pm\pi^\mp) = (2.27 \pm 0.25) \times 10^{-5}$ measured at the B factories [123, 121].

The final selection has been applied to a sample of 10^7 forward $b\overline{b}$ events. In an enlarged B^0 mass window ($\pm 950\,\mathrm{MeV}/c^2$ around the true B^0 mass) four events are kept by the selection using resolved π^0 and one by the selection using merged π^0. From these numbers, we compute 90% CL upper limits for the background-over-signal ratio of 15 and 5.3, respectively, or 7.1 on average.

9.3.8 $B^0 \to \overline{D}^0 K^{*0}$

The simultaneous measurement of the rates for the decays $B^0 \to \overline{D}^0(K^+\pi^-)K^{*0}$, $B^0 \to D^0_{CP}(K^+K^-)K^{*0}$, $B^0 \to D^0(\pi^+K^-)K^{*0}$ and their CP conjugates, where $K^{*0} \to K^+\pi^-$, allows the CKM angle γ to be extracted, without the need of flavour tagging or proper-time determination. The reconstruction and selection of the first two modes was studied [124] using $B^0 \to \overline{D}^0(K\pi)K^{*0}$ and $B^0 \to \overline{D}^0(KK)K^{*0}$ events, and is summarized here. The efficiency for selecting $B^0 \to D^0K^{*0}$ is assumed to be equal to that of $B^0 \to \overline{D}^0K^{*0}$.

Table 9.3: Cuts applied to select $B^0 \to \overline{D}^0(K\pi)K^{*0}$ and $B^0 \to \overline{D}^0(KK)K^{*0}$ events. Transverse momenta (p_T) are in MeV/c, and impact parameters (IP) are with respect to the primary vertex, unless specified otherwise.

Requirement	$K\pi$	KK
$\overline{D}^0$ mass-constrained vertex $\chi^2 <$	25	25
B^0 vertex χ^2 $<$	10	10
IP_B/σ_{IP_B} $<$	3.8	5.0
$\max(IP_{K^*}/\sigma_{IP_{K^*}}, IP_D/\sigma_{IP_D})$ $>$	1	1
$\min_{i=1}^4(IP_i/\sigma_{IP_i})$ $>$	2.4	2.3
IP_D/σ_{IP_D} w.r.t. K^{*0} vertex $<$	5	3.5
θ (mrad) $<$	45	14
$\min(p_{T K^*}, p_{T D})$ $>$	900	900
$\max(p_{T K^*}, p_{T D})$ $>$	0	2000
$\sum_{i=1}^4 \ln(p_{T i})$ $>$	27.7	24.0
$\sum_{i=1}^4 \ln(IP_i/\sigma_{IP_i})$ $>$	7.0	5.0

Tracks are identified as kaons and pions using the combined particle-identification information. K^{*0} ($\overline{D}^0$) candidates are selected as $K^+\pi^-$ ($K^+\pi^-$ or K^+K^-) pairs having a good quality vertex with $\chi^2 < 20$ and an invariant mass within $\pm 150\,\mathrm{MeV}/c^2$ ($\pm 50\,\mathrm{MeV}/c^2$) of the nominal K^{*0} ($\overline{D}^0$) mass. For the $B^0 \to \overline{D}^0(K\pi)K^{*0}$ case where the combinatorial background is more severe the K^{*0} mass cut is tightened to $\pm 80\,\mathrm{MeV}/c^2$. The momentum of the $\overline{D}^0$ candidates is improved by refitting the two-track vertex under the D^0 mass constraint. The B^0 candidates, formed with $\overline{D}^0K^{*0}$ pairs are required to survive cuts applied on the following variables (cut values are given in Table 9.3):

- the χ^2 of the B^0 vertex;
- the impact parameter significances IP/σ_{IP} of the B^0, $\overline{D}^0$, K^{*0} and their daughters with respect to the primary vertex;
- the impact parameter significance of the $\overline{D}^0$ with respect to the K^{*0} vertex;
- the angle θ between the B^0 momentum and the flight direction defined by the primary and B^0 decay vertices;
- the $\overline{D}^0$ and K^{*0} transverse momenta p_T;
- the sum of $\ln(p_T)$ and the sum of $\ln(IP/\sigma_{IP})$, where the sums run over the four final state tracks.

The requirements on the latter two variables are very effective in rejecting the inclusive $b\overline{b}$ background, as shown in Fig. 9.24.

The invariant $\overline{D}^0K^{*0}$ mass distribution for selected B^0 candidates in $B^0 \to \overline{D}^0(K\pi)K^{*0}$ events is displayed in Fig. 9.25; a D^0 mass constraint is applied, which improves the B^0 mass resolution

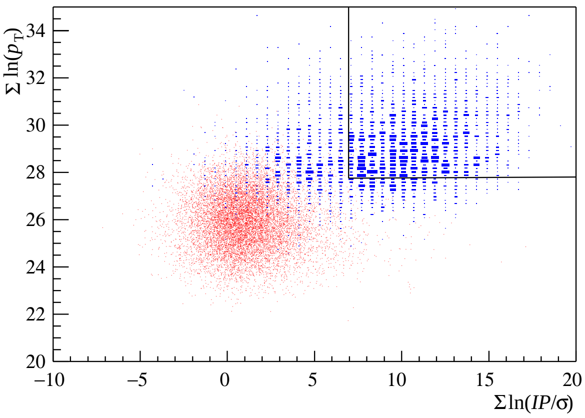

Figure 9.24: The sum of the logarithms of the $p_{\rm T}$ (in MeV/c) for the 4 final state particles forming a $\rm B^0 \to \overline{D}{}^0(K\pi)K^{*0}$ candidate versus the sum of the logarithms of their impact parameter significances, for inclusive $\rm b\overline{b}$ background (red points at small values) and signal (blue boxes spread at higher values). The lines indicate the selection cuts on these two variables.

(single Gaussian fit) from 15 to 11 MeV/c^2. The $\rm B^0 \to \overline{D}{}^0(KK)K^{*0}$ channel has a similar resolution. After all the above cuts, no forward $\rm b\overline{b}$ background event (from a sample of 10^7) falls within ±500 MeV/c^2 of the true $\rm B^0$ mass. For the final selection, $\rm B^0$ candidates must have a reconstructed mass within ±25 MeV/c^2 of the true $\rm B^0$ mass.

9.4 Summary of event yields

This section summarizes the efficiencies, signal yields and background estimates for various B-decay channels. The following channels are included, in addition to those described in the previous section:

- $\rm B^0 \to D^{*-}\pi^+$ ($\rm D^{*-} \to \bar{D}{}^0\pi^- \to K^+\pi^-\pi^-$) [125] for another way of measuring the angle γ;
- $\rm B^0_s \to J/\psi(\mu\mu)\eta$ ($\eta \to \gamma\gamma$) [126] and $\rm B^0_s \to \eta_c\phi$ ($\eta_{\rm c} \to \pi^+\pi^-\pi^+\pi^-, \pi^+\pi^-K^+K^-$) [127] as pure CP eigenstates to increase the sensitivity, together with $\rm B^0_s \to J/\psi\phi$, to the $\rm B^0_s$ mixing phase;
- $\rm B^0 \to \mu^+\mu^-K^{*0}$ [128] and $\rm B^0_s \to \phi\phi$ [129] as interesting channels to look for new physics in loop diagrams;
- $\rm B^0 \to J/\psi K^{*0}$ [130] and $\rm B^+ \to J/\psi K^+$ [120], which can be used as control channels; and

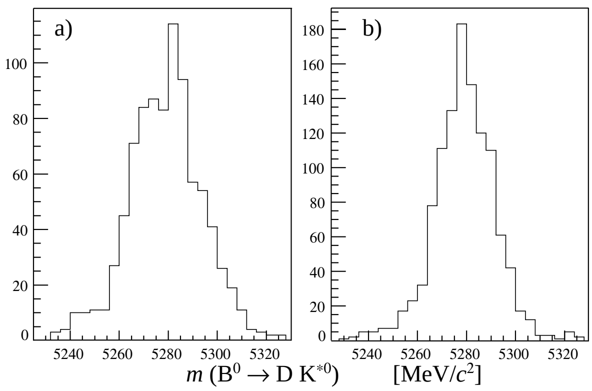

Figure 9.25: Invariant mass distribution of selected $\rm B^0 \to \overline{D}{}^0(K\pi)K^{*0}$ candidates in signal events, before (a) and after (b) $\rm D^0$ mass constraint.

- $\rm B_c^+ \to J/\psi(\mu\mu)\pi^+$ [131] for high statistics measurements of the $\rm B_c^+$ mass and lifetime.

In all these channels, $\rm K^{*0}$ and ϕ mesons are reconstructed in the $\rm K^+\pi^-$ and $\rm K^+K^-$ mode respectively. Only long tracks are used, with the exception of the "slow" pions from $\rm D^*$ decays which are also reconstructed as upstream tracks; the use of upstream tracks increases the yield of fully reconstructed $\rm B^0 \to D^{*-}\pi^+$ decays by ∼15% at constant purity [125]. A preliminary study has indicated that the $\rm B^0 \to D^{*-}\pi^+$ yield can be increased by a factor 4 by using an inclusive reconstruction of the $\rm \overline{D}{}^0$, but that is not applied here.

The total signal efficiency is obtained as the fraction of events containing a signal B decay that are triggered, reconstructed, and selected with offline cuts for physics analysis. It is given by various factors. A possible way to break it down is

$$\varepsilon_{\rm tot} = \varepsilon_{\rm det} \times \varepsilon_{\rm rec/det} \times \varepsilon_{\rm sel/rec} \times \varepsilon_{\rm trg/sel}\,,$$

where $\varepsilon_{\rm det}$ is the detection efficiency[1] (including the geometrical acceptance in 4π and all material effects in the detector, like secondary interactions), $\varepsilon_{\rm rec/det}$ is the reconstruction efficiency on detected events (track finding efficiency and neutral cluster reconstruction[2]), $\varepsilon_{\rm sel/rec}$ is the efficiency of the offline selection cuts on the reconstructed events (designed to discriminate against

---

[1] In practice $\varepsilon_{\rm det}$ contains everything which is not accounted for by the other factors, and is computed as $\varepsilon_{\rm tot}/(\varepsilon_{\rm rec/det} \times \varepsilon_{\rm sel/rec} \times \varepsilon_{\rm trg/sel})$.

[2] For photons we require $E_{\rm T} > 200$ MeV in the definition of the numerator of $\varepsilon_{\rm det}$, while we do not include the loss due to conversions; the latter is accounted for in $\varepsilon_{\rm rec/det}$ since the reconstruction of photons converted before the magnet will be attempted in the future.

Table 9.4: Summary of the signal efficiencies, untagged annual signal yields and background-over-signal (B/S) ratios from inclusive $\mathrm{b\overline{b}}$ events. The meaning of the breakdown of the total efficiency $\varepsilon_{\mathrm{tot}}$ is explained in the text. The annual signal yields include both the indicated decays and their charge conjugates. Quoted errors on B/S are from the Monte Carlo statistics; estimates based on less than 10 Monte Carlo background events are quoted as 90% CL upper limits.

Decay channel	Factors (in %) forming $\varepsilon_{\mathrm{tot}}$(in %) $\varepsilon_{\mathrm{det}} \times \varepsilon_{\mathrm{rec/det}} \times \varepsilon_{\mathrm{sel/rec}} \times \varepsilon_{\mathrm{trg/sel}} = \varepsilon_{\mathrm{tot}}$				Assumed visible BR (in 10^{-6})	Annual signal yield	B/S ratio from incl. $\mathrm{b\overline{b}}$ back.
	$\varepsilon_{\mathrm{det}}$	$\varepsilon_{\mathrm{rec/det}}$	$\varepsilon_{\mathrm{sel/rec}}$	$\varepsilon_{\mathrm{trg/sel}}$	$\varepsilon_{\mathrm{tot}}$			
$\mathrm{B^0 \to \pi^+\pi^-}$	12.2	91.6	18.3	33.6	0.688	4.8	26. k	< 0.7
$\mathrm{B^0 \to K^+\pi^-}$	12.2	92.0	25.2	33.2	0.94	18.5	135. k	0.16 ± 0.04
$\mathrm{B^0_s \to \pi^+K^-}$	12.0	92.1	13.5	36.7	0.548	4.8	5.3 k	< 1.3
$\mathrm{B^0_s \to K^+K^-}$	12.0	92.5	28.6	31.1	0.988	18.5	37. k	0.31 ± 0.10
$\mathrm{B^0 \to \rho\pi}$	6.0	65.5	2.0	36.0	0.028	20.	4.4 k	< 7.1
$\mathrm{B^0 \to D^{*-}\pi^+}$	9.4	77.7	18.5	27.4	0.370	71.	206. k	< 0.3
$\mathrm{B^0 \to \overline{D}^0(K\pi)K^{*0}}$	5.3	81.8	22.9	35.4	0.354	1.2	3.4 k	< 0.5
$\mathrm{B^0 \to D^0_{CP}(KK)K^{*0}}$	5.2	81.4	29.4	31.2	0.390	0.19	0.59k	< 2.9
$\mathrm{B^0_s \to D^-_s\pi^+}$	5.4	80.6	25.0	31.1	0.337	120.	80. k	0.32 ± 0.10
$\mathrm{B^0_s \to D^{\mp}_s K^{\pm}}$	5.4	82.0	20.6	29.5	0.269	10.	5.4 k	< 1.0
$\mathrm{B^0 \to J/\psi(\mu\mu)K^0_S}$	6.5	66.5	53.5	60.5	1.39	19.8	216. k	0.80 ± 0.10
$\mathrm{B^0 \to J/\psi(ee)K^0_S}$	5.8	60.8	17.7	26.5	0.164	20.0	25.6 k	0.98 ± 0.21
$\mathrm{B^0 \to J/\psi(\mu\mu)K^{*0}}$	7.2	82.7	35.1	69.9	1.462	59.	670. k	0.17 ± 0.03
$\mathrm{B^+ \to J/\psi(\mu\mu)K^+}$	11.9	89.6	44.8	68.7	3.28	68.	1740. k	0.37 ± 0.02
$\mathrm{B^0_s \to J/\psi(\mu\mu)\phi}$	7.6	82.5	41.6	64.0	1.672	31.	100. k	< 0.3
$\mathrm{B^0_s \to J/\psi(ee)\phi}$	6.7	76.5	22.0	28.0	0.315	31.	20. k	0.7 ± 0.2
$\mathrm{B^0_s \to J/\psi(\mu\mu)\eta}$	10.1	69.6	10.1	64.8	0.461	7.6	7.0 k	< 5.1
$\mathrm{B^0_s \to \eta_c\phi}$	2.6	69.5	15.8	27.	0.078	21.	3.2 k	< 1.4
$\mathrm{B^0_s \to \phi\phi}$	6.7	79.7	37.9	23.2	0.470	1.3	1.2 k	< 0.4
$\mathrm{B^0 \to \mu^+\mu^-K^{*0}}$	7.2	82.4	16.1	73.5	0.704	0.8	4.4 k	< 2.0
$\mathrm{B^0 \to K^{*0}\gamma}$	9.5	86.8	5.0	37.8	0.156	29.	35. k	< 0.7
$\mathrm{B^0_s \to \phi\gamma}$	9.7	86.3	7.6	34.3	0.220	21.2	9.3 k	< 2.4
$\mathrm{B^+_c \to J/\psi(\mu\mu)\pi^+}$	11.5	89.3	20.7	60.8	1.30	680.	14.0 k	< 0.8

background), and $\varepsilon_{\mathrm{trg/sel}}$ is the combined L0+L1 efficiency on offline-selected events. The high-level trigger (HLT), which is expected to have a very high efficiency, is not considered here. Flavour tagging efficiency is not included here and is discussed in Sect. 9.5. The values of all these different factors, together with their products, are given in Table 9.4. As expected, both $\varepsilon_{\mathrm{det}}$ and $\varepsilon_{\mathrm{rec/det}}$ are larger for lower multiplicity channels. Track reconstruction efficiencies are defined and discussed in Sect. 7.3, while trigger performance is discussed in a separate TDR [3]. The selection efficiencies are fairly large (typically between 10% and 30%), given the high background rejection that needs to be achieved.

The annual signal event yield is computed as

$$S = L_{\mathrm{int}} \times \sigma_{\mathrm{b\overline{b}}} \times 2 \times f_{\mathrm{B}} \times \mathrm{BR}_{\mathrm{vis}} \times \varepsilon_{\mathrm{tot}}\,, \qquad (9.4)$$

for a nominal annual integrated luminosity of $L_{\mathrm{int}} = 2\,\mathrm{fb}^{-1}$ ($10^7\,\mathrm{s}$ at $2 \times 10^{32}\,\mathrm{cm}^{-2}\mathrm{s}^{-1}$) and a $\mathrm{b\overline{b}}$ production cross section of $\sigma_{\mathrm{b\overline{b}}} = 500\,\mu\mathrm{b}$. The probability for a $\overline{\mathrm{b}}$-quark to hadronize into a hadron is assumed to be $f_{\mathrm{B}} = 39.1\%$ for B^0 or B^+ [121], 10.0% for $\mathrm{B}^0_{\mathrm{s}}$ [121], and 8×10^{-4} for $\mathrm{B}^+_{\mathrm{c}}$ [131]. The factor 2 takes into account the production of both b- and $\overline{\mathrm{b}}$-hadrons. The visible branching ratio $\mathrm{BR}_{\mathrm{vis}}$, given in Table 9.4, is the product of all branching ratios involved in the b-hadron decay of interest. The individual branching ratios are assumed to be equal to the central values given in Table 9.5 and [121]. Note that the $\mathrm{J}/\psi \to \ell^+\ell^-$ branching ratios are increased by the $\mathrm{J}/\psi \to \ell^+\ell^-\gamma$ radiative contribution, which is also included in the Monte Carlo signal samples. Furthermore, all branching ratios are taken to be averages for the specified decay and its CP conjugate.

The estimates of the inclusive $\mathrm{b\overline{b}}$ background levels, quoted in the last column of Table 9.4, are assumed to correspond to the most significant contribution to the combinatorial background. They are based on a sample of 10^7 inclusive $\mathrm{b\overline{b}}$ events where at least one b-hadron is emitted forward within 400 mrad of the beam line (we assume that all other events do not contribute). This sample of fully-simulated events corresponds to only 4 minutes of data-taking under nominal conditions. To cope with the limited Monte Carlo statistics, the B mass cut is relaxed when analyzing these events, and the background under the B mass peak is estimated assuming a linear dependence on the reconstructed B mass, after removal of events with a true signal decay (or similar decays which will necessarily lead to a reconstructed mass outside the tight window). In addition, in order to further increase the effective $\mathrm{b\overline{b}}$ statistics, all B/S ratios are estimated without applying the trigger. It should be noted that, for most channels, this estimation is done using the same samples as the ones used to optimize the cuts, hence the procedure is not unbiased.

Table 9.5: Assumed branching ratios (branching ratios not listed here are taken from [121]).

Decay	BR (in 10^{-6})	estimated as	Ref.
$\mathrm{B}^0_{\mathrm{s}} \to \mathrm{K}^+\mathrm{K}^-$	18.5 ± 1.2	$\mathrm{B}^0 \to \mathrm{K}^+\pi^-$	[121]
$\mathrm{B}^0_{\mathrm{s}} \to \pi^+\mathrm{K}^-$	4.8 ± 0.5	$\mathrm{B}^0 \to \pi^+\pi^-$	[121]
$\mathrm{B}^0 \to \rho\pi$	20	see Sect. 9.3.7	
$\mathrm{B}^0 \to \mathrm{D}^0\mathrm{K}^{*0}$	7.0	see Sect. 9.6.5	
$\mathrm{B}^0 \to \mathrm{D}^0_{\mathrm{CP}}\mathrm{K}^{*0}$	35	see Sect. 9.6.5	
$\mathrm{D}^0_{\mathrm{CP}} \to \mathrm{K}^+\mathrm{K}^-$	8240	$2 \times (\mathrm{D}^0 \to \mathrm{K}^+\mathrm{K}^-)$	[121]
$\mathrm{B}^0_{\mathrm{s}} \to \mathrm{D}^-_{\mathrm{s}}\pi^+$	2760 ± 250	$\mathrm{B}^0 \to \mathrm{D}^-\pi^+$	[121]
$\mathrm{B}^0_{\mathrm{s}} \to \mathrm{D}^-_{\mathrm{s}}\mathrm{K}^+$	200 ± 60	$\mathrm{B}^0 \to \mathrm{D}^-\mathrm{K}^+$	[121]
$\mathrm{B}^0_{\mathrm{s}} \to \mathrm{D}^+_{\mathrm{s}}\mathrm{K}^-$	27 ± 10	$\mathrm{B}^0 \to \mathrm{D}^+_{\mathrm{s}}\pi^-$	[121]
$\mathrm{B}^0_{\mathrm{s}} \to \mathrm{D}^\mp_{\mathrm{s}}\mathrm{K}^\pm$	227 ± 61	sum of above two	
$\mathrm{B}^0_{\mathrm{s}} \to \phi\gamma$	43 ± 4	$\mathrm{B}^0 \to \mathrm{K}^{*0}\gamma$	[121]
$\mathrm{B}^0_{\mathrm{s}} \to \phi\phi$	5.2	SM prediction	[132]
$\mathrm{B}^0 \to \mu^+\mu^-\mathrm{K}^{*0}$	1.19 ± 0.39	SM prediction	[133]
$\mathrm{B}^0_{\mathrm{s}} \to \mathrm{J}/\psi\eta$	283 ± 17	$(\mathrm{B}^0 \to \mathrm{J}/\psi\mathrm{K}^0)/3$	[121]
$\mathrm{B}^0_{\mathrm{s}} \to \eta_{\mathrm{c}}\phi$	1310 ± 640	see below[a)]	[121]
$\mathrm{B}^+_{\mathrm{c}} \to \mathrm{J}/\psi\pi^+$	10^4		[131]

[a)] $(\mathrm{B}^0 \to \eta_{\mathrm{c}}\mathrm{K}^0) \times (\mathrm{B}^0_{\mathrm{s}} \to \mathrm{J}/\psi\phi)/(\mathrm{B}^0 \to \mathrm{J}/\psi\mathrm{K}^0)$

Background levels from some specific b-hadron decays have been discussed in the previous section. The selections involving a J/ψ were also tuned such as to reject all events in a sample of prompt J/ψ corresponding approximately to the same luminosity as the inclusive $\mathrm{b\overline{b}}$ sample. For the $\mathrm{B}^0 \to \mu^+\mu^-\mathrm{K}^{*0}$ selection, we also considered muons from semileptonic b-hadron decays and found $B/S = 0.5 \pm 0.1$ from events with two $\mathrm{b} \to \ell$ decays and $B/S < 1.1$ from events with $\mathrm{b} \to \mathrm{c}\mu$, $\mathrm{c} \to \mu$ cascade decays [128].

In order to study the robustness of the signal efficiencies as a function of the detector performance and PYTHIA generator settings we have generated a few special signal Monte Carlo samples for each of the two following conditions, as described in Sect. 6.3:

- the "global robustness test", which correspond to a significantly worse overall detector performance than assumed nominally (many parameters such as efficiency, noise, cross-talk and alignment are degraded simultaneously) as well as conservative settings for the PYTHIA generator leading to an increase in

Table 9.6: Change in untagged signal efficiencies and annual yields under two different conditions, relative to the nominal assumptions.

Decay channel	Global robustness test	CDF tuning of PYTHIA generator
$\mathrm{B_s^0} \to \mathrm{K^+K^-}$	−31%	+6%
$\mathrm{B_s^0} \to \mathrm{D_s^{\mp}K^{\pm}}$	−36%	+19%
$\mathrm{B^0} \to \mathrm{J}/\psi(\mu\mu)\mathrm{K_S^0}$	−32%	+2%
$\mathrm{B_s^0} \to \mathrm{J}/\psi(\mu\mu)\phi$	−29%	+3%
$\mathrm{B_s^0} \to \mathrm{J}/\psi(\mathrm{ee})\phi$	−36%	+5%
$\mathrm{B^0} \to \mathrm{K^{*0}}\gamma$	−28%	+16%

average track multiplicity;

- the "CDF tuning of PYTHIA", which corresponds to the nominal detector performance but with PYTHIA settings extrapolated (to LHC energy) from a recent tuning on CDF data, leading to a lower track multiplicity than those assumed by default.

These special samples of events were analyzed without retuning the reconstruction algorithms nor the selection cuts. However the trigger thresholds were changed in order to maintain the nominal trigger output rates of 1 MHz after L0 and 40 kHz after L1. The variations obtained on the untagged signal efficiencies and yields are shown in Table 9.6. The changes in the B/S ratios have not been studied.

Large uncertainties exist on the production cross sections at 14 TeV, as well as on the branching ratios of some channels, which have not been taken into account in the above robustness studies. The dependence on some of these parameters ($\mathrm{BR_{vis}}$, $\sigma_{\mathrm{b\bar{b}}}$, …) can be seen directly from Eq. (9.4). The dependence on the inelastic cross section, currently assumed to be $\sigma_{\mathrm{inel}} = 80\,\mathrm{mb}$, can be argued as follows: if the average number of pp collisions per bunch crossing is a fixed number obtained by adjusting the instantaneous luminosity at Point 8, then $L_{\mathrm{int}} \propto 1/\sigma_{\mathrm{inel}}$ and hence $S \propto \sigma_{\mathrm{b\bar{b}}}/\sigma_{\mathrm{inel}}$.

9.5 Flavour tagging

Flavour tagging, i.e. the identification of the initial flavour of reconstructed $\mathrm{B^0}$ and $\mathrm{B_s^0}$ mesons [134], is necessary in order to study decays involving CP asymmetries and flavour oscillations.

The statistical uncertainty on the measured CP asymmetries is directly related to the effective tagging efficiency $\varepsilon_{\mathrm{eff}}$, also known as "$\epsilon D^2$", which is defined here as

$$\varepsilon_{\mathrm{eff}} = \varepsilon_{\mathrm{tag}}(1-2w)^2\,,$$

where $\varepsilon_{\mathrm{tag}}$ is the tagging efficiency (probability that the tagging procedure gives an answer) and w is the wrong tag fraction (probability for the answer to be incorrect when a tag is present). The probabilities $\varepsilon_{\mathrm{tag}}$ and w are calculated as

$$\varepsilon_{\mathrm{tag}} = \frac{R+W}{R+W+U}\,, \quad w = \frac{W}{R+W}\,,$$

where R, W, U are the number of correctly tagged, incorrectly tagged, and untagged events, respectively.

Flavour tagging is performed using several algorithms, all using long tracks and particle identification for leptons and kaons based on optimized cuts on the combined $\Delta \ln \mathcal{L}$ quantities (see Sect. 8.3).

9.5.1 Opposite-side tagging

Opposite-side tagging algorithms determine the flavour of the b-hadron accompanying the reconstructed B meson under study. They use the charge of the lepton from semileptonic b decay and of the kaon from the $\mathrm{b} \to \mathrm{c} \to \mathrm{s}$ decay chain. They also use the charge of the inclusive secondary vertex reconstructed from b-decay products (vertex charge). When the accompanying b hadron is a neutral B meson, due to the possibility of flavour oscillations all these methods have an intrinsic dilution.

To select opposite-side tag lepton candidates, a momentum $p > 5\,\mathrm{GeV}/c$ and $p_{\mathrm{T}} > 1.2\,\mathrm{GeV}/c$ are required, reducing the contribution from $\mathrm{b} \to \mathrm{c} \to \ell$ decays which tag the wrong charge. In case of multiple candidates, the one with highest p_{T} is chosen. Figure 9.26 shows for opposite-side muon tag candidates the p_{T} distribution and the effective efficiency as a function of the p_{T} cut. Once the B meson has been reconstructed in the event, which passed Level-0 and Level-1 trigger, the probability that the lepton from a semileptonic decay of the opposite b-hadron is produced in the detector acceptance ($15 < \theta < 250\,\mathrm{mrad}$) is 8.7% and 6.3% for muons and electrons, respectively. With the condition that the particle is reconstructed as a long track, these fractions become 8.1% and 5.1%. The particle identification and selection cuts reduce them to 5.7% and 2.8%, respectively.

To select opposite-side tag kaon candidates, a momentum $p > 3\,\mathrm{GeV}/c$, $p_{\mathrm{T}} > 0.4\,\mathrm{GeV}/c$ and an impact parameter with respect to the primary vertex with significance $\mathrm{IP}/\sigma_{\mathrm{IP}} > 3.7$ are required. These cuts enhance the contribution of kaons from

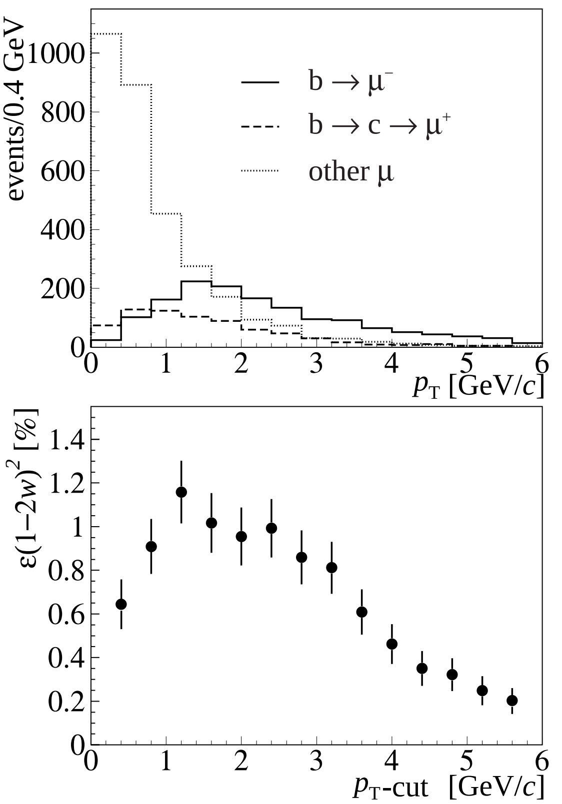

Figure 9.26: Upper plot: p_T distribution for opposite-side muon tag candidates, having $p > 5\,\mathrm{GeV}/c$, after Level-0 and Level-1 trigger. Lower plot: effective efficiency as a function of the minimum p_T required. The events used are $\mathrm{B_s^0} \to \mathrm{K^+K^-}$.

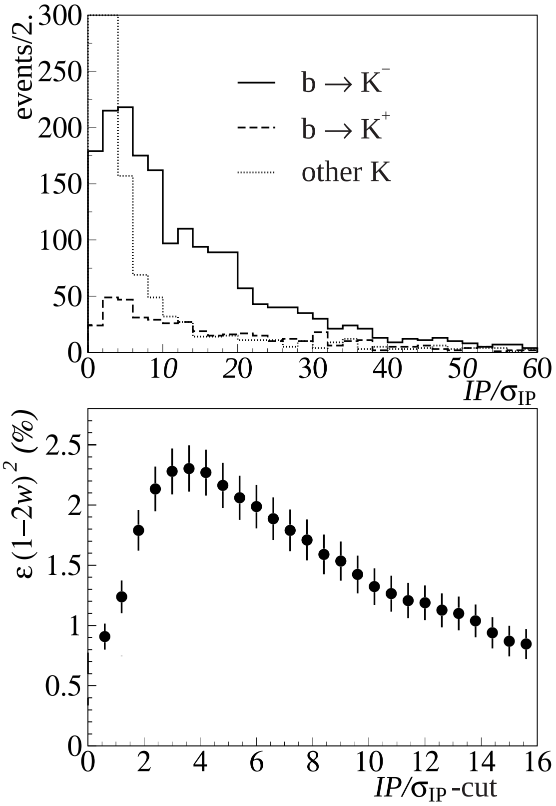

Figure 9.27: Upper plot: Distribution of the significance $\mathrm{IP}/\sigma_\mathrm{IP}$ for opposite-side kaon tag candidates, after p and p_T cuts have been applied and after Level-0 and Level-1 trigger. Lower plot: effective efficiency as a function of the minimum $\mathrm{IP}/\sigma_\mathrm{IP}$ required. The events used are $\mathrm{B_s^0} \to \mathrm{K^+K^-}$.

b decays with respect to kaons produced in the fragmentation. Figure 9.27 shows the distribution of the significance $\mathrm{IP}/\sigma_\mathrm{IP}$ for opposite-side kaon tag candidates, after p and p_T cuts have been applied, and the effective efficiency as a function of $\mathrm{IP}/\sigma_\mathrm{IP}$. About 33% of the triggered events have a kaon produced in the decay of the accompanying b hadron carrying the right tag charge, in the detector acceptance. The momentum spectrum of these kaons is quite soft and about 16% of them decay before reaching the tracking chambers. The fraction of triggered events having the tagging kaon reconstructed as a long track is 21%. The cuts for selection and particle identification reduce it to 11%.

If more than one opposite-side tag kaon candidate is present in the event, the charges of all candidates are summed and the result is used as flavour tag.

An inclusive reconstruction of the accompanying b-decay vertex is used to determine the b-vertex charge. The inclusive secondary vertex reconstruction starts using two tracks as seeds. Track pairs compatible with a $\mathrm{K_S^0}$ decay are excluded. Other tracks are then included if they satisfy kinematic criteria on impact parameters, χ^2 of the secondary vertex and distance from the primary vertex. The vertex charge, Q_vtx, is defined as the sum of the charges of all tracks associated to the vertex. Figure 9.28 shows the distribution of the vertex charge when the decaying b hadron is charged.

9.5.2 Same-side tagging

Same-side tagging algorithms determine directly the flavour of the signal B meson exploiting the correlation in the fragmentation decay chain. The method is used to tag $\mathrm{B_s^0}$ mesons. If a $\mathrm{B_s^0}$ $(\overline{\mathrm{b}}\mathrm{s})$ is produced in the fragmentation of a $\overline{\mathrm{b}}$ quark, an extra $\overline{\mathrm{s}}$ is available to form a kaon, which is charged in about 50% of the cases and neutral otherwise.

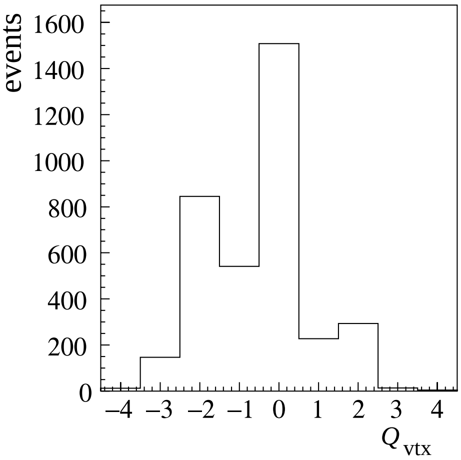

Figure 9.28: Vertex charge distribution when the decaying b hadron is a B^-.

These kaons emerge from the primary vertex and are correlated in phase space with the B_s^0. They are selected requiring an impact parameter with respect to the primary vertex with a significance $IP/\sigma_{IP} < 2.5$, a difference in pseudo-rapidity with respect to the reconstructed B_s^0 $|\Delta\eta| < 1$, a difference in ϕ angle $|\Delta\phi| < 1.1$ and $|\Delta m| < 1.5\,\mathrm{GeV}/c^2$, where Δm is the difference between the mass of the B_s^0K combination and the mass of the reconstructed B_s^0. For this tag we require also $p > 4\,\mathrm{GeV}/c$ and $p_T > 0.4\,\mathrm{GeV}/c$.

Table 9.7: Tagging performance for $B^0_{(s)} \to h^+h^-$ signal events passing trigger and offline cuts. Uncertainties are statistical.

Tag	ε_{tag} (%)	w (%)	ε_{eff} (%)
μ	11.1±0.3	35.3±1.1	1.0±0.2
e	5.2±0.2	35.6±1.7	0.4±0.1
K_{opp}	16.6±0.3	31.2±0.9	2.4±0.2
Q_{vtx}	24.3±0.6	39.9±0.8	1.0±0.2
Combined (B^0)	40.9±0.4	34.6±0.7	3.9±0.3
K_{same}	17.5±0.4	32.8±1.2	2.1±0.3
Combined (B_s^0)	49.8±0.5	32.8±0.8	5.9±0.5

Table 9.8: Performance of the combined tag for different signal decays passing trigger and offline cuts. Uncertainties are statistical.

Channel	ε_{tag} (%)	w (%)	ε_{eff} (%)
$B^0 \to \pi^+\pi^-$	41.8±0.7	34.9±1.1	3.8±0.5
$B^0 \to K^+\pi^-$	43.2±1.4	33.3±2.1	4.8±1.0
$B^0 \to J/\psi(\mu\mu)K^0_S$	45.1±1.3	36.7±1.9	3.2±0.8
$B^0 \to J/\psi(\mu\mu)K^{*0}$	41.9±0.5	34.3±0.7	4.1±0.3
$B_s^0 \to K^+K^-$	49.8±0.5	33.0±0.8	5.8±0.5
$B_s^0 \to \pi^+K^-$	49.5±1.8	30.4±2.6	7.6±1.7
$B_s^0 \to D_s^-\pi^+$	54.6±1.2	30.0±1.6	8.7±1.2
$B_s^0 \to D_s^\mp K^\pm$	54.2±0.6	33.4±0.8	6.0±0.5
$B_s^0 \to J/\psi(\mu\mu)\phi$	50.4±0.3	33.4±0.4	5.5±0.3

9.5.3 Tagging performance

When more than one primary vertex has been reconstructed in the event, all single particle tags are required to have an impact parameter significance in excess of 3.7 with respect to any primary vertex which was not chosen as the $b\overline{b}$ production vertex.

The final decision on the production flavour of the reconstructed B candidate is taken using the charge of the tagging particle, or the secondary vertex charge, when only one tag is available. The same-side kaon tag is used only for B_s^0 candidates. If there are more than one tag, the vertex charge is ignored and the final decision is taken as follows: if both the muon and the electron tag are available, the one with the highest p_T i.e. highest probability to come from a $b \to \ell$ decay, is used. If two single-track tags are available and they disagree, the B candidate remains untagged. If three single-track tags are available, the decision taken by the majority of them is used.

In order to determine the performance of this combined tagging decision, events are sorted in different categories according to which tags were included in the final decision; the performance is first determined in each category, and the total effective efficiency is obtained as the sum of the effective efficiencies determined in each category separately. This procedure is more powerful than simply measuring the performance of the combined tag after lumping all categories together.

Results for tagging efficiencies, wrong tag probabilities and effective efficiencies are shown in Table 9.7 for $B^0 \to \pi^+\pi^-$, $B^0 \to K^+\pi^-$, $B_s^0 \to K^+K^-$ and $B_s^0 \to \pi^+K^-$ signal decays passing the trigger and offline selection. The performance is shown for each tag independently, as well as for the combined tagging decision. Table 9.8 gives the combined performance for several more channels. Differences occur between channels because the accompanying b-hadron is biased by the trigger, and, through the $b\overline{b}$ correlation, by the acceptance and offline selection cuts on the reconstructed B.

As expected, the tagging performance is better in events with a single visible collision, but remains very reasonable for events with multiple

Table 9.9: Effective tagging efficiency for different sub-samples of $B_s^0 \to D_s^{\mp}K^{\pm}$ events (after trigger but before offline cuts), defined by the number of visible collisions, or by the PYTHIA process type [70] (for single-collision events).

Sample	fraction	$\varepsilon_{\rm eff}$ (%)
All		7.1 ± 0.3
Single collision	73%	7.5 ± 0.4
Multiple collisions	27%	6.6 ± 0.6
$f + f \to f + f$	9%	7.5 ± 1.2
$f + g \to f + g$	45%	6.5 ± 0.5
$g + g \to f + \overline{f}$	18%	10.2 ± 1.0
$g + g \to g + g$	27%	8.0 ± 0.7

collisions. This is illustrated in Table 9.9, with triggered $B_s^0 \to D_s^{\mp}K^{\pm}$ events, where all four B_s^0 final state particles are reconstructed in the detector. The tagging performance also depends rather strongly on the $b\overline{b}$ production mechanism, as different processes produce different $b\overline{b}$ correlations (see Table 9.9). For example, when a $b\overline{b}$ pair is produced back-to-back as in $g + g \to f + \overline{f}$, the b hadrons tend to be more cleanly separated in azimuthal angle, and this improves the tagging performance for this particular process.

Differences in tagging performance between a reconstructed B containing a $\overline{b}$ or a b quark at production have been examined with the $B^0 \to J/\psi K^{*0}$ channel and found to be smaller than 0.9%, consistent with zero with the present Monte Carlo statistics.

All results presented in this section use the truth information to determine whether a tag is correct or not, and the quoted uncertainties on the performance arise from the present Monte Carlo statistics. In order to reduce the dependence on the Monte Carlo, it will be possible, in a real physics analysis, to determine the wrong tag fractions directly from the data. This can be done for decays to flavour-specific final states by measuring the amplitude of the B^0 or B_s^0 oscillations, i.e. of the $\cos(\Delta m\, t)$ term in the mixing asymmetry. However, this is not possible for a non flavour-specific channel (e.g. $B^0 \to J/\psi K_S^0$ or $B_s^0 \to D_s^{\mp}K^{\pm}$); in this case, we will be able to use another channel with the same topology ($B^0 \to J/\psi K^{*0}$ or $B_s^0 \to D_s^- \pi^+$ in our examples) for which the trigger and the selection have a very similar response and hence introduce the same bias on the tagging performance.

9.6 Expected sensitivities to physics parameters

The sensitivities of LHCb to some CP observables have been assessed by the use of "toy Monte Carlo" programs. These programs generate event samples for certain assumptions of the physics parameters to be measured, and with the statistics expected at LHCb. Whenever possible, the characteristics of these samples (signal resolution, efficiency, purity, etc.) are taken from the studies with fully-simulated events described above. Due to the lack of fully-simulated background statistics, however, assumptions need to be made for the properties of background events. In the real analyses, these properties will be extracted from the data (e.g. looking at the sidebands in the B mass distribution). Systematic effects will be monitored from the data as well, whenever this is possible (e.g. using control channels without expected CP violation to determine the asymmetry between b-hadron and $\overline{b}$-hadron production). Unless specified otherwise, we assume no production asymmetry, and perfect knowledge of all signal and background parameters, except for those left free in the fits. The background-over-signal ratios B/S are taken to be the central values of the estimates obtained from the fully simulated inclusive $b\overline{b}$ sample. In the cases of the $B_s^0 \to D_s^{\mp}K^{\pm}$, $B^0 \to \overline{D}^0 K^{*0}$ and $B^0 \to D_{CP}^0 K^{*0}$ selections, where these central values would be derived based on only 1, 0 and 0 background events respectively, the assumed value of B/S is taken as half of the upper limit shown in Table 9.4. This is justified by the existence of additional cuts, not applied in the selections presented here, which are efficient for the signal and are expected to further reduce the background [117, 124].

In the studies involving time-dependent analyses, the proper-time distributions of the samples are fitted to extract estimates of the statistical uncertainties to be expected in the actual measurements. With the exception of $B^0 \to J/\psi K_S^0$, where the large, and (by the time of the experiment) well known asymmetry serves mainly as a calibration, unbinned maximum likelihood fits are used. The likelihood is defined as

$$\mathcal{L} = \prod_i \left[f_i^{\rm sig} \mathcal{L}_i^{\rm sig} + (1 - f_i^{\rm sig}) \mathcal{L}_i^{\rm bkg} \right] ,$$

where the product runs over all events, and the signal probability, $f_i^{\rm sig}$, is derived for each B candidate individually, based on the reconstructed mass. The signal and background likelihoods, $\mathcal{L}_i^{\rm sig}$ and $\mathcal{L}_i^{\rm bkg}$ contain the time dependence according to the physics parameters for which they are evaluated and according to the expected mistag probabilities. The analytical decay rates are convoluted with proper-time resolution functions and weighted with acceptance functions, both obtained from the full simulation. The time-resolution functions are single or double Gaussians and take advantage of the per-candidate computed proper-time resolution. Overall scale factors for the widths of the time resolution are fixed to match the observed time resolution in the full simulation (see Fig. 9.18 for instance). Such scale factors may be left free in the fit, providing a handle on possible systematic effects in the time resolution.

For the analytical decay rates, used for the generation of the events and the signal likelihoods, we have for initial[3] B or $\overline{\mathrm{B}}$ decaying to a final state f or its CP-conjugated state $\overline{f}$ at proper time t:

$$\begin{array}{rcl}
\Gamma_{\mathrm{B}\to f}(t) & = & \dfrac{|A_f|^2}{2} e^{-\Gamma t}\left[I_+(t)+I_-(t)\right] , \\
\Gamma_{\overline{\mathrm{B}}\to f}(t) & = & \dfrac{|A_f|^2}{2}\left|\dfrac{p}{q}\right|^2 e^{-\Gamma t}\left[I_+(t)-I_-(t)\right] , \\
\Gamma_{\overline{\mathrm{B}}\to \overline{f}}(t) & = & \dfrac{|\overline{A}_{\overline{f}}|^2}{2} e^{-\Gamma t}\left[\overline{I}_+(t)+\overline{I}_-(t)\right] , \\
\Gamma_{\mathrm{B}\to \overline{f}}(t) & = & \dfrac{|\overline{A}_{\overline{f}}|^2}{2}\left|\dfrac{q}{p}\right|^2 e^{-\Gamma t}\left[\overline{I}_+(t)-\overline{I}_-(t)\right] ,
\end{array} \tag{9.5}$$

where A_f ($\overline{A}_{\overline{f}}$) is the instantaneous $\mathrm{B}\to f$ ($\overline{\mathrm{B}}\to\overline{f}$) decay amplitude, and $\Gamma = (\Gamma_{\mathrm{L}}+\Gamma_{\mathrm{H}})/2$ is the average decay width of the two mass eigenstates $\mathrm{B_L}$ and $\mathrm{B_H}$ given by

$$|B_{\mathrm{L,H}}\rangle = \frac{1}{\sqrt{|p|^2+|q|^2}}(p|B\rangle \pm q|\overline{B}\rangle) .$$

Introducing the two complex quantities (of which the real and imaginary part are observables)

$$\lambda_f = \frac{q}{p}\frac{\overline{A}_f}{A_f} \quad\text{and}\quad \overline{\lambda}_f = \frac{p}{q}\frac{A_{\overline{f}}}{\overline{A}_{\overline{f}}} ,$$

the functions $I_\pm(t)$ are expressed by

$$\begin{array}{rcl}
I_+(t) & = & (1+|\lambda_f|^2)\cosh(\Delta\Gamma\, t/2) \\
 & & -2\,\mathrm{Re}(\lambda_f)\sinh(\Delta\Gamma\, t/2) , \\
I_-(t) & = & (1-|\lambda_f|^2)\cos(\Delta m\, t) \\
 & & -2\,\mathrm{Im}(\lambda_f)\sin(\Delta m\, t)
\end{array}$$

(and similarly for $\overline{I}_\pm(t)$ replacing λ_f with $\overline{\lambda}_f$), where $\Delta m = m_{\mathrm{H}} - m_{\mathrm{L}}$ and $\Delta\Gamma = \Gamma_{\mathrm{L}} - \Gamma_{\mathrm{H}}$ are the mass and decay-width differences.

We assume here $|q/p| = 1$, an approximation which is valid to a few per mil, even in the presence of new physics. Then, the CP asymmetry, defined for a CP eigenstate $f = \overline{f}$, is given by

$$\begin{array}{rcl}
\mathcal{A}_f^{\mathrm{CP}}(t) & = & \dfrac{\Gamma_{\overline{\mathrm{B}}\to f}(t) - \Gamma_{\mathrm{B}\to f}(t)}{\Gamma_{\overline{\mathrm{B}}\to f}(t) + \Gamma_{\mathrm{B}\to f}(t)} \\
 & = & \dfrac{\mathcal{A}_f^{\mathrm{dir}}\cos(\Delta m\, t) + \mathcal{A}_f^{\mathrm{mix}}\sin(\Delta m\, t)}{\cosh(\Delta\Gamma\, t/2) - \mathcal{A}_f^{\Delta}\sinh(\Delta\Gamma\, t/2)} ,
\end{array}$$

where

$$\mathcal{A}_f^{\mathrm{dir}} = \frac{|\lambda_f|^2-1}{|\lambda_f|^2+1} , \quad \mathcal{A}_f^{\mathrm{mix}} = \frac{2\,\mathrm{Im}(\lambda_f)}{|\lambda_f|^2+1} ,$$

and

$$\mathcal{A}_f^{\Delta} = \frac{2\,\mathrm{Re}(\lambda_f)}{|\lambda_f|^2+1} .$$

The relative decay-width difference $\Delta\Gamma/\Gamma$ is expected to be of the order of 10% for $\mathrm{B_s^0}$ mesons [135], while it can be safely neglected for $\mathrm{B^0}$ mesons. If $\Delta\Gamma = 0$ is assumed, the CP asymmetry reduces to

$$\mathcal{A}_f^{\mathrm{CP}}(t) = \mathcal{A}_f^{\mathrm{dir}}\cos(\Delta m\, t) + \mathcal{A}_f^{\mathrm{mix}}\sin(\Delta m\, t) .$$

The quantity $\mathcal{A}_f^{\mathrm{dir}}$ parametrizes direct CP violation (in decay amplitudes), while $\mathcal{A}_f^{\mathrm{mix}}$ is related to mixing-induced CP violation. These parameters depend on the angles of the CKM unitarity triangles. A discussion can be found in [136].

9.6.1 Mixing-induced and direct CP violation in $\mathrm{B^0}\to \mathrm{J}/\psi\mathrm{K_S^0}$ decays

For the $\mathrm{B^0}\to \mathrm{J}/\psi\mathrm{K_S^0}$ decay, the Standard Model expectations are $\mathcal{A}^{\mathrm{dir}} = 0$ (i.e. $|\lambda| = 1$) and $\mathcal{A}^{\mathrm{mix}} = \mathrm{Im}(\lambda) = \sin(2\beta)$, and have been confirmed by the B-factories. New physics could, however, affect these parameters at the level of precision reached by LHCb. The statistical sensitivity on these parameters with one year of data is assessed [118] from toy Monte Carlo samples generated as follows:

- the number of tagged signal and background events are randomly distributed around 91k and 61k respectively (the same tagging efficiency is assumed on the $\mathrm{b\overline{b}}$ background as for the signal);
- the true proper-time distribution of the signal is generated with $|\lambda| = 1$ and $\mathrm{Im}(\lambda) = 0.73$, and is multiplied by an acceptance function determined from the full Monte Carlo sample; for the background, no CP asymmetry is

---

[3] B represents either $\mathrm{B^0}$ or $\mathrm{B_s^0}$ mesons.

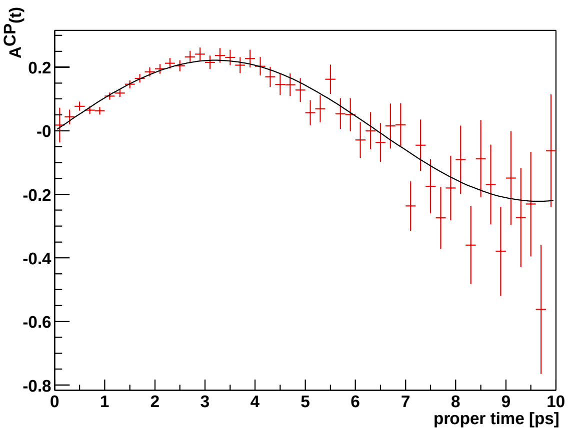

Figure 9.29: Background-subtracted CP asymmetry with $\mathrm{B}^0 \to \mathrm{J}/\psi(\mu\mu)\mathrm{K}^0_\mathrm{S}$ decays in one year of data.

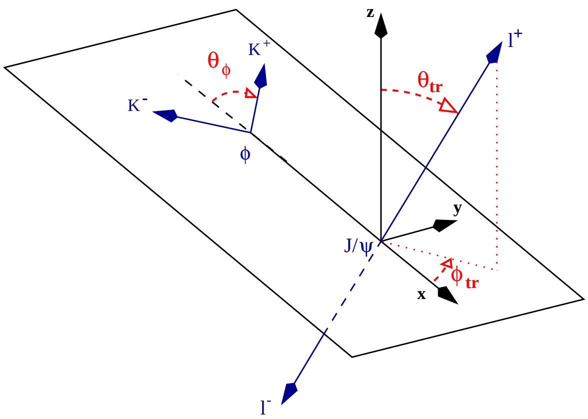

Figure 9.30: Definition of the transversity angle θ_tr in the $\mathrm{B}^0_\mathrm{s} \to \mathrm{J}/\psi(\ell^+\ell^-)\phi(\mathrm{K}^+\mathrm{K}^-)$ decay.

generated and an effective lifetime of 0.78 ps is used (consistent with that observed in the full $\mathrm{b}\overline{\mathrm{b}}$ Monte Carlo sample after a loose set of cuts) with the same acceptance function as for the signal;

- the true proper time of each event is smeared with a double Gaussian resolution obtained from the full Monte Carlo signal sample;
- the mistag probability is set to $w = 34.3\%$ for signal events, and equal numbers of background events are tagged as B^0 or $\overline{\mathrm{B}}^0$.

In each sample, the background is subtracted statistically, based on the parametrization used in the generation. A binned maximum likelihood fit of the function $\mathcal{A}^\mathrm{CP}(t) \times (1-2w)$ is then performed on the background-subtracted CP asymmetry, with $\mathrm{Im}(\lambda)$ and $|\lambda|$ as the only free parameters (see example of Fig. 9.29). The parameter w is fixed to the result obtained from a fit to a control sample of $\mathrm{B}^0 \to \mathrm{J}/\psi\mathrm{K}^{*0}$ decays, corresponding to one year of data and generated with $w = 34.3\%$. The absolute statistical uncertainty obtained on w, $\pm 0.11\%$, is then propagated to the $\mathrm{B}^0 \to \mathrm{J}/\psi\mathrm{K}^0_\mathrm{S}$ results.

The average total statistical uncertainties on $\mathcal{A}^\mathrm{mix}$ and $|\lambda|$ are found to be 0.022 and 0.023 respectively.

9.6.2 B^0_s mixing phase and decay-width difference with $\mathrm{B}^0_\mathrm{s} \to \mathrm{J}/\psi\phi$

The channel $\mathrm{B}^0_\mathrm{s} \to \mathrm{J}/\psi\phi$ is the SU(3) analogue of $\mathrm{B}^0 \to \mathrm{J}/\psi\mathrm{K}^0_\mathrm{S}$. As such it can be used to determine the phase ϕ_s due to B^0_s-$\overline{\mathrm{B}}^0_\mathrm{s}$ oscillations. In the Standard Model, the CKM picture predicts that this phase difference should be small, $\phi_\mathrm{s} = -2\chi = -2\eta\lambda^2$, of the order of -0.04. The observation of a large CP asymmetry in this channel would therefore be a striking signal for physics beyond the Standard Model.

Compared to $\mathrm{B}^0 \to \mathrm{J}/\psi\mathrm{K}^0_\mathrm{S}$, this channel presents several challenges:

1. Due to the fact that both J/ψ and ϕ are vector mesons, there are three distinct amplitudes contributing to this decay: two CP even, and one CP odd. Fortunately, the two CP components can be disentangled on a statistical basis by taking into account the distribution of the so-called transversity angle, θ_tr, defined as the angle between the positive lepton and the ϕ decay plane in the J/ψ rest frame (see Fig. 9.30).
2. The CP-even and CP-odd components are expected to have a non-negligible relative decay-width difference $\Delta\Gamma_\mathrm{s}/\Gamma_\mathrm{s}$ of the order of 10%.
3. The oscillation frequency Δm_s of the time-dependent CP asymmetry is very large, requiring excellent proper-time resolution.

The values of the physics parameters are extracted [137] using an unbinned maximum likelihood fit to the proper time, $\cos\theta_\mathrm{tr}$, and $m_{\mathrm{B}^0_\mathrm{s}}$ distributions. For this channel, the signal likelihood is given by the sum of the CP-even and the CP-odd components:

$$\begin{aligned}\mathcal{L}^\mathrm{sig}_i &= R_\mathrm{T}\,\mathcal{L}^\mathrm{sig}_\mathrm{odd}(t_i,\sigma_{t,i})\left(1+\cos^2\theta_{\mathrm{tr},i}\right)/2\\ &\quad +(1-R_\mathrm{T})\,\mathcal{L}^\mathrm{sig}_\mathrm{even}(t_i,\sigma_{t,i})\left(1-\cos^2\theta_{\mathrm{tr},i}\right),\end{aligned}$$

Table 9.10: Expected statistical precision on $\sin\phi_s$ and $\Delta\Gamma_s/\Gamma_s$ after one year of data taking, for various values of physics parameters. Unless otherwise specified, $\Delta m_s = 20\,\mathrm{ps}^{-1}$, $\Delta\Gamma_s/\Gamma_s = 0.1$, $\sin\phi_s = -0.04$, $R_T = 0.2$.

Δm_s in ps^{-1}	15	20	25	30
$\sigma(\sin\phi_s)$	0.057	0.064	0.075	0.088
$\sigma(\Delta\Gamma_s/\Gamma_s)$	0.018	0.018	0.018	0.018

$\Delta\Gamma_s/\Gamma_s$	0	0.1	0.2
$\sigma(\sin\phi_s)$	0.059	0.064	0.070
$\sigma(\Delta\Gamma_s/\Gamma_s)$	0.015	0.018	0.019

$\sin\phi_s$	0	−0.04	−0.1	−0.2
$\sigma(\sin\phi_s)$	0.064	0.064	0.064	0.066
$\sigma(\Delta\Gamma_s/\Gamma_s)$	0.018	0.018	0.018	0.018

R_T	0.1	0.2	0.3
$\sigma(\sin\phi_s)$	0.050	0.064	0.084
$\sigma(\Delta\Gamma_s/\Gamma_s)$	0.015	0.018	0.019

where R_T is the fraction of the decays given by the CP-odd amplitude. The resolution of θ_{tr}, observed to be 20 mrad in the full Monte Carlo, is included in the event generation.

The fit is performed on the interval $[0.2, 20]$ ps, where the full simulation shows the acceptance to be constant to a good approximation. Hence a flat acceptance function is used for this channel.

The background proper-time distribution is again obtained from the full Monte Carlo simulation of inclusive $b\overline{b}$ events, with less stringent cuts, and is described by the sum of a prompt component, formed by two Gaussians, and a lifetime component, formed by the convolution of an exponential with the same two Gaussians. The lifetime is found to be 0.55 ps. In the interval $[0.2, 20]$ ps, 12.5% of the events are due to the prompt component. Finally, the distribution of θ_{tr} is assumed to be flat for the background.

The fit proceeds in three steps. First the mass distribution is fitted, and the per-candidate signal probability is determined. Next, the sidebands, defined as those candidates for which the reconstructed mass deviates by more than $75\,\mathrm{MeV/c^2}$ from the nominal B_s^0 mass, are used to determine the background parameters. Finally, candidates within a window of $\pm 50\,\mathrm{MeV/c^2}$ are used to determine the signal parameters $\sin\phi_s$, R_T, $\Delta\Gamma_s/\Gamma_s$, $1/\Gamma_s$, Δm_s and w. To allow a determination of the latter two, this fit is performed simultaneously on both $B_s^0 \to J/\psi\phi$ and $B_s^0 \to D_s^-\pi^+$ events.

To determine the sensitivity of $\sin\phi_s$ and $\Delta\Gamma_s/\Gamma_s$, events are generated for a series of likely values of R_T, Δm_s, $\Delta\Gamma_s/\Gamma_s$ and $\sin\phi_s$. For each setting, 1000 experiments are simulated, each corresponding to one year of LHCb data-taking (100k signal events with $\varepsilon_{tag} = 50\%$, $w = 35\%$ and 15k background events in the signal region). The average error obtained from the ensemble of experiments is quoted as sensitivity in Table 9.10.

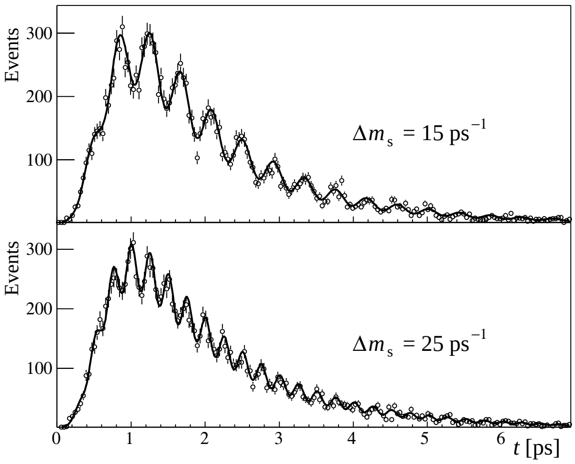

Figure 9.31: Proper-time distribution of simulated $B_s^0 \to D_s^-\pi^+$ candidates that have been flavour-tagged as having not oscillated, for two different values of Δm_s. The data points represent one year of data, while the curves correspond to the maximized likelihood.

9.6.3 Δm_s with $B_s^0 \to D_s^-\pi^+$ and γ with $B_s^0 \to D_s^\mp K^\pm$

The decay $B_s^0 \to D_s^-\pi^+$ is a flavour-specific B decay in which only a single tree diagram contributes. In this case the generic decay formula Eq. (9.5) can be applied with the constraint $\lambda = \overline{\lambda} = 0$ and a flavour asymmetry can be defined:

$$\mathcal{A}^{\mathrm{flav}} = \frac{\Gamma_{\overline{B}\to f} - \Gamma_{B\to f}}{\Gamma_{\overline{B}\to f} + \Gamma_{B\to f}} = -D\,\frac{\cos(\Delta m_s\, t)}{\cosh(\Delta\Gamma_s\, t)}\,,$$

where D is a dilution factor due to wrong tagging and experimental resolution. From this asymmetry the B_s^0 oscillation frequency Δm_s and, optionally, the decay width difference $\Delta\Gamma_s$ can be determined.

The decay $B_s^0 \to D_s^\mp K^\pm$ can proceed through two tree decay diagrams, the interference of which gives access to the phase $\gamma + \phi_s$, and hence to the CKM angle γ if ϕ_s is determined otherwise (e.g. with $B_s^0 \to J/\psi\phi$). In this case the generic formula is applied with $|\lambda| = |\overline{\lambda}| \approx 0.5$, $\arg(\lambda) = \Delta_{T1/T2} + (\gamma + \phi_s)$ and $\arg(\overline{\lambda}) = \Delta_{T1/T2} - (\gamma + \phi_s)$.

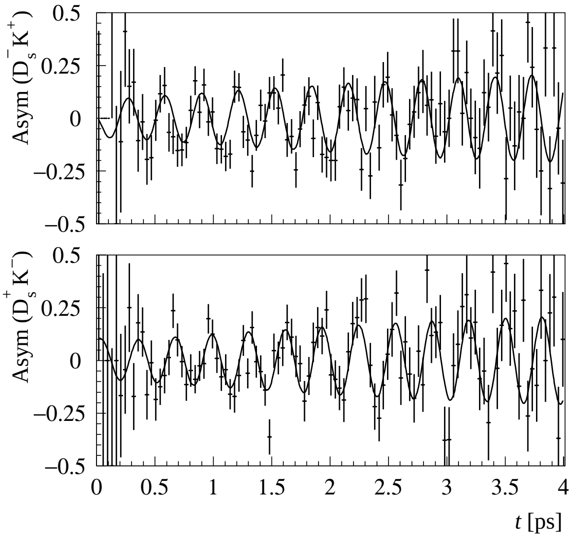

Figure 9.32: Time-dependent $\overline{\mathrm{B}}{}^0_\mathrm{s}$-$\mathrm{B}^0_\mathrm{s}$ asymmetry of simulated $\mathrm{D}_\mathrm{s}^-\mathrm{K}^+$ (top) and $\mathrm{D}_\mathrm{s}^+\mathrm{K}^-$ (bottom) candidates for $\Delta m_\mathrm{s} = 20\,\mathrm{ps}^{-1}$. The data points represent five years of data, while the curves correspond to the maximized likelihood.

Here $\Delta_{\mathrm{T1/T2}}$ denotes the strong phase difference between the two tree diagrams of Fig. 9.3.

In this study [138], $\mathrm{B}^0_\mathrm{s} \to \mathrm{D}_\mathrm{s}^-\pi^+$ and $\mathrm{B}^0_\mathrm{s} \to \mathrm{D}_\mathrm{s}^\mp\mathrm{K}^\pm$ signal events are generated for different settings of the physics parameters $\gamma+\phi_\mathrm{s}$, $\Delta_{\mathrm{T1/T2}}$ and Δm_s, while $\Delta\Gamma_\mathrm{s}/\Gamma_\mathrm{s}$ is fixed to 10%. The acceptance and decay time resolutions of both decays are taken from Sect. 9.3. Background events are generated with a lifetime that is half the lifetime of B-mesons, and according to the mass distribution observed in the full simulation.

Since the $\mathrm{B}^0_\mathrm{s} \to \mathrm{D}_\mathrm{s}^-\pi^+$ and $\mathrm{B}^0_\mathrm{s} \to \mathrm{D}_\mathrm{s}^\mp\mathrm{K}^\pm$ events are topologically similar the same mistag rate is assumed. A value of $w = 32\%$ was used in the event generation. In the fit, the likelihoods of all tagged $\mathrm{B}^0_\mathrm{s} \to \mathrm{D}_\mathrm{s}^-\pi^+$ and $\mathrm{B}^0_\mathrm{s} \to \mathrm{D}_\mathrm{s}^\mp\mathrm{K}^\pm$ events are simultaneously maximized by varying the parameters Δm_s, $|\lambda| = |\overline{\lambda}|$, $\arg(\lambda)$, $\arg(\overline{\lambda})$ and w. The mistag rate w is then effectively determined (with a relative precision of 1.5%) from the amplitude of the $\mathcal{A}^{\mathrm{flav}}$ asymmetry in the $\mathrm{B}^0_\mathrm{s} \to \mathrm{D}_\mathrm{s}^-\pi^+$ event sample while being applied at the same time to measure the CP asymmetry in the $\mathrm{B}^0_\mathrm{s} \to \mathrm{D}_\mathrm{s}^\mp\mathrm{K}^\pm$ sample. The value of the weak phase $\gamma+\phi_\mathrm{s}$ follows from the difference of the fitted parameters $\arg(\lambda) - \arg(\overline{\lambda})$.

Figure 9.31 shows the $\mathrm{B}^0_\mathrm{s} \to \mathrm{D}_\mathrm{s}^-\pi^+$ decay rate as a function of proper time t, for one year of data and two different values of Δm_s. The maximized likelihood is shown as well. The $\mathrm{B}^0_\mathrm{s} \to \mathrm{D}_\mathrm{s}^\mp\mathrm{K}^\pm$ asymmetries are shown in Fig. 9.32. Their amplitudes increase with t due to the lower background level at high values of t.

The expected statistical uncertainties on Δm_s and $\gamma+\phi_\mathrm{s}$ are shown in Tables 9.11 and 9.12. The dependence of the $\gamma+\phi_\mathrm{s}$ sensitivity on the B/S ratio and the decay time resolution is shown in Figs. 9.33 and 9.34.

In order to estimate the highest Δm_s value that can be measured, the $\cos(\Delta m_\mathrm{s} t)$ term in the expression of the flavour asymmetry was multiplied with an amplitude factor A. Data were generated for an infinite Δm_s value and then fitted with A as a free parameter. The uncertainty σ_A on A is shown in Fig. 9.35, where it can be seen that the requirement $5\sigma_A < 1$ (for an observation with a statistical significance of at least 5σ) is satisfied up to $\Delta m_\mathrm{s} = 68\,\mathrm{ps}^{-1}$. The effect of a change in the decay time resolution by ±10% is also shown.

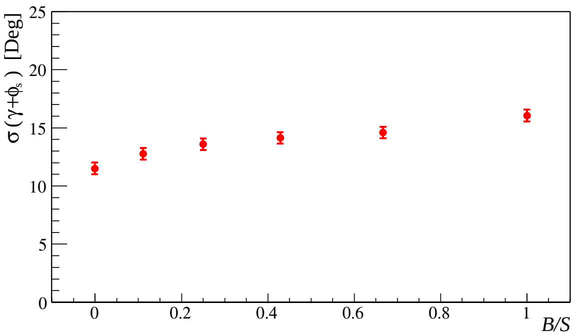

Figure 9.33: Statistical uncertainty on $\gamma+\phi_\mathrm{s}$ for one year of data as a function of the B/S ratio in the $\mathrm{B}^0_\mathrm{s} \to \mathrm{D}_\mathrm{s}^\mp\mathrm{K}^\pm$ selection.

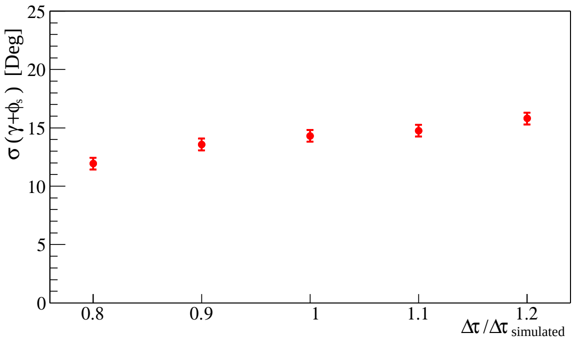

Figure 9.34: Statistical uncertainty on $\gamma+\phi_\mathrm{s}$ for one year of data as a function of the decay time resolution in the $\mathrm{B}^0_\mathrm{s} \to \mathrm{D}_\mathrm{s}^\mp\mathrm{K}^\pm$ selection, relative to that determined in the full simulation.

Table 9.11: Statistical precision on $\Delta m_{\rm s}$ (in $\rm ps^{-1}$) with one year of data.

$\Delta m_{\rm s}$	15	20	25	30
$\sigma(\Delta m_{\rm s})$	0.009	0.011	0.013	0.016

Table 9.12: Expected statistical uncertainty on $\gamma+\phi_{\rm s}$ for one year of data. Unless otherwise specified, $\Delta m_{\rm s} = 20\,\rm ps^{-1}$, $\Delta\Gamma_{\rm s}/\Gamma_{\rm s} = 0.1$, $\gamma+\phi_{\rm s} = 65°$ and $\Delta_{\rm T1/T2} = 0°$. All values are given in degrees, except $\Delta m_{\rm s}$ in $\rm ps^{-1}$.

$\Delta m_{\rm s}$	15	20	25	30
$\sigma(\gamma+\phi_{\rm s})$	12.1	14.2	16.2	18.3

$\Delta\Gamma_{\rm s}/\Gamma_{\rm s}$	0	0.1	0.2
$\sigma(\gamma+\phi_{\rm s})$	14.7	14.2	12.9

$\gamma+\phi_{\rm s}$	55	65	75	85	95	105
$\sigma(\gamma+\phi_{\rm s})$	14.5	14.2	15.0	15.0	15.1	15.2

$\Delta_{\rm T1/T2}$	-20	-10	0	$+10$	$+20$
$\sigma(\gamma+\phi_{\rm s})$	13.9	14.1	14.2	14.5	14.6

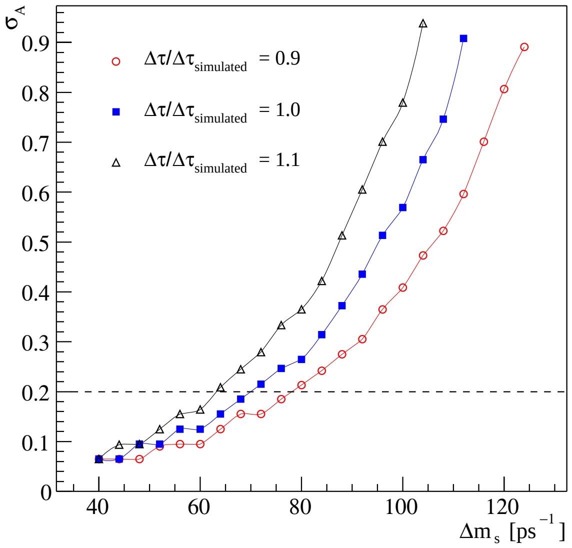

Figure 9.35: Statistical uncertainty on the $\rm B^0_s$ oscillation amplitude A as a function of $\Delta m_{\rm s}$. An observation of $\Delta m_{\rm s}$ with a statistical significance above 5-sigma is possible up to $68\,\rm ps^{-1}$ (where $\sigma_A = 1/5$). Also shown are the results for the cases where the decay time resolution would be better or worse by 10%. These expectations are for one year of data.

9.6.4 γ with $\rm B^0 \to \pi^+\pi^-$ and $\rm B^0_s \to K^+K^-$

The combination of the $\rm B^0 \to \pi^+\pi^-$ and $\rm B^0_s \to K^+K^-$ measurements provides a promising strategy to determine the CKM angle γ [114].

In the Standard Model, $\mathcal{A}^{\rm dir}_{\pi\pi}$ and $\mathcal{A}^{\rm mix}_{\pi\pi}$ can be expressed as

$$\begin{aligned}\mathcal{A}^{\rm dir}_{\pi\pi} &= \frac{2d\sin\vartheta\sin\gamma}{\xi}\,,\\ \mathcal{A}^{\rm mix}_{\pi\pi} &= -\frac{1}{\xi}\left[\sin(\phi_{\rm d}+2\gamma) - 2d\cos\vartheta\sin(\phi_{\rm d}+\gamma)\right.\\ &\qquad \left. + d^2\sin\phi_{\rm d}\right]\,, \qquad (9.6)\end{aligned}$$

with

$$\xi = 1 - 2d\cos\vartheta\cos\gamma + d^2\,,$$

where the hadronic parameters d and ϑ represent the magnitude and phase of the penguin-to-tree amplitude ratio of the decay transition [114]. Analogously, $\mathcal{A}^{\rm dir}_{\rm KK}$ and $\mathcal{A}^{\rm mix}_{\rm KK}$ can be written as:

$$\begin{aligned}\mathcal{A}^{\rm dir}_{\rm KK} &= -\frac{2\widetilde{d}'\sin\vartheta'\sin\gamma}{\xi'}\,,\\ \mathcal{A}^{\rm mix}_{\rm KK} &= -\frac{1}{\xi'}\left[\sin(\phi_{\rm s}+2\gamma) + 2\widetilde{d}'\cos\vartheta'\sin(\phi_{\rm s}+\gamma)\right.\\ &\qquad \left. + \widetilde{d}'^2\sin\phi_{\rm s}\right]\,, \qquad (9.7)\end{aligned}$$

with

$$\xi' = 1 + 2\widetilde{d}'\cos\vartheta'\cos\gamma + \widetilde{d}'^2\,,$$

where $\widetilde{d}' = d'\,(1-|V_{\rm us}|^2)/|V_{\rm us}|^2$, and d' and ϑ' are the analogs of d and ϑ for the $\rm B^0_s \to K^+K^-$ decay.

In the limit of exact U-spin symmetry of the strong interactions, the relations $d = d'$ and $\vartheta = \vartheta'$ hold, and the measurements of the four asymmetry coefficients allow the simultaneous determination of $\phi_{\rm d}$ and γ, provided that $\phi_{\rm s}$ is determined elsewhere (from $\rm B^0_s \to J/\psi\phi$ for instance) or considered negligibly small as expected in the Standard Model. Moreover, $\phi_{\rm d}$ will be accurately known at the time of LHCb, and its precision will be further increased by the LHCb $\rm B^0 \to J/\psi K^0_S$ measurement, thus allowing a more precise determination of γ.

The sensitivity on $\mathcal{A}^{\rm dir}$ and $\mathcal{A}^{\rm mix}$ is estimated from toy Monte Carlo samples [139]. Signal events are generated for different settings of the physics parameters d, ϑ, γ, $\phi_{\rm s}$, $\Delta\Gamma_{\rm s}$ and $\Delta m_{\rm s}$. The proper-time acceptance and resolution functions used in the generation are determined from the full simulation. Combinatorial background events are generated with mass and proper time distributed according to what observed in fully simulated $\rm b\overline{b}$ samples, selected after trigger and slightly loosened offline selection cuts [116].

Since the $\rm B^0 \to \pi^+\pi^-$ and the $\rm B^0 \to K^+\pi^-$ ($\rm B^0_s \to K^+K^-$ and $\rm B^0_s \to \pi^+K^-$) events are topologically similar, the same tagging efficiency and mistag probability are assumed. The values used in the generation are taken from the full simulation, which gives $\varepsilon_{\rm tag} = 41.8\%$ and $w = 34.9\%$ ($\varepsilon_{\rm tag} = 49.8\%$ and $w = 33.0\%$).

The uncertainties and correlations on $\mathcal{A}^{\rm dir}$ and $\mathcal{A}^{\rm mix}$ are determined by maximizing an unbinned extended likelihood. In order to determine the mistag probability, the $\mathrm{B}^0 \to \mathrm{K}^+\pi^-$ ($\mathrm{B}^0_\mathrm{s} \to \pi^+\mathrm{K}^-$) sample is included in the same fit, together with the $\mathrm{B}^0 \to \pi^+\pi^-$ ($\mathrm{B}^0_\mathrm{s} \to \mathrm{K}^+\mathrm{K}^-$) sample. There are 17 free parameters in the fit. In addition to $\mathrm{Re}(\lambda)$, $\mathrm{Im}(\lambda)$, and the $\mathrm{K}\pi$ charge asymmetry, the fit determines $\Delta\Gamma$, Δm, Γ, w, two signal yields, the mean and resolution of the B-meson mass distribution, and six parameters for the mass and proper-time distributions of the background. Once the maximum of the likelihood function is found, uncertainties and correlation for $\mathcal{A}^{\rm dir}$ and $\mathcal{A}^{\rm mix}$ are calculated by a Monte Carlo error propagation using the full covariance matrix returned by the fit.

In order to improve the resolutions on the CP-violating parameters, for the $\mathrm{B}^0_\mathrm{s} \to \mathrm{K}^+\mathrm{K}^-$ and $\mathrm{B}^0_\mathrm{s} \to \pi^+\mathrm{K}^-$ combined fit, expected knowledge on $\Delta\Gamma_\mathrm{s}$ and Γ_s from $\mathrm{B}^0_\mathrm{s} \to \mathrm{J}/\psi\phi$ and Δm_s from $\mathrm{B}^0_\mathrm{s} \to \mathrm{D}^-_\mathrm{s}\pi^+$ (see the previous two sections) is included in the fit by multiplying the total likelihood with Gaussian priors. For $\mathrm{B}^0 \to \pi^+\pi^-$ and $\mathrm{B}^0 \to \mathrm{K}^+\pi^-$, current knowledge of Γ_d and Δm_d [121] is used.

The mistag probability w is determined with a relative precision of 1.0% for $\mathrm{B}^0 \to \pi^+\pi^-$ and $\mathrm{B}^0 \to \mathrm{K}^+\pi^-$ (between 6.1% and 9.1% for $\mathrm{B}^0_\mathrm{s} \to \mathrm{K}^+\mathrm{K}^-$ and $\mathrm{B}^0_\mathrm{s} \to \pi^+\mathrm{K}^-$, depending on Δm_s).

The resulting uncertainties and correlations on $\mathcal{A}^{\rm dir}$ and $\mathcal{A}^{\rm mix}$ and the uncertainties on the charge asymmetries, corresponding to nominal true values of the physics parameters and for one year of data taking, are shown in Table 9.13 (for $\mathrm{B}^0_\mathrm{s} \to \mathrm{K}^+\mathrm{K}^-$ and $\mathrm{B}^0_\mathrm{s} \to \pi^+\mathrm{K}^-$ also the results of a scan on the true values of Δm_s and $\Delta\Gamma_\mathrm{s}/\Gamma_\mathrm{s}$ are reported). The larger error on w for $\mathrm{B}^0_\mathrm{s} \to \mathrm{K}^+\mathrm{K}^-$ and $\mathrm{B}^0_\mathrm{s} \to \pi^+\mathrm{K}^-$, due to the smaller yield of $\mathrm{B}^0_\mathrm{s} \to \pi^+\mathrm{K}^-$, has the effect of introducing a sizeable dependence of the resolutions and correlations of $\mathcal{A}^{\rm dir}$ and $\mathcal{A}^{\rm mix}$ on their true values. For $\mathrm{B}^0 \to \pi^+\pi^-$ and $\mathrm{B}^0 \to \mathrm{K}^+\pi^-$ only a moderate dependence is observed. The results of a study of this dependence are reported in [139]. Due to correlation, the experimental probability density functions (p.d.f.s) for $\mathcal{A}^{\rm dir}$ and $\mathcal{A}^{\rm mix}$ are best described by bi-variate Gaussians.

Table 9.13: Statistical uncertainties and correlations on $\mathcal{A}^{\rm dir}$ and $\mathcal{A}^{\rm mix}$ for $\mathrm{B}^0 \to \pi^+\pi^-$ and $\mathrm{B}^0_\mathrm{s} \to \mathrm{K}^+\mathrm{K}^-$ and uncertainties on charge asymmetries for $\mathrm{B}^0 \to \mathrm{K}^+\pi^-$ ($\mathcal{A}_{\mathrm{K}\pi}$) and $\mathrm{B}^0_\mathrm{s} \to \pi^+\mathrm{K}^-$ ($\mathcal{A}_{\pi\mathrm{K}}$), corresponding to one year of data. Unless otherwise specified, $\Delta m_\mathrm{s} = 20\,\mathrm{ps}^{-1}$, $\Delta\Gamma_\mathrm{s}/\Gamma_\mathrm{s} = 0.1$, $\gamma = 65°$, $\vartheta = 160°$, $d = 0.3$, $\phi_\mathrm{s} = -0.04$.

$\sigma(\mathcal{A}^{\rm dir}_{\pi\pi})$	0.064
$\sigma(\mathcal{A}^{\rm mix}_{\pi\pi})$	0.055
$\rho(\mathcal{A}^{\rm dir}_{\pi\pi}, \mathcal{A}^{\rm mix}_{\pi\pi})$	−0.43
$\sigma(\mathcal{A}_{\mathrm{K}\pi})$	0.0035

Δm_s in ps^{-1}	15	20	25	30
$\sigma(\mathcal{A}^{\rm dir}_{\mathrm{KK}})$	0.043	0.051	0.060	0.076
$\sigma(\mathcal{A}^{\rm mix}_{\mathrm{KK}})$	0.058	0.067	0.077	0.093
$\rho(\mathcal{A}^{\rm dir}_{\mathrm{KK}}, \mathcal{A}^{\rm mix}_{\mathrm{KK}})$	−0.24	−0.22	−0.20	−0.17
$\sigma(\mathcal{A}_{\pi\mathrm{K}})$	0.024	0.024	0.024	0.024

$\Delta\Gamma_\mathrm{s}/\Gamma_\mathrm{s}$	0	0.1	0.2
$\sigma(\mathcal{A}^{\rm dir}_{\mathrm{KK}})$	0.054	0.051	0.047
$\sigma(\mathcal{A}^{\rm mix}_{\mathrm{KK}})$	0.070	0.067	0.061
$\rho(\mathcal{A}^{\rm dir}_{\mathrm{KK}}, \mathcal{A}^{\rm mix}_{\mathrm{KK}})$	−0.20	−0.22	−0.21
$\sigma(\mathcal{A}_{\pi\mathrm{K}})$	0.023	0.024	0.024

The p.d.f.s of the four asymmetry terms $\mathcal{A}^{\rm dir}_{\pi\pi}$, $\mathcal{A}^{\rm mix}_{\pi\pi}$, $\mathcal{A}^{\rm dir}_{\mathrm{KK}}$ and $\mathcal{A}^{\rm mix}_{\mathrm{KK}}$ and of the weak phases ϕ_d and ϕ_s can be propagated into p.d.f.s for the quantities γ, d and ϑ. Using a Bayesian approach one can obtain a joint p.d.f.:

$$F(\gamma,d,\vartheta) \propto \int G_\pi(\mathcal{A}^{\rm dir}_{\pi\pi},\mathcal{A}^{\rm mix}_{\pi\pi})\,G_\mathrm{K}(\mathcal{A}^{\rm dir}_{\mathrm{KK}},\mathcal{A}^{\rm mix}_{\mathrm{KK}}) \times F_0(\gamma,d,\vartheta)\,g_0^{\mathrm{d}}(\phi_\mathrm{d})\,g_0^{\mathrm{s}}(\phi_\mathrm{s})\,\mathrm{d}\phi_\mathrm{d}\,\mathrm{d}\phi_\mathrm{s}\,,$$

where the dependence of the asymmetry coefficients on ϕ_d, ϕ_s, γ, d, and ϑ is given by the constraints of Eqs. (9.6) and (9.7). G_π and G_K are the bivariate Gaussian p.d.f.s for the asymmetry coefficients as determined experimentally, while F_0, g_0^d and g_0^s are *prior* p.d.f.s describing previous independent measurements or theoretical expectations of these quantities. Ignoring any *a priori* knowledge on γ, d, and ϑ, we use a uniform distribution for F_0, while g_0^d and g_0^s are described by Gaussians with the resolutions obtained from $\mathrm{B}^0 \to \mathrm{J}/\psi\mathrm{K}^0_\mathrm{S}$ and $\mathrm{B}^0_\mathrm{s} \to \mathrm{J}/\psi\phi$, respectively.

The sensitivity on γ is explored for different values of the physics parameters γ, d, ϑ, ϕ_s, and also Δm_s and $\Delta\Gamma_\mathrm{s}/\Gamma_\mathrm{s}$, since the resolutions on $\mathcal{A}^{\rm dir}_{\mathrm{KK}}$ and $\mathcal{A}^{\rm mix}_{\mathrm{KK}}$ depend on these last two. The results are shown in Table 9.14. Since the resulting p.d.f. for γ can be asymmetric for some of the input parameters, we quote the resolutions as half of the range covered by 68% confidence intervals (calculated as highest posterior density intervals).

As an example, Fig. 9.36 shows the confidence regions for d and γ in the (d, γ) plane for one year

Table 9.14: Statistical uncertainty on γ for one year of data. Unless otherwise specified, $\Delta m_{\rm s} = 20\,{\rm ps}^{-1}$, $\Delta\Gamma_{\rm s}/\Gamma_{\rm s} = 0.1$, $\gamma = 65^\circ$, $\vartheta = 160^\circ$, $d = 0.3$, $\phi_{\rm s} = -0.04$. $\Delta m_{\rm s}$ values are given in ${\rm ps}^{-1}$, $\phi_{\rm s}$ values in radians, while γ, ϑ and $\sigma(\gamma)$ are given in degrees.

$\Delta m_{\rm s}$	15	20	25	30
$\sigma(\gamma)$	4.0	4.9	5.9	8.5

$\Delta\Gamma_{\rm s}/\Gamma_{\rm s}$	0	0.1	0.2
$\sigma(\gamma)$	5.2	4.9	4.5

γ	55	65	75	85	95	105
$\sigma(\gamma)$	5.8	4.9	4.3	4.7	4.7	4.7

ϑ	120	140	160	180	200
$\sigma(\gamma)$	3.8	3.8	4.9	6.7	5.2

d	0.1	0.2	0.3	0.4
$\sigma(\gamma)$	1.8	2.7	4.9	9.0

$\phi_{\rm s}$	0	-0.04	-0.1	-0.2
$\sigma(\gamma)$	4.9	4.9	4.9	5.4

of data, together with the one-dimensional p.d.f.s for d and γ.

Within the considered parameter ranges and for one year's statistics, secondary fake solutions are observed, which have a smaller probability than the correct solution. These solutions (erroneously) imply small values of d (< 0.15) and large values of γ ($> 160^\circ$). They can be eliminated with larger statistics or by combining the measurement of d and γ with information from other analyses (i.e. starting from a non-uniform prior in d and γ). The wrong solutions are ignored in the determination of the resolutions given in Table 9.14. Furthermore our study assumes exact U-spin symmetry for the penguin-to-tree amplitude ratio. In practice, the validity of this symmetry can be checked from the data itself by, for instance, extracting the parameters d, d' and γ for given assumptions for ϑ.

9.6.5 γ with $\mathrm{B^0 \to \overline{D}{}^0 K^{*0}}$, $\mathrm{D^0 K^{*0}}$

The method [115] relies on the measurement of six time-integrated decay rates:

$$\begin{aligned}
\Gamma_+ &= \Gamma(\mathrm{B^0 \to D^0 K^{*0}})\,,\\
\Gamma_- &= \Gamma(\mathrm{B^0 \to \overline{D}{}^0 K^{*0}})\,,\\
\Gamma_{\rm CP} &= \Gamma(\mathrm{B^0 \to D^0_{CP} K^{*0}})\,,\\
\overline{\Gamma}_+ &= \Gamma(\mathrm{\overline{B}{}^0 \to D^0 \overline{K}{}^{*0}})\,,\\
\overline{\Gamma}_- &= \Gamma(\mathrm{\overline{B}{}^0 \to \overline{D}{}^0 \overline{K}{}^{*0}})\,,\\
\overline{\Gamma}_{\rm CP} &= \Gamma(\mathrm{\overline{B}{}^0 \to D^0_{CP} \overline{K}{}^{*0}})\,.
\end{aligned}$$

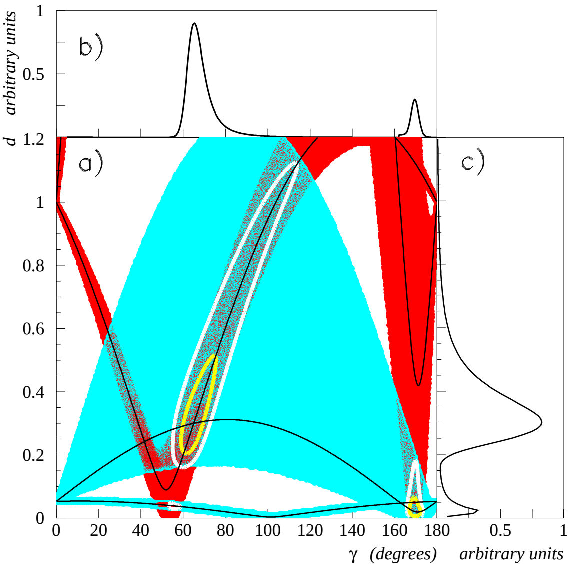

Figure 9.36: (a) Confidence regions in the (d, γ) plane for one year of data generated with $\Delta m_{\rm s} = 20\,{\rm ps}^{-1}$, $\Delta\Gamma_{\rm s}/\Gamma_{\rm s} = 0.1$, $\gamma = 65^\circ$, $\vartheta = 160^\circ$, $d = 0.3$, $\phi_{\rm s} = -0.04$; the darker (red) bands delimit the 95% confidence region obtained by combining the two contraints of Eq. (9.6) from $\mathrm{B^0 \to \pi^+\pi^-}$; the lighter (cyan) bands delimit the 95% confidence region obtained by combining the two constraints of Eq. (9.7) from $\mathrm{B^0_s \to K^+K^-}$; the black solid curves represent analytical relations between d and γ obtained with perfect knowledge of the true values of the asymmetry coefficients (the intersection at $d = 0.3$ and $\gamma = 65^\circ$ corresponds to the solution); the light (yellow and white) deformed ellipses enclose the 68% and 95% confidence regions obtained by using all four constraints as described in the text. (b) p.d.f. for γ, $F(\gamma) = \int F(\gamma, d, \vartheta){\rm d}d{\rm d}\vartheta$. (c) p.d.f. for d, $F(d) = \int F(\gamma, d, \vartheta){\rm d}\gamma{\rm d}\vartheta$. In the plots, the presence of the satellite fake solution is clearly visible.

The rates fulfill the following relations:

$$\begin{aligned}
\Gamma_+ &= \overline{\Gamma}_- \equiv g_1\,,\\
\Gamma_- &= \overline{\Gamma}_+ \equiv g_2\,,
\end{aligned}$$

and

$$\begin{aligned}
\Gamma_{\rm CP} &= \frac{g_1+g_2}{2} + \sqrt{g_1 g_2}\cos(\Delta+\gamma)\,,\\
\overline{\Gamma}_{\rm CP} &= \frac{g_1+g_2}{2} + \sqrt{g_1 g_2}\cos(\Delta-\gamma)\,,
\end{aligned} \qquad (9.8)$$

from which one can extract the CKM angle γ as well as the strong phase difference Δ between the two tree diagrams of Fig. 9.5.

Table 9.15: Expected statistical precision on γ for different values of γ after one year of data taking. The value of Δ is set to 0. The line labeled "Fail" indicates how often no measurement can be made (see text).

γ	55°	65°	75°	85°	95°	105°
$\sigma(\gamma)$	9.0°	8.2°	7.6°	7.1°	7.0°	7.0°
Fail	3%	0.5%	0%	0%	0%	0%

All rates can be determined from the reconstructed numbers of events for the six decay modes, after the reconstruction efficiencies and D^0 branching fractions have been taken into account. In the following, we assume negligible uncertainties on the reconstruction efficiencies and D^0 branching fractions.

As shown in Table 9.4, 3.4k $B^0 \rightarrow \overline{D}{}^0 K^{*0}$ plus $\overline{B}{}^0 \rightarrow D^0 \overline{K}{}^{*0}$ reconstructed decays are expected after one year of data taking. The branching fraction for the $B^0 \rightarrow D^0 K^{*0}$ decay is suppressed compared to that for $B^0 \rightarrow \overline{D}{}^0 K^{*0}$ [121], by a factor assumed to be equal to $\bar{\eta}^2 + \bar{\rho}^2 = 0.147$, using the central values of $\bar{\rho} = \rho(1 - \lambda^2/2) = 0.162$ and $\bar{\eta} = \eta(1 - \lambda^2/2) = 0.347$ estimated in [107]. With the same total efficiency, we thus expect to collect 0.49k $B^0 \rightarrow D^0 K^{*0}$ plus $\overline{B}{}^0 \rightarrow \overline{D}{}^0 \overline{K}{}^{*0}$ decays in one year. Using the total efficiencies given in Table 9.4, the expected number of reconstructed $B^0 \rightarrow D^0_{CP} K^{*0}$ and $\overline{B}{}^0 \rightarrow D^0_{CP} \overline{K}{}^{*0}$ decays can be calculated for given values of γ and Δ using Eq. (9.8). For example, the $B^0 \rightarrow D^0_{CP} K^{*0}$ branching ratio quoted in Table 9.5 and the yield of 0.59k for $B^0 \rightarrow D^0_{CP} K^{*0}$ plus $\overline{B}{}^0 \rightarrow D^0_{CP} \overline{K}{}^{*0}$ decays quoted in Table 9.4 correspond to the assumptions $\gamma = 65°$ and $\Delta = 0$.

With these numbers, we generate sets of measurements for the six decay modes assuming Poisson statistics [124]. The statistical fluctuations for the number of signal events are scaled by $\sqrt{1 + B/S}$, where B/S is the background-over-signal ratio assumed for each of the six decay rates: we use 0.3 for the $B^0 \rightarrow \overline{D}{}^0 K^{*0}$ mode and its CP conjugate (corresponding to half of the limit quoted in Table 9.4), 1.8 for the $B^0 \rightarrow D^0 K^{*0}$ mode and its CP conjugate (derived from the previous one assuming the same absolute background level), and B/S ratios which depend on γ and Δ for the $B^0 \rightarrow D^0_{CP} K^{*0}$ mode and its CP conjugate. If $\gamma = 65°$ and $\Delta = 0$, the latter ratios are both equal to 1.4 (half of the upper limit given in Table 9.4); for other assumptions, these ratios are recomputed according to Eq. (9.8) and using the same absolute background level.

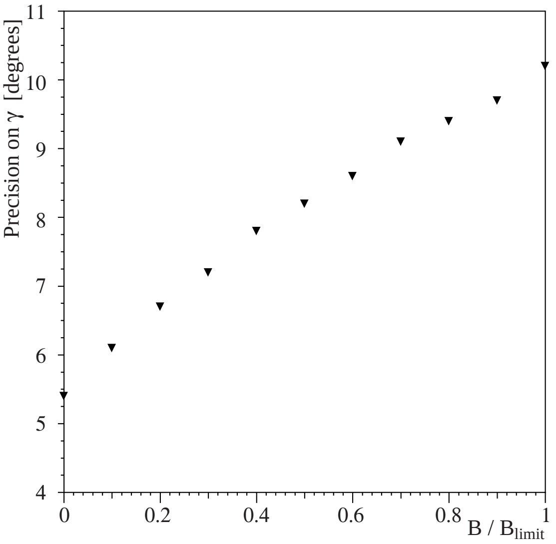

Figure 9.37: Expected statistical precision on γ as a function of the assumed background levels in the six $B^0 \rightarrow D^0 K^{*0}$ decay modes, after one year of data taking. The horizontal scale goes from no background ($B = 0$) to the background levels B_{limit} corresponding to the upper limits from Table 9.4. The phases are fixed to $\gamma = 65°$ and $\Delta = 0°$.

Table 9.15 summarizes the expected statistical precision on γ for six values of γ after one year of data taking. This precision is obtained as the width of a Gaussian fitted to the distribution of the γ values obtained in 100k independent sets of Monte Carlo experiments. Due to the statistical fluctuations in the generated number of events, some experiments can fail to provide a measurement for γ, because the measured rates imply $\cos(\Delta + \gamma)$ or $\cos(\Delta - \gamma)$ outside the interval $[-1, +1]$. These cases are excluded from the estimation of the precision on γ, and their frequencies, indicated in Table 9.15 for one year of data, vanish with increasing statistics. Within the range of γ considered here, the precision on γ remains unchanged for $-20° < \Delta < 20°$. Figure 9.37 shows the dependence of the precision on γ on the assumed background levels.

9.7 Systematic effects

In order to exploit the large statistical samples expected in the LHCb experiment, systematic errors due to acceptance, detection efficiency, decay-time resolution, production asymmetries, tagging performance and trigger efficiency, must be well understood.

In the time-dependent asymmetry between the B and $\overline{\mathrm{B}}$ decays into a given final state, the effect of acceptance cancels out to first order. An example is the extraction of $\sin 2\beta$ from the time-dependent CP asymmetry between the initial $\overline{\mathrm{B}}^0$ and B^0 decaying into $\mathrm{J}/\psi\mathrm{K}^0_\mathrm{S}$. For the study of B^0_s and $\overline{\mathrm{B}}^0_\mathrm{s}$ decaying into $\mathrm{D}^\pm_\mathrm{s}\mathrm{K}^\mp$, two time-dependent B^0_s–$\overline{\mathrm{B}}^0_\mathrm{s}$ asymmetries can be constructed from the same final states necessary for the γ extraction.

A difference in the detection efficiency between positively and negatively charged particles would introduce a fake CP asymmetry. This is particularly important for the flavour tagging and CP violation measurements with final states which are not CP eigenstates. If the detection efficiency is different between the left- and right-hand sides of the spectrometer, the detection efficiency for the positive and negative particles will differ due to the magnetic field of the spectrometer dipole. This will be corrected by regularly changing the polarity of the magnetic field.

Detailed understanding of the B^0 proper-time resolution is not very important since it is much smaller than the B^0–$\overline{\mathrm{B}}^0$ oscillation period. For the B^0_s meson studies, such understanding of the proper-time resolution will be important, since its oscillation is much more rapid. This can be investigated by measuring the lifetimes of particles which are well known. Multi-particle production due to the interaction of the primary particles with the material of the detector at well known positions can also be used for this study.

The tagging performance is best understood using control samples. Flavour-specific decays such as $\mathrm{B}^0\to\mathrm{D}^-\pi^+$, $\mathrm{B}^0\to\mathrm{J}/\psi\mathrm{K}^{*0}$ and $\mathrm{B}^0_\mathrm{s}\to\mathrm{D}^-_\mathrm{s}\pi^+$, which are suitable to measure B–$\overline{\mathrm{B}}$ oscillations, can be used to extract the wrong tag fraction. They also provide the difference between the b and $\overline{\mathrm{b}}$ flavour tagging efficiencies. Final states of the $\mathrm{B}^\pm$ decays such as $\mathrm{J}/\psi\mathrm{K}^\pm$ can also be used to extract the wrong tag fraction and the difference in the tagging efficiencies. In addition, control samples are used to test the production asymmetry. The production asymmetry does not depend on lifetime, and can therefore be extracted with high precision from the decay asymmetry of many non-CP as well as CP-violating decay modes of neutral B mesons. As seen from Table 9.4, LHCb is able to reconstruct various control samples with high statistics.

It must be noted that tagging performance depends on the reconstructed final state due to selection and trigger. Therefore, it is important that the control channels have decay characteristics similar to those of the final states being studied (e.g. $\mathrm{J}/\psi\mathrm{K}^{*0}$ for $\mathrm{J}/\psi\mathrm{K}^0_\mathrm{S}$ and $\mathrm{D}^-_\mathrm{s}\pi^+$ for $\mathrm{D}^-_\mathrm{s}\mathrm{K}^+$). A sizeable fraction of the events will be triggered by more than one trigger component, such as high-p_T muons and hadrons. Those events can be used to calibrate the trigger efficiencies.

9.8 Conclusions

In this document, the performance of the LHCb experiment has been illustrated by the measurement of the angle γ in three different ways:[4]

I. Time-dependent decay asymmetries in $\mathrm{B}^0_\mathrm{s}\to\mathrm{D}^\mp_\mathrm{s}\mathrm{K}^\pm$ decays combined with the CP asymmetry in the $\mathrm{B}^0_\mathrm{s}\to\mathrm{J}/\psi\phi$ decays, giving $\sigma(\gamma) =$ 14–15° without theoretical uncertainty.

II. Time-dependent CP asymmetries in $\mathrm{B}^0\to\pi^+\pi^-$ and $\mathrm{B}^0_\mathrm{s}\to\mathrm{K}^+\mathrm{K}^-$ decays, in combination with $\mathrm{B}^0\to\mathrm{J}/\psi\mathrm{K}^0_\mathrm{S}$ and $\mathrm{B}^0_\mathrm{s}\to\mathrm{J}/\psi\phi$ respectively, giving $\sigma(\gamma) =$ 4–6° assuming U-spin symmetry.

III. Time-integrated rates of $\mathrm{B}^0\to\mathrm{D}^0\mathrm{K}^{*0}$, $\mathrm{B}^0\to\overline{\mathrm{D}}^0\mathrm{K}^{*0}$ and $\mathrm{B}^0\to\mathrm{D}^0_\mathrm{CP}\mathrm{K}^{*0}$ decays, giving $\sigma(\gamma) =$ 7–8° without theoretical uncertainty.

The current Standard Model analysis of the CKM parameters using the processes generated by the tree and box diagrams leads to the following most likely values of $\bar\rho$ and $\bar\eta$ [107]

$$(\bar\rho,\ \bar\eta) \approx (0.162,\ 0.347)\,, \tag{9.9}$$

which correspond to

$$\beta \approx 22.5^\circ, \qquad \gamma \approx 65^\circ\ .$$

If there is no new physics affecting the B meson system via loop processes, all three methods should yield measurements consistent with $\gamma \approx 65^\circ$.

There is an interesting hint that γ could be different: the analysis of the measurements of CP-averaged $\mathrm{B}\to\pi\pi, \mathrm{K}\pi$ rates indicates that a γ value around or above 90° is preferred [140]. To illustrate a possible scenario, let us assume that the B^0–$\overline{\mathrm{B}}^0$ oscillation amplitude is affected by new physics, in such a way that the new physics contribution to Δm_d is about -30% of the Standard Model contribution, with a phase difference of a few degrees compared to the Standard Model. However $|V_\mathrm{ub}|$

---

[4] All statistical uncertainties given in this section are the expectations for a nominal year of data taking, defined as 10^7 s at $2\times10^{32}\ \mathrm{cm}^{-2}\mathrm{s}^{-1}$ luminosity with $500\,\mu$b of $\mathrm{b}\overline{\mathrm{b}}$ production cross section, i.e. 10^{12} $\mathrm{b}\overline{\mathrm{b}}$ pairs produced.

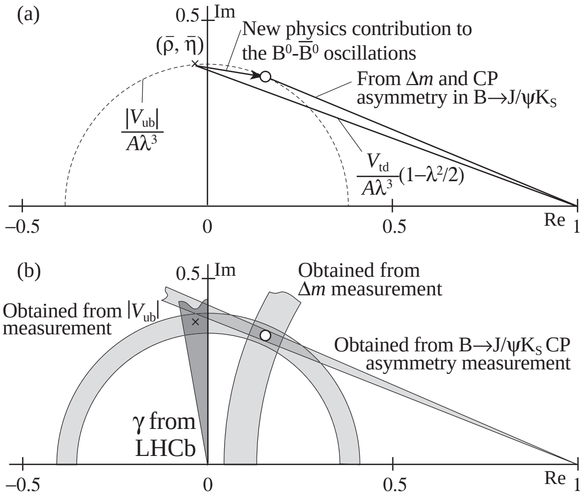

Figure 9.38: The CKM parameters $\bar{\rho}$ and $\bar{\eta}$ in the complex plane including the effect due to possible new physics: (a) The point marked by × is the CKM parameter position $(\bar{\rho},\ \bar{\eta})$ and the open circle indicates the currently favoured $(\bar{\rho},\ \bar{\eta})$ from the Standard Model analysis based on $|V_{\mathrm{ub}}|$, Δm_{d} and CP asymmetry in $\mathrm{B}^0 \rightarrow \mathrm{J}/\psi\mathrm{K}^0_{\mathrm{S}}$ decays. The new physics contribution is also indicated. (b) Possible picture with LHCb results for γ from Methods I and II after one year of data taking. It is assumed that $|V_{\mathrm{ub}}|$ is determined with an error of 5% and the hadronic uncertainty in the theoretical calculation of Δm_{d} is 10%.

would remain unchanged. This could then lead to $\gamma = 95°$, corresponding to

$$(\bar{\rho},\ \bar{\eta}) = (-0.033,\ 0.382)\,.$$

In this situation, illustrated in Fig. 9.38 (a), the constraints from the current measurements of Δm_{d} and the CP asymmetry between B^0 and $\overline{\mathrm{B}}{}^0$ decaying to $\mathrm{J}/\psi\mathrm{K}^0_{\mathrm{S}}$ would still give, together with the $|V_{\mathrm{ub}}|$ measurement, the solution shown in Eq. (9.9).

For this scenario, Method I will measure $\gamma = 95°$ since it gives the phase of V_{ub} even if new physics contributes to the oscillations. Similarly, Method II will provide $\gamma = 95°$, if the U-spin symmetry is valid. Thus, the LHCb experiment will measure the real value of γ (different from 65°) with an accuracy of better than 5° with the first year of data taking. Figure 9.38 (b) illustrates the LHCb measurement, which would clearly signal the existence of new physics in the B–$\overline{\mathrm{B}}$ oscillations and allow to separate the contributions from the Standard Model and from new physics. It is interesting to note that the value of γ measured by Method III reveals whether new physics also affects the D^0–$\overline{\mathrm{D}}{}^0$ mixing.

If instead new physics appears in the b → d penguin diagrams, the currently known CKM parameters of Eq. (9.9) are the correct values, and the γ measurements from Methods I and III will give $\gamma \approx 65°$. However, the γ measurement from Method II will yield a different value.

Finally new physics may contribute to both the oscillations and penguin diagrams. Method I will still yield the correct value of γ, while Method II will give a value different from the CKM parameters. Again the result of Method III, when compared to that of Method I, will indicate whether new physics appears in the D^0–$\overline{\mathrm{D}}{}^0$ mixing.

This demonstrates how these three different γ measurements at LHCb would isolate new physics.

Note that the extraction of γ with Methods I and II requires the ability to resolve the fast $\mathrm{B}^0_{\mathrm{s}}$–$\overline{\mathrm{B}}{}^0_{\mathrm{s}}$ oscillations, even in presence of new physics. LHCb will be able to measure Δm_{s} up to a value of $\sim 68\,\mathrm{ps}^{-1}$, far beyond the Standard Model expectation. These methods also require a good knowledge of ϕ_{s} (equal to -2χ in absence of new physics), which LHCb will be able to measure with a precision of[5] $\sigma(\phi_{\mathrm{s}}) = 0.058$ for $\Delta m_{\mathrm{s}} = 20\,\mathrm{ps}^{-1}$.

If new physics appears in B–$\overline{\mathrm{B}}$ oscillations, it is also expected that the $\mathrm{B}^0_{\mathrm{s}} \rightarrow \mu^+\mu^-$ decay will be affected. The branching fraction is $\sim 3.5 \times 10^{-9}$ in the Standard Model, but new physics might increase this significantly. For the reconstruction of a final state with such a small branching fraction, estimating background becomes really difficult before the start of the experiment. A careful study of this decay [142], previously made with the TP detector design, showed that the major source of background are pairs of muons coming from the semileptonic decays of both the b- and $\overline{\mathrm{b}}$-hadron in $\mathrm{b}\overline{\mathrm{b}}$ events. With a dedicated very high statistics Monte Carlo sample of this event type, it was estimated that 48 signal events (with Standard Model branching ratio) can be reconstructed after three years of data taking, with an expected contamination of 118 background events, corresponding to a statistical significance of $S/\sqrt{S+B} = 3.7$. A dedicated study to investigate the background with the new setup is in progress. However, since the muon detection performance of the reoptimized detector is unchanged from that of the TP design, we anticipate that this performance figure will be main-

---

[5] The result of Sect. 9.6.2 is scaled here to the current knowledge of tagging performance for $\mathrm{B}^0_{\mathrm{s}} \rightarrow \mathrm{J}/\psi\phi$ given in Sect. 9.5.

tained.

If new physics appears in the b → s penguin processes, decays such as $B^0 \to \mu^+\mu^- K^{*0}$, $B^0 \to K^{*0}\gamma$, $B_s^0 \to \phi\gamma$ and $B_s^0 \to \phi\phi$ (which are governed by pure penguin diagrams) will be affected and this will be studied in great detail by LHCb. A recently observed difference by the BELLE collaboration between the CP asymmetry in $B^0 \to J/\psi K_S^0$ decays and that in $B^0 \to \phi K_S^0$ decays [141] might indeed be the first sign of this. The LHCb detector has no trouble to trigger and reconstruct final states with ϕ or K_S^0 mesons. The performance for the reconstruction of the $B^0 \to \phi(K^+K^-)K_S^0(\pi^+\pi^-)$ decay is under investigation.

Similarly to the $B^0 \to \pi^+\pi^-$ decays, the b → d penguin diagrams contribute to $B^0 \to \rho\pi$ decays. The $\rho\pi$ final states have the advantage that combinations of γ and β can be measured without including other decay modes in the Standard Model framework. If new physics contributes to the b → d penguin processes, the measurement of γ obtained in this way will no longer correspond to the CKM value given by Method I. Since π^0 from those decays are rather energetic, they are well reconstructed in LHCb detector. Backgrounds and the sensitivity to γ are under investigation.

Important features of the LHCb experiment for the above studies are:

- Measurements in both the B^0 and B_s^0 systems.
- Excellent decay time resolution, needed for the CP violation study in the B_s^0 system.
- A trigger which is efficient both for the final states that contain leptons and those with hadrons only.
- Excellent particle identification and mass resolution to suppress background, in particular from the b-hadron decays with the same topologies as the signal.

In summary, the reoptimized LHCb experiment can trigger and reconstruct many different b-hadron decay final states with high statistics, as demonstrated in this document using representative decay modes with kinematics and decay products which are common to many interesting channels. This will enable LHCb to extract the CKM parameters and disentangle possible new physics.

Chapter 10 Plan and Cost of the Experiment

10.1 Schedules and milestones

Figure 10.1 shows the layout of the experimental area. The cohabitation with the LHC machine in the experimental area requires careful planning and follow-up of progress, to minimize the interference with the installation of the LHCb detector. On the LHC machine side, the installation of the general services, the cryogenic lines in the tunnel and the installation of the cryogenics boxes in UX85 are planned for the years 2003 and 2004. These activities have to be coordinated with the installation of general infrastructure for the detector, the assembly of the magnet and the assembly of the muon filter.

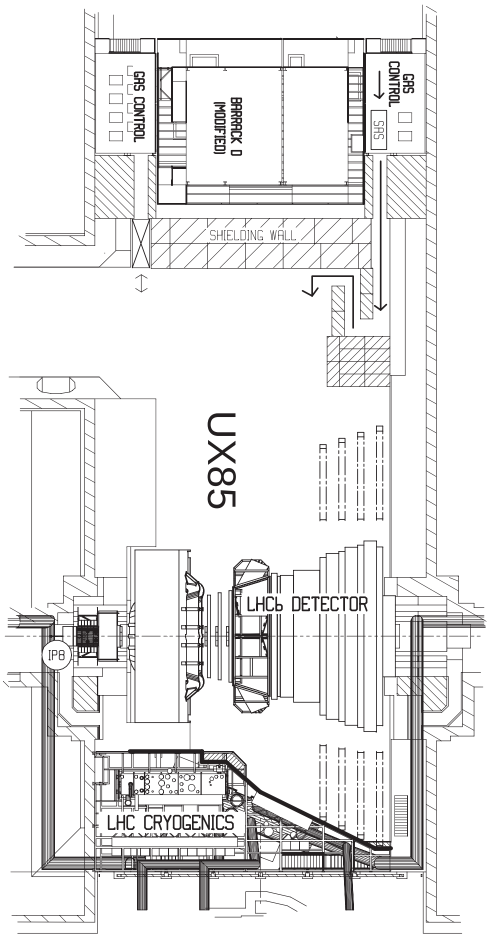

Figure 10.1: Layout of the LHCb experimental area (from above).

Later on, the injection test that will possibly take place would require beam passing through the experimental area of Point 8. This test is presently planned for April 2006 and will interfere with the assembly of the detector at a critical phase when the installation of the beam pipe, the VELO detector and RICH 1 will have to be coordinated with the requirements of the injection test. Figure 10.2 gives an overview of the installation schedule and the LHC machine activities.

The important milestones for the three projects RICH 1, Trigger Tracker (TT) and the beam pipe are given in Tables 10.1, 10.2 and 10.3. In line with the global schedule, the milestones are set such as to achieve the goal of finishing individual system commissioning in September 2006. This leaves six months for the global commissioning of the detector with the experiment ready for beam in April 2007.

In the following the schedules for the different project items affected by the reoptimization are presented. The project schedule for the VELO detector remains unchanged. In Fig. 10.3 the project schedule for the RICH 1 detector is shown; this schedule is very tight.

Figure 10.4 shows the project schedule for the TT station. This detector will be pre-assembled and tested as much as possible on the surface. Its installation in the experimental area will take place only after the LHC machine injection test (if the test takes place) and will be finished by July 2006, leaving 3 months for sub-system commissioning.

Figure 10.5 shows the project schedule for the beam pipe. If the prototype beam pipe is acceptable, the order for the final beam pipe can be placed such that there is ample time left to pre-assemble and test the complete beam pipe on the surface prior to installation in early 2006.

Overall, the system schedules are in agreement with the requirements for the installation schedule. The sequence of the detector installation could be modified within certain constraints, if need arises,

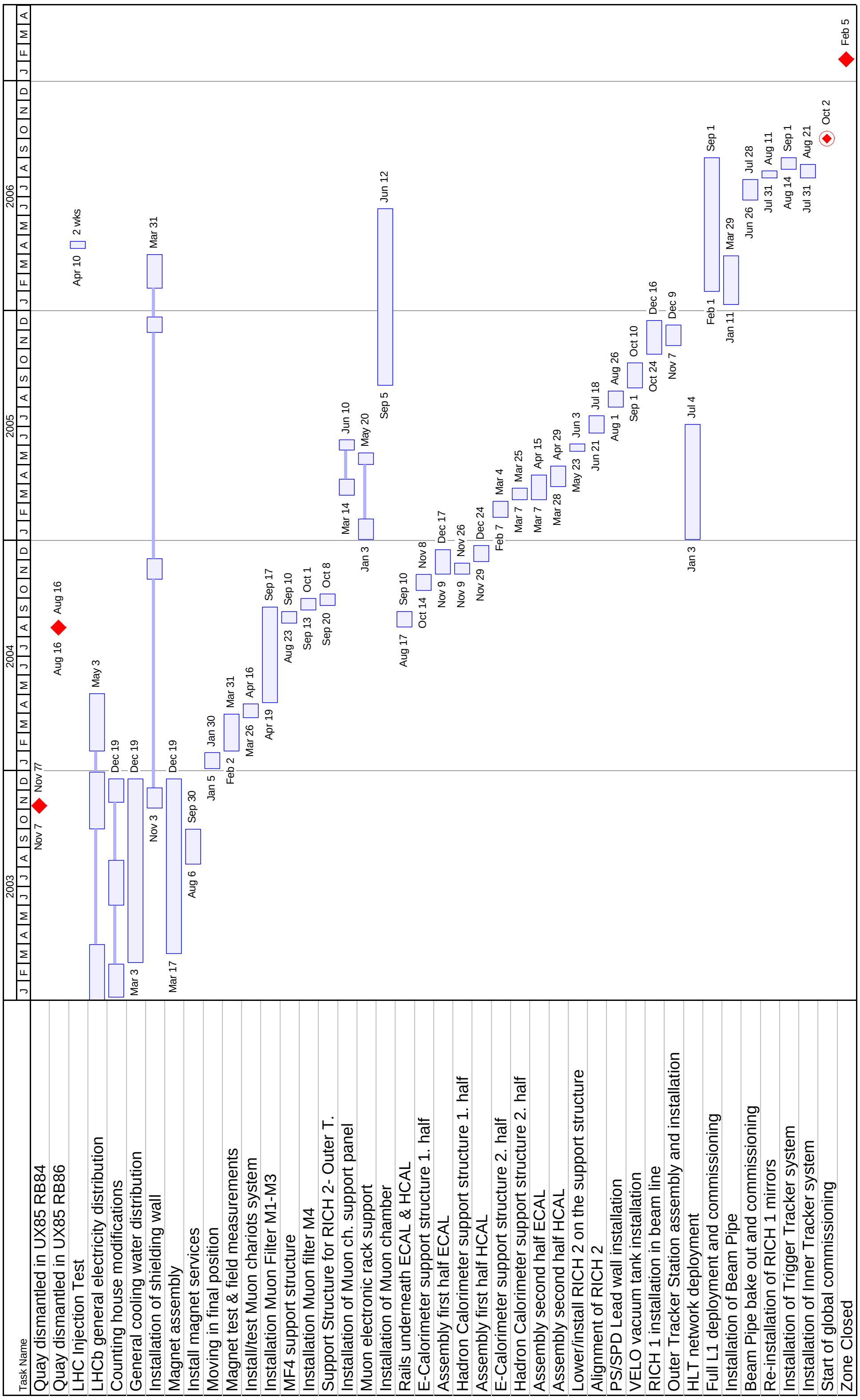

Figure 10.2: Installation summary schedule and major tasks.

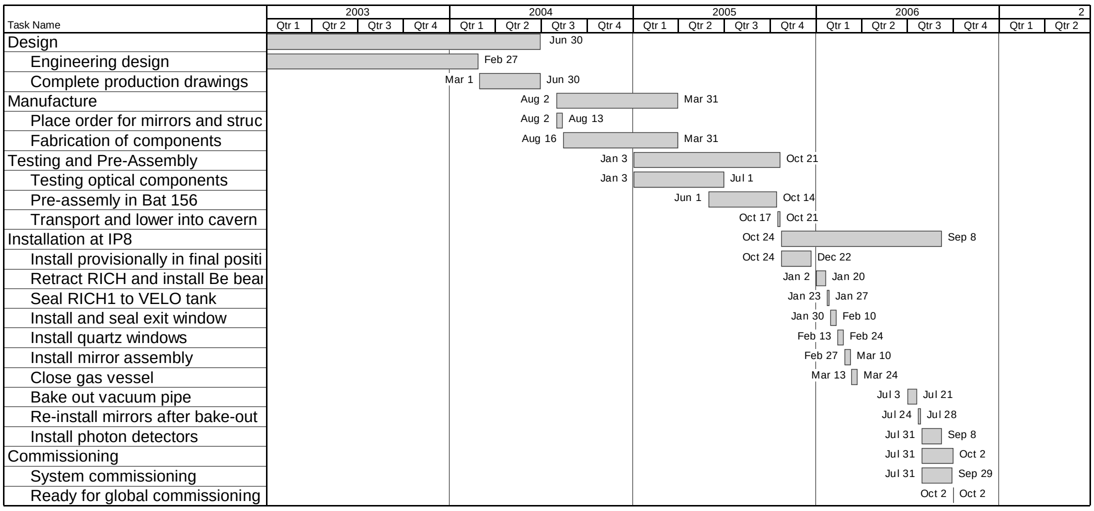

Figure 10.3: Project schedule for RICH 1.

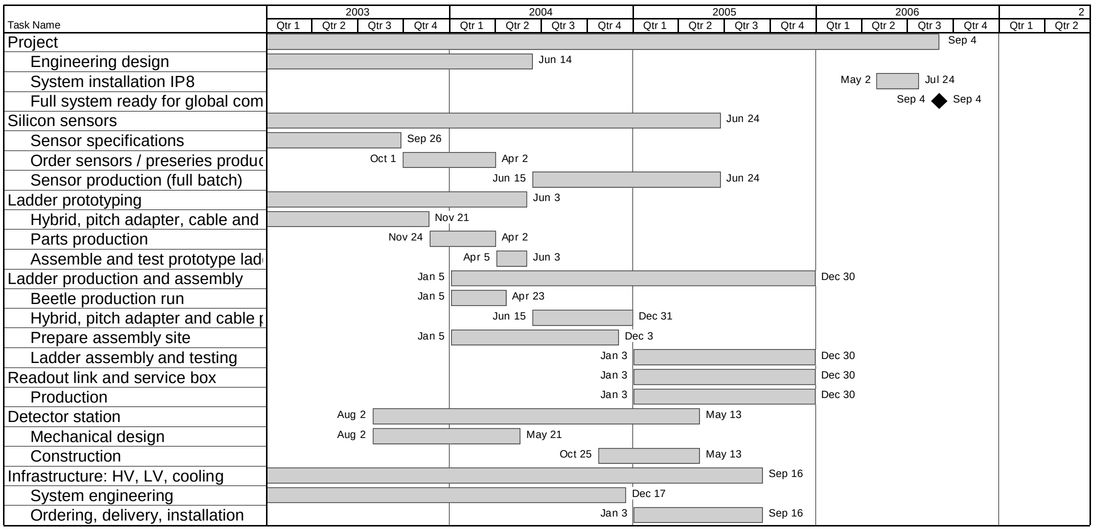

Figure 10.4: Project schedule for the Trigger Tracker (TT).

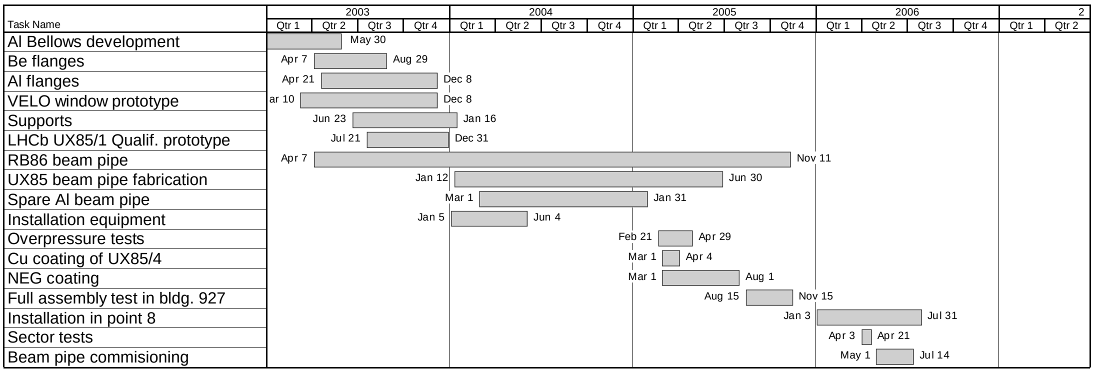

Figure 10.5: Project schedule for the beam pipe.

because of the open geometry of the detector. However, the installation also depends critically on the timely progress of the machine installation and this imposes careful coordination and monitoring of both activities.

Table 10.1: Milestones for the RICH 1 detector.

Milestone	**Date**
Mechanics and optics	
Engineering Design Review	June 2004
Production drawings completed	September 2004
Order for mirrors and structure placed	November 2004
Begin assembly at CERN	September 2005
Mirrors produced and tested	September 2005
Installation and commissioning	
RICH 1 begin installation in IP8	December 2005
System commissioned with > 50% photon detectors	September 2006

Table 10.2: Milestones for the TT station.

Milestone	**Date**
Project	
Engineering design finished	October 2004
Full system ready for global commissioning	September 2006
Silicon sensors	
Final order placed	October 2004
10% sensors delivered	April 2005
All sensors delivered	October 2005
L0 electronics	
10% hybrids assembled and tested	April 2005
All hybrids assembled and tested	October 2005
Mechanics	
Detector station box ready for mounting ladders	August 2005

Table 10.3: Milestones for the beam pipe.

Milestone	**Date**
UX85/1 qualification prototype delivered	December 2003
Engineering Design Review	December 2003
Be beam pipe order placed	June 2004
Be beam pipe delivered	June 2005
Beam pipe installed	July 2006

10.2 Cost of the experiment

The Memorandum of Understanding (MoU) for the detector construction of November 2000 set the cost of the LHCb detector to be 75.05 MCHF [143]. From the very beginning of the reoptimization studies, we have strived to keep the cost of the resulting detector within this limit. The planned detector changes have reduced the cost of the Outer Tracker, where the number of planes of chambers is now smaller, but have also led to an increase in costs for other sub-detectors owing to the use of more technologically advanced materials.

The design of the Trigger Tracker has been affected by the reoptimization work in order to improve the performance of the trigger. As described in this document, the major change is that it is made entirely from silicon strip detectors rather than a mixture of the straw Outer Tracker and silicon Inner Tracker. Since the silicon detector has to cover a larger area, the cost of the station has increased. Table 10.4 summarizes the cost of the Trigger Tracker.

Reoptimization of VELO resulted in a reduction in the number of silicon sensors. However, the cost per station has increased in order to maintain the high detection efficiency with thinner silicon sensors than proposed in the TDR. As a result, the cost of the VELO system remains unchanged compared to the estimate given in the TDR [4].

Compared to the design of the tracking station described in the Inner Tracker TDR [6], no change has been introduced by the reoptimization work. Further development in the electronics since the submission of the TDR has allowed the cost of the IT to be reduced by 680 kCHF.

In the Outer Tracker TDR, eight stations were foreseen for the Outer Tracker. This is now reduced to three large stations downstream of the magnet. As a result, the cost of the Outer Tracker is reduced

Table 10.4: Cost estimate for the Trigger Tracker in kCHF.

Item	Number of units	Cost (kCHF)
Sensors	1110	1732
L0 electronics		269
FE chips	1600	
Hybrid	530	
Substrates	530	
Pitch adaptors	530	
Interconnects	336	
Readout links	6359	530
L1 electronics		490
L1 board	67	
Readout unit	6	
Crates	6	
Mechanics		200
Infrastructure		180
HV	1	
LV	1	
Cooling system	1	
Total		3401

by 3074 kCHF with respect to the cost given in the TDR [2].

Table 10.5 summarizes the cost of the RICH 1 mechanics which has increased by 492 kCHF compared to that given in the TDR [7]. This has been necessary in order to decrease the material budget and protect the photon detector from the magnetic field introduced to improve the trigger performance. The design change also requires a slight increase in the area to be covered by the photon detector. The cost for the service equipment evaluated to be 365 kCHF in the TDR has also increased by 60 kCHF.

RICH 2 has not been affected by the reoptimization work. However, the cost of its mechanics has increased by 71 kCHF with respect to the TDR cost [7].

The baseline solution for photon detection recently changed from the hybrid photodiode (HPD) to the multianode photomultiplier (MaPMT). Technical details of the change and its consequences will be described in an addendum to the RICH TDR. A costing has been made for MaPMT's with analogue read-out, as binary read-out of MaPMT's has not yet been proven to work. The use of MaPMT's and the increase of the area to be covered by the photon detector in RICH 1 results in a cost increase of 341 kCHF compared with that estimated in the TDR. The analogue read-out electronics involves an additional cost of 925 kCHF, which has to be added to the overall RICH cost.

Table 10.5: Cost estimate for the RICH 1 mechanics in kCHF.

Item	Number of units	Cost (kCHF)
Superstructure	1	380
Spherical mirror	4	170
Plane mirror	16	33
Mirror supports	4	94
Photodetector support	2	110
Quartz window	2	50
Aerogel	50 l	134
Shielding box	2	150
Total		1121

Table 10.6: The currently estimated cost of the LHCb detector in MCHF. The estimate for the total cost given in the MoU in November 2000 is also indicated.

Subsystem	Cost [MCHF]
VELO	4.82
IT	2.47
TT	3.40
OT	6.23
RICH	9.57
Calorimeters	15.06
Muon Detector	6.93
Muon filter	4.00
Level-0 trigger	2.43
DAQ and CPU farm	5.71
ECS and TFC	1.58
Computing infrastructure	0.71
Infrastructure	4.00
Magnet	6.00
The current total cost	72.91
MoU cost in 2000	75.05

The calorimeter system has not been affected by the reoptimzation work and its construction is progressing well. The current cost estimate of the system is 300 kCHF less than that given in the TDR [8].

Several modifications have been introduced to the Muon system since the approval of TDR, such as replacing the RPC part by MWPC. Details of the modifications can be found in the Addendum to the Muon TDR submitted to the LHCC [10].

The revised cost of the system is 100 kCHF more than that given in its TDR [9].

As described in the Trigger TDR [3], the Level-0 Trigger architecture remains unchanged from that of the Technical Proposal [1]. The evolution of the Level-1 trigger implementation has resulted in a design where the Level-1 and High Level Trigger algorithms are executed in the same CPU farm. The cost of the total system which includes the Level-1/HLT farm and the data acquisition system is 5711 kCHF.

The costs for the Experimental Control System (ECS) and Computing Infrastructure remain unchanged compared to those given in the Online TDR [144].

The cost of the magnet remains unchanged from that given in the TDR [5].

Table 10.6 summarises the cost of the experiment after the reoptimization work. Compared to the MoU estimate of November 2000, it shows a cost reduction of 2.14 MCHF.

References

[1] LHCb Collaboration, S. Amato *et al.*, Technical Proposal, CERN–LHCC/98–4.

[2] LHCb Collaboration, P.R. Barbosa Marinho *et al.*, Outer Tracker Technical Design Report, CERN–LHCC/2001–24.

[3] LHCb Collaboration, R. Antunes Nobrega *et al.*, Trigger Technical Design Report, CERN–LHCC/2003–31.

[4] LHCb Collaboration, P.R. Barbosa Marinho *et al.*, Vertex Locator Technical Design Report, CERN–LHCC/2001–11.

[5] LHCb Collaboration, S. Amato *et al.*, Magnet Technical Design Report, CERN–LHCC/2000–7.

[6] LHCb Collaboration, A. Franca Barbosa *et al.*, Inner Tracker Technical Design Report, CERN–LHCC/2002–29.

[7] LHCb Collaboration, S. Amato *et al.*, RICH Technical Design Report, CERN–LHCC/2000–37.

[8] LHCb Collaboration, S. Amato *et al.*, Calorimeter System Technical Design Report, CERN–LHCC/2000–36.

[9] LHCb Collaboration, P.R. Barbosa Marinho *et al.*, Muon System Technical Design Report, CERN–LHCC/2001–10.

[10] LHCb Collaboration, Addendum to the Muon System Technical Design Report, CERN–LHCC/2003–2.

[11] G. Corti and G. von Holtey, “Study of beam pipe induced background in the LHCb detector for the optimization of the vacuum chamber design”, LHCb/2003–85.

[12] J. Knaster, “Interface specification of the LHCb beam vacuum chamber”, LHC–VC8–ES–1, EDMS: 382798.

[13] C. Benvenuti *et al.*, “Vacuum properties of TiZrV non-evaporable getter films”, Vacuum **60** (2001) 57.

[14] J. Knaster, “Technical specification for the supply of aluminium forgings for ultra-high vacuum applications for the vertex window of LHCb”, DO–20078/LHC/LHC.

[15] R. Nieminen, METLAB Oy test report No. 2932/2.

[16] G. Arnau-Izquierdo, “Creep test of a forged EN-AW-6061-T652 block at 150°C under 150 MPa stress”, EDMS: 372760.

[17] J.M. Dalin, “Examen par ultrasons”, EDMS: 353556.

[18] A. Gerardin, “Metallurgical analysis of an EN AW-5754 aluminium bellows”, EDMS: 326971.

[19] A. Gerardin, “Metallurgical observations of electron beam welds EN AW 2219 to AlBe Met 162 and AlBe Met 162 to AlBe Met 162”, EDMS: 362624.

[20] J. Knaster *et al.*, “Mechanical analysis of the LHCb vacuum chamber: buckling analysis”, EST–ME/2003–6.

[21] Minutes of the LHCb VELO engineering design review, LEA–LI–ER–2 v1.0, EDMS: 365579.

[22] R. Veness *et al.*, “Study of minimized UHV flanges for LHC experiments”, Vac. Tech. Note 2000–27.

[23] CERN Safety Instructions IS No. 25, EDMS: 335747. `http://edms.cern.ch/file/335747/LAST_RELEASED/IS25_E.pdf`

[24] J. Knaster *et al.*, “LHCb beam pipe installation procedure”, LHC–VC8–IP–1, EDMS: 399872.

[25] H. Dijkstra and T. Ruf, “Further optimization of the VELO material”, LHCb/2001–99.

[26] J.F.J. van den Brand *et al.*, “Material choice for the vacuum container around the LHCb VELO detector”, LHCb/2003–55.

[27] J.P. Palacios, “Material distribution in the VELO—an update”, LHCb/2003–72.

[28] T. Bowcock and J. Carroll, “Prototype LHCb VELO Module Design”, LHCb/2003–87.

[29] L. Wiggers *et al.*, “R-sensor sectors and strip pitch”, LHCb/2003–12.

[30] S. Biagi *et al.*, “LHCb VELO sensor review”, LHCb/2003–58.

[31] A. Gouldwell *et al.*, “Guard ring width impact on impact parameter performances and structure simulations”, LHCb/2003–34.

[32] M. Adinolfi *et al.* "LHCb RICH 2 Engineering Design Review Report", LHCb–EDR/2002–9.

[33] E. Albrecht *et al.*, Nucl. Inst. and Methods, **A488** (2002) 110.

[34] G. Wilkinson *et al.*, "A simulation study of the LHCb RICH performance", LHCb/2000–66; `http://lhcb-rich.web.cern.ch/lhcb-rich/html/agenda_991103.html`

[35] N. van Bakel *et al.* "The Beetle reference manual", LHCb/2001–46.

[36] A. Chamonal, *et al.* "Multianode photo multiplier tube signal response to magnetic fields up to 35 mT", LHCb/2003–42.

[37] H. Dijkstra, *et al.* "The relevance of the magnetic field in the Level-1 trigger", LHCb/2003–110.

[38] A. Papanestis, "Limits of software compensation for mirror misalignment of the RICH detector", LHCb/2001–141.

[39] N. Akopov *et al.*, Nucl. Inst. and Methods, **A479** (2002) 511.

[40] M. Laub, "Development of opto-mechanical tools and procedures for the new generation RICH-detectors at CERN", LHCb/2001–130.

[41] T. Bellunato *et al.*, "Light composite mirrors for RICH detectors: production, characterization and stability tests", LHCb/2003–76, submitted to Nucl. Inst. and Methods A.

[42] C. D'Ambrosio *et al.*, "An experimental setup to measure the long-term stability of large-mirror supports", LHCb/2000–20.

[43] INTAS-679 European Project.

[44] T. Bellunato *et al.*, "Performance of aerogel as Cherenkov radiator", LHCb/2003–29, submitted to Nucl. Inst. and Methods A.

[45] G. Corti and L. Shekhtman, "Radiation background in the LHCb experiment", LHCb/2003–83.

[46] A.R. Buzykaev *et al.*, Nucl. Inst. and Methods, **A494** (2002) 491.

[47] A. Braem *et al.*, Nucl. Inst. and Methods **A478** (2002) 400.

[48] R. Forty, Nucl. Inst. and Methods **A384** (1996) 167.

[49] `http://irradiation.web.cern.ch/irradiation/irrad1.htm`

[50] `http://irradiation.web.cern.ch/irradiation/irrad2.htm`

[51] `http://www.mds.nordion.com`

[52] P. Loveridge, "Finite element calculations of the RICH 1 mechanical structure". `http://agenda.cern.ch/age?a021709`

[53] S. Cuneo *et al.*, "A proposal for a supporting structure for the MaPMT's of RICH 2", LHCb/2000–5.

[54] O. Steinkamp, "Layout and R&D for an all-silicon TT station", LHCb/2002–56.

[55] P. Moreira *et al.*, "A radiation tolerant gigabit serializer for LHC data transmission", 7th Workshop on Electronics for LHC Experiments, CERN–LHCC/2001–34.

[56] M. Andrieux *et al.*, Nucl. Inst. and Methods **A426** (1999) 332.

[57] "GEANT detector description and simulation tool", CERN Program Library long writeup W5013 (1994).

[58] M. Agari *et al.*, "Testbeam results on multi-geometry prototype sensors for the LHCb Inner Tracker", LHCb/2002–58.

[59] N. Virmani *et al.*, "GLAST LAT silicon strip detector (SSD) quality and robustness assurance", GLAST LAT–CR–00082–03.

[60] M. Krammer, "Experience on silicon sensor performance and quality for a large area detector", Proc. 11th Int. Workshop on Vertex Detectors (VERTEX 2002), Hawaii, 3–8 Nov. 2002, to be published in Nucl. Inst. and Methods A.

[61] R.P. Bernhard *et al.*, "Measurements of prototype ladders for the silicon tracker with a laser", LHCb/2003–75.

[62] M. Agari *et al.*, "Testbeam measurements on prototype ladders for the LHCb TT station", LHCb/2003–82.

[63] J. Gasser *et al.*, "Capacitance measurements on silicon micro-strip detectors for the TT station of the LHCb experiment", LHCb/2003–81.

[64] S. Heule, “Simulation und Messung von Silizium-Streifen-Detektoren”, Diplomarbeit, Universität Zürich, 2003 (in german), LHCb note in preparation.

[65] C. Hill, “CDF layer 00”, and K. Hanagaki, “D0 layer 0”, both in Proc. 11th Int. Workshop on Vertex Detectors (VERTEX 2002), Hawaii, 3–8 Nov. 2002, to be published in Nucl. Inst. and Methods A.

[66] ANSOFT Maxwell SV, `http://www.ansoft.com/maxwellsv`

[67] Linear Technology LTspice/SwitcherCAD III, `http://www.linear.com/software`

[68] A. Vollhardt, “A prototype for the silicon tracker data readout system”, LHCb/2003–45.

[69] A. Vollhardt, “Neutron irradiation results for the LHCb silicon tracker readout system components”, LHCb/2003–48.

[70] T. Sjöstrand *et al.*, Computer Physics Commun. **135** (2001) 238.

[71] QQ program, `http://www.lns.cornell.edu/public/CLEO/soft/QQ`.

[72] T. Sjöstrand and M. van Zijl, Phys. Rev. D **36** (1987) 2019.

[73] UA5 Collaboration, G.J. Alner *et al.*, Phys. Reports **154** (1987) 247.

[74] CDF Collaboration, F. Abe *et al.*, Phys. Rev. D **59** (1999) 32001.

[75] CDF Collaboration, D. Acosta *et al.*, Phys. Rev. D **65** (2002) 072005.

[76] UA5 Collaboration, G.J. Alner *et al.*, Z. Phys. C **33** (1986) 1.

[77] CDF Collaboration, F. Abe *et al.*, Phys. Rev. D **41** (1989) 2330.

[78] P. Bartalini *et al.*, LHCb/1999–28, contribution to the 1999 Workshop on Standard Model Physics (and more) at the LHC, CERN 2000–4, May 2000.

[79] R. Field, private communication, and talks available at `http://www.phys.ufl.edu/~rfield/cdf/rdf_talks.html`; we have considered the PYTHIA 6.2 settings referred to as “tune A” on `http://www.phys.ufl.edu/~rfield/cdf/tunes/rdf_tunes.html`.

[80] M. Needham, “Inner and Outer tracker occupancies in the Light LHCb detector”, LHCb/2002–32.

[81] A. Tsaregorodtsev, “Muon system parametrized background — algorithm and implementation”, LHCb/2000–11;
E. Aslanides *et al.*, “Performance of the muon trigger with a realistic simulation”, LHCb/2002–42.

[82] G. Corti and G. von Holtey, “Machine halo in LHCb for various vacuum conditions”, LHCb/2003–86.

[83] A. Polouektov *et al.*, “First results from LHCb Inner Tracker performance studies using new digitization software”, LHCb/2001–118;
M. Needham, “New data model, digitization and reconstruction algorithms for the Inner Tracker”, LHCb/2002–30.

[84] M. Merk *et al.*, “An improved digitization procedure for the Outer Tracker”, LHCb/2001–55.

[85] M. Benayoun and O. Callot, “The forward tracking, an optical model method”, LHCb/2002–8.

[86] R. Forty, “Track Seeding”, LHCb/2001–109.

[87] J. van Tilburg, “Matching VELO tracks with seeding tracks”, LHCb/2001–103.

[88] Y. Xie, “Short track reconstruction with VELO and TT”, LHCb/2003–100.

[89] R. Hierck, “Track following in LHCb”, LHCb/2001–112.

[90] R. Hierck *et al.*, “Performance of the LHCb OO track-fitting software”, LHCb/2000–86.

[91] O. Callot, “Improved robustness of the VELO tracking”, LHCb/2003–17.

[92] M. Needham, “Tracking performance and robustness tests”, LHCb/2003–20.

[93] R. Forty and O. Schneider, “RICH pattern recognition”, LHCb/1998–40.

[94] T. Gys *et al.*, “The use of Pixel Hybrid Photon Detectors in the RICH counters of LHCb”, LHCb/2000–64.

[95] F. Muheim *et al.*, “Proposal for Multianode Photomultiplier tubes as photodetectors for the LHCb RICH”, LHCb/2000–65.

[96] `http://j.home.cern.ch/j/jonesc/www/OORich/reco/RichOODoc/index.html`

[97] J.R.T. de Mello Neto and M. Gandelman, “Muon ID performance with the reoptimized LHCb detector”, LHCb/2003–89.

[98] H. Terrier and I. Belyaev, “Particle identification with LHCb calorimeters”, LHCb/2003–92.

[99] V. Breton, N. Brun and P. Perret, “A clustering algorithm for the LHCb electromagnetic calorimeter using cellular automaton”, LHCb–2001–123.

[100] O. Deschamps *et al.*, “Photon and neutral pion reconstruction”, LHCb/2003–91.

[101] Y. Xie, “$\mathrm{K^0_S}$ reconstruction”, LHCb/2003–88.

[102] G. Pakhlova and I. Belyaev, “Radiative B decays with LHCb”, LHCb/2003–90.

[103] F. Machefert, P. Robbe, M.-H. Schune, O. Deschamps and A. Robert, “$\mathrm{B^0} \to \pi^+\pi^-\pi^0$ reconstruction”, LHCb/2003–77.

[104] M. Kobayashi and T . Maskawa, Prog. Theor. Phys. **49** (1973) 652.

[105] N. Cabibbo, Phys. Rev. Lett. **10** (1963) 531.

[106] L. Wolfenstein, Phys. Rev. Lett. **51** (1983) 1945.

[107] For one of the most recent CKM analyses, see M. Battaglia *et al.*, “The CKM matrix and the unitarity triangle”, `arXiv:hep-ph/0304132`, 2003.

[108] BABAR Collaboration, B. Aubert *et al.*, Phys. Rev. Lett. **87** (2001) 091801.

[109] BELLE Collaboration, K. Abe *et al.*, Phys. Rev. Lett. **87** (2001) 091802.

[110] BABAR Collaboration, B. Aubert *et al.*, Phys. Rev. Lett. **89** (2002) 201802;
BELLE Collaboration, K. Abe *et al.*, Phys. Rev. D **66** (2002) 071102.

[111] BABAR Collaboration, B. Aubert *et al.*, Phys. Rev. Lett. **89** (2002) 281802.

[112] BELLE Collaboration, K. Abe *et al.*, Phys. Rev. D **68** (2003) 012001.

[113] R. Aleksan, I. Dunietz and B. Kayser, Z. Phys. C **54** (1992) 653.

[114] R. Fleischer, Phys. Lett. B **459** (1999) 306.

[115] M. Gronau and D. Wyler, Phys. Lett. B **265** (1991) 172;
I. Dunietz, Phys. Lett. B **270** (1991) 75.

[116] V. Vagnoni *et al.*, “Selection of $\mathrm{B^0_{(s)}} \to \mathrm{h^+h^-}$ decays at LHCb”, LHCb/2003–123.

[117] A. Golutvin, R. Hierck, J. van Hunen, M. Prokudin and R. White, “$\mathrm{B^0_s} \to \mathrm{D_s^{\mp}K^{\pm}}$ and $\mathrm{B^0_s} \to \mathrm{D_s^-}\pi^+$ event selection”, LHCb/2003–127.

[118] S. Amato, J.R.T. de Mello Neto and C. Nunes, “The LHCb sensitivity to $\sin(2\beta)$ from $\mathrm{B^0} \to \mathrm{J}/\psi(\mu\mu)\mathrm{K^0_S}$ asymmetry”, LHCb/2003–107.

[119] H. Terrier and B. Pietrzyk, “$\mathrm{B^0} \to \mathrm{J}/\psi(\mathrm{ee})\mathrm{K^0_S}$ selection”, LHCb/2003–125.

[120] G. Raven, “Selection of $\mathrm{B^0_s} \to \mathrm{J}/\psi\phi$ and $\mathrm{B^+} \to \mathrm{J}/\psi\mathrm{K^+}$”, LHCb/2003–118.

[121] Particle Data Group, K. Hagiwara *et al.*, Phys. Rev. D **66** (2002) 010001, and 2003 off-year partial update for the 2004 edition available on the PDG web site: `http://pdg.lbl.gov/`.

[122] BABAR Collaboration, The BaBar Physics Book, P. Harrison and H. Quinn eds., 2002.

[123] BABAR Collaboration, B. Aubert *et al.*, `arXiv:hep-ex/0306030`, BABAR-PUB/03-013, submitted to Phys. Rev. Lett.

[124] K. Akiba and M. Gandelman, “γ sensitivity with $\mathrm{B^0} \to \mathrm{D^0K^{*0}}$”, LHCb/2003–105.

[125] L. Allebone and U. Egede, “Exclusive selection of $\mathrm{B^0} \to \mathrm{D^{*-}}\pi^+$”, LHCb/2003–126.

[126] B. Carron, “The $\mathrm{B^0_s} \to \mathrm{J}/\psi(\mu\mu)\eta(\gamma\gamma)$ reconstruction at LHCb”, LHCb/2003–102.

[127] L. Fernández, “The $\mathrm{B^0_s} \to \eta_c(4\mathrm{h})\phi(\mathrm{K^+K^-})$ reconstruction at LHCb”, LHCb/2003–101.

[128] J.H. Lopes, “Study of the rare $\mathrm{B^0}$ decay to $\mathrm{K^{*0}(K^+\pi^-)}\mu^+\mu^-$ with the LHCb detector”, LHCb/2003–104.

[129] S. Barsuk and I. Belyaev, “The $\mathrm{B^0_s} \to \phi\phi$ reconstruction at LHCb”, LHCb/2003–094.

[130] L. de Paula and E.C. de Oliveira, “The control channel $\mathrm{B}^0 \rightarrow \mathrm{J}/\psi(\mu\mu)\mathrm{K}^{*0}$”, LHCb/2003–108.

[131] O.P. Yushchenko, “Search for the $\mathrm{B}_\mathrm{c}^+ \rightarrow \mathrm{J}/\psi(\mu\mu)\pi^+$ decay with the LHCb spectrometer”, LHCb/2003–113.

[132] D. Du and L. Guo, J. Phys. G **23** (1997) 525.

[133] A. Ali, E. Lunghi, C. Greub and G. Hiller, Phys. Rev. D **66** (2002) 034002.

[134] M. Calvi, O. Dormond and M. Musy, “LHCb flavour tagging performance”, LHCb/2003–115.

[135] M. Beneke and A. Lenz, J. Phys. G **27** (2001) 1219.

[136] P. Ball *et al.*, “B decays at the LHC”, `arXiv:hep-ph/0003238`, proceedings of the workshop on “Standard Model Physics (and more) at the LHC”, CERN 2000–4.

[137] G. Raven, “Sensitivity studies of χ and $\Delta\Gamma$ with $\mathrm{B}_\mathrm{s}^0 \rightarrow \mathrm{J}/\psi(\mu\mu)\phi(\mathrm{K}^+\mathrm{K}^-)$”, LHCb/2003–119.

[138] R. Hierck, J. van Hunen and M. Merk, “The sensitivity for Δm_s and $\gamma + \phi_\mathrm{s}$ from $\mathrm{B}_\mathrm{s}^0 \rightarrow \mathrm{D}_\mathrm{s}^-\pi^+$ and $\mathrm{B}_\mathrm{s}^0 \rightarrow \mathrm{D}_\mathrm{s}^\mp\mathrm{K}^\pm$ decays”, LHCb/2003–103.

[139] V. Vagnoni *et al.*, “CP sensitivity with $\mathrm{B}_{(\mathrm{s})}^0 \rightarrow \mathrm{h}^+\mathrm{h}^-$ decays at LHCb”, LHCb/2003–124.

[140] M. Beneke, G. Buchalla, M. Neubert and C.T. Sachrajda, Nucl. Phys. B **606** (2001) 245; updated in M. Beneke, `arXiv:hep-ph/0207228`.

[141] BELLE Collaboration, K. Abe *et al.*, `arXiv:hep-ex/0308035`, submitted to Phys. Rev. Lett.

[142] E. Polycarpo, “Analysis of the LHCb sensitivity to the rare decay $\mathrm{B}_\mathrm{s}^0 \rightarrow \mu^+\mu^-$”, LHCb/2002–27.

[143] Memorandum of Understanding, LHCb–RRB–D/2000–24 rev.

[144] LHCb Collaboration, P.R. Barbosa Marinho *et al.*, Online System Technical Design Report, CERN–LHCC/2001–40.